TECHNISCHE
UNIVERSITÄT
DRESDEN

Fakultät für Mathematik und Naturwissenschaften Fachrichtung Physik, Institut für Angewandte Physik
Lehrstuhl für Halbleiterspektroskopie

Integration of III-V compound nanocrystals in silicon via ion beam implantation and flash lamp annealing

Rene Wutzler
Born on: 25th December 1988 in Karl-Marx-Stadt jetzt Chemnitz

Dissertation

to achieve the academic degree

Doktor der Naturwissenschaften (Dr. rer. nat.)

First referee
Prof. Dr. Manfred Helm
Second referee
Prof. Dr. Johannes Heitmann

Submitted on: 21st March 2017
Defended on: 26th September 2017

TECHNISCHE
UNIVERSITÄT
DRESDEN

Fakultät für Mathematik und Naturwissenschaften Fachrichtung Physik, Institut für Angewandte Physik

Lehrstuhl für Halbleiterspektroskopie

Abstract

The progress in device performance of modern microelectronic technology is mainly driven by down-scaling. In the near future, this road will probably reach a point where physical limits make even more down-scaling impossible. The substitution of single components material-wise over the last decades, like high-k dielectrics or metal gates, has been a suitable approach to foster performance improvements. In this scheme, the integration of high-mobility III-V compound semiconductors as channel materials into Si technology is a promising route to follow for the next one or two device generations. III-V integration, today, is conventionally performed by using techniques like molecular beam epitaxy or wafer bonding which utilize solid phase crystallization but suffer to strain due to the lattice mismatch between III-V compounds and Si. An alternative approach using sequential ion beam implantation in combination with a subsequent flash lamp annealing is presented in this work.

Using this technique, nanocrystals from various III-V compounds have been successfully integrated into bulk Si and Ge as well as into thin Si layers which used either SOI substrates or were grown by plasma-enhanced chemical vapour deposition. The III-V compounds which have been fabricated are GaP, GaAs, GaSb, InP, InAs, GaSb and $\mathrm{In_xGa_{1\text{-}x}As}$ with variable composition. The structural properties of these nanocrystals have been investigated by Rutherford backscattering, scanning electron microscopy and transmission electron microscopy, including bright-field, dark-field, high-resolution, high-angle annular dark-field and scanning mode imaging, electron-dispersive x-ray spectroscopy and energy-filtered element mapping. Furthermore, Raman spectroscopy and X-ray diffraction have been performed to characterise the nanocrystals optically.

In Raman spectroscopy, the characteristic transversal and longitudinal optical phonon modes of the different III-V compounds have been observed. These signals proof that the nanocrystals have formed by the combination of ion implantation and flash lamp annealing. Additionally, the appearance of the typical phonon modes of the respective substrate materials verifies recrystallization of the substrate by the flash lamp after amorphisation during implantation. In the bulk Si samples, the nanocrystals have a circular or rectangular lateral shape and they are randomly distributed at the surface. Their cross-section has either a hemispherical or triangular shape. In bulk Ge, there are two types of precipitates: one at the surface with arbitrary shape and another one buried with circular shape. For the thin film samples, the lateral shape of the nanocrystals is more or less arbitrary and they feature a block-like cross-section which is limited in height by the Si layer thickness. Regarding crystalline quality, the nanocrystals in all samples are mainly single-crystalline with only a few number of stacking faults. However, the crystalline quality in the bulk samples is slightly better than in the thin films. The X-ray diffraction measurements display the (111), (220)

and (311) Bragg peaks for InAs and GaAs as well as for the $In_xGa_{1-x}As$ where the peaks shift with increasing In content from GaAs towards InAs.

The underlying formation mechanism is identified as liquid phase epitaxy. Hereby, the ion implantation leads to an amorphisation of the substrate material which is then molten by the subsequent flash lamp annealing. This yields a homogeneous distribution of the implanted elements within the melt due to their strongly increased diffusivity in the liquid phase. Afterwards, the substrate material starts to recrystallize at first and an enrichment of the melt with group-III and group-V elements takes place due to segregation. When the temperature is low enough, the III-V compound semiconductor starts to crystallize using the recrystallized substrate material as a template for epitaxial growth.

In order to gain control over the lateral nanocrystal distribution, an implantation mask of either aluminium or nickel is introduced. Using this mask, only small areas of the samples are implanted. After flash lamp treatment, nanocrystals form only in these small areas, which allows precise positioning of them. An optimal implantation window size with an edge length of around 300 nm has been determined to obtain one nanocrystal per implanted area. During an additional experiment, the preparation of Si nanowires using electron beam lithography and reactive ion etching has been conducted. Hereby, two different processes have been investigated; one using a ZEP resist, a lift-off step and a Ni hard mask and another one using a hydrogen silsesquioxane resist which is used directly as a mask for etching. The HSQ-based process turned out to yield Si nanowires of better quality. Combining both, the masked implantation and the Si nanowire fabrication, it might be possible to integrate a single III-V nanocrystal into a Si nanowire to produce a III-V-in-Si-nanowire structure for electrical testing.

TECHNISCHE
UNIVERSITÄT
DRESDEN

Fakultät für Mathematik und Naturwissenschaften Fachrichtung Physik, Institut für Angewandte Physik

Lehrstuhl für Halbleiterspektroskopie

Zusammenfassung

Der Fortschritt in der Leistungsfähigkeit der Bauelemente moderner Mikroelektroniktechnologie wird hauptsächlich durch das Skalieren vorangetrieben. In naher Zukunft wird dieser Weg wahrscheinlich einen Punkt erreichen, an dem physikalische Grenzen weiteres Herunterskalieren unmöglich machen. Der Austausch einzelner Teile auf Materialebene, wie Hoch-Epsilon-Dielektrika oder Metall-Gate-Elektroden, war während der letzten Jahrzehnte ein geeigneter Ansatz, um die Leistungsverbesserung voranzubringen. Nach diesem Schema ist die Integration von III-V-Verbindungshalbleiter mit hoher Mobilität ein vielversprechender Weg, dem man für die nächsten ein oder zwei Bauelementgenerationen folgen kann. Heutzutage erfolgt die III-V-Integration konventionell mit Verfahren wie der Molekularstrahlepitaxie oder dem Waferbonden, welche die Festphasenkristallisation nutzen, die aber aufgrund der Gitterfehlanpassung zwischen III-V-Verbindungen und Silizium an Verspannungen leiden. In dieser Arbeit wird ein alternativer Ansatz präsentiert, welcher die sequenzielle Ionenstrahlimplantation in Verbindung mit einer darauffolgenden Blitzlampentemperung ausnutzt.

Mit Hilfe dieses Verfahrens wurden Nanokristalle verschiedener III-V-Verbindungshalbleiter erfolgreich in Bulksilizium- und -germaniumsubstrate sowie in dünne Siliziumschichten integriert. Für die dünnen Schichten wurden hierbei entweder SOI-Substrate verwendet oder sie wurden mittels plasmagestützer chemischer Gasphasenabscheidung gewachsen. Die hergestellten III-V-Verbindungen umfassen GaP, GaAs, GaSb, InP, InAs, InSb und $\mathrm{In_xGa_{1\text{-}x}As}$ mit veränderbarer Zusammensetzung. Die strukturellen Eigenschaften dieser Nanokristalle wurden mit Rutherford-Rückstreu-Spektroskopie, Rasterelektronenmikroskopie und Transmissionselektronenmikroskopie untersucht. Bei der Transmissionelektronenmikroskopie wurden die Hellfeld-, Dunkelfeld-, hochauflösenden, “high-angle annular dark-field” und Rasteraufnahmemodi sowie die energiedispersive Röntgenspektroskopie und die energiegefilterte Elementabbildung eingesetzt. Darüber hinaus wurden Ramanspektroskopie- und Röntgenbeugungsmessungen durchgeführt, um die Nanokristalle optisch zu charakterisieren.

Mittels Ramanspektroskopie wurden die charakteristischen transversal- und longitudinal-optischen Phononenmoden der verschiedenen III-V-Verbindungen beobachtet. Diese Signale beweisen, dass sich unter Verwendung der Kombination von Ionenstrahlimplantation und Blitzlampentemperung Nanokristalle bilden. Weiterhin zeigt das Vorhandensein der typischen Phononenmoden der jeweiligen Substratmaterialien, dass die Substrate aufgrund der Blitzlampentemperung rekristallisiert sind, nachdem sie durch Ionenimplantation amorphisiert wurden. In den Bulksiliziumproben besitzen die Nanokristalle eine kreisförmige oder rechteckige Kontur und sind in zufälliger Anordnung an der Oberfläche verteilt. Ihr Querschnitt zeigt entweder eine Halbkugel- oder dreieckige Form. Im Bulkgermanium gibt es zwei Arten von Ausscheidungen: eine mit willkürlicher Form an der Oberfläche und eine andere, vergrabene mit sphärischer

Form. Betrachtet man die Proben mit den dünnen Schichten, ist die laterale Form der Nanokristalle mehr oder weniger willkürlich und sie zeigen einen blockähnlichen Querschnitt, welcher in der Höhe durch die Siliziumschichtdicke begrenzt ist. Bezüglich der Kristallqualität sind die Nanokristalle in allen Proben mehrheitlich einkristallin und weisen nur eine geringe Anzahl an Stapelfehlern auf. Jedoch ist die Kristallqualität in den Bulkmaterialien ein wenig besser als in den dünnen Schichten. Die Röntgenbeugungsmessungen zeigen die (111), (220) und (311) Bragg-Reflexe des InAs und GaAs sowie des $\mathrm{In_xGa_{1\text{-}x}As}$, wobei sich hier die Signalpositionen mit steigendem Gehalt an Indium von GaAs zu InAs verschieben.

Als zugrundeliegender Bildungsmechanismus wurde die Flüssigphasenepitaxie identifiziert. Hierbei führt die Ionenstrahlimplantation zu einer Amorphisierung des Substratmaterials, welches dann durch die anschließende Blitzlampentemperung aufgeschmolzen wird. Daraus resultiert eine homogene Verteilung der implantierten Elemente in der Schmelze, da diese eine stark erhöhte Diffusivität in der flüssigen Phase aufweisen. Danach beginnt zuerst das Substratmaterial zu rekristallisieren und es kommt aufgrund von Segregationseffekten zu einer Anreicherung der Schmelze mit den Gruppe-III- und Gruppe-V-Elementen. Wenn die Temperatur niedrig genug ist, beginnt auch der III-V-Verbindungshalbleiter zu kristallisieren, wobei er das rekristallisierte Substratmaterial als Grundlage für ein epitaktisches Wachstum nutzt.

In der Absicht Kontrolle über die laterale Verteilung der Nanokristalle zu erhalten, wurde eine Implantationsmaske aus Aluminium beziehungsweise Nickel eingeführt. Durch die Benutzung einer solchen Maske wurden nur kleine Bereiche der Proben implantiert. Nach der Blitzlampentemperung werden nur in diesen kleinen Bereichen Nanokristalle gebildet, was eine genaue Positionierung dieser erlaubt. Es wurde eine optimale Implantationsfenstergröße mit einer Kantenlänge von ungefähr 300 nm ermittelt, damit sich nur ein Nanokristall pro implantierten Bereich bildet. Während eines zusätzlichen Experiments wurde die Präparation von Siliziumnanodrähten mit Hilfe von Elektronenstrahllithografie und reaktivem Ionenätzen durchgeführt. Hierbei wurden zwei verschiedene Prozesse getestet: einer, welcher einen ZEP-Lack, einen Lift-off-Schritt und eine Nickelhartmaske nutzt, und ein anderer, welcher einen HSQ-Lack verwendet, der wiederum direkt als Maske für die Ätzung dient. Es stellte sich heraus, dass der HSQ-basierte Prozess Siliziumnanodrähte von höherer Qualität liefert. Kombiniert man beides, die maskierte Implantation und die Siliziumnanodrahtherstellung, miteinander, sollte es möglich sein, einzelne III-V-Nanokristalle in einen Siliziumnanodraht zu integrieren, um eine III-V-in-Siliziumnanodrahtstruktur zu fertigen, welche für elektrische Messungen geeignet ist.

Contents

Acknowledgement

A PhD thesis is never the merit of a single person although mainly this single person gets the credit for it. In my case, there were many people who advised, supported, helped and pushed me during the last three and a half years and without whom this work would not have been possible. I am very grateful to all of them and even when they are not named directly in the following, I, nevertheless, owe them a lot.

First, and foremost, I want to express my inexpressible gratitude to Dr. Lars Rebohle, my direct supervisor, for his passionate guidance and advise. He kept me focussed towards the several goals during my thesis and pulled me away from several of my lunatic ideas. He supported me from the beginning to the end and without him, I would have stumbled right at the start.

To the man, who made my work on III-V integration in Si possible, literally, Dr. Sławomir Prucnal, I am very grateful. He initiated the topic in our group before I even could think of doing a PhD and then thoroughly introduced me into his subject. At every time, I could benefit from his knowledge and support.

I want to thank Dr. Wolfgang Skorupa, my official direct supervisor, for all the experience in ion implantation and flash lamp annealing (FLA), for all the scientific incentive and pressure, and for all the constructive and sometimes nasty questions.

Furthermore, I am thankful to Prof. Manfred Helm for the academic supervision at the TU Dresden and for the opportunity to realise my doctorate at the Helmholtz-Zentrum Dresden-Rossendorf (HZDR), for his constructive criticism and for refereeing my thesis. I also want to thank Prof. Johannes Heitmann from the TU Bergakademie Freiberg for taking the second referee spot for my thesis, for his cooperation, patience and effort for submitting two unfortunately fruitless project proposals together with us as well as for his helpful comments in my final phase of writing.

My special thanks goes to Thomas Schumann for the introduction to the FLA system, the unnumbered flashes, we did in order to anneal my samples, and for his company in an abandoned building.

I want to thank the people from the Ion Beam Center at the HZDR, namely Roman Böttger and Stefan Eisenwinder for the planning of all the implantations as well as their execution and for their feedback and comments, René Hübner for the many TEM images, he made from my samples, and for his effort in explaining all the details which

could be seen on them, for his discussion and large interest in my topic, Annette Kunz for the preparation of TEM samples and lamellae I needed for investigating the microstructure of my nanocrystals, Elfi Christalle for all the SEM images, she carefully did, although I sometimes did not properly explain what I wanted to see, Lothar Bischoff for the FIB-cut preparation and investigation of the Si nanowire samples, although the underlying SiO_2 was a pain, Matthias Voelskow and Felipe Bregolin for the RBS measurements and their data interpretation, Jörg Grenzer and Andrea Scholz for the XRD measurements and data analysis and the discussion about amorphous and highly-disordered substrate materials, Stefan Facsko and Martin Engler for the AES measurements, the AFM introduction and the conductive AFM measurements although not shown in this work, and Gabriele Schnabel for the careful cleaning, etching and oxidising of my samples.

I am also grateful to the Nanofabrication group of our institute for their intense support and communication during implantation mask and Si nanowire fabrication. Hereby, my thanks go to Dr. Yordan Georgiev as he pushed the electron beam lithography business and introduced the HSQ-based process, to Dipjyoti Deb for all his experience and testing in Si nanowire production, Tommy Schönherr and Claudia Neisser for all the electron beam writing and the careful mask preparations, and Bernd Scheumann for the reactive ion etching and playing around with recipes.

Further gratitude goes to the recent and former members of our Semiconductor Materials group: Wolfgang Skorupa, Lars Rebohle, Sławomir Prucnal, Viton Heera, Matthias Voelskow, Shengqiang Zhou, Thomas Schumann, Ilona Skorupa, Yonder Berencen, Bernadeta Pelic, Felipe Bregolin, Jan Fiedler, Denise Reichel and Susette Germer, for the support during the whole time, for all the test talks, for the all the comments and suggestions, for all the answered questions and for the sometimes necessary distraction from scientific topics.

Finally, I want to thank my family and my friends, who supported me the whole time, kept me grounded and offered distraction from science whenever possible. Special thanks, hereby, goes to Christina, my wife, who went through all the deep valleys of frustration and desperation with me and pushed me to get this thing done.

Thank you!

René Wutzler
HZDR
Dresden, 2017

List of Abbreviations

Notation	**Description**
2TA	second harmonic of the transverse acoustic phonon mode
AC	alternating current
AFM	atom force microscopy
ART	aspect ratio trapping
CVD	chemical vapour deposition
DWELL	quantum dots-in-a-well
EBL	electron beam lithography
EDXS	energy-dispersive X-ray spectroscopy
EFTEM	energy-filtered TEM
ELO	epitaxial lateral overgrowth
ELPE	explosive liquid phase epitaxy
ELPN	explosive liquid phase nucleation
EOR	end-of-range defects
ESPE	explosive solid phase epitaxy
ESPN	explosive solid phase nucleation
fcc	face-centred cubic
FET	field effect transistor
FFT	Fast Fourier Transform
FLA	flash lamp annealing
FWHM	full-width at half maximum
GeOI	Germanium-on-Insulator
HAADF-STEM	high-angle annular dark-field STEM
HEMT	high-electron-mobility transistor
HRTEM	high-resolution TEM
HSQ	hydrogen silsesquioxane
IBE	ion beam etching
IC	integrated circuit
ICP	inductively coupled plasma
IR	infrared
LED	light emitting diode
LO	longitudinal optical (phonon mode)
LPE	liquid phase epitaxy

Notation	**Description**
LVM	local vibrational mode
MBE	molecular beam epitaxy
MOCVD	metal-organic chemical vapour depostion
MOS	metal oxide semiconductor
NC	nanocrystal
NW	nanowire
PECVD	plasma-enhanced chemical vapour deposition
PLA	pulsed laser annealing
PMMA	poly(methyl methacrylate)
QD	quantum dot
QDIP	quantum dot infrared photodetector
QW	quantum well
QWIP	quantum well infrared photodetector
RBS	Rutherford Backscattering
RF	radio frequency
RIBE	reactive ion beam etching
RIE	reactive ion etching
RTP	rapid thermal processing
SAG	selective area growth
SEM	scanning electron microscopy
SIMOX	separation by implantation of oxygen
SL	superlattice
SOI	Silicon-on-Insulator
SPC	solid phase crystallization
SPE	solid phase epitaxy
SRIM	“The Stopping and Range of Ions in Matter” code
STEM	scanning TEM
TEM	transmission electron microscopy
TO	transverse optical (phonon mode)
UV	ultraviolet
VLS	vapour-liquid-solid
XRD	X-ray diffraction

List of Symbols

Notation	Description
A	slope of a linear equation
B	intersection with the ordinate for a linear equation
C	factor for the relative size of impurity and host atoms (Enskog's theory)
D	diffusion coefficient
E_{G}	band gap energy
E	energy
G	Gibbs free energy
H	enthalpy
K_0	atomic valence
L_{D}	diffusion length
M	exciton translational mass
N_{A}	Avogadro constant
N	number of atoms
P	pressure
R	radius
T_{melt}	melting temperature
T	temperature
V_{charge}	charging voltage of a capacitor used during FLA
V	volume
Z	Zeldovich factor for nucleation
Δa	lattice mismatch
$\Phi_{l,n}$	n-th root of the spherical Bessel function of order l
Ψ	chemical potential
β	rate at which an atom attaches to a nucleus during the nucleation process
γ	surface tension
κ	volume compressibility at room temperature
λ	wavelength
μ_{Exciton}	exciton reduced mass
μ_{e}	electron mobility

Notation	**Description**
μ_h	hole mobility
ν_s	reduced mass of impurity and host atoms (Enskog's theory)
ω	wavenumber
ρ	atomic density
σ_FLA	energy density of a flash lamp pulse
σ	diameter of a hard sphere (Enskog's theory)
θ	XRD scattering angle
$\boldsymbol{J}$	diffusion flux
ξ	deviation from Vegard's law
a	lattice parameter
c	concentration of a substance
d	lattice plane distance
e	elementary charge
f	Goldschmidt atomic diameter (distance between two neighbouring atoms)
$g(\sigma)$	radial distribution function of the hard sphere diameter (Enskog's theory)
j	nucleation rate
k_B	Boltzmann constant
k	segregation coefficient
m_e	effective mass of an electron
m_h	effective mass of a hole
n	integer giving the order of diffraction
q	reciprocal space coordinate
s	height of a spherical cap
t	time
x	composition value in an $\mathrm{A_xB_{1\text{-}x}C}$ material

1 Introduction

In a scientific work on semiconductor physics or materials science related to semiconductors, no one gets around talking about a specific element which is the carthorse of the information age - silicon. Si-based technology penetrates almost every area of life and is nearly impossible to avoid. Si is found in an endless number of devices on earth, like PCs, cell phones, air planes and cars to name only a few, in earth's orbit, on the moon, in our solar system and even beyond. Almost everybody is in contact with one or another Si-based application in his all-day life and most people cannot even think of a life without Si technology, although they might not even know it.

The odyssey of semiconductor technologies, which nowadays approaches extreme physical limitations, started already in the nineteenth century with the experimental description of the conductivity increase with an increasing temperature using silver sulphide by *Michael Faraday* [1]. This temperature dependent behaviour is typical for semiconductors. Later in this century, two major properties of semiconducting materials were discovered: photoconductivity and rectification. The effect of light on conductivity was first observed in selenium by *Willoughby Smith* in 1873 [2]. Using the same material, in 1876 *Adams* and *Day* described the possibility to produce electricity by shining light on selenium [3]. This discovery led to the invention of the first solar cell in 1883 by *Charles Fritts* [4]. The effect of rectification was first documented by *Ferdinand Braun* in 1875 [5]. Semiconductor rectifiers found their application in reception of radio waves and a first detector made from lead sulfite was patented by *Jagadis C Bose* in 1904 [6]. The introduction of Si as a radio wave detector followed shortly afterwards by *Greenleaf W Pickard* in 1906 [7]. At that time, these rectifiers had their physical limitations and broke down on many occasions. Furthermore, the physical background was not well understood. In the early years of the 20th century, quantum mechanics evolved and helped to enlighten the physics behind semiconductors. *Alan H Wilson* was the first to describe the band theory of semiconductors in 1931 [8, 9].

Further technological steps were then taken in the thirties and forties of the 20th century. Due to the improvement of material purity of silicon and later on germanium, the quality of semiconductor rectifiers improved significantly. With this improvement in quality, now, much effort was devoted to replace vacuum tubes, which had promoted technologies like radio and television, by a solid-state equivalent. The first references of such a device date back to patents by *Julius E Lilienfeld* in 1930 [10, 11] and

1933 [12] and *Oskar Heil* in 1935 [13] on field effect transistors (FETs). However, their work remained almost unnoticed since they did not present any publications nor functioning devices. The next milestone on the journey of Si-based technology is the discovery of the p-n junction by *Russell S Ohl* in 1946 [14]. He used poly-crystalline Si which was accidentally doped and observed light sensitivity, revealing the photovoltaic effect of his samples. Shortly afterwards, *John Bardeen* and *Walter H Brattain* at *Bell Telephone Laboratories* presented their point contact transistor in Ge, which is nowadays known as the invention of the transistor and marks the breakthrough for modern semiconductor technology [15, 16]. *William B Shockley* described the theory behind the point contact transistor extending *Ohl's* p-n junction theory in 1949 [17]. He proved that the function of the transistor is based on a bulk effect, in contrast to *Bardeen* and *Brattain* who thought it was surface related, and presented a slightly different device - the junction transistor. *Shockley*, *Bardeen* and *Brattain* were awarded with the Nobel prize "for their researches on semiconductors and their discovery of the transistor effect" in 1956 [18].

In the following years, new preparation methods resulted in higher quality materials and, in 1952, the industrial production of transistors, still based on Ge, gathered speed. First "transistorized" consumer applications appeared on the market. Due to the high manufacturing costs of transistors, they were mainly installed in portable devices where low power demand and small size were important, like hearing aids and small radios [19]. In 1954, the first transistor based on silicon was achieved almost simultaneously by *Gordon K Teal* from *Texas Instruments* and *Morris Tanenbaum* from *Bell Labs* promising superior properties over Ge-based transistors [20–22]. Further technological improvements like controlled doping by diffusion [23] and the introduction of SiO_2 into the technological process [24] led to improved device characteristics throughout the 1950s. At the end of this decade, the next big leap in Si technology was taken with introducing the concept of integrated circuits (ICs) by *Jack S Kilby* [25] and *Robert N Noyce* [26]. This concept allowed to connect multiple device on one chip where previously single devices had to be connected with wires. *Kilby* was awarded the Nobel prize in 2000 "for his part in the invention of the integrated circuit" [27]. In parallel, *Dawon Kahng* was the first to demonstrate a transistor based on the field effect, as it was already proposed by *Lilienfeld* in the 1920s, using a metal oxide semiconductor (MOS) structure [28]. The MOS structures combined with the concept of ICs slowly penetrated the market and were mainly used for military and aerospace applications since their production cost were higher than the discrete conventional transistors. In 1963, the configuration of using complementary MOS transistors for a low power circuit was presented by *Frank M Wanlass* [29, 30] which then became today's manufacturing principle of choice.

The continuous progress of Si technology and the steadily increasing number of integrated components per circuit, inspired *Gordon Moore* to his (in)famous prediction which is widely known as "Moore's law". By evaluating the development of ICs from 1959 to 1965 and extrapolating this trend, *Moore* predicted a doubling of the number of components in an IC every year until 1975 [31]. In the following years, semiconductor industry grew rapidly and a specialisation of companies took place leading to dedicated front-end and back-end manufacturers as well as equipment and material suppliers. New design innovations like the poly-Si gate [32, 33] and the Schottky-barrier diode [34, 35] improved memory and logic applications by increasing speed and reducing costs and power consumption. The concept of scaling MOS technology [36, 37] described the relation between the device dimension, power demand and performance, and paved the way for more complex architectures. In 1975, *Moore* recognized that his prediction was fulfilled and expanded it to future developments that the components on a chip double in number every two years [38]. “Moore’s law” evolved into the economical driving force of the semiconductor technology and even today the industry tries to keep up with it. For a more detailed historical survey on the evolution of semiconductor technology, I recommend reading references [39–41].

For about 30 years, geometric scaling – reducing the physical dimension of the device – was sufficient to maintain “Moore’s law” down to the 90 nm node and several hundreds of millions of transistors on one chip in the middle of 2000s [41, 42]. At that time, physical limitations for further down-scaling appeared and a significant leakage current due to tunneling affected device performance [42]. To ensure a further performance increase, an alternative to geometric scaling had to be considered. The substitution of SiO_2 by a high-k material as gate dielectric, a metal gate instead of poly-Si and the introduction of strained silicon were such approaches to ensure performance improvements [43–45]. These approaches are called equivalent scaling and enabled the progress to smaller nodes. Additional new design and architecture concepts like multi-gate and FinFET devices or even gate-all-around structures help to achieve smaller nodes until today [46–48]. Another possibility is the introduction of high mobility channel materials, like Ge or III-V compound semiconductors [49–52]. III-V compounds feature generally higher electron mobilities than Si which makes them suitable for the low-power and high-speed applications of the future [53, 54]. However, the integration of III-Vs into Si is challenging due to a typical large lattice mismatch. There are several techniques like molecular beam epitaxy (MBE), metal-organic chemical vapour depostion (MOCVD) or wafer bonding capable of integrating III-V compound semiconductors into Si technology but they usually obtain III-V/Si interfaces which are strained as they employ a solid phase process [55, 56]. An alternative method is the combination of ion beam implantation and flash lamp annealing (FLA) which utilizes a crystallization of the III-V compounds from the liquid phase and is therefore able to reduce the strain between Si and the particular III-V material.

In the course of the present work, this alternative route for III-V integration in Si has been examined. The main objective has been to investigate the capability of a sequential ion implantation combined with a subsequent FLA for the nanocrystal (NC) fabrication of several III-V compound semiconductors in bulk Si and to characterise these NCs regarding their microstructural properties. Additionally, the transfer of the aforementioned preparation technique to other substrate materials, namely Ge, and structures, namely thin Si films, should be evaluated. Another task has been the development of a detailed description of the liquid phase formation mechanism based on the observed experimental results. Finally, a device concept utilizing Si nanowires and local ion implantation should be developed for electrical characterisation of the III-V NCs. In order to present the results achieved towards these objectives, this work is organised in the following way: After the introduction in chapter 1, chapter 2 briefly describes the physical background including some basic physics of structures at the nano-scale and the two main physical processes involved in NC formation in this work, namely diffusion and crystallization. Chapter 3 presents the state-of-the-art regarding III-V compound semiconductors in Si technology and covers the significance of this group of materials as well as the integration techniques. After that, the experimental methods employed during this work are addressed in chapter 4. It is divided into three sections which deal with the simulations, the sample preparation techniques and characterization methods, respectively. The subsequent chapter 5 on the integration of III-V compound semiconductor NCs in silicon presents the results that have been achieved in the course of this work including the fabrication of III-V NCs in bulk materials and thin films as well as the control of their lateral position by a masked implantation. Chapter 6 gives a detailed description of the formation mechanism responsible for the NC formation. In chapter 7, the combination of top-down Si nanowire (NW) preparation and masked ion implantation in order to built a III-V-in-Si-nanowire structure is presented as a future perspective. Finally, a summary is given in chapter 8.

2 Basics

2.1 Physics of semiconductor nanostructures

A semiconductor is a crystalline or amorphous solid material which features a band gap energy larger than 0 eV and lower than approximately 4 eV [57]. The limits are metals, with a band gap energy of 0 eV, on the one side featuring low resistivity, and insulators on the other side featuring high resistivities, e.g. a dielectric like SiO_2. Typical representatives of semiconductors are group-IV elements, i.e. Si and Ge, and compound semiconductors combining group-III and -V or group-II and -VI elements. One could think that semiconductors are element combinations with four valence electrons in sum. However, there are exceptions like the group-IV and -VI compound PbS. Furthermore, there are organic materials, namely carbohydrate polymers with π-bonds, which feature similar electronic properties as the inorganic semiconductors. A characteristic property of each semiconductor is its electronic band structure with a specific electronically forbidden energy range – the band gap. The electrical properties of a semiconductor can easily be manipulated by the introduction of impurities into the crystal structure, which is called doping. Doping is generally done by elements which have either one electron less or one electron more than the elements of the doped material, in order to achieve charge transport by holes or electrons, respectively. The most prominent example is the doping of Si by B or P to fabricate p-type or n-type Si for microelectronic applications.

Another possibility to influence the properties of semiconductor materials is size or, more precisely, the reduction of their dimensionality. When the size of a semiconductor is reduced from bulk material towards smallest scales, the characteristic properties can change dramatically. For example, the melting point of CdS decreases from 1400 °C for bulk material down to about 400 °C for particles with a size of about 1.5 nm [58]. When reducing dimensionality of a bulk material, the first step is a confinement in one dimension of space which leads to a two-dimensional structure. Such thin layers are often referred to as quantum wells (QWs) or superlattices (SLs). The density of states changes from a smooth band with a $E^{\frac{1}{2}}$-dependency to a staircase function. A further confinement in a second direction results in a one-dimensional body which is called NW or nanorod. For one-dimensional structures, the density of states has a $E^{-\frac{1}{2}}$-dependency, leading to a spike-like function. A final confinement in three dimensions

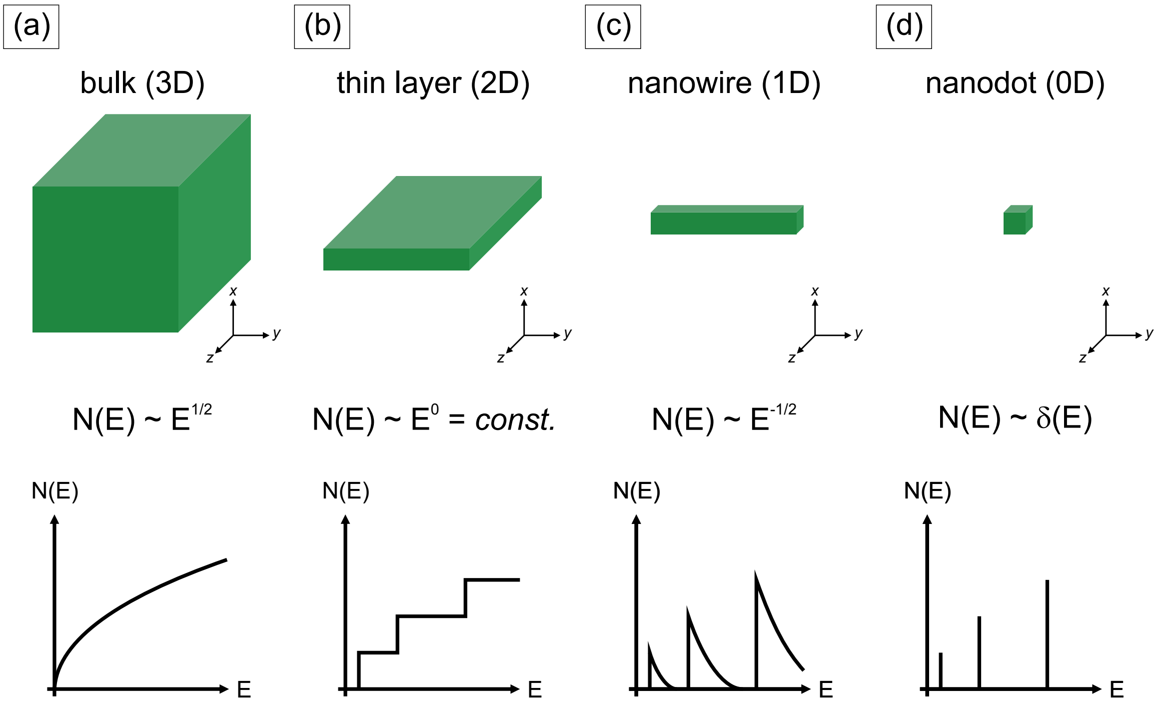

Figure 2.1.1: Schematic overview over dimensionality of nanostructures for (a) bulk material, (b) a thin film, (c) a nanowire, and (d) a nanodot including their respective density of states.

results in zero-dimensional structures which are also known as quantum dots (QDs), nanodots, nanoclusters or NCs. The density of states of such 0D particle behaves like a δ-function and shows discrete energy levels. Figure 2.1.1 schematically depicts the different dimensionalities of nanostructures with their respective densities of states.

The change of the band structure of a semiconductor with decreasing size is known as quantum confinement effect. One of the most obvious effects due to quantum confinement is the change of the optical properties of a material. In CdS and CdSe colloidal NCs, the band gap energy changes depending on the particle size over a wide range [59, 60]. The change of the band gap energy implies a change in the emission wavelength and, therefore, leads to a different colour visible by the naked eye [61], when such NC of different size are dispersed in a solution. Luminescence as well as absorption of these NCs are accounted to interband transitions between electron and hole quantum levels. The energy of these electron (E^e) and hole quantum levels (E^h) can be approximated by [62–64]

$$E^{e,h}_{l,n} = \frac{\hbar^2}{2 \cdot m_{e,h} \cdot R^2_{\mathrm{NC}}} \cdot \Phi^2_{l,n} \tag{2.1}$$

where m_{e}, m_{h} are the effective mass of an electron and hole, respectively, R_{NC} is the radius of a spherical NC and $\Phi_{l,n}$ is the n-th root of the spherical Bessel function of order l. Equation (2.1) assumes spherical NCs which are embedded in an infinite potential barrier and uses an effective mass approximation as well as parabolic bands [62, 65]. As the electrons and holes within these quantum levels interact with each other, an additional Coulomb energy term ($e^2/4\pi\epsilon_0\epsilon_{\mathrm{r}}R_{\mathrm{NC}}$) has to be considered [66, 67]. The influence of the Coulomb energy gradually becomes a smaller correction with decreasing crystal size, as it is proportional to $1/R_{\mathrm{NC}}$, while the quantization energy goes with $1/R_{\mathrm{NC}}^2$. Furthermore, there is an interdependence between the NC radius and the Bohr radius of the bulk exciton R_{B} which is defined by

$$R_{\mathrm{B}} = \frac{4 \cdot \pi \cdot \hbar^2 \cdot \epsilon_0 \cdot \epsilon_{\mathrm{r}}}{\mu_{\mathrm{Exciton}} \cdot e^2} \tag{2.2}$$

where μ_{Exciton} is the exciton reduced mass, given by $\mu_{\mathrm{Exciton}}^{-1} = m_{\mathrm{e}}^{-1} + m_{\mathrm{h}}^{-1}$, and e is the elementary charge. Using the Bohr radius as a classification parameter, three different regimes can be determined: (1) a weak, (2) an intermediate and (3) a strong confinement regime [62–67]. The weak confinement regime is defined by $R_{\mathrm{NC}} \gg R_{\mathrm{B}}$. In this regime, electrons and holes are considered as connected excitons. The energy shift ΔE of the ground state of such an exciton is approximately

$$\Delta E \approx \frac{\hbar^2 \cdot \pi^2}{2 \cdot M \cdot R_{\mathrm{NC}}^2} \tag{2.3}$$

where M denotes the exciton translational mass, $M = m_{\mathrm{e}} + m_{\mathrm{h}}$. However, in the strong confinement regime, where $R_{\mathrm{NC}} \ll R_{\mathrm{B}}$, electrons and holes are single independent particles, and the energy shift can be written as

$$\Delta E \approx \frac{\hbar^2 \cdot \pi^2}{2 \cdot \mu_{\mathrm{Exciton}} \cdot R_{\mathrm{NC}}^2}. \tag{2.4}$$

In semiconductors, there is generally a rather big discrepancy between the effective masses of electrons and holes and, therefore, the Bohr radii of electrons R_{e} and holes R_{h} are quite different. This leads to the third and most common case in small crystallites which is the intermediate regime when $R_{\mathrm{e}} > R_{\mathrm{NC}} > R_{\mathrm{h}}$. In this case, the electron movement is much faster than the hole movement. The electrons see an almost static potential from the holes, while the holes move within an average potential of the electrons. The hole movement is constrained to the centre of the NC, leading to a donor-like exciton behaviour [62, 64]. Besides these exciton confinement effects, low-dimensional semiconductor structures exhibit strong linear and non-linear optical and electro-optical effects, like the quantum-confined Stark effect [68, 69].

In semiconductor technology, nanostructures usually are not separated entities, they are surrounded by other materials, like in QWs, SLs or core-shell NWs. The materials combined in these structures feature different energy band gaps and due to this band gap mismatch, the conduction and valence bands of the different materials usually do not align with one another and a band offset evolves. The band offset acts as potential barrier surrounding the electronic states of the encapsulated nanostructures and leads to the confinement of electrons and holes. Such a square-like confinement potentials can be achieved by preparing heterostructures like a $\mathrm{Al_xGa_{1\text{-}x}As/GaAs/Al_xGa_{1\text{-}x}As}$ QW [70]. Depending on the particular band gaps of the involved semiconductors, the arrangement of the electron bands can be different. In figure 2.1.2, the possible types of band gap alignment are depicted schematically: type I, type IIa and type IIb alignment, where the type IIb alignment is actually a special case of the type IIa alignment [57].

The semiconductors A and B have different energy band gaps E_{G}(A) and E_{G}(B), respectively, where $E_{\mathrm{G}}(A) > E_{\mathrm{G}}(B)$. In type I band gap alignment, which is also

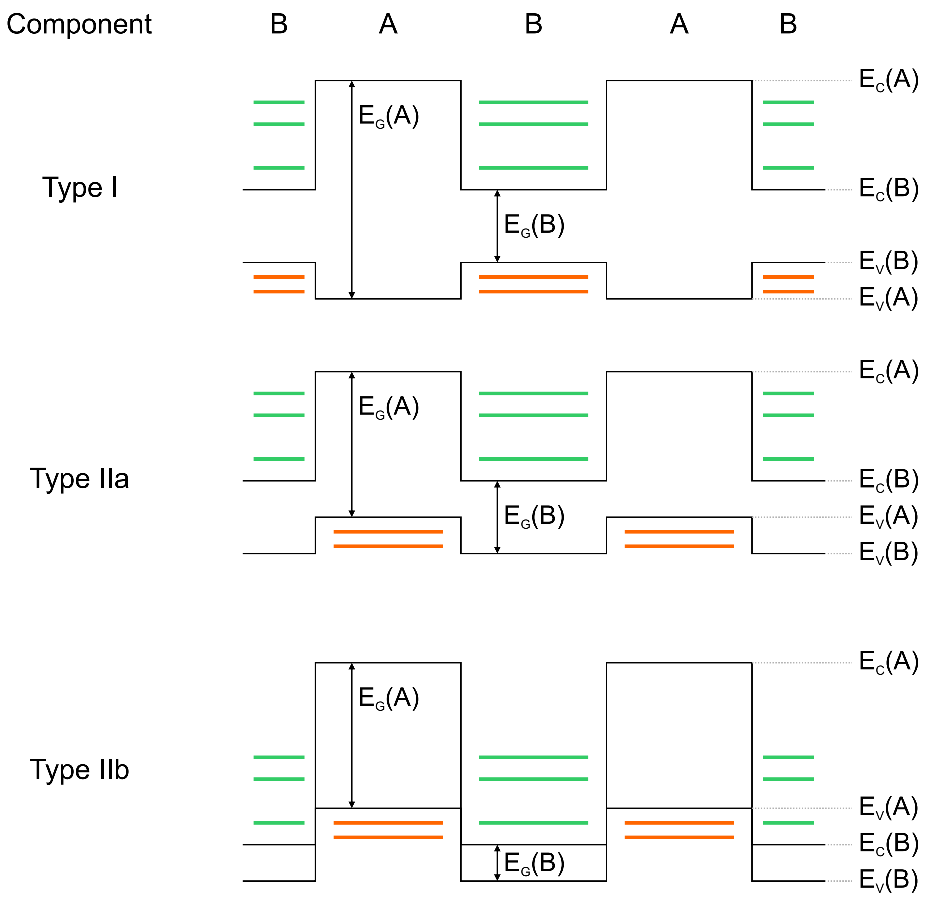

Figure 2.1.2: Band gap alignment types of a semiconductor heterostructure consisting of two components A and B with energy band gaps $E_{\mathrm{G}}(\mathrm{A})$ and $E_{\mathrm{G}}(\mathrm{B})$, respectively. The green and orange lines displays the quantum energy levels of the electrons and holes confined in the particular layers, respectively.

called straddling type, the energy of the conduction band of component B $E_{\mathrm{C}}(\mathrm{B})$ is smaller than the conduction band energy of component A $E_{\mathrm{C}}(\mathrm{A})$ while the energy of the valence band of component B $E_{\mathrm{V}}(\mathrm{B})$ is larger than the valence band energy of component A $E_{\mathrm{V}}(\mathrm{A})$. Therefore, a potential well is formed for both charge carriers within component B leading to a confinement of these two species in the material with smaller band gap. In these potential wells, electron and hole quantum levels form, depicted by the green and orange lines in figure 2.1.2. An example for type I band gap alignment is the InP/AlAs heterostructure [71]. If the energies of conduction and valence band of component A are both larger than their respective counterparts from component B (or vice versa), type II band gap alignment arises. The type II band gap alignment can be separated into two subtypes. Type IIa alignment, also called staggering type, occurs when, in addition to the previously mentioned condition, the difference between the conduction band energies (or valence band energies) of both components is smaller than the band gap energy of large band gap material. In this case, the potential wells for the both charge carrier species are formed in the different components and the electrons and holes are spatially separated, e.g. seen in figure 2.1.2, where the electrons are confined in component B while the holes are confined in component A. Type IIa band gap alignment is observed in InAs/AlSb heterostructures [72]. However, if the difference between the conduction band energies (or valence band energies) is larger than the band gap energy of the large band gap material, type IIb alignment, the broken gap, is present. In this case, there is no gap between electron and holes states, e.g. in an InAs/GaSb heterostructure [73].

When a sample consists of several QWs, the potential is a periodical function which is determined by the periodicity of the QW arrangement. The electrons and holes are confined in their particular wells and have discrete energy levels similar to electrons in a one-dimensional lattice of atoms [74]. However, when the width of the QWs is decreased, the electrons and holes have a higher probability of presence within the neighbouring QWs and their wavefunctions interact with each other and form so-called minibands [75, 76]. The charge transport of electrons within QW structures or SLs can be conducted either by miniband conduction where the electrons are moving within the minibands or via tunneling from one QW to the next QW (hopping conduction) [76, 77]. For QDs, the energy necessary to add excess electrons or holes is inversely proportional to the particle size. This dependency is originating from the charges already present in the QD blocking further charging (Coulomb blockade) [78, 79]. Such a behaviour can be seen in the conductance of single-electron transistors [80, 81].

2.2 Diffusion

A simple definition of a diffusion process is the transport of matter from one point in space to another one due the thermal movement of its particles. The main driving force for a diffusion process is a spatial gradient in the chemical potential, which can be caused by concentration gradient of the diffusing material, for example. A general description of diffusion can be done by using Fick's laws [82]:

$$\boldsymbol{J} = -D\nabla c \tag{2.5}$$

$$\frac{\partial c}{\partial t} = \nabla \cdot (D\nabla c) \tag{2.6}$$

where $\boldsymbol{J}$ is the diffusion flux of particles, D is the diffusion coefficient and c is the particle concentration. The diffusion flux points in the opposite direction than the concentration gradient and, therefore, diffusion tends to achieve a homogeneous distribution of the diffusing particles. These two simple equations can become more complicated when the medium is anisotropic, the diffusion coefficient is concentration dependent or when there is a sink for the diffusing particles, e.g. a chemical reaction. Microscopically, diffusion is associated with the Brownian motion of particles which is a thermally induced statistical spatial fluctuation of such a particle in matter. *Einstein* and *Smoluchowski* were the first to describe the Brownian motion theoretically and they related the mean square displacement of the diffusing particles to the diffusion coefficient [83, 84]. The mean diffusion length L_D of a particle, which is the square root of the mean square displacement, is given by

$$L_\mathrm{D} = \sqrt{D \cdot t}, \tag{2.7}$$

Table 2.2.1: Diffusion coefficients of various group-III and -V elements in Si for the liquid phase (D_L) and the solid phase (D_S) at 1400 °C as well as segregation coefficients (k).

Element	D_L (cm^2/s)	D_S (cm^2/s)	k
Ga	4.8×10^{-4} [85]	1.0×10^{-10} [86]	0.008 [87, 88]
In	6.9×10^{-4} [85]	2.6×10^{-10} [86]	0.0004 [88, 89]
N	2.6×10^{-4} [90]	1.0×10^{-5} [86]	0.0007 [91]
P	5.1×10^{-4} [85]	3.4×10^{-7} [86]	0.35 [87, 89]
As	3.3×10^{-4} [85]	6.0×10^{-12} [86]	0.3 [87]
Sb	1.5×10^{-4} [85]	7.1×10^{-12} [86]	0.023 [88]

where t represents the diffusion time and D is the diffusion coefficient of the particular species. In table 2.2.1, the diffusion coefficients of several atomic species in Si, which are relevant for this work, are given. As diffusion in the solid and liquid phase plays a role for the III-V integration in Si, the diffusion coefficients in both phases are compared, where the values for the solid phase are given for a temperature close to the melting point of Si. The diffusion coefficients in liquid Si (D_L) are several orders of magnitude higher than in solid Si close to the melting point (D_S). Additionally, the segregation coefficients k of the group-III and -V elements are inserted, which will be discussed in section 2.3.

2.2.1 Diffusion in the solid phase

As most solids have a crystalline order, diffusion is heavily influenced by the crystal lattice. On an atomic scale, the diffusion within a crystal lattice can be described by a random walk of particles. The atoms jump from one lattice or interstitial site to the next very fast and a large number of these jumps can be detected macroscopically as a diffusion process. For the jumps itself, the atoms need to overcome a potential barrier when traversing from one local state to the other and the rates for forward and backward movement are determined by the activation energies and follow an Arrhenius law [92].

To have one atom change its place, there has to be an open site. Such an open space is called vacancy and it is a common point defect in crystalline media. Vacancies evolve when an atom leaves its actual lattice site and moves into an interstitial position [93]. In order to have an impact on the diffusion process, a considerable amount of vacancies has to be available. Besides their function as “vehicles for diffusion” [82], vacancies induce energy levels within the band gap of semiconductors and can affect electrical and optical properties.

The final diffusion mechanism is heavily dependent on the lattice of the matrix material, as the structure of the lattice defines the lattice site position and the available paths of the diffusing agent. Furthermore, size, charge and chemical nature of the diffusing species play a role as well as the presence of vacancies. Figure 2.2.1 depicts several diffusion mechanisms which can occur in solids.

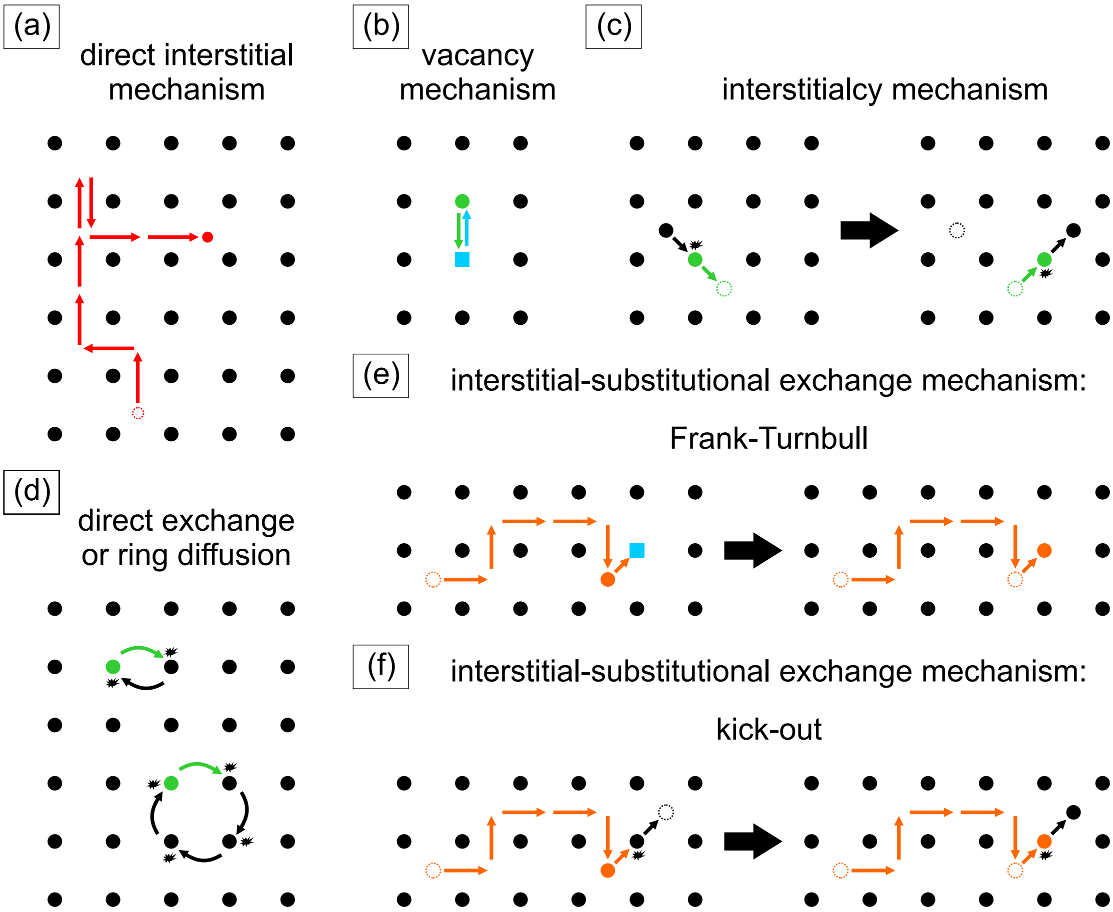

Figure 2.2.1: Diffusion mechanisms in crystalline solids.

When the diffusing atom is situated at an interstitial site within the surrounding matrix, it can move from one interstitial site to the next by atomic jumps. This process is named direct interstitial mechanism and is displayed in figure 2.2.1(a) where the red atom denotes the diffusing atom within the host lattice symbolised by the black atoms. During the jump from one interstitial site to the next, no defect is necessary to mediate the diffusion process and, therefore, direct interstitial diffusion is a relatively fast mechanism for atoms smaller than the atoms of the host matrix. A typical example is the diffusion of hydrogen in metals [94]. When the diffusing atoms are bigger than the host atoms, diffusion via the direct interstitial mechanism is much slower. A different diffusion mechanism is the vacancy mechanism, as seen in figure 2.2.1(b). In this mechanism, the specific atom (green) diffuses through the crystal lattice by occupying a neighbouring empty lattice site, a vacancy (blue), simply by jumping into it. Hereby, the original lattice site of the diffusing atom becomes a vacancy itself and the vacancy moves through the crystal lattice as well [95]. Vacancies can also accumulate and form divacancies which also mediate diffusion.

The third diffusion mechanism shown in figure 2.2.1(c) is the interstitialcy mechanism, or indirect interstitial mechanism. When an interstitial atom has about the same size as the host atoms, it is able to kick out a host atom from its lattice site and takes its spot. The displaced atom is then situated on an interstitial site [96]. The initial interstitial atom can also be a self-interstitial, the same element as the matrix; then the interstitialcy mechanism is responsible for the self-diffusion [97]. Another diffusion mechanism is the direct exchange which is displayed in figure 2.2.1(d). During direct exchange, the adjacent atoms sitting on lattice sites change their places. This process has a high activation energy and is therefore relatively improbable [98]. When more than two neighbouring atoms are involved, a ring mechanism of diffusion can occur, where the atoms change places in ring-like manner which is energetically more favourable than the direct exchange of two atoms [99]. The last two diffusion mechanisms in figures 2.2.1(e) and (f) are interstitial-substitutional exchange mechanisms and are combinations of the previously mentioned diffusion mechanisms. Both mechanism needs a diffusing species which can occupy interstitial as well as substitutional sites in the host material. In the Frank-Turnbull mechanism (e), the diffusing atom is initially on an interstitial site and moves through the crystal lattice via the interstitial mechanism until it comes close to a vacancy which is then filled by the diffusing atom [100]. When there is no vacancy available, the diffusing atom can kick-out an lattice atom from its site similar to the interstitialcy mechanism (f) [101].

The kind of diffusion mechanism is mainly dependent on the structural properties of the diffusing agents and the host matrix, for example crystal structure or atom size. Besides these parameters, diffusion itself is also dependent on the temperature and the pressure. The temperature dependence of the diffusion coefficient D is very strong and can be given by an Arrhenius-type equation, in general:

$$D = D_0 \cdot \exp(-\frac{H_{\mathrm{Diff}}}{k_{\mathrm{B}} \cdot T}) \tag{2.8}$$

where D_0 is the pre-exponential factor, H_{Diff} denotes the activation enthalpy of diffusion, k_{B} is the Boltzmann constant and T represents the temperature. The parameters D_0 and H_{Diff} are usually determined by experimental measurements of the diffusion coefficient at different temperatures, e.g. using mechanical sectioning, radioactive tracer atoms or spreading resistance profiling. The diffusion coefficient can increase by several orders of magnitude by increasing the temperature from low temperatures to temperatures close to the melting point as it can be seen in figure 2.2.2(a), where the temperature dependence of the diffusion coefficient of several group-III and -V atoms in Si are displayed using data from [86]. In figure 2.2.2(b), the temperature range close to the melting point of Si is enlarged and the diffusion coefficient in molten Si are included, taking data from [85] and neglecting a change of the diffusion coefficients with temperature in the melt. Comparing the diffusion coefficients in the solid phase, the different elements do not show significant differences except for N which is diffusing considerably faster than the other elements. At the transition from solid to molten Si, there is a sudden jump in the diffusion coefficients of all elements.

The influence of pressure is much smaller than the effect of temperature. In the normal pressure range, the pressure dependence of the diffusion coefficient is negligible. At hydrostatic pressures, the diffusion coefficient can be altered by changing the pressure, although the effect remains still small compared to the temperature dependence [102]. Diffusion can furthermore be influenced by additional factors like grain boundaries or extended defects which enhance impurity diffusion. Another diffusion mechanism important in solid state physics is the diffusion at the surface or at interfaces between two different materials.

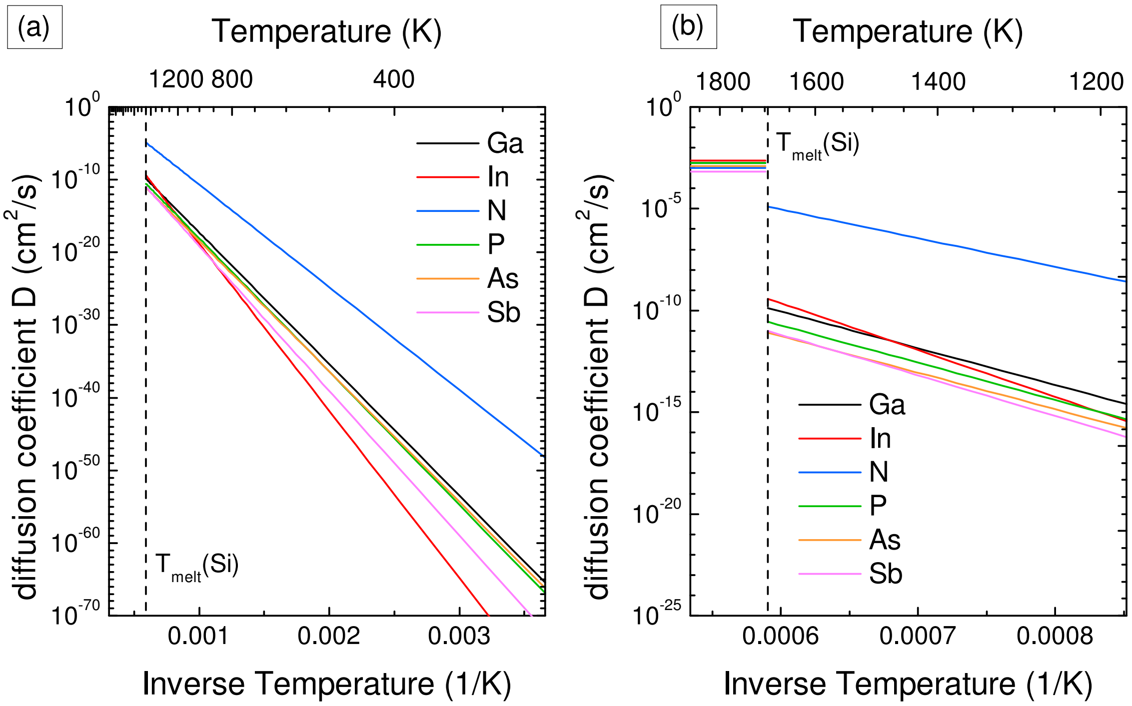

Figure 2.2.2: Temperature dependence of several group-III and -V elements in Si.

2.2.2 Diffusion in the liquid phase

In the liquid phase, diffusion typically is faster than in solid material. In two-component liquids, Fick's phenomenological equations (2.5) and (2.6) describe diffusion relatively well. However, in systems with more components, Fick's equations are not accurate anymore, as other driving forces than a concentration gradient come into play. For example, in three-component systems, a diffusion barrier, where there is no diffusion although a concentration gradient is present, reverse diffusion against the concentration gradient or osmotic diffusion without a concentration gradient can occur [103]. In order to describe such systems, the Maxwell-Stefan theory is used [104]. In contrast to solid phase diffusion, diffusion mechanisms in liquids are not as explored as in solids and, hence, diffusion processes in liquids are mainly modelled numerically using molecular dynamics simulations [105, 106].

For the scope of this work, diffusion processes in semiconductor melts close to the melting point are of importance. Molten Si and Ge behave like metallic liquids [107–109]. In metallic liquids, two kinds of diffusion processes are distinguished, self-diffusion and solute diffusion. Hereby, self-diffusion describes the diffusion when neighbouring atoms are identical, while solute diffusion considers the movement of impurity atoms diluted in the liquid material. For self-diffusion, the diffusion coefficient can be modelled using a modified Stokes-Einstein formula and the melting point viscosity of the metallic liquid in combination with the Arrhenius-type equation (2.8) for diffusion [110, 111], and is empirically given by

$$D = D_0 \cdot \exp\left(-\frac{16.0 \cdot T_{\mathrm{melt}}^{1.07}}{N_{\mathrm{A}} \cdot k_{\mathrm{B}} \cdot T}\right) \tag{2.9}$$

where T_melt is the melting point of the metallic liquid, the unit of the term $16 \cdot T_\mathrm{melt}^{1.07}$ is J/mol, and N_A is the Avogadro constant. For the description of solute diffusion in liquid metals, four different models are usually considered [112–115]: (1) the fluctuation theory, which accounts diffusion to local density fluctuations of the liquid, (2) the critical fluctuation model which considers that a critical size of these density fluctuations is necessary for diffusion to occur leading to thermally activated diffusion process, (3) Enskog's theory of dense fluids which uses the masses and hard sphere diameters of the impurity and host atoms as well as the density of the liquid to determine the diffusion coefficients, and (4) the "hole" model which is similar to the vacancy mechanism in solid materials. For (1) and (2), the diffusion coefficient has quadratic dependence on the temperature of the liquid. In (3) the diffusion coefficient of the impurities can be approximated by [114, 115]

$$D = \frac{3 \cdot C}{8 \cdot \rho \cdot \sigma^2 \cdot g(\sigma)} \cdot \left(\frac{k_\mathrm{B} \cdot T}{\pi \cdot \nu_\mathrm{s}}\right)^{1/2} \tag{2.10}$$

where C is a factor for the relative size of impurity and host atoms, ρ is the atomic density, σ represents the diameter of the hard spheres and $g(\sigma)$ is its corresponding radial distribution function, and ν_s is the reduced mass of impurity and host atoms. Using the "hole" model (4), the diffusion coefficient obeys a Arrhenius-type equation and can be determined by [113, 116]

$$D = D_0 \cdot \frac{f_\mathrm{h}}{f_\mathrm{i}} \exp\left(-\frac{0.17 \cdot T_\mathrm{melt} \cdot (16 + K_0)}{T}\right) \tag{2.11}$$

where f_h and f_i are the Goldschmidt atomic diameters of the host and impurity atoms, respectively, and K_0 denotes the atomic valence of the impurity atom. For all four theories, there are specific systems were these models are relatively accurate. For semiconductors, like Si and Ge, the "hole" model yields predictions which are in good agreement with experiments [111]. Table 2.2.1 lists the diffusion coefficients D_L of several group-III and -V in molten Si.

2.3 Crystallization mechanisms

Crystallization is a phase transformation process where atoms arrange in a highly-ordered structure (crystal). This process can occur from a vapour phase, a solution or in melts, and from amorphous or disordered solid material. It is mainly dependent on the thermodynamics of the involved phases and takes place when the system deviates from thermal equilibrium. Considering a single component system, two different phases are in thermal equilibrium when their chemical potentials $\Psi(P,T)$ are equal. Figure 2.3.1 displays the phase diagramm of such a single component system. The thermal equilibria of two phases are depicted by the black lines separating the different phases. When the temperature or pressure rises, one of the two involved phases becomes stable while the other one transforms. The point where all three curves meet is the triple point O. The end point of the liquid-vapour equilibrium lines is the critical point O'.

The deviations from thermal equilibrium can be induced by a change of temperature or pressure. The decreases of temperature from point $Y(P_0, T_{melt})$ to point $Y'(P_0, T)$

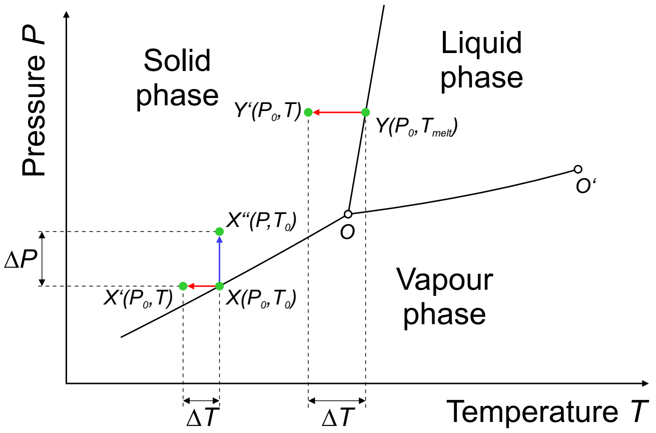

Figure 2.3.1: Phase diagram of a single component system. The solid black lines display the two-phase equilibria. The meeting point of these three lines is the triple point O and the end point of the liquid-vapour equilibrium line is the critical point O'. Deviations from the equilibria are displayed by the and blue arrows for a decrease of temperature (under-cooling) and an increase of pressure (supersaturation), respectively. (drawn after [117])

for the liquid-solid transition (solidification) and from $X(P_0, T_0)$ to $X'(P_0, T)$ for the vapour-solid transition (deposition) denoted by the red arrows cause an under-cooling of either melt or vapour and triggers the crystallization process. On the other hand, an increase of the pressure as given from point $X(P_0, T_0)$ to point $X''(P, T_0)$ displayed by the blue arrow establishes a supersaturation and also triggers the crystallization process. The change of the chemical potential $\Delta\Psi$ due to under-cooling is expressed by

$$\Delta\Psi = \frac{\Delta H_{\mathrm{i}}}{T_{\mathrm{i}}} \cdot \Delta T \tag{2.12}$$

where H_{i} is the melting or sublimation enthalpy depending on which phase transition is examined, T_{i} is the corresponding phase transition temperature and ΔT is the amount of under-cooling. For the supersaturation case, the change of the chemical potential $\Delta\Psi$ is given by

$$\Delta\Psi = k_{\mathrm{B}} \cdot T \cdot \ln \frac{P}{P_0} \tag{2.13}$$

where P_0 is the equilibrium vapour pressure and P is the real pressure. In the case of a supersaturated solution, equation (2.13) can be transformed into a concentration dependent form

$$\Delta\Psi = k_{\mathrm{B}} \cdot T \cdot \ln \frac{c}{c_0} \tag{2.14}$$

where c_0 and c are the equilibrium and real concentration of the dissolved substance, respectively.

The crystallization process itself can be separated in two steps: (1) nucleation and (2) crystal growth. The initial point of nucleation is due to density fluctuations in the homogeneous medium. Within these density fluctuations small agglomerates form and depending on the stability of the bulk phase, these nuclei dissolve again ($\Psi_{\mathrm{bulk}} < \Psi_{\mathrm{nuclei}}$) or tend to grow further when a certain critical size is reached ($\Psi_{\mathrm{bulk}} > \Psi_{\mathrm{nuclei}}$) [117]. In the latter case, the system gains energy by forming a nucleus of the new phase. However, this energy gain is counterbalanced by the surface energy of the interface between the bulk phase and the nucleus. Combining both for a spherical nucleus, the difference of the Gibbs free energy for nucleation $\Delta G_{\text{nucleation}}$ is given by [118, 119]

$$\Delta G_{\text{nucleation}} = \frac{4}{3} \cdot \pi \cdot R^3_{nucleus} \cdot \Delta G_v + 4 \cdot \pi \cdot R^2_{\text{nucleus}} \cdot \gamma \tag{2.15}$$

where R_{nucleus} is the radius of the formed nucleus and γ is its surface tension. ΔG_v represents the difference of the Gibbs free energy between the two phases and can be expressed by $\Delta G_v = -N \cdot (\Psi_{\text{bulk}} - \Psi_{\text{nucleus}})$ with N being the number of atoms contributing to the nucleus formation. Equation (2.15) obtains a maximum at the critical radius R_{c} given by

$$R_c = -\frac{2 \cdot \gamma}{\Delta G_v}. \tag{2.16}$$

If the radius of the formed nucleus is smaller than R_{c}, the nucleus disappears again but when the radius of the nucleus exceeds R_{c} then it continues to grow. In order to form such a nucleus, the nucleation barrier with the critical energy ΔG^* given by

$$\Delta G^* = \frac{16 \cdot \pi}{3} \cdot \frac{\gamma^3}{\Delta G_v^2} \tag{2.17}$$

has to be overcome. The rate equation for the formation of nuclei which have a radius larger than R_{c} can be determined by [118–121]

$$j = \beta \cdot N_{\text{nucleus}} \cdot Z \cdot \exp\left(-\frac{\Delta G^*}{k_{\text{B}} \cdot T}\right) \tag{2.18}$$

using the rate at which an additional atom attaches to the forming nucleus β, the number of nucleation sites N_{nucleus} and the Zeldovich factor for nucleation Z. Nucleation can occur spontaneously from any nucleation site within the bulk phase (homogeneous nucleation) [122] or at foreign nucleation sites, e.g. impurities or surfaces (heterogeneous nucleation) [123]. These foreign sites can promote the nucleation process by lowering the nucleation barrier. If a foreign surface acts as nucleation site, the nucleus will possess a droplet form with a certain contact angle depending on the surface energies of the two phases [124]. Depending on this contact angle, the nucleation barrier is lowered. Heterogeneous nucleation at a foreign surface is responsible for the epitaxial growth of thin layers.

When the nucleus has overcome the critical size, it continues to grow by accumulating further atoms from the surrounding bulk phase to its surface. On the surface an additional atom or molecule can occupy different positions, as shown in figure 2.3.2, and depending on its position the number of bonds with the crystal are different. A crystal surface consists of terraces which have steps from one to another. The steps, in turn, can have kinks [125]. If an additional atom is located in the positions 1 and 2 of figure 2.3.2, it has more bonds which are connected to the crystal than dangling bonds. Therefore, it is incorporated within the crystal. In the positions 4 and 5, the atom is adsorbed either at a step or at the surface of a terrace, respectively, and has more dangling bonds than bonds connected to the crystal. Hence, it is only weakly bonded to the crystal and is capable of moving along the step or on the terrace until it reaches a more stable position. The kink position (3, green) has an equal number of connected and dangling bonds. The growth of the crystal but also its dissolution takes

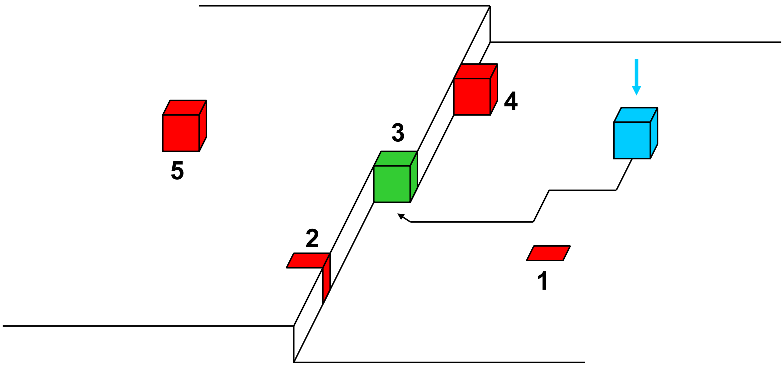

Figure 2.3.2: Possible positions of an adatom on a surface.

mainly place at these kink positions. If a solute atom (blue) adsorbs at the crystal surface, it moves into kink positions and by consecutive filling of these kink positions the crystal grows. On the other hand, if several atoms detach from kink positions, the crystal dissolves [126, 127]. However, in a supersaturated or under-cooled bulk phase, the amount of atoms adsorbing at the crystal is larger than the number of atoms detaching from it [128]. The adsorbed atoms are incorporated into the crystal lattice and the crystal grows epitaxially.

On flat surfaces, nucleation and crystal growth can be employed to grow thin layers. Depending on the ratio between the surface free energy of the substrate material, the surface free energy of the deposited material and the free energy of the interface between both, different growth modes can occur. If the surface free energy of the substrate material is bigger than the surface free energy of the epitaxial layer and the free energy of the interface together, the Frank-van-der-Merve growth mode is expected and the deposited material grows layer-by-layer on top of the substrate material (2D growth). In contrast, if the surface free energy of the substrate is smaller, Volmer-Weber growth mode occurs and epitaxial three-dimensional islands form (3D growth). A third mode, called Stranski-Krastanov growth mode, is a mixture of the both aforementioned growth modes, where at first a thin wetting layer is formed which is followed by the formation of three-dimensional islands on top [129].

In the scope of this work, the recrystallization of amorphous silicon (a-Si) is of significant importance. This recrystallization can be achieved either via the solid phase or via the liquid phase. Amorphous silicon has the tendency to crystallize by itself, since the Gibbs free energy of a-Si is higher than that of crystalline Si (c-Si) [130]. At room temperature, the crystallization process may eventually happen but as a activation energy has to be overcome for nucleation and crystal growth it is rather improbable. However, a dedicated thermal treatment can initiate the crystallization process. Nucleation and crystallization of a-Si layers have been observed in the range of 500 °C to 600 °C [131–133] using furnace annealing. Hereby, the recrystallization mechanism is accounted to solid phase crystallization (SPC) [134, 135]. In principle, SPC, or solid phase epitaxy (SPE) when a c-Si substrate is used as epitaxial template, utilizes the attachment of atoms to kink position at the terraces of the c-Si surface using the solid phase diffusion mechanisms for the supply with additional atoms from the amorphous Si [134]. The growth rate of c-Si grains in the a-Si layer by this mechanism is in the range of a few nm/s for temperatures above 650 °C [135, 136].

During furnace annealing, the heating up ramp is usually not very steep and, therefore, the annealed system remains in the thermal equilibrium. However, with short-time annealing methods like FLA or pulsed laser annealing (PLA), the heating ramps are much steeper which can result in non-equilibrium crystallization. Hereby, crystallization is ignited locally within the material by nucleation and crystallization of small precipitates in an under-cooled system. Both processes release latent heat which is immediately consumed for heating up the surrounding material. When the release of latent heat is larger than the heat dissipation, a heat wave can propagate through the thin layer pushing the crystallization front away from the ignition centre [137–139]. Such a process is called explosive and can be classified into four different regimes [140]: (1) explosive solid phase nucleation (ESPN), (2) explosive solid phase epitaxy (ESPE), (3) explosive liquid phase nucleation (ELPN), and (4) explosive liquid phase epitaxy (ELPE). When the temperature is below the melting point of the amorphous material, the phase transition from the amorphous to the crystalline phase occurs due to bulk-induced nucleation and growth, yielding polycrystalline material. This process is termed as ESPN and can turn into ESPE when there is a crystalline substrate acting as epitaxial template. However, when the temperature is above the melting point of the amorphous material but still below the melting of the crystalline phase, ELPN and ELPE occur. The amorphous phase is molten into the liquid phase which then transforms into the crystalline phase either by bulk nucleation and growth (ELPN) or epitaxial growth on a crystalline template (ELPE). The velocity of the lateral crystallization front can reach up to 15 m/s which is several orders of magnitude larger than normal SPC [141, 142]. Explosive crystallization processes can occur vertically and laterally and have been reported in Si [143, 144] and Ge [145].

Using PLA, the laser beam heats the material locally and ignites the explosive crystallization process [146, 147]. During FLA, the whole wafer is heated and, in contrast to PLA, no hot spot is formed. However, the wafer edges act as heat sinks and are, therefore, at a higher temperature than the centre of the wafer. This temperature gradient leads to a heat wave propagation from the edges to the centre inducing an explosive crystallization process [148, 149]. In the case of thin a-Si layers, this process yields polycrystalline Si with large grains [150]. For FLA, explosive crystallization has been observed in the solid as well as in the liquid phase which can occur separately or simultaneously [148, 151–153].

When dealing with multiple component systems during a crystallization process, two other effects come into play: (1) the solid solubility of impurities and (2) segregation. The solid solubility describes the amount of an impurity which can be distributed within a host material without forming a secondary phase, e.g. clusters [154]. Segregation refers to the enrichment of an impurity in a host material at an internal interface which can be a grain boundary in a polycrystalline matrix or a liquid/solid interface during crystallization. Grain boundaries can act as sinks during diffusion of impurity atoms and, therefore, can be easily decorated by metal impurities, for example. At a liquid/solid interface, the impurity atoms can be either incorporated into the solid phase or remain in the liquid. The ratio between impurity concentration in both phases is defined as segregation coefficient k and is given by [89]

$$k = \frac{c_\mathrm{s}}{c_\mathrm{l}}, \tag{2.19}$$

where c_s and c_l denote the impurity concentration in the solid and liquid phase, respectively. In silicon, most impurities have segregation coefficients below one, implying that they are enriched in the liquid Si phase. The segregation coefficients of several group-III and -V elements in Si are given in table 2.2.1. Segregation effects are employed during the casting of Si ingots by the Czochralski method, for instance, where most of the impurities accumulate at the edges of the ingot which can then be removed by cutting.

3 III-V compound semiconductors in silicon technology

3.1 Motivation for the III-V integration into silicon technology

III-V compound semiconductors are tetrahedrally bonded alloys of elements located in group III and V of the periodic table. Most of these compounds feature a zincblende crystal structure which is a face-centred cubic (fcc) lattice, except the III-nitrides, where the stable configuration is the wurtzite structure. Figure 3.1.1 displays the unit cell of the diamond crystal structure, as it is present in the elemental semiconductor Si, in comparison with the zincblende structure. In Si, the base of the diamond unit cell is occupied by two Si atoms (grey balls) located at $\boldsymbol{r} = (0, 0, 0)$ and $\boldsymbol{r} = (a/4, a/4, a/4)$, where a is the lattice parameter of Si. The transition from the diamond to the zincblende structure is performed by substituting the first Si atom by a group-III atom (green) while the second one is replaced by a group-V atom (red), exemplarily shown for the binary III-V compound InAs. With this substitution, the covalent character of the bonding is decreased and the bonding gets partly ionic as there is a charge transfer between the group-III and group-V species. By introducing a second cationic species (group-III ion, like Ga^+, blue) which substitutes a certain amount of the In^+ ions, a ternary compound like $\mathrm{In_xGa_{1-x}As}$ can be formed. An advantageous feature of these ternary III-V compounds is the tunability of their material properties, like the band gap energy, by changing the alloy composition [155, 156].

In general, compound semiconductors – III-Vs in particular – feature some advantages over the conventional Si semiconductor technology. The two major properties are the mobility of charge carriers and the direct band gap. Figures 3.1.2(a) and (b) display the band gap energies and the charge carrier mobilities of several III-V compounds in comparison to Si and Ge over the lattice parameter, respectively. The data for these two figures is taken from table 3.1.1 which also includes the lattice parameters and the melting points of these substances.

Considering the electron mobility, the III-V compounds are superior to Si and even to Ge but for the hole mobility, the III-V compounds are on par with Si and are

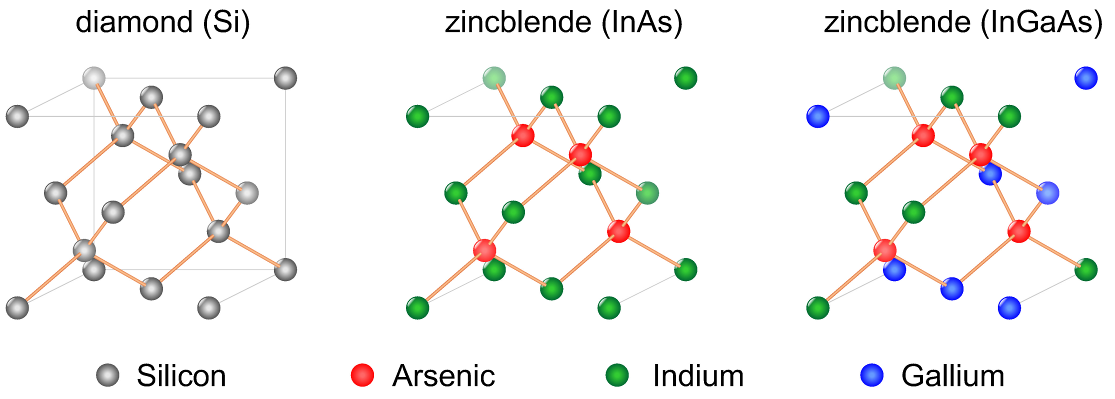

Figure 3.1.1: Unit cell of a diamond crystal structure, i.e. Silicon. Substitution of Si ions by cations (In^+) and anions (As^-) results in zincblende structure, i.e. InAs. Introduction of a second cationic species (Ga^+) gives a ternary compound semiconductor, i.e. InGaAs.

surpassed by Ge. The gain in mobility by replacing the Si channel material by a III-V channel for n-MOS devices directly benefits the drive current and hence the overall performance of the device [157]. Consequently, the limits of further down-scaling in current device technology could be overcome or at least pushed a little farther when introducing high-mobility channel materials. Along with the high mobility, transistors based on III-V compounds also show tremendous frequency response characteristics, which makes them suitable for high frequency applications [158, 159].

The band gap energies of the III-V compounds, as shown in figure 3.1.2(b), cover a large bandwidth of the electromagnetic spectrum. Starting from InSb ($E_\mathrm{G} = 0.17\,\mathrm{eV}$) in the mid-range infrared (IR), this bandwidth spans over GaP ($E_\mathrm{G} = 2.26\,\mathrm{eV}$) in the green all the way towards AlN ($E_\mathrm{G} = 4.9\,\mathrm{eV}$) in the ultraviolet (UV) and can be accessed completely by either binary compounds directly or band gap engineering of ternary and quaternary III-V compounds. This broad range of accessible wavelengths makes III-V compounds suitable for numerous optoelectronic applications.

III-V compounds are employed for light detection in the IR. Such detectors can be made of SLs combining different III-V compounds, mainly based on InAs, InSb, GaSb and their ternary or quaternary alloys, as in so called quantum well infrared photodetectors (QWIPs) [156, 160–164]. A different configuration are quantum dot infrared photodetectors (QDIPs) which utilize self-assembled III-V QDs embedded within a barrier layer that can also be stacked multiple times [165–169]. An advantage of QDIPs over QWIPs is that they can detect light under normal incidence due to the selection rules of polarized light [170] which result from the three-dimensional confinement of the QDs. Another type of III-V based detectors is a hybrid of both types using a quantum dots-in-a-well (DWELL) structure combining the normal incidence sensitivity of the QDs with the possibility to tune the detection wavelength as it can be done with QWs [171–173]. In all three kinds of IR photodetectors, the detection wavelength can be adjusted by the proper choice of the particular III-V compounds exploiting intra-band transitions enabling detection in the deeper IR [174, 175] but also by modulating the size of either the QDs or QWs due to confinement effects. The quantum confinement itself can lead to a blue shift of the absorption [64, 176].

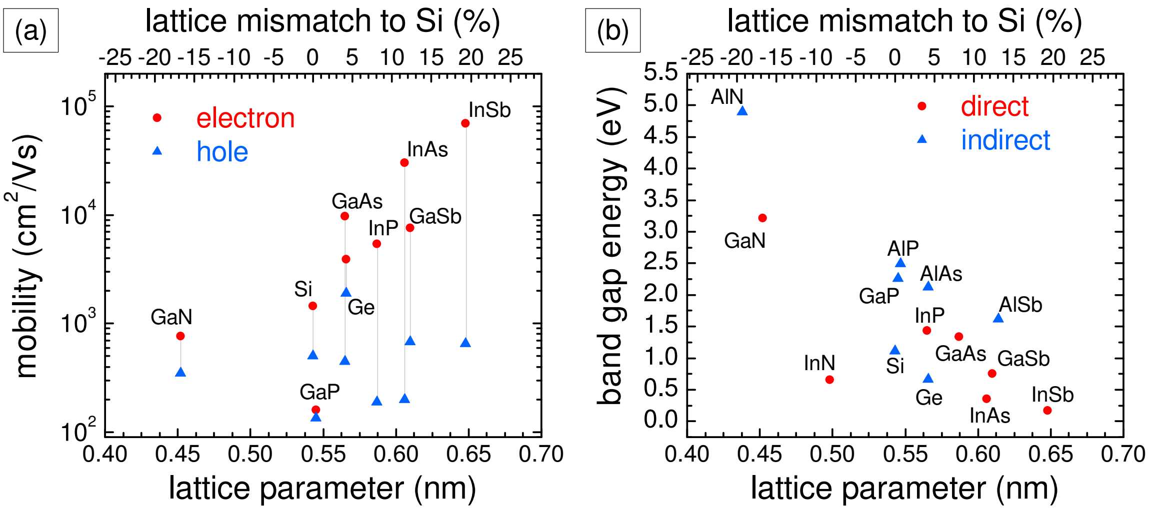

Figure 3.1.2: (a) Electron (red) and hole mobilities (blue) of Si, Ge and several III-V compound semiconductors versus their lattice parameter and lattice mismatch to Si. (b) Band gap energies for Si, Ge and several III-Vs. Data taken from table 3.1.1.

Table 3.1.1: Lattice parameter (a), band gap energy (E_G), melting point (T_melt) and electron (μ_e) and hole (μ_h) mobilities at 300 K of Si, Ge and several III-V compound semiconductors with zincblende crystal structure. The superscript marks direct (d) and indirect (i) band gaps.

	a (nm)	E_G (eV)	T_melt (°C)	μ_e (cm^2/Vs)	μ_h (cm^2/Vs)
Si	0.543 [177]	1.11^i [178]	1414 [179]	1450 [180]	500 [180]
Ge	0.566 [181]	0.66^i [182]	936 [183]	3900 [184]	1900 [184]
GaN	0.452 [185]	3.21^d [186]	2518 [187]	760 [188]	350 [189]
GaP	0.545 [190]	2.26^i [191]	1457 [192]	160 [193]	135 [193]
GaAs	0.565 [190]	1.43^d [194]	1241 [195]	9750 [196]	450 [197]
GaSb	0.610 [198]	0.75^d [199]	718 [200]	7620 [201]	680 [202]
InP	0.587 [203]	1.34^d [204]	1067 [195]	5370 [205]	190 [206]
InAs	0.606 [203]	0.35^d [207]	948 [195]	30000 [208]	200 [208]
InSb	0.648 [198]	0.17^d [209]	527 [200]	70000 [210]	650 [211]

Of course, the optical properties of III-V compounds cannot only be exploited by the usage as detectors; they are also used for light emission. Light emitting diodes (LEDs) and lasers based on III-V compound semiconductors are highly commercialised and present in every field of life, nowadays. Such LEDs and lasers are also employing QDs and QWs. They can be made of a variety of binary, ternary and quaternary III-V alloys in order to access a broad range of the spectrum. The research and utilization of light emission from III-V compounds started already in the sixties and seventies of the 20th century with the development of LEDs using bulk materials made of GaAs emitting in the IR [212–214], GaP emitting green light [215, 216] and GaN emitting in the blue to yellow part of the visible spectrum [217–219]. Additionally, light emission in the violet range of the spectrum was achieved by doping GaN materials with Mg [220], although most of these devices did not reach commercial success. The big breakthrough for blue LEDs came in the 1980s with the introduction of a MOCVD for the fabrication of Zn-doped GaN layers [221]. In the late eighties and nineties of the last century, the improvement of structural quality of GaN [222, 223], the addition of InN or AlN to GaN devices [224] as well as new device concepts, like buffer layers [225, 226], heterostructures [227, 228] or QW and multi-QW [229, 230] structures, steadily improved the performance of these blue LEDs. This improvement peaked in the development of GaN-based laser diodes [231–233]. The main contributors to this development, *Akasaki*, *Amano* and *Nakamura*, were awarded with the Nobel prize in physics in 2014 “for the invention of efficient blue light-emitting diodes which has enabled bright and energy-saving white light sources” [234]. For a more detailed historical breakdown of the development of LEDs with the focus on GaN based devices, a modern review is written by *Maruska* and *Rhines* [235].

Other fields of application that can be accessed by III-V compound semiconductors are non-volatile memories and photovoltaics. The exploitation of III-V compounds in non-volatile memory devices is based on the usage of III-V NCs embedded in either dielectrics [236, 237] or in III-V multilayer structures [238] reaching data retention times compatible with modern memory technologies [239, 240]. The use of III-V compounds in photovoltaics started after the development of MOCVD-grown thin III-V layers by using a $\mathrm{Ga_xIn_{1\text{-}x}P}$ on GaAs multijunction approach [241]. In the beginning, it was almost solely designated for space applications. At that time, the costs for economic use on a terrestrial scale were too high, however, for spacecraft powering the costs of the solar modules did not matter [242]. In the last decade, significant progress has been made to increase the efficiency of multilayer III-V solar cells to make them applicable for terrestrial energy harvesting [243–247]. State-of-the-art multijunction solar cells based on III-V compound semiconductors reach efficiencies of 29.8 % for one sun [248] and 46 % when used in concentrator geometry [249].

The big challenge for III-V based technology is the integration of III-V compound semiconductors into the Si process technology. As the lattice parameters of III-Vs differ from Si, there is a lattice mismatch between these materials. The lattice mismatch Δa between a III-V compound semiconductor and a Si substrate material is defined by

$$\Delta a = \frac{a_{\text{III-V}} - a_{\text{Si}}}{a_{\text{Si}}}, \tag{3.1}$$

where $a_{\text{III-V}}$ and a_{Si} are the lattice parameters of the particular III-V compound and Si, respectively. In figures 3.1.2(a) and (b), the lattice mismatch to Si is depicted on the upper abscissae ranging from about −20 % for AlN on one side to about 20 % for InSb on the other side. When these III-V compounds are deposited or grown on Si, the large lattice mismatches lead to the formation of defects, e.g. dislocations, which deteriorate the crystalline quality and therefore the electrical and optical properties [55, 56, 250–252].

3.2 Conventional III-V integration techniques

3.2.1 Deposition methods

The most common method to combine III-V compound semiconductors with Si process technology is the utilization of a chemical vapour deposition (CVD) technique. During a CVD process, different chemical reactants in the gas phase react close to the surface of a substrate in order to deposit thin layers of a specific material. The two mainly used CVD processes for the deposition of III-V material on Si are MBE and MOCVD. These two techniques are capable of growing high quality material epitaxially on a substrate layer-by-layer. A schematic of the thin layer deposition by CVD techniques is displayed in the upper part of figure 3.2.1. The precursor gases, e.g. trimethyl gallium ($Ga(CH_3)_3$) and arsine (AsH_3) for GaAs, are flowing over the substrate. When coming into contact with the surface of the heated substrate, the chemical reaction

$$\mathrm{Ga(CH_3)_3} + \mathrm{AsH_3} \longrightarrow 3\,\mathrm{CH_4}\uparrow + \mathrm{GaAs} \tag{3.2}$$

takes place and GaAs is grown epitaxially at the substrate surface while the methane is transported away. During the deposition process, different epitaxial growth modes occur depending on the attractive forces between deposited atoms and the substrate material as well as between the deposited atoms themselves. These growth modes are Frank-van-der-Merve mode, Stranski-Krastanov mode and Volmer-Weber mode, as described in section 2.3. In Stranski-Krastanov growth mode, which is also referred to as self-organization, the three-dimensional islands with sizes of few nanometres are formed on top of a wetting layer. Therefore, self-organization is the common growth mode for III-V QDs on or in other III-V materials or Si, e.g. used in QDIPs or DWELL devices [253–260].

When growing a III-V material on Si by MBE or MOCVD, the lattice mismatch has an influence on the growth mode. For a small lattice mismatch, the thin layer will adopt the lattice parameter of the bulk material leading to a strained layer. With the intent to reduce the lattice mismatch and the inherent strain, misfit dislocations form when the growing layer exceeds a critical layer thickness [261–264]. These misfit dislocations can effect the optical as well as the electric properties of devices made from such epitaxially grown layers to large extents, e.g. acting as non-radiative recombination centres [265–267]. Several approaches have been developed to reduce the dislocation density and to improve the layer quality. One of these approaches is the epitaxial lateral overgrowth (ELO) which uses a thin SiO_2 mask on top of a previously deposited, thick III-V layer. The SiO_2 mask is lithographically patterned and in the openings the layer growth is then continued until the mask is laterally overgrown by the III-V layer. The dislocation are stopped by the intermediate mask material and the layer above has a

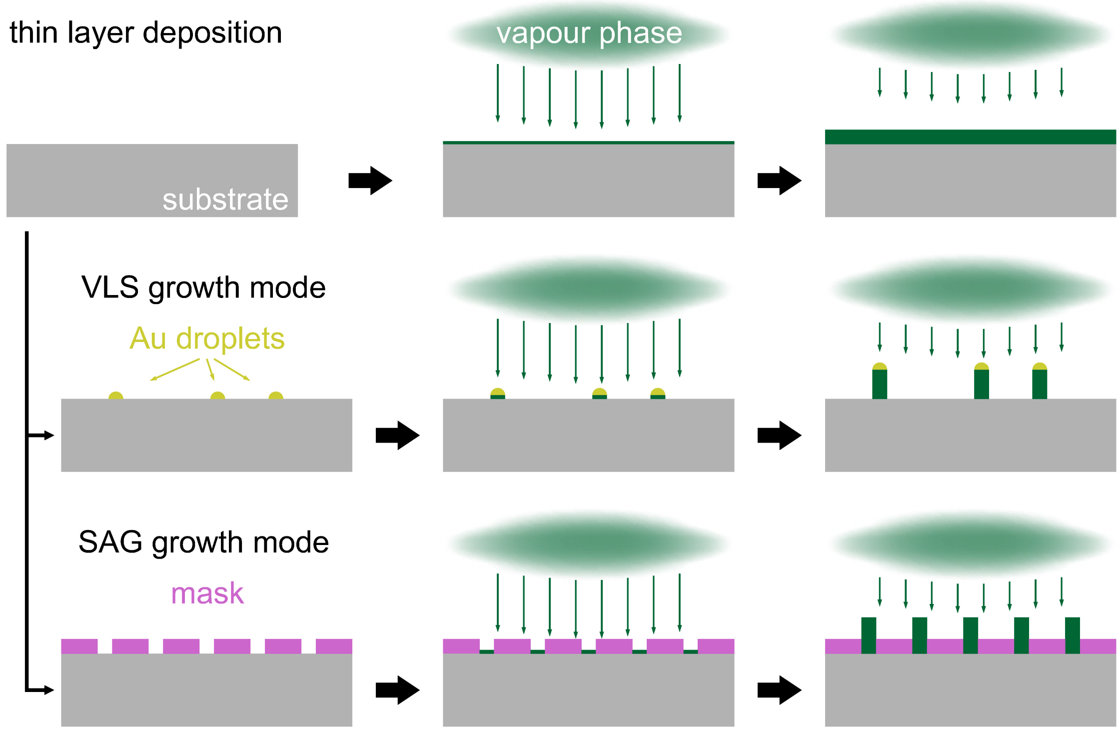

Figure 3.2.1: Schematic for the integration of III-V compound semiconductor into Si via deposition methods.

reduced dislocation density [268–270]. Another method to reduce the number of misfit dislocation is epitaxial necking or aspect ratio trapping (ART). This method employs a lithography step similar to the ELO approach, however, during ART the mask is used for a reactive ion etching (RIE) step with the purpose to etch trenches into the substrate material. The III-V material is then grown within these trenches and most of the evolving misfit dislocations are trapped in the trenches due to their 45° angle to the substrate material [271–274].

Besides the growth of thin layers or QDs, the fabrication of III-V NWs on Si substrates is another integration possibility. There are several approaches to achieve the NW growth [275]. The two most common ways – vapour-liquid-solid (VLS) growth and selective area growth (SAG) – are depicted in figure 3.2.1. During VLS growth [276, 277], a NW is grown by using catalyst droplets randomly distributed on the substrate surface. The metal catalyst, most commonly gold [278], is used to form an alloy with the deposit material from the vapour phase. This alloy has a very low melting point and, therefore, remains in the liquid phase. The droplet acts as a sink for the incoming vapour phase material and the alloy gets supersaturated due to the constant support from the vapour phase. The deposited atoms within the droplet diffuse towards the liquid/solid interface between the droplet and the substrate material, where they attach to the surface and build small islands. These small islands grow and coalesce and finally form a thin layer of the specific material. This process continues and, with time, new material is deposited layer-by-layer resulting in the growth of a single NW with the catalyst droplet on top [276, 277, 279]. Using this technique, a variety of III-V compounds have been brought into the form of NWs, including GaAs [280], InAs [281], InP [282] and GaP [283, 284]. The arsenide- and phosphide-based NWs can contain a relatively high number of twin boundaries and stacking faults, due to the occurrence of mixed wurtzite and zincblende phases [285]. This polytypism affects their optical [286] and electrical properties [287] but can be controlled using a two-temperature process [288]. For the fabrication of nitride-based NWs, catalyst particles are not necessary, as these compounds can spontaneously be formed on Si substrates using N-rich conditions during growth from the gas phase [253, 289]. Considering the growth by metal catalysts, there is a contamination of the III-V NWs by particles from the catalyst [290]. Contamination with Au atoms, for example, may affect the carrier recombination within the NWs and, therefore, compromises their electrical and optical properties as observed in Si and Ge NWs grown by Au-assisted VLS growth [278, 290–292]. An alternative in order to avoid the contamination from the metal catalyst is the usage of self-catalyzed growth, e.g. by employing a Ga droplet for the growth of GaAs NWs [293–296].

Another method to grow III-V NWs on Si is SAG which utilizes a pre-patterned SiO_2 mask, similar to the ELO method, to induce the NW formation only in the opened mask windows [297–301]. This method has three advantages: (1) the position of the NWs can be controlled precisely due to the electron beam lithography (EBL) patterning of the mask, (2) it is a catalyst-free technique and, therefore, avoids the contamination by metal atoms, and (3) threading dislocations due to the lattice mismatch between III-V compound and Si substrate are trapped inside of the mask windows, like in the ELO method. All of the aforementioned NW growth methods are capable of producing numerous different III-V compound semiconductor NWs on Si but there is also the possibility to grow NWs made of multiple compounds. Typical multi-component NWs are either axial hybrid [302, 303] or core/shell structures [304, 305], where different materials alternate either in growth direction or coaxial from an inner core to an outer shell, respectively. III-V NWs on Si, in general, find applications in various electrical and optical fields, including vertical surrounding gate transistors [55, 306, 307], single-electron transistors or tunnel FETs [308–310], nanoneedle LEDs or avalanche photodiodes [311, 312], and nanolasers [313, 314].

3.2.2 Wafer bonding

A different technique for the integration of III-V compound semiconductors into Si technology is wafer bonding. Wafer bonding refers to a process where two flat and clean surfaces are brought into close contact to each other and then bond together due to the local van-der-Waals forces. Using the adhesive forces, a thin layer can be transferred from a carrier substrate onto a host substrates, as it is depicted in figure 3.2.2. In the first step, both substrates are brought into close contact in order to form a single object. This bonding step can be achieved by different processes which can generally be separated into two groups: (1) direct wafer bonding where carrier and host substrate are brought into direct contact and (2) bonding with an intermediate layer [315]. The direct wafer bonding techniques have a high demand for clean and very flat surfaces of both wafers in order to avoid interface contamination and bubbles and to achieve strong bonding [316, 317]. As the two different substrates are in direct contact, a good thermal conductivity is achieved. However, at the elevated temperatures during annealing, which is necessary for strengthening the bonds, different thermal expansion coefficients of the bonded materials lead to a different material expansion and induce the evolution

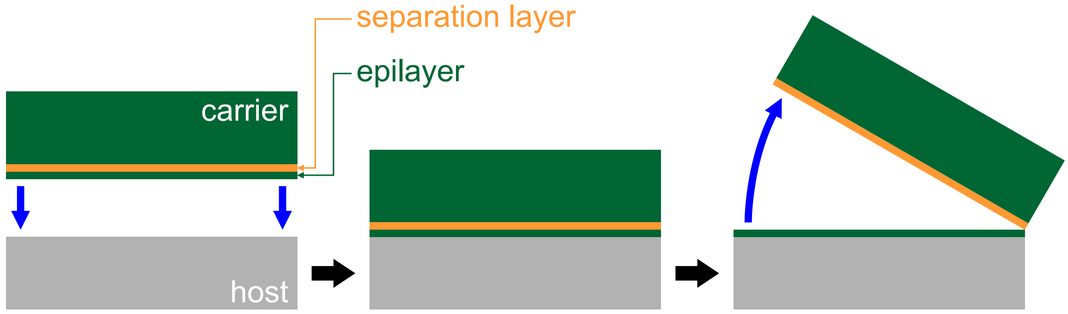

Figure 3.2.2: Schematic for the integration of III-V compound semiconductor into Si via wafer bonding methods.

of dislocations at the bonding interface [318]. Furthermore, interface states present at the bonding interface alter the electrical and optical properties [319]. Nevertheless, a sophisticated surface conditioning as well as a clean environment enables direct wafer bonding to prepare very abrupt interfaces [320, 321].

For the second group of wafer bonding techniques, the intermediate layer can be of different nature. Metal layers are used in solder or eutectic bonding methods, for example in the packaging of microelectromechanical system [322, 323]. Dielectrics and polymers can be used as bonding material as well and find application for integrated electronics [324–326] and optical device technology [327–329]. The advantages of using an intermediate layer are the low bonding temperatures, the ability to compensate surface inhomogeneities and the versatility to combine numerous different material [330, 331].

The next step during a wafer bonding process is the separation of the thin bonded layer from the carrier substrate. There are several possibilities how this separation can be performed. A very direct approach is thinning of the carrier substrate where the thickness of the carrier substrate is reduced by mechanical polishing and/or chemical etching until the favoured thickness is achieved [332, 333]. As the carrier substrate is almost completely removed by grinding or etching, thinning is not affordable for expensive materials. Another separation method is the cleavage of the two substrates. Hereby, the separation layer is mechanically fragile, e.g. porous, and by applying a lateral force this layer is split [334, 335]. The epilayer is transferred to the host substrate and the carrier substrate can be reused after the mechanical cleavage. Besides these two methods, the separation can be performed by a selective chemical etching of the separation layer [336]. The last and most sophisticated technique is the so-called ion-cut process. During this method, an ion beam implantation of H^+ or He^+ ions below the surface of the carrier wafer is performed. The implanted ions damage the substrate material which leads to the formation of the mechanically weak region. A subsequent low temperature annealing, the H^+ and He^+ ions tend to form bubbles. These bubbles extend with further annealing until cracks parallel to the surface form. These extended cracks can then be utilized to split the wafer. This process is also known as Smart-Cut^{TM} [337]. The industrial production of Silicon-on-Insulator (SOI) and Germanium-on-Insulator (GeOI) substrates is mainly based on this wafer bonding technique [337, 338], however, this process is also employed for bonding several other materials including III-V compounds, e.g. GaAs [339], InP [340], GaSb [341] and GaN [342].

Regarding III-V integration into Si technology, wafer bonding finds application in different areas. III-V-on-insulator substrates prepared by wafer bonding are used as templates for the epitaxial growth of III-V multilayer systems for high-electron-mobility transistors (HEMTs) [343]. A large benefit of wafer bonding is the scalability. Large scale integration for the preparation of III-V-on-insulator substrates with diameters up to 300 mm is possible [344]. Such large substrates are suitable for the high-yield fabrication of III-V MOSFETs [345–347]. In combination with dedicated lithography and etching steps, wafer bonding has the capability to produce nano-scale architectures like finFETs [348]. By using a flexible transfer substrate, pre-patterned III-V layers can be "printed" in order to achieve nano-scale electronics on conventional Si substrates [349] but also on flexible substrates [350]. Combining a high electron mobility III-V compound with a high hole mobility III-V or Ge, even complementary MOS architectures are possible by using this technique [351–353]. Besides electronic applications, wafer bonding is also suitable to fabricate layer systems for optical devices. The applications for photonics include LEDs and lasers based on QDs [354–358], which can probably be utilized for on-chip and intra-chip communication [359], and multijunction solar cells [360–362].

3.3 III-V integration via ion beam implantation - an alternative route

The integration of III-V compound semiconductors into Si by ion beam implantation is an alternative to the conventional approaches using MBE, MOCVD or wafer bonding. The synthesis of NCs with this method is performed simply by combining an ion implantation step and a thermal annealing step to initiate cluster formation, as depicted schematically in figure 3.3.1. Usually, ion implantation is employed for doping semiconductors to fabricate p-n-junctions. Early adoptions of ion implantation in order to form NCs have been done in the 90s of the last century. At first, SiO_2 layers have been implanted with Si^+ and Ge^+ ions which led to the formation of Si and Ge NCs embedded in a SiO_2 matrix, respectively [363–366]. The formation of these particles is accounted to nucleation from a solid solution which is supersaturated due to ion implantation and subsequent Ostwald ripening [367–369].

Consequently, the introduction of various III-V and II-VI compound semiconductors into different dielectric matrix materials has also been achieved [370]. For example, GaAs nanoparticles within a SiO_2 matrix have been prepared which emitted light in the visible range due to excitons in the NCs [371, 372]. The pioneering work in this particular field is mainly accounted to the group around *C W White* at the *Oak Ridge National Laboratory*, which conducted an extensive study on integration of various group-IV, III-V and II-VI in SiO_2, Al_2O_3 and Si by ion beam synthesis [370, 373–378]. Besides semiconductor NCs, they also investigated metallic and ferromagnetic NCs [379–381]. The formation of the NCs as well as their size and structural properties depend on several factors. The implantation fluence and the temperature during implantation affect the constitution of the implanted substrate region, namely the amorphisation of the top region, which influences the NC formation during the subsequent thermal treatment and, hence, the NC size and crystal structure [382].

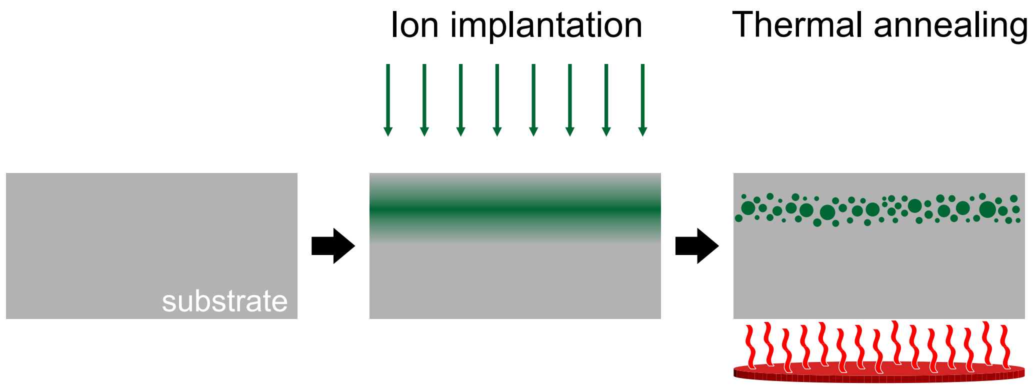

Figure 3.3.1: Schematic for the integration of III-V compound semiconductor into Si via ion beam implantation and thermal annealing.

Furthermore, the implantation sequence has an impact on the final NC size distribution, as it was shown for InAs NCs in Si, where samples implanted with As^+ at first showed a particle size distribution located around the projected range, while In^+-first implanted samples displayed different size distributions separated in depth [378]. The various III-V compounds integrated into Si by ion beam synthesis generally grow epitaxially within the Si substrate and show a spherical shape with a rather broad size distribution [383–385]. Recently, the formation of ternary III-V compounds in Si by ion implantation and rapid thermal processing (RTP) has been reported [386].

With the substitution of the conventional annealing methods (furnace, RTP) by FLA in the millisecond-range, *Prucnal et al.* at the *Helmholtz-Zentrum Dresden-Rossendorf* were the first to report the formation of InAs precipitates in Si at such short timescales [387]. These precipitates showed the characteristic InAs phonon mode in Raman spectroscopy as well as a strong photoluminescence signal corresponding to InAs proving their crystalline nature. Additionally, they were able to improve the InAs NC size distribution in Si in comparison with conventionally annealed samples and to suppress the out-diffusion of the implanted ion species by using FLA [388]. In subsequent works, several other III-V compounds have also been integrated into Si by the combination of sequential ion implantation and FLA including InP [389] and GaAs [390]. This integration process mainly yields hemispherical or triangular NCs which are located at the surface of the Si substrate. In order to exploit these III-V NCs, an additional RIE step of the Si substrate has been conducted. These experiments resulted in the fabrication of III-V-NC-on-Si-nanocolumns including the III-V compounds InAs [391] and InP [389] as the III-V NCs act as etching mask for the substrate material. When biased via conductive atom force microscopy (AFM), such III-V-NC-on-Si-nanocolumns show a p-n-heterojunction behaviour where the III-V compound acts as n-type and the Si nanocolumn as p-type material. Figure 3.3.2 depicts the cross-section transmission electron microscopy (TEM) micrograph of an InAs-NC-on-Si-nanocolumn (a) and its corresponding current-voltage characteristic (b).

Furthermore, this process has been adopted to other substrates than bulk Si. By the implantation of SOI substrates, hybrid substrates consisting of III-V NCs within the thin Si layer have been fabricated as well [392]. In combination with a masking procedure, the ion implantation/FLA integration method is capable of implementing III-V segments into VLS-grown Si nanowires randomly distributed on a substrate wafer

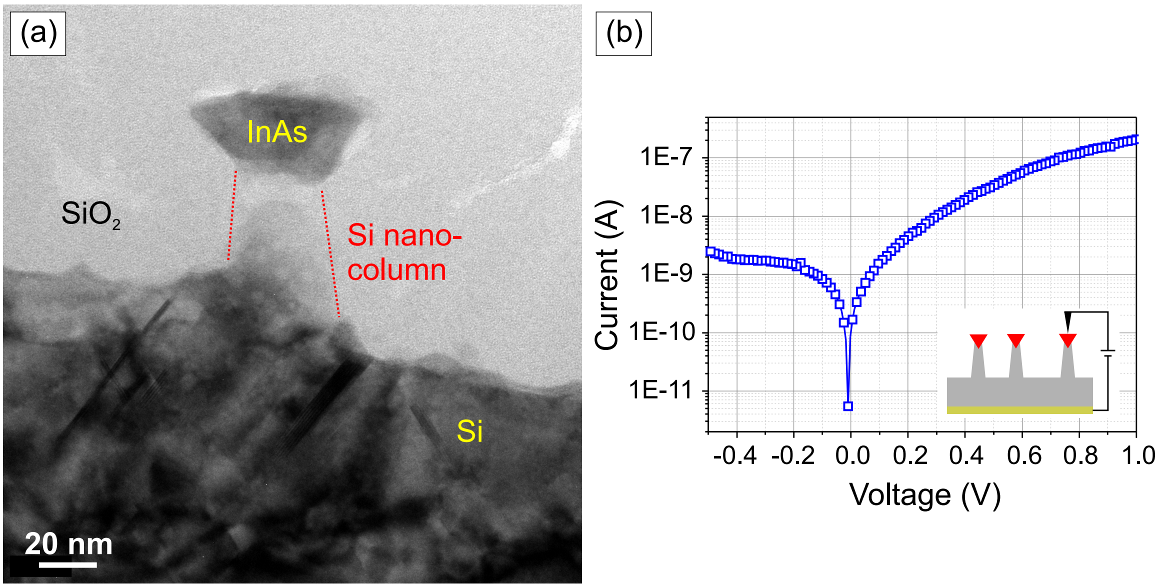

Figure 3.3.2: InAs-NC-on-Si-nanocolumn prepared by sequential ion implantation, FLA and RIE by *S Prucnal*. (a) Cross-section TEM image. (b) Current-voltage characteristic recorded by conductive AFM showing p-n-heterojunction behaviour. (Reprinted (adapted) with permission from [391]. Copyright 2011 American Chemical Society.)

[393]. These III-V segments obtain good crystalline quality and possess atomically sharp interfaces to the surrounding Si. Such III-V-in-Si-nanowires have recently been employed for avalanche LEDs emitting in the visible range [394]. In the frame of this work, we were able to present an alternative substrate for the integration of various III-V compounds in thin Si by the substitution of the SOI by a similar layer system grown by plasma-enhanced chemical vapour deposition (PECVD) [395]. Furthermore, we demonstrated the integration of InAs and GaAs in Ge substrates with this method, lately [396].

4 Methods

In this chapter, the employed experimental methods are addressed, including simulations, sample preparation processes, and characterisation techniques. The first part covers simulations of the implantation profiles of the group-III and -V ions, and the simulation of the temperature distribution in a silicon wafer during FLA. The second part focuses on the sample processing methods, which range from thin layer deposition over ion beam implantation and FLA to techniques dedicated to small scale device fabrication for the preparation of implantation masks and nanowires. In the last part of this chapter, the utilised characterisation methods are presented, including the structural and optical measurement techniques.

4.1 Simulations

4.1.1 Sequential ion implantation of group-III and -V ions

In this work, the integration of III-V compound semiconductors into Si is performed by ion beam implantation. In order to have the implanted ions at a depth which is useful for nanocrystal formation, the correct implantation energy has to be chosen. Especially in the thin layer systems, the projected range has to lie in the centre of the Si layer and not in the surrounding SiO_2 layers. Therefore, the implantation profiles have been simulated by using "The Stopping and Range of Ions in Matter (SRIM)" code [397]. The SRIM code can be used for the three-dimensional simulation of ion paths in layer systems. However, it is not possible to simulate multiple implantations at once. Sputtering or a change in the composition of the substrate material during implantation can alter the starting parameters for the simulation of a second implantation step and, in turn, lead to a different projected range of the implanted ions. For simplicity, it is assumed that the first implantation does not affect the following implantation(s) and that simulating the particular depth profiles, separately, gives the same result as simulating multiple consecutive implantations.

For the simulations, different layer stacks are used depending on the layer system which should be implanted, namely, a "capping layer/substrate" and a "capping layer/device layer/box layer/substrate" stack. Schematics of both layer stacks are given in figure

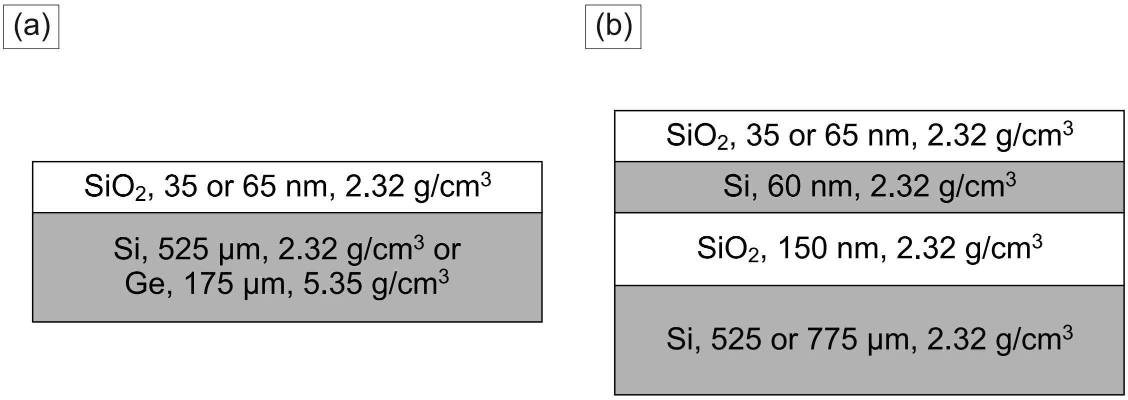

Figure 4.1.1: Two-layer (a) and multilayer stack (b) used during SRIM simulation of the implantation depth. The particular layers include materials, layer thicknesses and mass densities.

4.1.1 including layer thicknesses and mass densities, which are taken from the SRIM integrated database. The ions, which have been simulated, are Ga^+ and In^+ for group III and N^+, P^+, As^+, and Sb^+ for group V, and the parameters have been set to 1×10^5 simulated ions at an incidence angle of 7° while the specific ion data has been taken from the SRIM database. The implantation energy has been varied to get overlapping depth profiles for the group-III and -V species approximately 30 nm below the capping layer/substrate interface in the two-layer system and centred in the Si device layer for the multilayer system. In figure 4.1.2, the simulated depth profiles of In and As implanted into the two-layer system (a) and the multilayer system (b) are shown, exemplarily. In both cases, the implantation energies are set to 200 keV and 150 keV for In^+ and As^+, respectively. These energies give an approximately equal projected range for both ion species, leading to an overlap of both depth profiles. Due to the difference in the ion masses, the As^+ profile is broader than the In^+ profile which results in different peak atom concentrations. Obviously, there is also a rather large amount of implanted ions present in the surrounding SiO_2 layers. In the multilayer system, the bulk Si is not implanted, therefore, no III-V compounds semiconductor nanocrystals should appear in this region. Furthermore, the total amount (area under the profile) of In^+ in the Si device layer is larger than the total amount of As^+, which leads to In excess and supports the precipitation of metallic In cluster (see section 5.2). Tables A.3.1 and A.3.2 in Appendix A.3 summarize the simulation results for the optimal implantation energy for the two-layer systems and the multilayer system, respectively. These results are used at the ion implantation step during sample preparation.

4.1.2 Temperature gradient during flash lamp annealing

The temperature during FLA is the most important parameter for the formation of the III-V compound semiconductor nanocrystals. If the temperature is too low, the implanted region does not melt and almost no III-V NCs are formed. If the temperature is too high, the capping layer is peeled off or the wafer breaks into pieces since FLA only heats the top part of the wafer while the back remains relatively cold leading to a temperature gradient and, hence, to mechanical stress. In order to promote NC

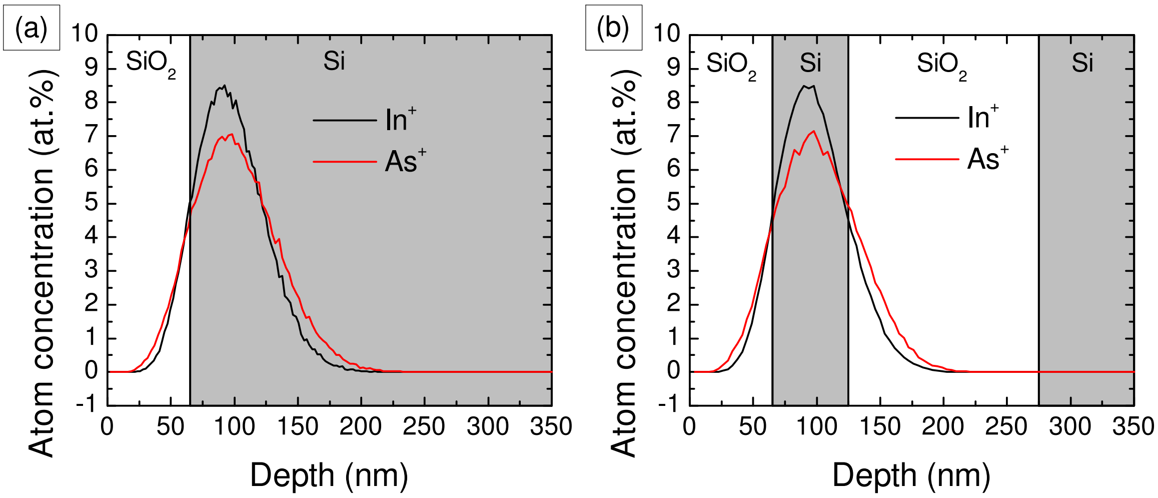

Figure 4.1.2: Depth profiles simulated with SRIM code for In$^+$ (black) and As$^+$ (red) implanted into the two-layer (a) and multilayer system (b) using an ion fluence of 3×10^{16} ions/cm^2 per ion species.

formation and to avoid wafer damage, a proper temperature window is crucial. During FLA it is challenging to measure the temperature directly, therefore, the temperature profile has been simulated using the energy density (σ_{FLA}) of the light pulse applied to the sample surface. The final temperature depends on a variety of parameters which can be divided into two groups, material and FLA tool parameters. The first includes optical constants, heat capacities, and thermal conductivity coefficients of the different layers but also the thickness of the substrate, while the second covers the reflectivity of chamber walls, preheating temperature, and the flash pulse properties itself, like flash pulse duration and energy density which is directly dependent on the charging voltage (V_{charge}) of the flash lamp capacitors.

The temperature simulation is separated into two steps. The first step is the simulation of the light absorption within different matrices with the aid of the wave transfer method [398]. The deduced absorption profile acts as a boundary condition for the second step, where the one-dimensional heat equation is solved using FlexPDE [399], a commercial software for solving partial differential equations. The preheating temperature is set to 470 °C, the chamber wall reflectance is assumed to be 90 %, the flash pulse duration is fixed at 20 ms, σ_{FLA} (V_{charge}) has been varied between 32.2 (2.0) and 92.6 J/cm^2 (3.4 kV) and for the cooling rate a fixed heat transfer coefficient has been used. The simulation has been performed for a plain Si wafer, but not for a layer stack. A SiO$_2$ capping layer would be transparent in the spectral range of the Xe flash lamps and would not absorb energy from the flash pulse but it would influence the reflectivity at the Si surface leading to slightly faster heating rates than in the simulation. A phase transition in the Si substrate is also not considered, although the calculated temperatures exceed the melting point of Si. However, the excess heat is consumed for the phase transition from solid to liquid Si.

Figure 4.1.3 displays the temperature profiles at the surface for different σ_{FLA} (a) and at a fixed σ_{FLA} of 92.6 J/cm^2 for different wafer depths (b). In both figures, the blue lines mark the melting temperatures of crystalline silicon and amorphous silicon. The

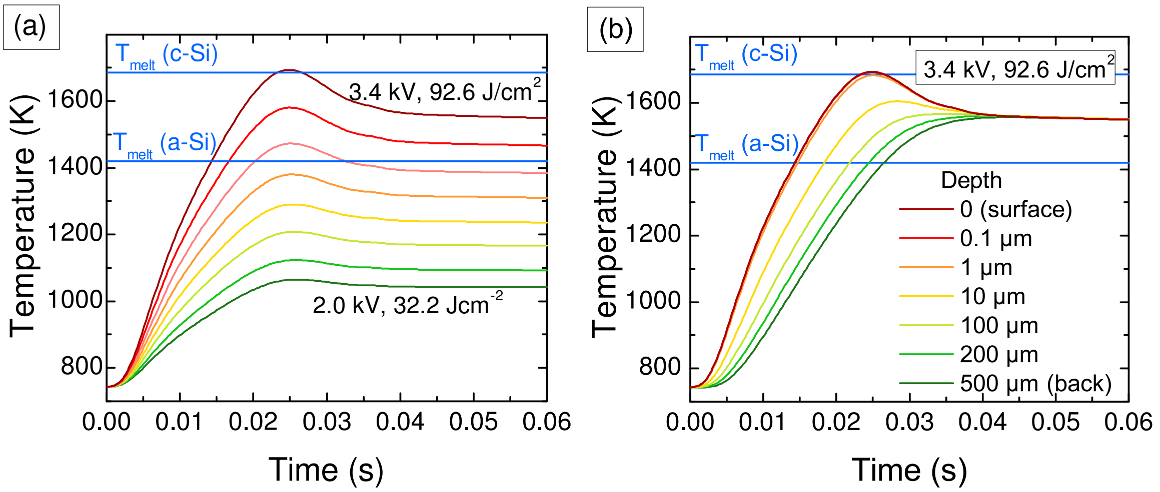

Figure 4.1.3: Simulated temperature profiles of a plain Si wafer during flash lamp annealing. (a) Temperature over time at the surface for V_{charge} (σ_{FLA}) ranging from 2.0 kV (32.2 J/cm^2) to 3.4 kV (92.6 J/cm^2) in 0.2 kV steps. (b) Temperature over time for a fixed V_{charge} (σ_{FLA}) of 3.4 kV (92.6 J/cm^2) for different depths in the wafer.

melting point of amorphous Si is about 200 K lower than that of crystalline Si [143]. The melting point depression due to the implanted ions is not taken into account. The temperature profiles show a very steep increase for the first 25 ms, where the flash pulse is applied to the sample surface. Afterwards, the temperature decreases relatively fast for the following 10 ms. Then a slow cooling rate accommodates after about 40 ms which lasts for several seconds until the sample finally cools down completely. When looking at the different σ_{FLA} in figure 4.1.3(a), higher σ_{FLA} result in faster heating rates, higher maximum temperatures and an offset in temperature where the slow cooling rate takes over. V_{charge} (σ_{FLA}) above 3.0 kV (72.2 J/cm^2) are sufficient to reach peak temperatures above the melting point of a-Si and, therefore, melt the implanted top region of the samples. When taking a melting point depression due to the implanted ions into account, even lower V_{charge} (σ_{FLA}) can be sufficient to melt the implanted region. The wafer depths, which were not implanted, remain crystalline and are not molten by the flash pulse, except for the highest V_{charge} (σ_{FLA}) but in this case the molten fraction of the c-Si is probably rather small. This is also supported by the temperature profiles at various wafer depths, depicted in figure 4.1.3(b) for the FLA at 3.4 kV (92.6 J/cm^2). When moving away from the surface, the heating rate decreases and also the starting point of heating up is slightly shifted to later times, but after about 40 ms, surface and backside temperatures match and the slow cooling rate begins. The uppermost 10 µm of the Si wafer have almost the same temperature profile leading to a homogeneous heating of the implanted region and ensures that all of the amorphized part is molten during FLA. The regions more than 100 µm below the surface stay significantly cold, which causes the fast cooling of the surface directly after the flash pulse.

In general, the simulation on the temperature profiles shows that V_{charge} (σ_{FLA}) above 2.8 kV (63.3 J/cm^2) is sufficient to melt the implanted region of the Si wafer. This is also valid for the thin Si layer embedded in SiO_2 in the multilayer system due to the

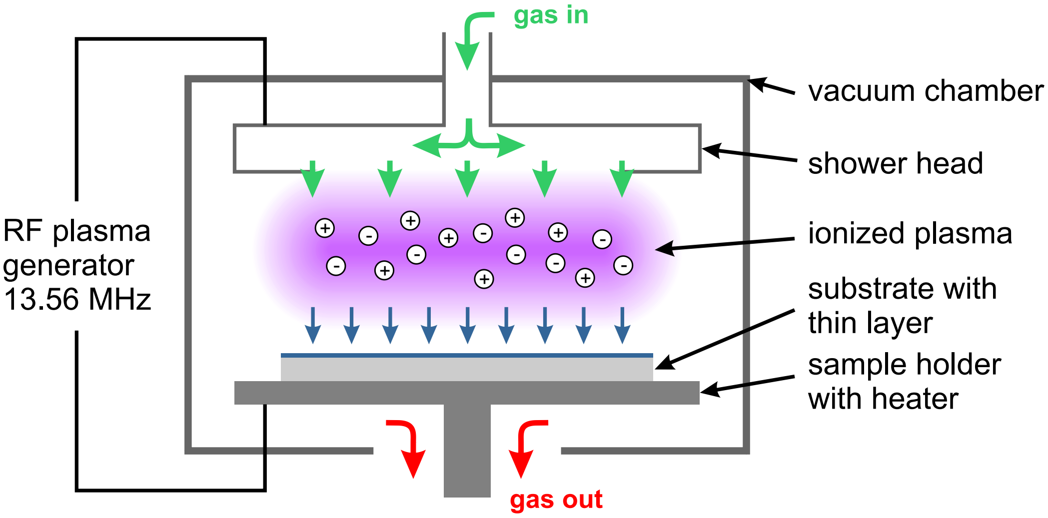

Figure 4.2.1: Schematic of a plasma-enhanced chemical vapour deposition (PECVD) chamber.

transparency of SiO_2 in the spectral range of the Xe flash lamps. The underlying c-Si is not molten since the simulated temperatures stay below its melting point. Furthermore, calculated temperatures above the melting point of a-Si are not probable as the liquid Si has a higher reflectivity than solid Si which reduces the energy transferred to the substrate. Finally, the simulation shows that cooling is dominantly driven by heat conduction to the backside of the wafer.

4.2 Sample preparation methods

4.2.1 Thin layer deposition

4.2.1.1 Plasma-enhanced chemical vapour deposition

Plasma-enhanced chemical vapour deposition (PECVD) is a method to produce thin layers of a variety of materials from a gaseous phase. The thin layer deposition takes place as a result of chemical reactions between the different source gases assisted by a plasma. Figure 4.2.1 depicts a schematic of a PECVD reactor. The mixture of reacting gases, mainly hydrogen gases of materials which shall be deposited, e.g. SiH_4 or NH_3, is introduced simultaneously into the reaction chamber through a shower head, ensuring a homogeneous gas in-flow. The shower head also acts as top electrode for plasma generation. The substrate is placed on a sample holder with integrated heating system and also acts as bottom electrode. The plasma can be generated by applying either a radio frequency (RF) or an alternating current (AC) between the two electrodes. Due to the electric field, the molecules of the reaction gases are dissociated and stripped off their electrons, producing free radicals and ions. These two species are responsible for the layer deposition on the substrate material. The reaction at the substrate's surface takes place at elevated temperatures. Since hydrogen gases are used as precursors, the final layers contain a considerable amount of hydrogen [400–402].

The hydrogen concentration can be reduced by heating the sample to higher temperatures and driving out the hydrogen directly after layer deposition. Nevertheless, there will still be some residual hydrogen in the deposited layers. The final layers are mainly amorphous or polycrystalline, although a subsequent heating step can already initiate the recrystallization process in the case of a-Si, for example. Thin film deposition by PECVD is a relatively fast method in comparison with sputter techniques and yields also good sidewall coverage. PECVD grown amorphous or polycrystalline Si:H layers, for example, find application in photovoltaics [403].

In this work, PECVD was used to produce SiO_2 capping layers for Si and Ge substrates and for the fabrication of $SiO_2/Si/SiO_2$ layer stacks on Si, in order to mimic SOI wafers. The deposition process starts with pumping the chamber down to vacuum conditions. Afterwards, the chamber is purged by pure N_2 gas und cleaned with N_2O gas for 1 min each. Then the actual deposition steps are performed using either a SiH_4/N_2O mixture for SiO_2 single layer deposition or a three-step procedure to grow the $SiO_2/Si/SiO_2$ layer stack. Hereby, the same SiH_4/N_2O mixture is employed for both SiO_2 layers while the a-Si layer is formed by a SiH_4/Ar gas mixture. During all deposition steps the temperature is kept constant at 350 °C. In the following, the sample is heated up to 700 °C to drive out hydrogen.

4.2.1.2 Electron beam evaporation

Electron beam evaporation is another thin film deposition technique but in contrast to PECVD, it is a physical vapour deposition method. It does not use a chemical reaction of precursor gases to form the layer material but the impact of electrons onto a target made of the material which shall be deposited on the substrate. A typical electron beam evaporation system is schematically shown in figure 4.2.2. The whole process takes place under vacuum conditions. Initially, electrons are emitted from a filament (e.g. tungsten) and are directed by a magnetic field towards a target consisting of the material which should be deposited on the sample. When the electrons hit the target, their high kinetic energy is transformed mainly into thermal energy, heating the target material. During this heating, atoms of the target are evaporated and form a vapour phase. The resulting vapour covers all surfaces within line-of-sight including the substrate. The substrate's surface is then coated with a thin layer of the desired material. Electron beam evaporation features high deposition rates and low process temperatures.

In the sample preparation process of this work, electron beam evaporation is used for metal deposition (Ni, Al). In combination with a patterning procedure by electron beam lithography, implantation and etching masks are fabricated, in order to enable local ion implantation and Si nanowire etching, respectively. For the implantation masks, 100 nm Ni are deposited at rates of 1.4 Å/s or 1.8 Å/s using an accelerating voltage of 10 kV and a beam current of 82.2 or 79.8 mA, respectively. The deposition is performed at room temperature under vacuum conditions with pressures of 3.6×10^{-6} Pa and 8.3×10^{-6} Pa. For the nanowire etching masks 50 nm Ni are deposited with a rate of 1.3 Å/s using an acceleration voltage of 10 kV, a beam current of 80 mA and a pressure of 4.2×10^{-6} Pa.

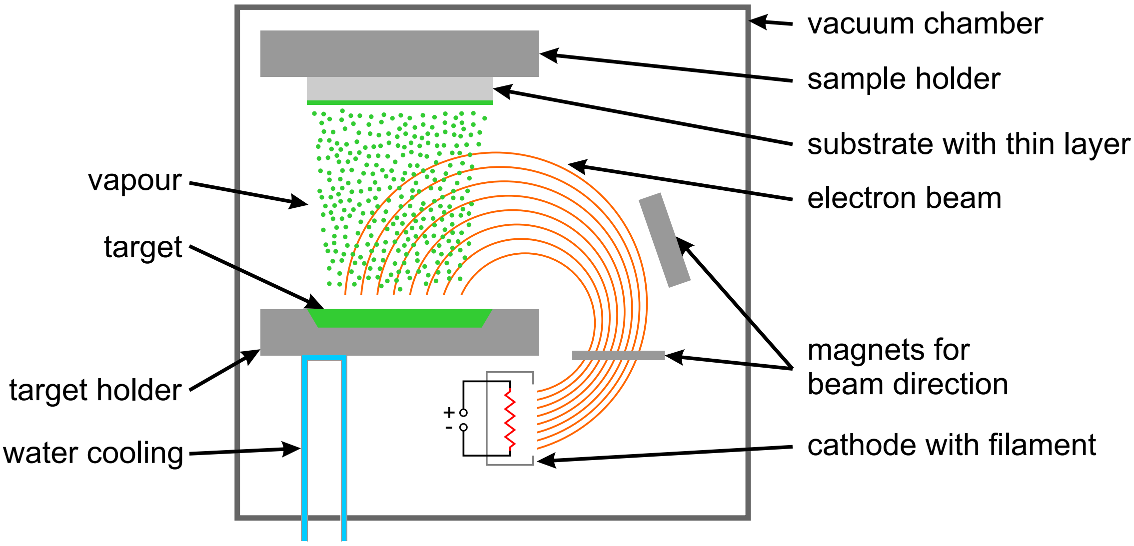

Figure 4.2.2: Schematic of an electron beam evaporation tool.

4.2.2 Ion beam implantation

Ion beam implantation is a technique to incorporate atoms (ions) accelerated by an electric field into a substrate where they interact with the substrate material at the nuclear and electronic scale. By this interaction, the properties of the substrate can be changed dramatically, i.e. amorphisation of a crystalline layer. In principle, every atom (ion) can be implanted into any type of substrate material, which makes this method very versatile. In figure 4.2.3, the general working principle is schematically depicted. The ion source generates the desired ion species and releases them into the accelerator. Electrical lenses are used to have control over the beam shape. The ions travel then through a mass separation system, consisting of an electromagnet and separation slit, where only the ions pass which shall be implanted. After mass separation, the ions are accelerated by an acceleration tube and directed by an X/Y scanner onto the substrate. During ion implantation, there are three main parameters besides the nature of the ion itself which play a role, the ion energy, the ion fluence and the beam current. The ion fluence is given in ions/cm^2 and determines the amount of ions that are implanted into the target material. In combination with the beam current, the ion fluence defines the overall implantation time. Furthermore, the beam current can also give an estimation of the heating of the implanted sample. The third parameter, the ion energy, describes the kinetic energy of the ions hitting the substrate. Taking into account the mass of the particular ion species and material properties of the substrate, the kinetic energy determines the projected range and the depth profile of the implantation. By tuning these three parameters, ion implantation can be suited to a variety of applications.

The most prominent and important application of ion implantation is doping in semiconductor technology. Hereby, mainly boron or phosphorus are implanted into Si to introduce dopant atoms, resulting in p-type (B) or n-type (P) material, which can then be exploited for the fabrication of devices, i.e. FETs or p-n diodes. Another field of application is the production of buried layers. For example, the implantation

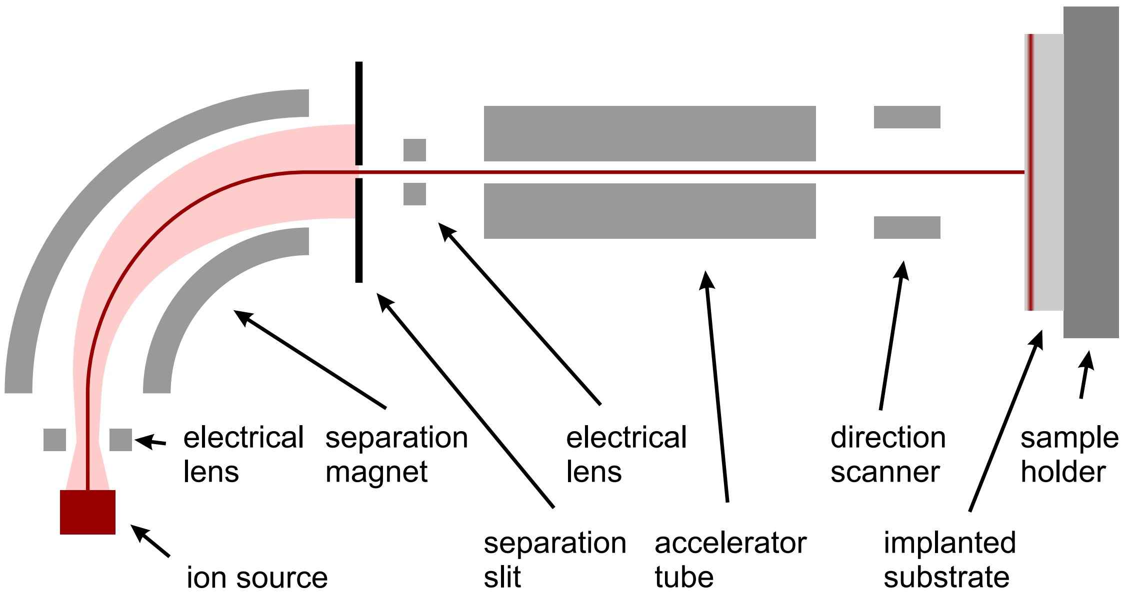

Figure 4.2.3: Schematic picture of an ion beam implantation system.

of oxygen into Si combined with a subsequent high temperature anneal leads to the formation of a buried silicon dioxide layer at a defined depth and creates a SOI substrate material. This process is called separation by implantation of oxygen (SIMOX) [404, 405] and wafers produced by this method are also used in this work. Besides the field of microelectronics, ion implantation can also be utilised for surface modification including surface hardening of metallic and ceramic materials [406], ion beam mixing [407] or ripple formation [408].

In this work, ion implantation is used to introduce of group-III and -V ions into a Si-based host matrix. The implantation of these ions is performed sequentially, and either two or three different ion species are implanted in order to form binary or ternary compound semiconductor NCs within Si, respectively. The range of ion species includes Ga^+ and In^+ for group-III and N^+, P^+, As^+ and Sb^+ for group-V. The implantations are conducted at a 500 kV Implanter from High Voltage Engineering Europe BV (Model B8385) with an IHC Bernas gas and solid phase ion source. In all sample series, the group-V ions have been implanted previous to the group-III ions. The implantation angle is set to 7° to avoid channeling of the implanted ions within the Si lattice. The samples are implanted at room temperature without additional cooling, which results in slight heating of the samples but the substrate temperature does not rise above 150 °C. Due to the high ion fluences between 1×10^{16} and 3×10^{16} ions/cm^2 for each ion, the top part of the substrate material is heavily damaged and the crystalline Si either as bulk material or thin layer is amorphised. For the multilayer system, a Si self-implant with an ion fluence of 6×10^{16} ions/cm^2 has been performed as a reference experiment. Additionally, an experiment using crystalline Ge as substrate material has been conducted in order to compare III-V NC formation in both materials. Implantation energies are chosen to result in depth profiles either closely beneath SiO_2/bulk interface or centred in the intermediate layer and are deduced from SRIM simulation values given in tables A.3.1 and A.3.2 in Appendix A.3.

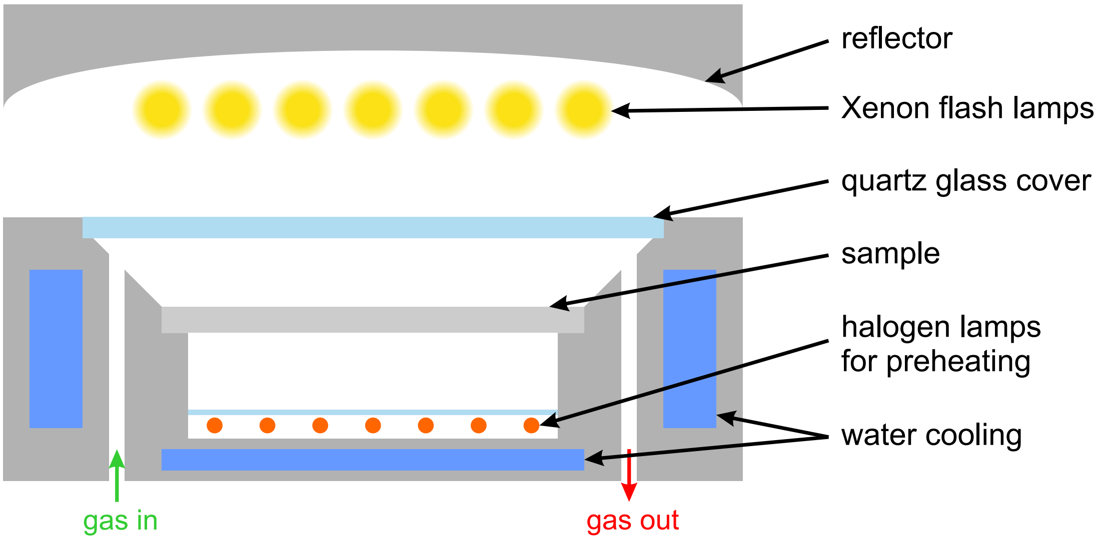

Figure 4.2.4: Schematic layout of the flash lamp annealing system.

4.2.3 Flash lamp annealing

Flash lamp annealing (FLA) is a thermal annealing technique which utilises a very short and intense light pulse. The general layout of flash lamp annealing system is depicted in figure 4.2.4. The annealing chamber consist of two sets of lamps, one lamp set for the preheating and another lamp set for the actual flash. The preheating system at the bottom below the sample uses halogen lamps, while in the flash system above the samples xenon lamps are employed. Behind both types of lamps reflectors are installed to direct more light towards the sample. A water cooling system prevents overheating and an additional gas system can be used to perform the flash lamp annealing under different ambients, for example Ar or N_2 atmosphere. The preheating is performed to heat the sample from the backside to a certain temperature and then the sub-second flash pulse is applied to quickly heat up the sample surface to the desired amount. During the flash pulse only the uppermost part of the sample is heated up, while the backside remains colder. The final temperature at the surface is determined by several material properties and can be simulated as presented in section 4.1.2 since a direct temperature measurement is very challenging. Therefore, the flash pulse parameters, namely pulse duration and charging voltage of the capacitors (V_{charge}), are taken as a measure when comparing different materials and systems.

The preheating can be performed up to a maximum temperature of 1100 °C and is necessary to reduce the mechanical stress within the substrate caused by the thermal gradient due to the fast and steep temperature ramp up at the surface during the flash pulse. Without preheating, it is possible that the substrate brakes apart or that thin films crack or peel off, especially at higher V_{charge}. The xenon flash lamps are discharge lamps, where a plasma strand is generated by the discharge of capacitors and then emits a typical high intensity light pulse in the visible range. The spectrum of the flash pulse is shown in figure 4.2.5(a). The capacitors can be charged to up to 4.4 kV and V_{charge} can be converted into an energy density (σ_{FLA}). The pulse duration is adjusted by using an electric circuit built of several capacitors and inductors, and can be varied between 130 µs and 20 ms.

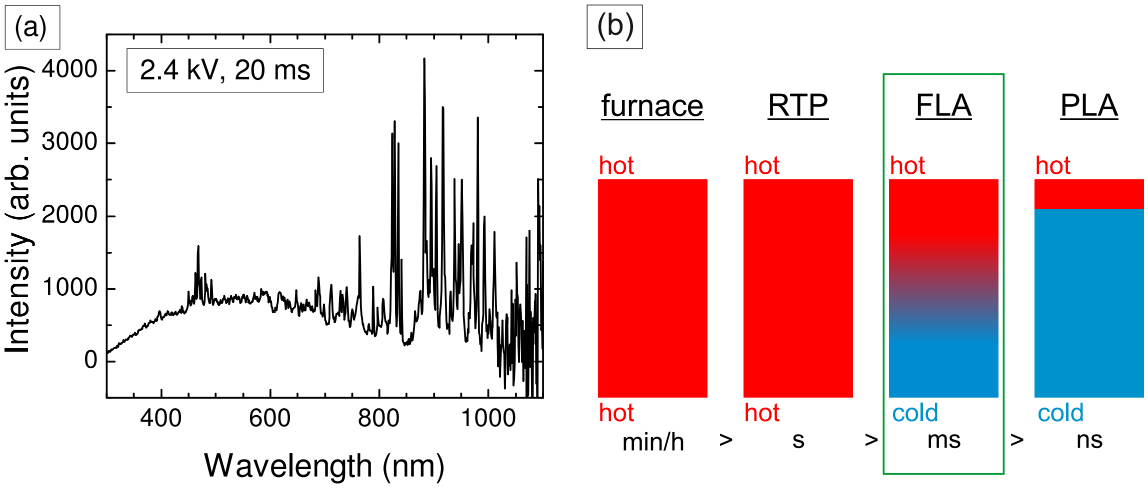

Figure 4.2.5: (a) Spectrum of a xenon flash lamp. (b) Comparison of temperature depth distributions and time domains of various annealing techniques.

In comparison with conventional annealing techniques like furnace annealing or RTP, the advantageous property of FLA is the limitation of heating only the uppermost region of the substrate. With the other treatments, the sample has the same temperature over the complete depth, while with FLA, there is a temperature gradient between the hot surface and the colder backside. Another advantage is the short time scale of FLA. A simple picture emphasizing both advantages of FLA is given in figure 4.2.5(b). Another annealing technique featuring these two properties on an even shorter time scale is PLA. However, for larger samples FLA and PLA show laterally inhomogeneous heating due to the arrangement of the lamps or the necessity of scanning with the laser beam, respectively.

In this work, FLA is used to induce III-V NC formation and Si recrystallization after ion beam implantation. In order to achieve this goal, temperatures above the melting points of amorphous Si and the particular III-V compound semiconductor are needed. According to the simulations presented in section 4.1.2, these temperatures can be reached in bulk silicon with FLA using V_{charge} between 2.8 and 3.4 kV at a pulse duration of 20 ms in combination with a preheating for 3 min at 470 °C. At shorter pulse durations, no III-V formation is observable. For the multilayer system, slightly higher V_{charge} (3.0 to 3.8 kV) are necessary due to larger sample thickness and different absorption behaviour for thin films. In the case of bulk Ge samples, V_{charge} is much lower (1.1 to 1.5 kV) due to a lower melting point, reduced wafer thickness and a higher absorption coefficient. The preheating parameters are the same for all samples and the FLA is performed in an Ar atmosphere.

4.2.4 Small scale device preparation techniques

This section covers all further techniques used for sample processing on small scales including electron beam lithography and chemical etching. The following methods have been employed for the fabrication of implantation masks and Si nanowires.

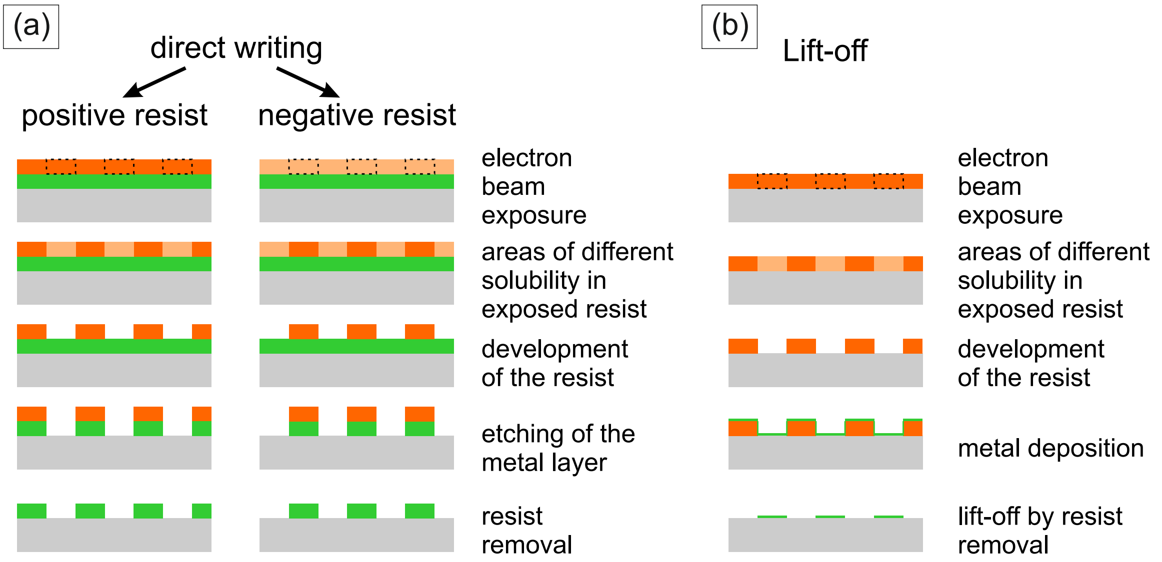

Figure 4.2.6: Different electron beam lithography processes in combination with metal deposition and etching steps. (a) Direct writing with positive and negative resist. (b) Lift-off process.

4.2.4.1 Electron beam lithography

Electron beam lithography (EBL) is a technique for the production of structures at the nanoscale. During this process a chemical resist is deposited on the substrate using spin coating. This resist is then exposed to a focused electron beam and the structures are written directly into the resist. Due to electron beam exposure, chemical bonds in the resist are either broken or established, depending on the type of resist, which results in a change of the solubility. Finally, the development of the resist takes place using dilution of the exposed or non-exposed areas by a solvent. The structures patterned in the resist by this procedure can be transferred to underlying materials, e.g. a metal layer, by chemical etching or a lift-off process. The possible electron beam lithography processes are depicted in figure 4.2.6. In figure 4.2.6(a), the combination of EBL and etching is displayed using either a positive or negative resist. The layer which shall be patterned has to be deposited before resist spin coating. After resist development, this layer is then etched by RIE or reactive ion beam etching (RIBE) and the structure of the resist is transferred. At the end, the residual resist is removed to uncover the structured layer. Depending on the type of resist, the areas exposed to the electron beam are removed (positive resist) or revealed (negative resist). Figure 4.2.6(b) shows the lift-off procedure. After the resist development step, a thin layer is deposited onto the substrate, i.e. by electron beam evaporation. The thin layer covers the remaining resist but also the surface of the substrate between the resist structures. Afterwards the resist is removed taking the material deposited on top of the structure with it. The material deposited in between the structures remains unaffected. In this process the thickness of the resist has to be much larger than the thickness of the deposited layer to ensure a good transfer of structures.

In this work all three of the presented processes are performed to fulfil different sample preparation tasks. Direct EBL writing with a positive resist in combination with

RIBE is used for the fabrication of metal hard masks for local ion implantation. For the implantation masks either an aluminium or a nickel layer has been covered by a poly(methyl methacrylate) (PMMA) or a ZEP-520 resist, which is a mixture of methyl styrene, chloromethyl acrylate copolymer and anisole. The thicknesses of the resists are approximately the same as the metal layer thicknesses which have been 150 nm and 100 nm for Al and Ni, respectively. The Si nanowires have been fabricated using two different approaches. The first one is the lift-off procedure where a 50 nm thick Ni layer was deposited on approximately 200 nm ZEP resist, which hereby acts as a negative resist. The second method is a direct EBL writing with the positive resist hydrogen silsesquioxane (HSQ), which is deposited directly on the SOI substrate, and chemical etching. HSQ forms a SiO_2 based network under electron beam exposure and has a better resolution feature size in comparison with PMMA or ZEP resists. The development of the polymer-based resists is performed by bathing the sample in n-amyl-acetate for 90 s and in isopropyl alcohol for 30 s, subsequently. The HSQ resist is sequentially developed by a NaOH/NaCl solution, deionised water and isopropyl alcohol. The removal of the residual resist after etching of the implantation masks is done by exposure to an oxygen plasma for 15 min. For the lift-off, the resist is removed in an acetone bath. EBL has been performed in a RAITH150 Two electron beam writer or an e-LINE Plus (both from RAITH GmbH). Both tools possess field emission cathodes capable of 30 kV acceleration voltage.

4.2.4.2 Etching techniques

Material removal by etching is employed in various ways in this work. This includes wet chemical etching for sample cleaning and layer removal, but also reactive etching techniques in order to fabricate nanoscale structures in metal layers or Si.

Wet chemical etching

Wet chemical etching utilises chemical reactions in an aqueous solution to dilute different materials, which can be used for removal of contaminations, to clean sample surfaces or to remove complete layers, like masking or capping layers. Si-based substrates are cleaned with a H_2O_2/H_2SO_4 solution and Ge substrates are cleaned with ethanol and isopropyl alcohol since Ge is etched by H_2O_2. Ni layers used as implantation or etching masks are removed using HNO_3 and ultra-sonic bathing. Another preparation step, where wet chemical etching is needed, is thinning of the commercial SOI substrates. These commercial SOI substrates have a Si device layer with 90 nm thickness. The size is reduced to 60 nm by a thermal oxidation step resulting in multilayer structures. These multilayer structures are on the one hand used as substrate material for ion implantation but on the other hand are these samples also the starting point for nanowire fabrication. Therefore, the thermal oxide is removed by wet chemistry using a HF solution. The resulting 60 nm Si layer on 150 nm SiO_2 is then structured into Si nanowires by EBL and RIE. Thinner Si layers have also been prepared by a sequence of thermal oxidation and oxide removal steps leading to additional Si thicknesses of 40, 20 and 10 nm.

Reactive ion etching (RIE)

Reactive ion etching (RIE) is, in contrast to the previously mentioned etching process, a dry etching. The working principle is very similar to PECVD presented in section 4.2.1.1 and the process setup is equal, see figure 4.2.1, however, the parameters are different. During RIE mainly fluorine, chlorine or bromine based gas mixtures are used, i.e. a $SF_6/O_2/Ar$ mixture for Si etching. After plasma generation, the ions from the gas mixture, i.e. F^-, accelerate towards the sample surface due to the electric field between top electrode and sample holder. At the surface, these ions react with the substrate material and the reaction products diffuse away. Due to the directionality of the ions caused by the applied field, RIE is highly anisotropic, which is a big difference to wet chemical etching being more isotropic. This anisotropy can be exploited by using masked samples to produce trenches or small scale structure, for example NWs.

In this work, RIE is applied to fabricate Si NWs from SOI substrates using either a Ni mask or a HSQ mask. When using the Ni mask, a $SF_6/O_2/Ar$ plasma with a ratio of 64/3/3 sccm is employed. The pressure is kept constant at 3 Pa while RF power, inductively coupled plasma (ICP) generator power as well as the etching times are varied to get the optimal etching rate. The RIE parameters for Si with HSQ mask are similar. All RIE processes are carried out at an SI 591 etching tool (SENTECH Instruments GmbH).

Reactive ion beam etching (RIBE)

Reactive ion beam etching (RIBE) is special form of ion beam etching (IBE). For IBE, inert gases are used in combination with an ion source to produce ions that are accelerated towards the sample and impact at the surface. This impact causes the transfer of kinetic energy and the target surface is sputtered resulting in an etching process of the sample. The speciality of RIBE is the use of reactive gases instead of inert gases which adds a chemical component to the physical process of sputtering. This combination of physical and chemical etching leads high etching rates and high aspect ratios in etched structures.

RIBE is performed during fabrication of the implantation masks for local ion implantation. Therefore, 100 nm thick Ni layers deposited by electron beam evaporation and covered by an EBL patterned resist are etched by a mainly physical process. The etching is conducted at an IonSys 500 Reactive Ion Beam Etcher (Roth & Rau AG)

4.3 Characterization methods

4.3.1 Structural characterisation

4.3.1.1 Rutherford Backscattering spectrometry

Rutherford Backscattering (RBS) is a structural characterisation technique which gives information about the composition of the surface region of a material. In order to investigate the sample, a high energy ion beam of a light element, i.e. He, is directed towards the surface. If the target material consists of heavier elements, which is usually the case, the incident ions are elastically scattered and an exchange of kinetic energy takes place during the collision. The scattering of incident ions occurs in all directions and some of the ions are backscattered. These backscattered ions are detected during RBS. The energy difference between the incident and the backscattered ions depends on the masses of the incident ion and the target atom and on the scattering angle (nuclear energy loss). Therefore, the energy of the detected backscattered ion at a certain angle is theoretically characteristic for a specific target atom. However, another process contributing to the energy loss of the incident ions is small angle scattering with electrons within the sample leading to an energy difference of ions scattered at the same element but at different depths (electronic energy loss). These two energy loss processes are exploited in RBS by taking an energy-resolved spectrum of the backscattered ions which enables the determination of the depth profiles of different elements in one material. Such depth profiles are used to examine the elemental composition of a material. The accuracy of RBS for multi-element materials depends mainly on the mass differences between single components. If two elements have a similar mass, they are hard to separate in the spectrum.

RBS is applied in this work to investigate the depth profiles of the implanted group-III and -V ions in the bulk Si samples and the thin layer Si samples. Ge samples are not investigated due to the similarity of atomic masses, e.g As, Ga and Ge. RBS is performed using a 1.2 MeV He^+ ion beam accelerated by a 2 MV van-de-Graaf particle accelerator. Backscattered He^+ ions have been detected by a semiconductor detector with a solid angle of 3.2 msr and a resolution of 15 keV at an angle of 170° to the incident beam which hits the sample surface perpendicularly. The energy spectra have been analysed by the NDF software [409].

4.3.1.2 Electron microscopy

Electron microscopy is a sophisticated structural characterisation method exploiting the interaction of an electron beam with the elements of a target material. The interaction of an electron with matter generates different signals which give information about the material's properties. Figure 4.3.1 shows the interaction cone of an electron beam with a sample and the corresponding signals. These signals can be detected either in a "reflection" mode using electrons and photons returning from the surface or in transmission mode for very thin samples.

Scanning electron microscopy

In scanning electron microscopy (SEM) a focused electron beam is used to scan the surface of a sample which can give information about topography or composition depending on the detected signal. Topography can be investigated by detecting secondary electrons generated by excitation of a target atom by the incident electron beam. Secondary electrons have low energies and, therefore, come only from the first few nanometres of the sample. Secondary electrons from deeper regions do not reach the surface and are not detected. Information on the composition of a sample is derived from the material contrast caused by backscattered electrons. Incident electrons scatter at the atoms of the substrate material and depending on the mean atomic number the intensity of their signal varies, where heavier elements give higher intensity.

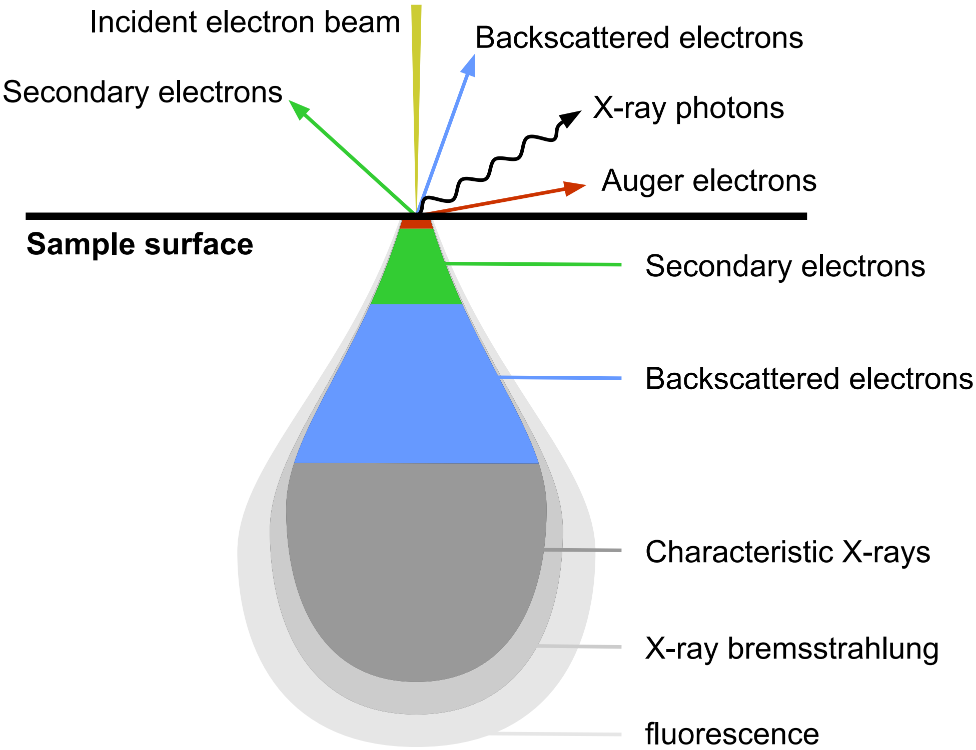

Figure 4.3.1: Interaction cone of an electron beam with a substrate material.

SEM images have mainly been taken at an S-4800 high resolution scanning electron microscope (Hitachi) capable of electron acceleration voltage up to 30 kV. Electron detection has been conducted at the stationary lower and upper SE detectors as well as at the YAG-type BSE detector for secondary and backscattered electrons, respectively. The control of EBL resist masks and the transfers to the hard masks has been directly performed in the electron beam writers RAITH150 Two and e-Line Plus which have been used for small scale structuring.

Transmission electron microscopy

Transmission electron microscopy (TEM) makes use of the electrons which traverse the sample. In order to collect such transmitted electrons, the sample has to be reasonably thin, resulting in a sophisticated sample preparation in contrast to SEM where no specific preparation is necessary. When the electrons of the incident beam pass through the sample, they can be absorbed or scattered. Atoms with higher atomic number or objects with a larger thickness scatter more than lighter or thinner objects, giving a mass or thickness contrast during imaging. In crystalline materials, the crystal structure also influences the diffraction of the electrons. There are different detection modes in TEM harnessing the different absorption, diffraction and other energy loss mechanisms.

Bright field imaging is the most common operational mode for a TEM, where the amount of transmitted electrons is detected giving dark areas for heavy elements or thicker regions and bright areas for light elements or thin material. Dark field imaging utilises the diffraction contrast of the electrons exposed to Bragg scattering at the crystal lattice. The detector is placed off-axis to the incident beam, so electrons scattered only slightly (light elements) appear dark while heavier elements show up as bright areas. In polycrystalline material, different crystal orientations also result in different intensities due to different scattering at the lattice planes. Since the electrons lose energy during scattering, they have different energies when they hit the detector. This energy loss is characteristic for the scattering element and by filtering specific energies, the distribution of the particular element can be mapped. This technique is called energy-filtered TEM (EFTEM).

A more advanced imaging mode is high-resolution TEM (HRTEM) which is able to display the structure even at an atomic scale. To achieve such high resolutions, the phase contrast of different electron waves caused by interaction with the sample is exploited. Fast Fourier Transform (FFT) of HRTEM images can be used to determine lattice plane distances and the crystal structure. Similar to SEM, TEM can also be performed in a scanning mode. Scanning TEM (STEM) is mainly executed using high-angle annular dark-field STEM (HAADF-STEM) and obtains a resolution comparable to HRTEM by focussing the electron beam to a very narrow spot and scanning over the sample. In combination with energy-dispersive X-ray spectroscopy (EDXS), an element mapping can be performed at high resolutions, since the interaction of the incident electrons also induces characteristic X-ray emission of the sample components.

Cross-sectional TEM imaging during this work has been performed with an image-corrected Titan 80-300 transmission electron microscope (FEI). The microscope has been operated at an acceleration voltage of 300 kV. Samples have been investigated in conventional bright-field mode as well as in dark-field and high-resolution modes. Additional HAADF-STEM in combination with EDXS is applied for studying chemical compositions of various samples. In order to perform element mapping with EDXS, a Li-drifted silicon detector (EDAX) attached to the Titan microscope has been on duty. For comparison, a Super-X detector system mounted to Talos microscope (FEI) has been employed for EDXS mapping.

4.3.2 Optical characterisation

4.3.2.1 Raman spectroscopy

Raman spectroscopy is an optical characterisation technique for the determination of phonon modes in various materials. It utilises an inelastic scattering process, where a phonon is generated or annihilated by transferring energy either from or to an incident photon, respectively. The frequency of the photon is shifted to lower or higher frequencies. This frequency shift (Raman shift) is characteristic for the particular material and can be influenced by temperature, stress and crystallite size, for example. The measurement setup usually employs a laser beam in the visible or near-infrared region illuminating the sample. The laser light interacts with the substrate material and different scattering mechanisms take place. Elastically scattered light at the frequency of the incoming laser frequency is filtered out and only the inelastically scattered photons are collected by a spectrometer. These photons are detected and their Raman shift gives information about the investigated material.

Raman spectroscopy has been used in this work to investigate recrystallization of Si and Ge after implantation and FLA. Furthermore, III-V NC formation by ion implantation and FLA is examined. The measurements have been conducted at LabRAM HR (Horiba Jobin Yvon) using a 532.14 nm Nd:YAG laser in backscattering geometry.

4.3.2.2 X-ray diffraction

X-ray diffraction (XRD) is an optical characterization technique which utilises the diffraction of X-rays in matter. X-ray diffraction (XRD) can be employed to determine the crystal structure of a material including lattice parameter, orientation and internal disorder. When X-rays hit a sample surface, they are scattered by the crystal lattice and an interference pattern evolves. The maxima of such an interference pattern are described by the Bragg equation,

$$n \cdot \lambda = 2 \cdot d \cdot \sin(\theta), \tag{4.1}$$

where n is an integer giving the order of diffraction, λ is the wavelength of the incident X-ray beam, d is the lattice plane distance and θ is the angle between atomic plane and scattered beam. For a set of parallel lattice planes, there is constructive interference giving only specific angles where reflection occurs. For a known incident X-ray wavelength, these specific angles can be used to calculate the lattice plane distances, which in turn results in the lattice parameter of a material. During the measurement, usually, an X-ray source emits an X-ray beam towards the sample surface and the scattered X-rays are detected by scanning over the different angles. The intensity is recorded as a function of the angle between incident and scattered beam (2θ).

In this work, XRD is performed at SOI samples with binary and ternary III-V NCs in order to determine crystallite size and internal strain of the NCs as well as the composition of the ternary compounds. For this purpose an Empyrean θ-θ four-circle diffractometer (Panalytical) is employed using Cu-Kα radiation ($\lambda = 0.154\,\text{nm}$) and a point detector. Scattered X-rays have been recorded in the 2θ range from 20° to 100° with step size of 0.1°.

5 Integration of III-V compound semiconductor nanocrystals in silicon

In this chapter, the experimental results of the integration of III-V compound semiconductor nanocrystals (NCs) are presented. The integration process has been carried out in different material systems, namely bulk silicon and Si thin films. In comparison to the bulk Si samples also one sample set with bulk germanium has been fabricated and investigated. For these substrate configurations, two different types of implantation are conducted. The first type is a planar implantation of the complete sample surface, yielding randomly distributed III-V nanocrystals. The second approach includes the preparation of an implantation mask for local implantation of group-III and -V ions in order to control the position of the NCs.

5.1 III-V nanocrystals in bulk materials

5.1.1 Preparation process

After a cleaning step, p-type Si (100) wafers and p-type Ge (100) wafers with a 6° miscut towards (111) are put into the PECVD chamber to deposit 35 nm of SiO_2 on the top surface. After the deposition of this capping layer, the samples have been sequentially implanted with As^+ followed by In^+ or Ga^+ ions. In Si samples, the implantation energies are set to 130 keV for In^+, 90 keV for Ga^+ and As^+, while in Ge the energies are 1380 keV and 130 keV, respectively, see also table A.3.1 in Appendix A.3. The implantation fluence is 3×10^{16} ions/cm^2 per ion species, resulting in a total fluence of 6×10^{16} ions/cm^2 in Si and Ge. This high fluence is sufficient to amorphize the top region of both materials. After implantation, the samples are treated with FLA for 20 ms at various energy densities (σ_{FLA}). Si samples are flashed with σ_{FLA} between 32.2 and 97.2 J/cm^2. The Ge samples need much less intensity due to lower wafer thickness, better thermal conductivity and lower melting point, therefore, energy densities are chosen within the range of 9.0 to 17.8 J/cm^2. The preheating parameters have been 3 min and 470 °C for both substrate materials.

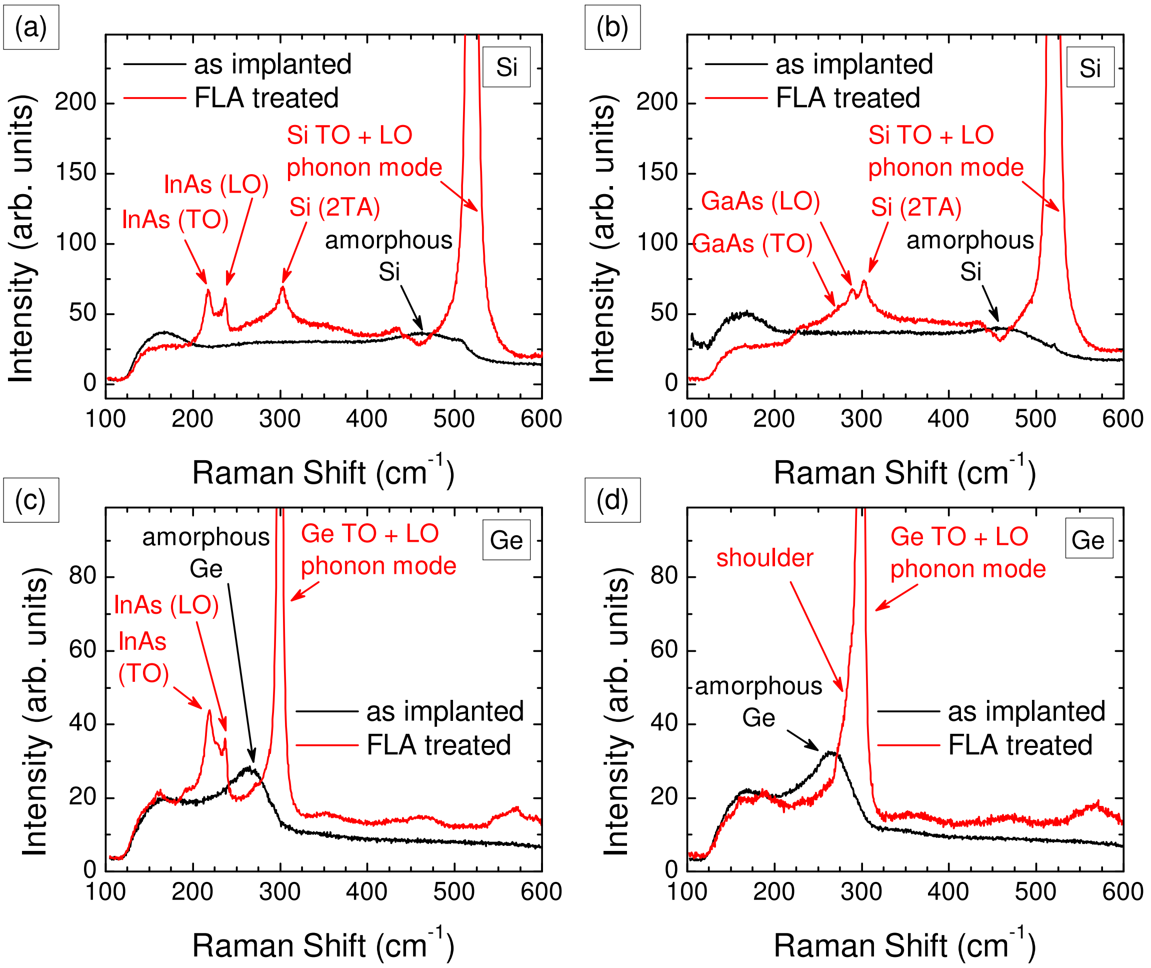

Figure 5.1.1: Raman spectra of bulk Si (a, b) and Ge (c, d) samples implanted with As^+ and In^+ (a, c) or As^+ and Ga^+ (b, d) ions and treated with FLA at 92.6 J/cm^2 and at 13.0 J/cm^2, respectively, in comparison with *as implanted* samples (black).

5.1.2 InAs and GaAs integrated into bulk Si and Ge

After preparation, the samples have been investigated at first by Raman spectroscopy in order to confirm recrystallization of the substrate material as well as the formation of III-V NCs. In figures 5.1.1(a) and (b) the Raman spectra of Si samples implanted with As^+/In^+ (a) and As^+/Ga^+ (b) ions are shown, comparing *as implanted* (black) and *FLA treated* (red) with σ_{FLA} of 92.6 J/cm^2. In both *as implanted* samples, the Raman spectrum only shows two broad peaks around 170 cm^{-1} and 480 cm^{-1} which belong to amorphous Si [410, 411]. In both *FLA treated* spectra, the typical phonon modes of crystalline Si can be observed. The main peak at 520 cm^{-1} represents the combined Si transverse optical (TO) and longitudinal optical (LO) phonon mode [412]. The second Si related peak is located around 303 cm^{-1} and originates from the second harmonic of the transverse acoustic (2TA) phonon mode. The disappearance of the amorphous Si peak and the evolution of the Si TO+LO and the Si 2TA phonon modes in the *FLA treated* curves confirm the recrystallization of the Si substrate material by FLA.

In figure 5.1.1(a) two additional peaks at 217 cm^{-1} and 237 cm^{-1} can be observed. These two peaks are attributed to the characteristic TO and LO phonon modes of crystalline InAs [413], respectively, which proves InAs NC formation by ion implantation and FLA. In figure 5.1.1(b) an additional peak can be observed on the low energy side of the Si 2TA peak. This peak at 289 cm^{-1} is caused by the LO phonon mode of crystalline GaAs [414, 415] confirming GaAs NC formation in Si. The corresponding GaAs TO phonon mode is also observable but gives a very weak signal at 272 cm^{-1}. Figures 5.1.1(c) and (d) display the Raman spectra of $\mathrm{As}^+/\mathrm{In}^+$ (c) and $\mathrm{As}^+/\mathrm{Ga}^+$ (d) implanted Ge wafers. Similar to the Si samples, only a broad peak can be observed in the *as implanted* spectra (black), which is centred at 265 cm^{-1} and accounts for phonons from amorphous Ge [416]. In the *FLA treated* samples annealed with an σ_{FLA} of 13.0 J/cm^2, the broad peak is vanished but a strong signal at 300 cm^{-1} appears. This strong peak is due to the combined Ge TO and LO phonon modes [417], giving evidence for the recrystallization of Ge after FLA. In figure 5.1.1(c), the double peak structure of crystalline InAs is visible, proving InAs NC formation also for Ge substrates. In figure 5.1.1(d), no GaAs related peaks can be observed, but the Ge TO+LO phonon mode possesses a relative large shoulder at the low energy side of the peak. Since the peak position of the GaAs LO phonon mode is located at 292 cm^{-1}, it is possible that this peak overlaps with the Ge TO+LO peak, which results in the observed shoulder. However, the formation of GaAs NCs in Ge cannot clearly be confirmed with Raman spectroscopy.

In figure 5.1.2, the dependency of the NC formation on σ_{FLA} has been investigated for the case of $\mathrm{As}^+/\mathrm{In}^+$ implanted Si samples. Figure 5.1.2(a) displays Raman spectra taken from samples annealed with different σ_{FLA} ranging from 32.2 (green) to 92.6 J/cm^2 (dark red). Comparing the *as implanted* spectrum (black) with the spectra of the annealed sample (colours), the most prominent difference is the crystalline Si TO+LO phonon mode at 520 cm^{-1}, showing that even the smallest energy density is sufficient to recrystallize the amorphized Si host material. The characteristic phonon modes of crystalline InAs, however, are not present in Raman spectra of samples annealed with σ_{FLA} lower than 46.4 J/cm^2 and become prominent only for σ_{FLA} of 54.5 J/cm^2 and above. Also the Si 2TA phonon peak evolves only in samples annealed with σ_{FLA} higher than 54.5 J/cm^2. The Si TO+LO phonon mode is much more intense than the characteristic phonon modes of InAs. This is due to the difference in the volume fraction excited by the incident laser beam. Since the spot size of the Nd:YAG laser is about 1 µm in diameter and the penetration depth in Si is of the same order of magnitude, the excited sample volume is much bigger than the InAs NCs and the main component, which is probed, is the surrounding Si host material.

For a semi-quantitative analysis, the peak areas beneath the three particular features have been integrated and plotted against σ_{FLA} in figure 5.1.2(b). Therefore, the InAs double peak structure, the Si 2TA phonon mode and the Si TO+LO phonon mode is integrated from 200 to 245 cm^{-1}, from 280 to 320 cm^{-1} and from 460 to 570 cm^{-1}, respectively. The base line has been set as a straight line between starting and end points of each integration interval in the particular spectrum. The shape of the three different curves is similar. At σ_{FLA} below 50 J/cm^2, there is only a small increase of the peak area with increasing σ_{FLA} until a steep increase between 46.4 and 54.5 J/cm^2 occurs. At higher σ_{FLA}, the peak area remains roughly constant with increasing σ_{FLA}. This behaviour can probably be related to a change in the recrystallization mechanism

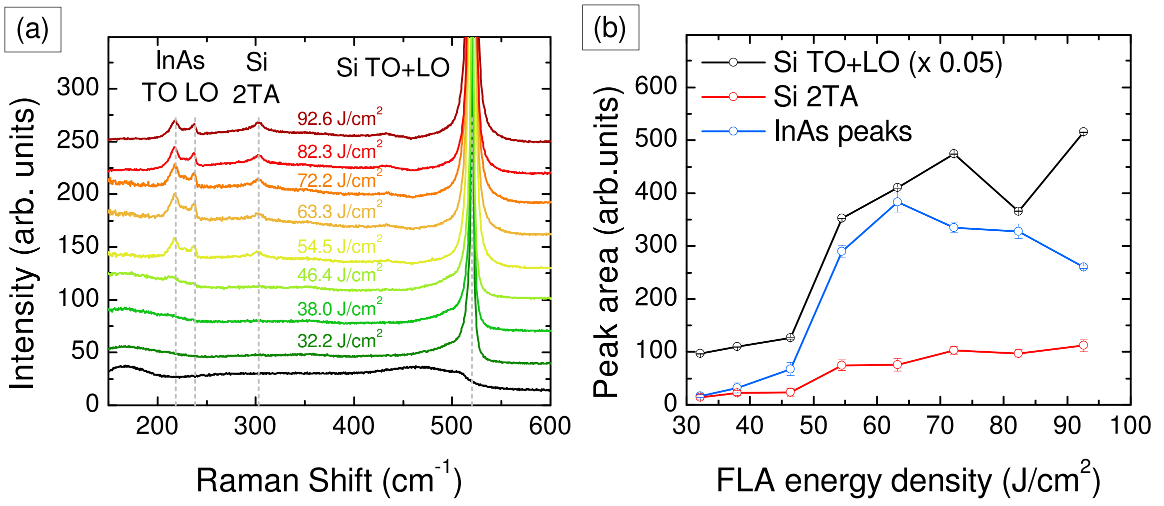

Figure 5.1.2: (a) σ_{FLA} dependent Raman spectra of InAs in bulk Si. Black curve displays *as implanted* spectrum. (b) Area under Raman peaks vs. σ_{FLA}.

from a solid phase to a liquid phase process by exceeding the temperature threshold needed for melting the implanted, amorphous top region of the Si substrate.

Figure 5.1.3 depicts the σ_{FLA} dependency of the Raman spectra for $\mathrm{As}^+/\mathrm{In}^+$ implanted bulk Ge samples. In figure 5.1.3(a), the Raman spectra taken from samples annealed with different σ_{FLA} are compared. Similar to the Si samples, the *as implanted* (black) sample shows only the amorphous Ge phonon peak while the annealed samples (colours) show the crystalline Ge TO+LO phonon peak and the characteristic InAs TO and LO phonon modes. In contrast to the Si samples, the InAs phonon modes are already present for the lowest σ_{FLA} ($9.0\,\mathrm{J/cm^2}$) used in this experiment. The general shape of the Raman spectra is independent of σ_{FLA} except for the highest value ($20.4\,\mathrm{J/cm^2}$), where two curves are depicted, which are displayed separately and enlarged in figure 5.1.3(c).

Figure 5.1.3(b) displays the dependency of the Raman peak area on σ_{FLA} for the InAs phonon peak structure and the Ge TO+LO phonon mode. In contrast to the Si substrates, there is no threshold behaviour visible for the investigated σ_{FLA}. This is probably due to the fact that the starting σ_{FLA} is already above such a threshold for Ge samples. Nevertheless, comparing the curve shapes of the Ge TO+LO and the InAs curves a difference is observed. The peak area under the Ge TO+LO peak (black) remains almost constant with increasing σ_{FLA}, showing that the recrystallization of Ge is mainly independent on the FLA treatment. However, the InAs peak area curve (red) is constant up to an σ_{FLA} of $14.0\,\mathrm{J/cm^2}$ but then decreases significantly. Higher σ_{FLA}, like $20.4\,\mathrm{J/cm^2}$, lead to a phase separation as indicated in the Raman spectra in figure 5.1.3(c) and displayed in the optical microscopy image in figure 5.1.3(d). In figure 5.1.3(c) the two curves enlarge the InAs double peak structure (left graph) and the Ge TO+LO phonon mode (right graph). The left graph shows the characteristic InAs phonon peaks only for the black curve but not for the red curve. An opposite behaviour is observed for the Ge TO+LO phonon mode in the right graph, where the red curve has a much higher intensity than the black curve. These differences in the Raman spectra originate from different measurement points on the sample. The

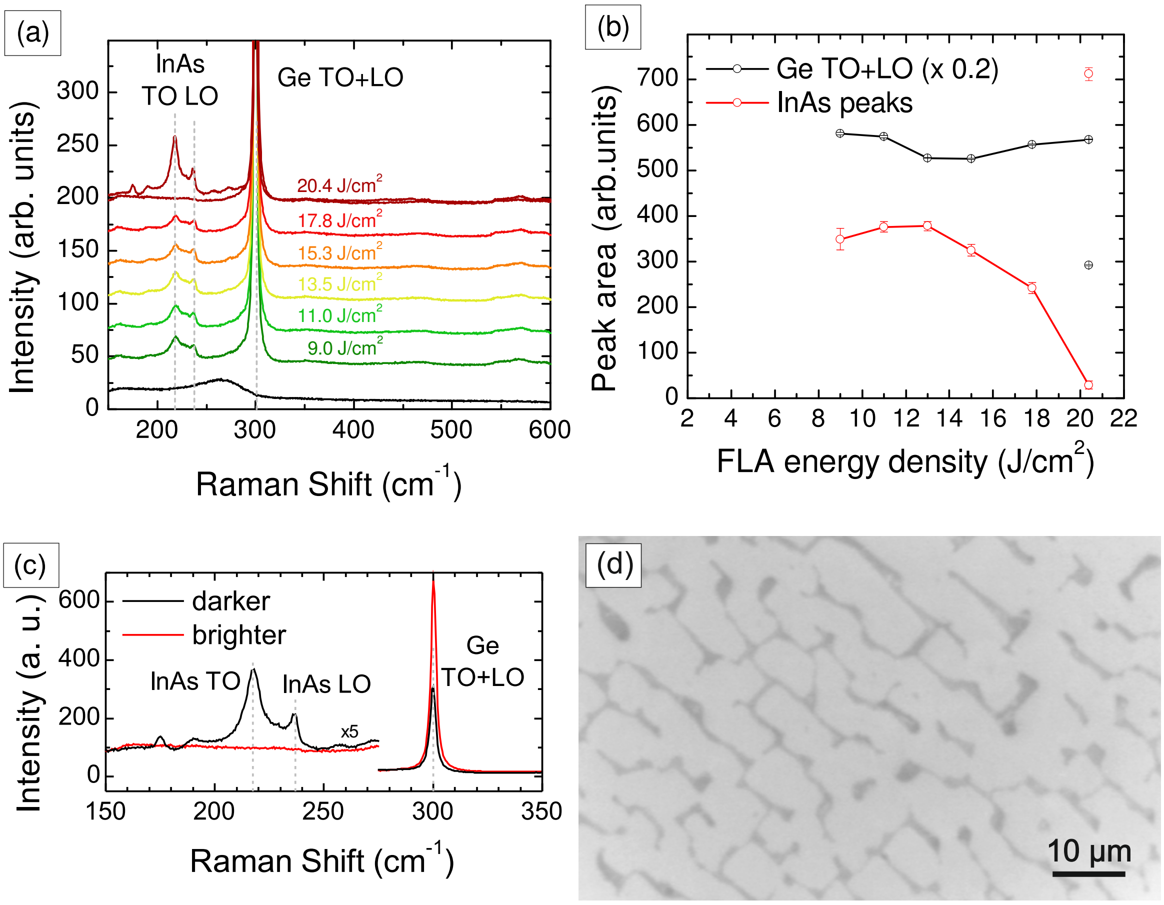

Figure 5.1.3: (a) σ_{FLA} dependent Raman spectra of InAs in bulk Ge. Black curve displays *as implanted* spectrum. (b) Area under Raman peaks vs. σ_{FLA}. (c) Raman spectra of the Ge sample annealed with 20.4 J/cm^2 and the corresponding optical microscopy image (d, magnification: 1000x) showing the phase separation of InAs (darker) and Ge (brighter) regions.

optical microscopy image in figure 5.1.3(d) depicts areas of different brightness on the sample surface. The Raman spectrum of the black curve has been taken at a darker region while the red spectrum is obtained from a brighter region. Due to the presence of the InAs peaks only for the darker areas, a phase separation of InAs and Ge is concluded to occur at higher σ_{FLA}. This phase separation leads also to surface topography which is expressed by the formation of large InAs droplets on top of the Ge which is detrimental for III-V integration. All other sample did not show this phase separation behaviour.

Figure 5.1.4 depicts the top-view SEM images of InAs and GaAs NCs in Si and InAs NCs Ge, and corresponding particle size distribution histograms for Si samples. The black/white contrast and the picture sharpness have been adjusted in all three SEM images in order to increase the contrast between the III-V NCs and the matrix materials, especially in figure 5.1.4(c). The histograms have been calculated using SEM pictures of the same samples but with lower magnification to improve statistics by a higher number of NCs. The particle size distribution has been determined using the open source software ImageJ [418]. Therefore, the SEM images have been processed

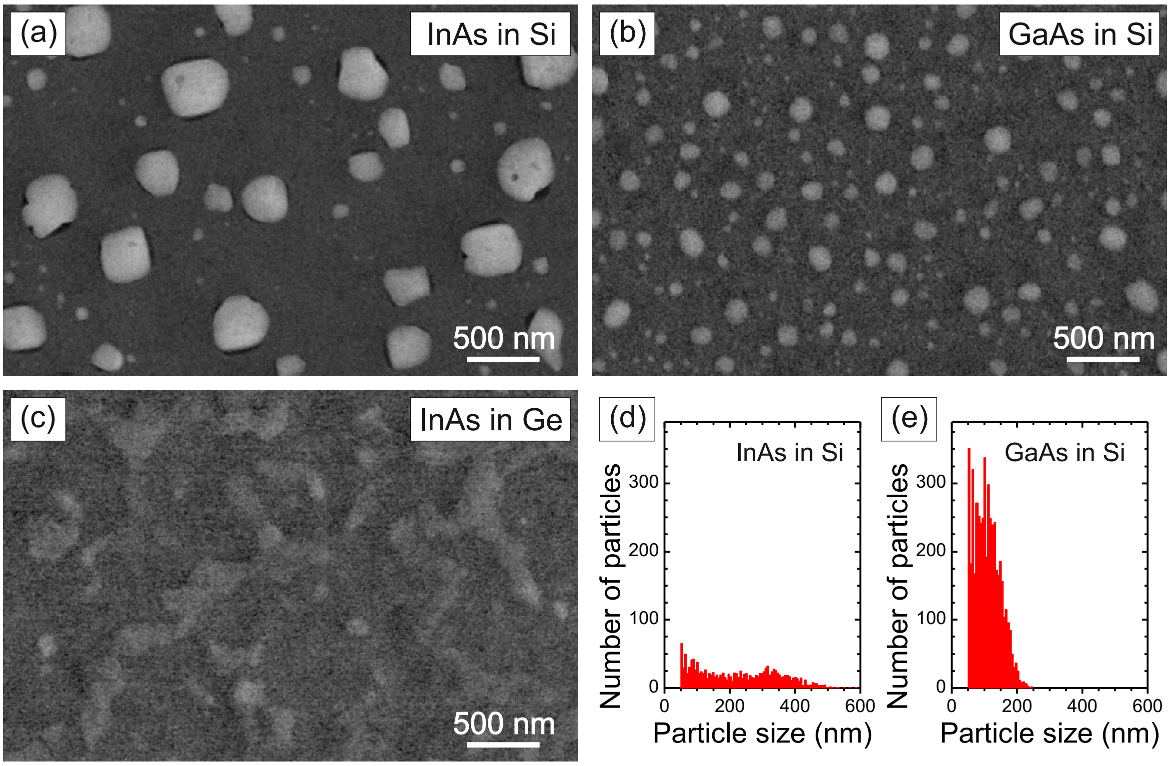

Figure 5.1.4: SEM images of III-V NCs in bulk Si and Ge. (a) InAs NCs in Si, (b) GaAs NCs in Si and (c) InAs NCs in Ge. Si and Ge samples have been FLA treated with σ_{FLA} of 92.6 J/cm^2 and 13.0 J/cm^2, respectively. (Black/white contrast and picture sharpness have been adjusted.) Particle size distributions of InAs NCs (d) and GaAs NCs in Si (e) have been calculated from the same images with lower magnification.

with a Gaussian blur to reduce the noise and then a black/white threshold has been applied. The resulting black/white image has been used to perform the particle analysis. The output gives the number of particles in the particular image with the associated area of each particle. This particle area is given in pixels and can be transformed into the length scale by using the resolution of the picture and the magnification used during SEM image acquisition. One pixel has a length of 20 nm, giving the area of one pixel with 400 nm^2. Due to image noise and the applied image processing steps, particles with an area of less than five pixels have been discounted during the determination of the particle size distribution. For the sake of comparability, all particles are assumed to be circular and the particle area is converted into a diameter of a circular particle, giving the particle size (abscissa in the histograms).

Figures 5.1.4(a) and 5.1.4(b) show InAs NCs and GaAs NCs in Si, respectively. The III-V compounds appear brighter due to a higher atomic mass than the surrounding Si. Both images display samples which have been annealed with FLA at 92.6 J/cm^2. In general, the InAs and GaAs NCs are well separated from one another and possess a lateral aspect ratio close to one. Comparing both III-V compounds, the InAs NCs are larger but the number of GaAs NCs is higher. This can also be seen in the particle size distribution histograms of these two samples (d, e). The mean value of the InAs NC size distribution is 206 nm with a standard deviation of 131 nm while the mean value of the GaAs NC size distribution is only 97 nm with a standard deviation of 45 nm.

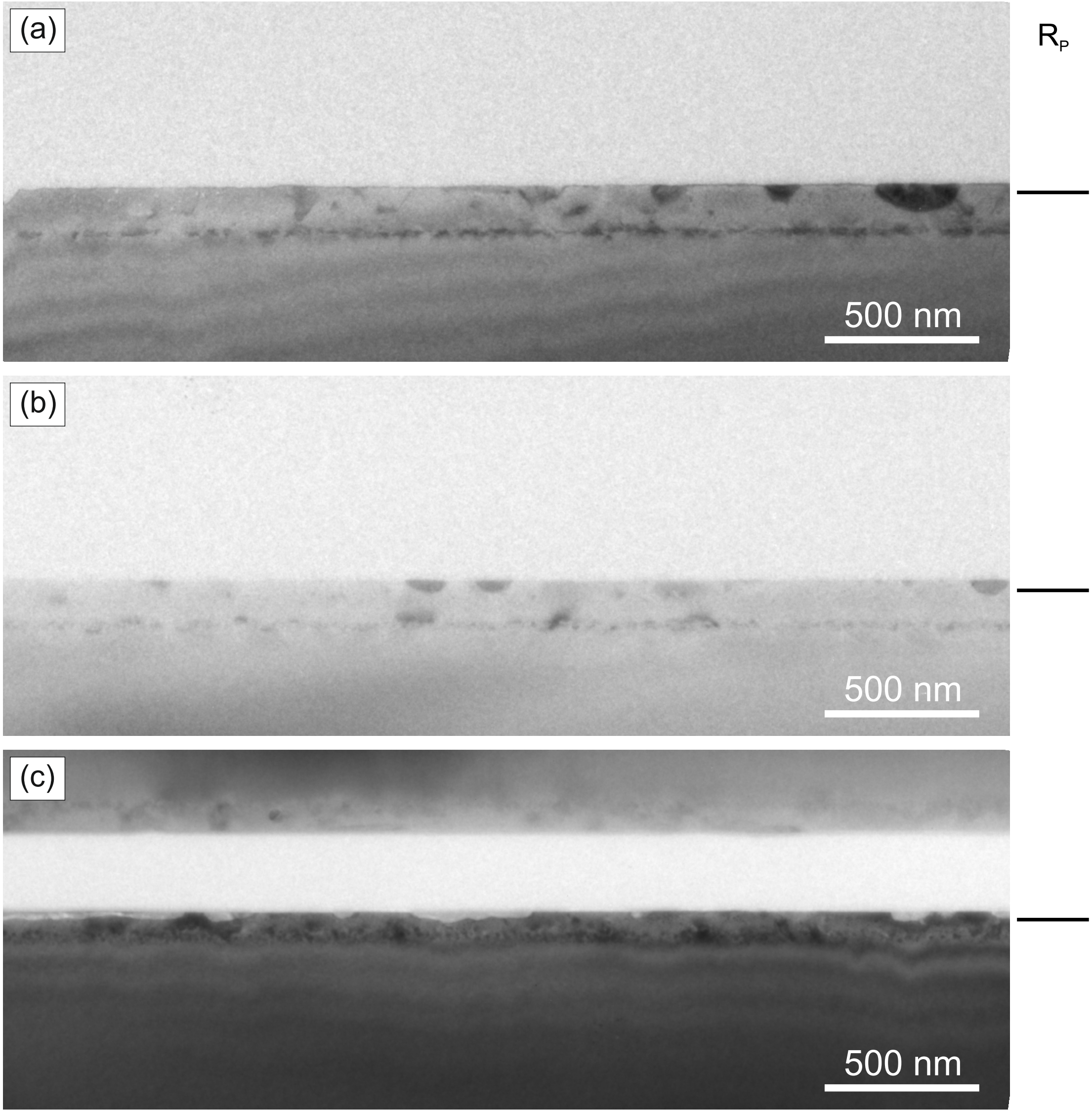

Figure 5.1.5: Cross-sectional TEM images of III-V NCs in bulk Si and Ge. (a) InAs NCs in Si, (b) GaAs NCs in Si, and (c) InAs NCs in Ge. Si and Ge samples have been FLA treated with a σ_{FLA} of 92.6 J/cm^2 and 14.0 J/cm^2, respectively.

In figure 5.1.4(c), the SEM image of As$^+$/In$^+$ implanted Ge annealed with FLA at 13.0 J/cm^2 is depicted. The InAs NCs can be distinguished from the surrounding Ge host material but the contrast is relatively poor due to the smaller mass differences of InAs to Ge than to Si. The InAs NCs possess an arbitrary shape and they seem to form connected agglomerates which can reach sizes of several µm. For the InAs NCs in the Ge matrix the assumption of NC circularity does not hold, therefore, the NC size distribution has not been calculated. For As$^+$/Ga$^+$ implanted Ge no SEM image is displayed. Ga, Ge and As stand right next to each other in the periodic table of elements leading to almost no mass contrast in SEM which makes it impossible to see GaAs NCs in Ge.

Figure 5.1.5(a) displays cross-sectional TEM images of the As$^+$/In$^+$ implanted Si wafer annealed with a σ_{FLA} of 92.6 J/cm^2. The image is divided into two parts. The upper part is brighter and consists of the glue which was used during preparation of the TEM lamella, while the lower part is dark and represents the Si substrate with incorporated InAs NCs. The SiO_2 capping layer has been removed previously to TEM sample preparation and, hence, is not visible in the TEM images. The dark regions at the surface of Si display the InAs NCs, which possess a hemispherical or trapezoidal shape and an extension of up to 130 nm into the Si substrate. The lateral NC dimension varies from a few tens of nm to 400 nm, like previously seen in the SEM images. The depth and the lateral extension of the NCs seem to have a fixed aspect ratio independent of the size of the NC, preserving the general shape. The dotted line of dark features at a depth of about 150 nm is caused by end-of-range (EOR) defects which form at an amorphous/crystalline Si interface during annealing.

In figure 5.1.5(b), a similar behaviour is observed for the As^+/Ga^+ implanted Si sample. Although the contrast is not as good as for the InAs NCs, GaAs NCs are visible. They have a hemispherical or trapezoidal shape as well and extend up to a depth of about 150 nm, but the lateral dimension is smaller than that of the InAs NCs. The EOR defects are also apparent in this image.

Figures 5.1.5(c) shows the cross-sectional TEM image of the As^+/In^+ implanted Ge sample annealed with a σ_{FLA} of 14.0 J/cm^2. It looks similar to the other two cross-sectional TEM images, including the InAs NCs located at the surface. However, the InAs NCs do not appear darker than the surrounding host Ge but brighter. A reason for this different behaviour may be an orientation difference between Ge substrate, which has been aligned parallel to the incident electron beam, and the InAs precipitates. Another possible explanation might be the crystalline quality of the InAs precipitates which are deficient and, therefore, possess a lot of diffraction sites. Nevertheless, the InAs NCs can be clearly distinguished from the surrounding Ge host material. In contrast to the InAs NCs in the Si matrix, their shape is flat and their height is only about 50 nm. They have no distinct aspect ratio. Furthermore, there are no visible EOR defects. For the As^+/Ga^+ implanted Ge, no distinct features can be observed which is similar to the SEM results.

Figure 5.1.6 presents two enlarged cross-sectional TEM images of an InAs (a) and a GaAs NC (e) in Si. The InAs NC (a) is shown partly at the left edge while the biggest portion of the image is occupied by the recrystallized Si substrate. The interface between Si and the InAs NC is depicted by a bright line and the adjacent area of the Si substrate appears also brighter than the Si on the right side of the image. The higher brightness is due an increased number of scattering sites, namely defects in Si. There is a big notch between the InAs NC and Si, which might be due to the release of a smaller NC during removal of the capping layer by etching of SiO_2. The single dislocation loop in the bottom right corner of the image is a representative of the EOR defects already seen in figure 5.1.5(a). On the right side of the image, a few bright spots can be observed. These bright spots can be seen in the implanted region over the whole sample. The magnification of these spots (see figure A.2.1 in Appendix A.2) revealed that there are amorphous inclusions within the recrystallized Si substrate. In figure 5.1.6(b), the interface region between the InAs NC and Si is depicted in a HRTEM image. The crystalline nature of both parts is nicely visible and, furthermore, both species, the InAs and the Si, are single-crystalline. Only a small, discontinuous band of a few nm directly at the interface is poorly ordered, proposing a defect-rich interface layer between InAs and Si. Nevertheless, the general crystal

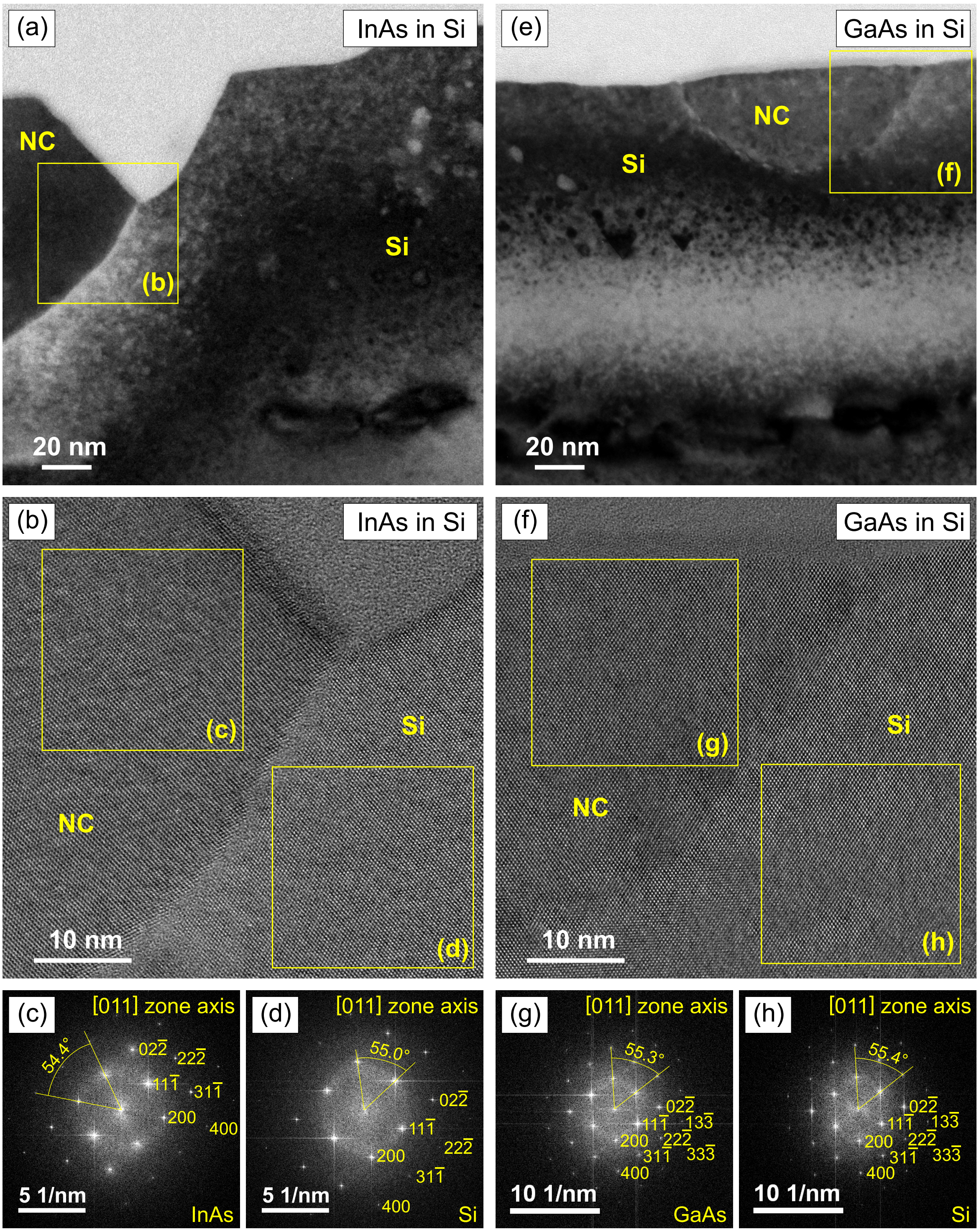

Figure 5.1.6: Cross-sectional TEM and HRTEM images of As^+/In^+ (a, b) and As^+/Ga^+ (e, f) implanted Si treated by FLA with a σ_{FLA} of $92.6\,\text{J/cm}^2$ and corresponding FFTs (c, d, g, h). FFTs are taken at the regions marked by yellow boxes and include main indizes of the particular substance and the characteristic angle for crystal structure determination.

structure seems to continue over this small band from the Si substrate into the InAs NC, making epitaxial growth favourable.

For further structural characterization, both crystalline areas have been used to generate the FFTs given in figures 5.1.6(c) and (d). Both figures show intense reflexes which are arranged in a symmetric, hexagonal pattern. The FFT can also be interpreted as an electron diffraction pattern and, therefore, be used for the characterization of the crystal structure and the material itself. The central spot represents the non-diffracted beam while the surrounding spots display diffractions from the different lattice planes within the crystal. In order to determine the crystal structure, the angle between two lines which connect one particular diffraction spot with the central spot is utilized. The measurement of this characteristic angle yields 54.4° and 55.0° for figures 5.1.6(c) and (d), respectively, which determines the crystal structure of both crystalline areas to be fcc which is oriented in the [011] zone axis. Using standard indexed diffraction patterns, the reflexes can be identified and indicated with their particular Miller indices. The analyses of the single reflexes yield the distances for each lattice plane in reciprocal space. For a known crystal structure, these lattice plane distances can be used to determine the lattice parameter and, therefore, the particular material. The analysis results of the spot patterns of figure 5.1.6(c) and (d) are given in table 5.1.1. The lattice parameter deduced from the spot pattern of figure 5.1.6(c) is 0.606(4) nm which fits well with the lattice parameter of InAs. This proves the existence of single-crystalline InAs NCs in Si formed by ion beam implantation and FLA. In figure 5.1.6(d) the spot pattern analysis gives a lattice parameter of 0.543(3) nm, fitting to the literature value of Si, which verifies recrystallization of Si by the FLA treatment. When comparing figures 5.1.6(c) and (d), it can be observed that the spot patterns are not identically oriented. While in the Si spot pattern, the axis of the (100) plane reflexes is perpendicular to the sample surface, the same axis in the InAs spot pattern is rotated counter-clockwise with a rotation angle of 70.6°. This rotation angle in reciprocal space represents the angle between two lattice planes in real space. Since both crystal structures are fcc, it is assumed that the InAs NC is [113]-oriented, as the angle between the (113) and (100) lattice planes is 72.5°.

A hemispherical GaAs NC is depicted in the cross-sectional TEM image of figure 5.1.6(e) and the corresponding HRTEM image is displayed in figure 5.1.6(f). Similar to figure 5.1.6(a), the GaAs NC is located directly at the surface, there are small, bright regions within the Si substrate, indicating amorphous inclusions, and there are several dislocation loops in the lower part of the image. But in contrast to the TEM image of the As^+/In^+ implanted sample, there is almost no contrast difference at the interface between the GaAs NC and the Si substrate. There is also a bright region at a depth of about 100 nm whose higher brightness can be accounted to a higher number of scatterers which possibly originating from interstitials or EOR defects.

The HRTEM image (f) shows a continuous crystalline order without any break at the interface between the slightly darker region on the left, representing the GaAs NC, and the brighter region on the right, representing the recrystallized Si. The analysis of the FFTs taken from both crystalline parts (5.1.6(g) and (h)) reveals a fcc crystal structure in [011] zone axis for both regions. The lattice parameters deduced from these spot patterns are given in table 5.1.1. The measured lattice parameters of 0.561(6) nm and 0.545(5) nm fit to the lattice parameters of GaAs and Si, respectively. When the spot patterns of the GaAs sample are compared with those of the InAs sample,

Table 5.1.1: Results of the spot pattern analysis of HRTEM images taken at As^+/In^+ and As^+/Ga^+ implanted Si samples treated by FLA with σ_{FLA} of 92.6 J/cm^2 and the As^+/In^+ implanted Ge sample annealed with a σ_{FLA} of 14.0 J/cm^2.

Figure	Mean lattice parameter (nm)	Material
5.1.6(c)	0.606(4)	InAs
5.1.6(d)	0.543(3)	Si
5.1.6(g)	0.561(6)	GaAs
5.1.6(h)	0.545(5)	Si
5.1.8(d)	0.607(4)	InAs
5.1.8(e)	0.571(4)	Ge
5.1.8(f)	0.606(3)	InAs
5.1.8(h)	0.570(6)	Ge

two differences can be observed. First, the spot patterns have an identical orientation, which, in combination with the almost defect-free interface, implies an epitaxial growth of the GaAs NCs within the Si matrix. Secondly, reflexes with higher Miller indices can be seen in the spot patterns of the GaAs sample, which is an indication for a higher crystalline quality of the GaAs NC as well as the recrystallized Si substrate than in the InAs sample.

In order to get information about the elemental composition, the InAs and GaAs NCs have been investigated by EDXS in combination with HAADF-STEM. The results are depicted in figure 5.1.7. The red boxes in the HAADF-STEM images of As^+/In^+ (a) and As^+/Ga^+ (b) implanted Si mark the regions where the EDX spectra (c-g) have been taken at. The coloured bars in the EDX spectra highlight the different element species. Figure 5.1.7(a) displays the HAADF-STEM image of As^+/In^+ implanted Si showing a big hemispherical, white region in the center, which represents the same InAs NC already seen in previous TEM images. The high brightness of the InAs is due to its higher atomic mass compared to the surrounding Si (grey) or air/glue (black). The EDXS spectra have been taken directly in the InAs NC (c) and in the surrounding Si (d). In figure 5.1.7(c), the EDXS spectrum of the InAs NC is displayed and signals for Si at 1.7 keV (yellow bar), In between 2.9 keV and 4.2 keV (red bar) and As at 1.3 keV, 10.5 keV and 11.8 keV (green bars) are detected. The appearance of the Si signal can have two origins, it can be due to Si incorporated in the InAs NC or Si being located behind the InAs NC due to the X-ray excitation volume of the electron beam (see section 4.3.1.2). Since the lateral dimension of the InAs NC is large, the second possibility seems rather improbable. This leads to the assumption that Si is incorporated in the InAs NC where it can act as an dopant. The EDXS spectrum of the surrounding Si matrix (d) shows only the Si signal at 1.7 keV (yellow bar), but with much higher counts than in the InAs NC. This implies that the surrounding Si matrix is free of group-III and -V material, at least up to the detection limit of the EDXS detector, and that the implanted ions have been driven out of the Si during FLA treatment.

The HAADF-STEM image in figure 5.1.7(b) displays the As^+/Ga^+ implanted Si sam-

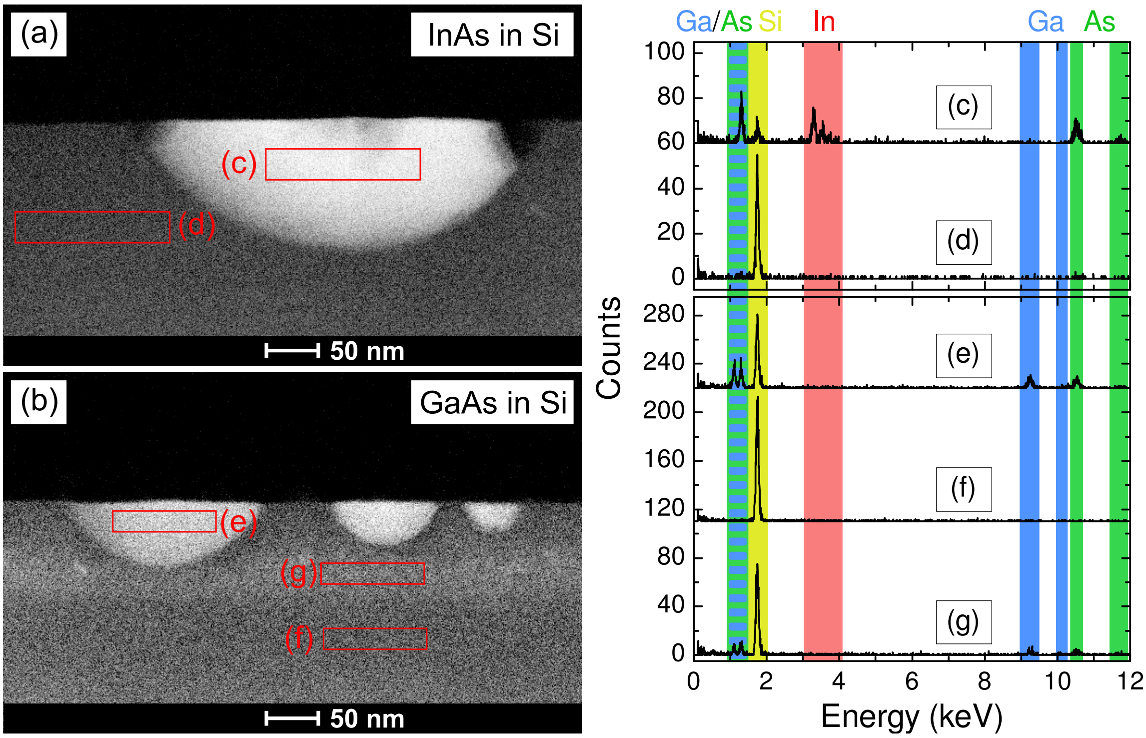

Figure 5.1.7: HAADF-STEM images of InAs (a) and GaAs (b) NCs in Si. EDXS spectra (c-g) have been taken at the regions marked by red boxes. Within the EDX spectra, the specific element peaks are highlighted by a red (In), yellow (Si), blue (Ga) and green (As) bar.

ple with three hemispherical bright areas at the surface representing three GaAs NCs. The surrounding Si matrix is darker but at a depth of approximately 100 nm a slightly brighter stripe can be observed. This increased brightness is due to a higher amount of scatterers and is identical to the bright region visible in the cross-sectional TEM image of the GaAs sample depicted in figure 5.1.6(e). For clarification of the composition of this region, an EDXS spectrum has been acquired from this area (g) additionally to the EDXS spectra recorded at the big GaAs NC (e) and the Si substrate region (f) below. The EDXS spectrum of the GaAs NC (e) shows signals for Si (yellow bar), Ga (blue bars), and As (green bars). The Si signal within the GaAs NC is again accounted to doping of GaAs by Si atoms, although it is much more intense than in the InAs NC. The EDXS spectrum of the Si host material (f), again, only shows the Si peak. Nevertheless, in the EDXS spectrum of the slightly brighter region of the Si substrate (g) also the peaks of Ga and As show up. Since no precipitates have been found in this region by HRTEM analysis and Ga and As are well-known dopants of Si, it is suspected that the Ga^+ and As^+ ions introduced during ion beam implantation are not completely consumed for the GaAs NC formation but also incorporated into the Si lattice during FLA treatment.

Figure 5.1.8 displays an enlarged cross-sectional TEM image (a) and two HRTEM images (b, c) of the As^+/In^+ implanted Ge sample with the corresponding FFTs (d-h) acquired from the areas marked by the yellow boxes. The cross-sectional TEM image (a) shows two big bright areas at the interface between the Ge substrate and the SiO_2 capping layer, which can be accounted to InAs precipitates. As already mentioned

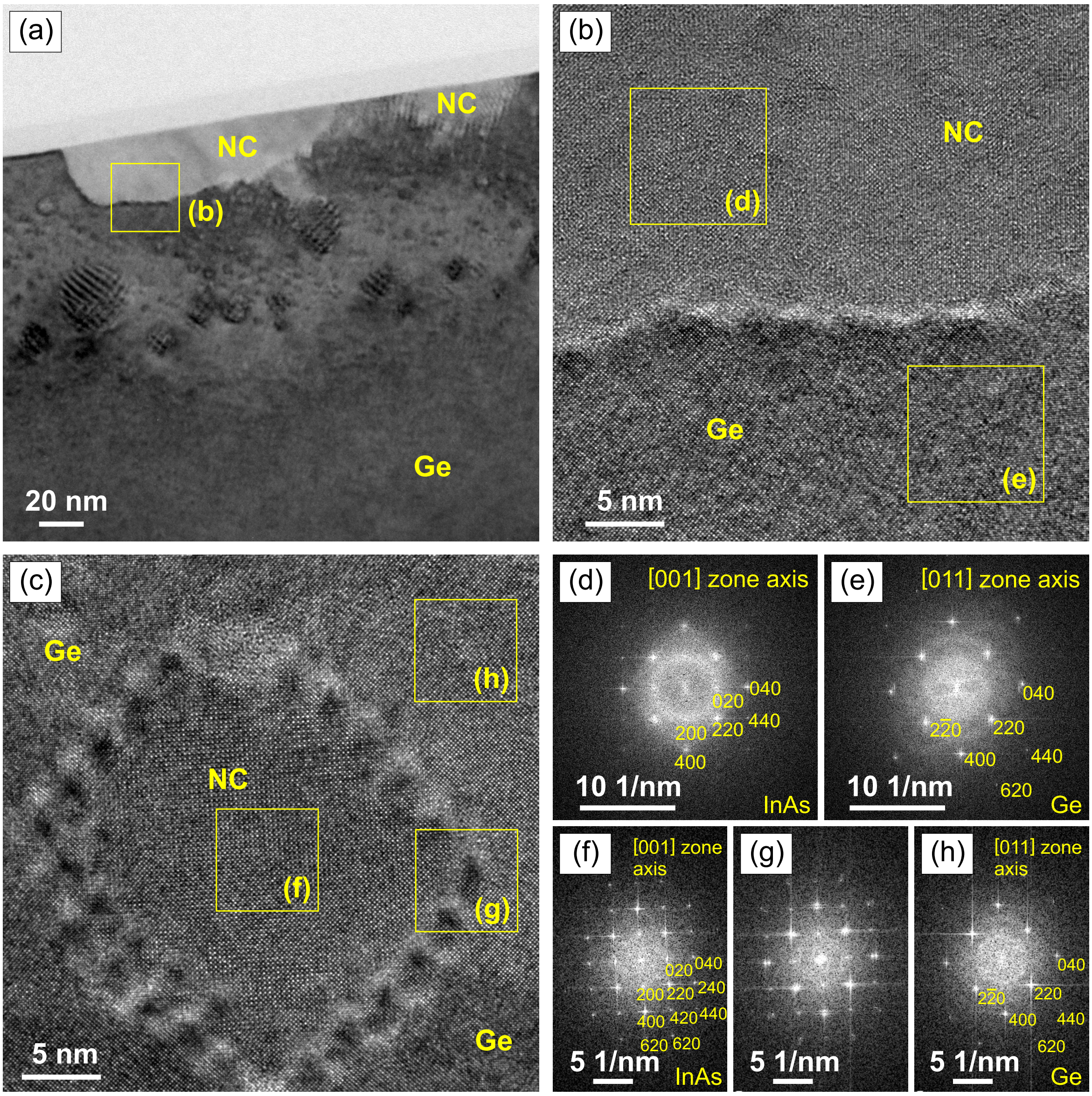

Figure 5.1.8: Cross-sectional TEM (a) and HRTEM (b, c) images of InAs NCs in Ge. The sample has been annealed by FLA with σ_{FLA} of 14 J/cm^2. HRTEM images have been taken at the lower interface of the big precipitate at the sample surface (b) and at one of the small circular precipitates at a depth of about 100 nm (c). Parts (d) to (h) give the corresponding FFTs taken at regions marked by the yellow boxes.

earlier, the higher brightness may be due to either a different orientation of the InAs precipitates and the Ge substrate or a high number of scatterers within the InAs due to a higher defect density or a combination of both effects. Additionally, there are smaller circular features at a depth of approximately 100 nm which show Moiré fringes. These features have a diameter which ranges from a few nm up to 50 nm. Moiré fringes appear when the probing electron beam is scattered at two specimen with a close periodicity, e.g. two materials with the same crystalline structure and only a small difference in their lattice parameters. For further investigation, the interface between the big InAs precipitate and Ge, and one of the small circular features have been studied by HRTEM.

The HRTEM image of the InAs/Ge interface region, depicted in figure 5.1.8(b), displays the InAs precipitate in the upper part while the lower part shows the recrystallized Ge matrix. Both parts have a good crystalline order, appearing to be single-crystalline after regrowth during FLA. Nevertheless, both regions have a low number of defects. The interface region shows a crystalline order but has also some disordered regions. However, a continuation of the crystal structure from the lower into the upper part is observed, proposing an epitaxial growth of the InAs on the regrown Ge crystal. The FFT of the upper part (d) shows a quadratic spot pattern but also includes a diffraction ring around the central spot. The crystal structure is identified as fcc in the [001] zone axis, which is different than in the Si samples. The single reflexes are indicated with their particular Miller indices, and the corresponding lattice plane distances and the deduced lattice parameter of 0.607(4) nm are in good agreement with literature values known from crystalline InAs. Therefore, the upper part of figure 5.1.8(b) and, in turn, the bright precipitates in figure 5.1.8(a) and 5.1.5(c), are proven to be crystalline InAs. However, the diffraction ring around the central spot is an indication for the deficiency of the InAs NC. The FFT of the lower part (e) shows the previously seen hexagonal spot pattern similar to the InAs spot pattern but this time there are diffraction rings around each particular reflex. The analysis of the FFT gives again the fcc crystal structure but in [011] zone axis like it has been previously seen in the Si samples. The lattice plane distances and, therefore, the recalculated lattice parameter of 0.571(4) nm matches the known value of Ge. The lattice parameters deduced from figure 5.1.8 are also shown in table 5.1.1.

In figure 5.1.8(c), the HRTEM image of one of the small circular features as well as its surrounding material shows a good crystalline order. In the interface region only very little disorder is visible and a Moiré pattern can be observed, indicating a crystalline transition from the surrounding matrix to the circular precipitate. FFTs are taken from the inner part, the interface region and the surrounding matrix and are depicted in figures 5.1.8(f-h). The FFT from the inner part (f) has a very high number of reflexes and looks almost identical to the FFT of the big InAs precipitate displayed in figure 5.1.8(d) but without the diffraction ring. The analysis of the reflexes proves the circular precipitate to be crystalline, fcc InAs oriented in the [001] zone axis. The absence of the diffraction ring and the increased number of reflexes in comparison with figure 5.1.8(d) is accounted to a better crystalline quality of this particular NC. The FFT of the surrounding material (h) gives the identical spot pattern as in figure 5.1.8(e), identifying the surrounding material as crystalline Ge. The lattice parameters deduced from both FFTs are also given in table 5.1.1. The FFT of the interface region (g) is an overlap of the InAs spot pattern from the inside and the Ge spot pattern from the surrounding material. The reflexes, which both patterns have in common, appear as double spots in the spot pattern of the interface region, e.g. (220) and the (400) reflections. This combined FFT verifies the assumption of the crystal structure continuation from the surrounding material into the circular InAs NC. This transition, in turn, proves an epitaxial growth of the InAs NC within the Ge matrix.

All in all, the suitability of ion beam implantation in combination with short-time FLA to integrate III-V compound semiconductors into group-IV bulk materials has been demonstrated. The III-V NC formation in Si, already achieved in previous works [387, 391], has been successfully reproduced and the transfer to a bulk Ge substrate has been conducted. Raman spectroscopy and electron microscopy results prove a recrystallization of Si and Ge after FLA as well as the formation of III-V NCs. The crystalline structure of InAs and GaAs precipitates has been investigated and single-crystalline clusters of high quality have been found. The formation of GaAs NCs in Ge could not be verified. The size of the NCs differs for both III-V species with the InAs NCs being generally bigger than the GaAs NCs. Furthermore, the size and shape of the NCs is different in Si and Ge. In Si, the III-V precipitates show a fixed aspect ratio in SEM and TEM images and their size ranges from several tens of nm to about 400 nm in diameter. In Ge, by contrast, two different kinds of NCs are observed. The NCs located at the Ge surface have an arbitrary shape and form coagulated chains which range up to several µm. However, the NCs located at a depth of about 100 nm are smaller and have a fixed aspect ratio close to one.

When comparing crystalline quality, the differences between both matrices are small. In Si, the InAs and GaAs NCs have a high crystalline quality and their particular interfaces to the surrounding show a continuation of the crystal structure, especially for GaAs. In Ge, the InAs precipitates at the surface are single-crystalline and deficient, but the circular NCs seem to have almost perfect crystal structure. The orientation of the investigated III-V NCs also varies between the different materials. While the specific GaAs NC in Si is [100]-oriented like the Si substrate, the InAs NC is [113]-oriented. The two particular InAs NCs in Ge do also not possess the same orientation as the Ge substrate. The variation of crystal orientation can be accounted to the different lattice mismatches and the attempt to reduce mechanical stress. The different shapes and sizes are assumed to be due to the different melting points of the various materials. This will be discussed in relation to the formation mechanism in chapter 6. Furthermore, the absence of GaAs NCs in Ge is also attributed to the melting point difference because GaAs in Ge is the only case where the melting point of the III-V compounds is higher than the melting point of the host material. In this case the implanted As^+ and Ga^+ ions are assumed to be completely distributed within the lattice of the bulk Ge substrate. Nevertheless, the other samples have also incorporated low amounts of the implanted ions, which leads to a doping effect of the substrate materials. But not only the substrates have incorporated III/V ions, also the III-V NCs are doped by Si and Ge during growth.

5.2 III-V nanocrystals in thin Si layers

5.2.1 Process

With the aim to have a better control over the NC dimensions, an approach of vertical confinement has been chosen. Therefore, thin Si layer systems are employed, in order to reduce the height of the final III-V NCs. For this purpose, two different thin layer systems have been used. At first, a SIMOX SOI substrate with an initial layer stack of 90 nm Si and 150 nm SiO_2 on bulk Si has been thermally oxidized to achieve a final Si layer thickness of 60 nm. The 65 nm thick, thermally grown SiO_2 layer has been utilized as capping layer to prevent the thin Si layer from sputtering during ion beam implantation. The second thin Si layer system has been fabricated using PECVD to mimic the SOI layer stack with the aim to reduce costs. Conventional p-type Si (100) wafer have been cleaned with a standard cleaning procedure. Afterwards, the wafers have been transferred into the PECVD chamber and a three-layer deposition step has been performed. The thin PECVD Si layer system consists of a 35 nm SiO_2 capping layer on a 60 nm Si layer on a 100 nm thick SiO_2 box layer on top of the bulk Si substrate.

In the following both kinds of thin Si layer systems have been implanted and treated with FLA. For the SOI samples, the wafers have been implanted with As^+ followed by Ga^+ or In^+ ions at an ion fluence of 3×10^{16} ions/cm^2 for the formation of binary III-V compounds semiconductors, or with As^+, Ga^+ and In^+ sequentially with various ion fluence ratios to achieve a total ion fluence of 6×10^{16} ions/cm^2 in order to form $In_xGa_{1-x}As$ NCs. The implantation energies have been chosen to achieve a projected range centred in the thin Si device layer. The implantation energies have been simulated with SRIM (see section 4.1.1) and are given in table A.3.2 in Appendix A.3. For the PECVD samples, the ion fluence has been 2×10^{16} ions/cm^2 per ion and the implantation energies have been adjusted to obtain the centred implantation profile for the thinner capping layer. The thin PECVD Si has been implanted with different group-III/-V combination in order to investigate other III-V compound semiconductors regarding their possibility to be fabricated by our method. Therefore, the samples have been implanted with N^+/Ga^+, P^+/Ga^+, As^+/Ga^+, Sb^+/Ga^+, and P^+/In^+ and the implantation energies are given table A.3.2 as well. σ_{FLA} ranged from 85.2 J/cm^2 to 117.8 J/cm^2, and from 46.6 J/cm^2 to 97.2 J/cm^2 for SOI and PECVD samples, respectively. The preheating temperature has been adjusted to 470 °C for both sample types. For the PECVD sample another preheating temperature of 600 °C has been used.

5.2.2 Binary III-V compounds in SOI samples

Figure 5.2.1 shows the Raman spectra of As^+/In^+ (a) and As^+/Ga^+ (b) implanted SOI samples which have been FLA treated with an σ_{FLA} of 97.2 kJ. The *as implanted* spectra (black) of both samples are very similar to each other and show a small peak for the Si TO+LO phonon mode at 520 cm^{-1} and broad peaks around 170 cm^{-1} and 480 cm^{-1} caused by amorphous Si. Due to the ion implantation, the thin Si layer of the SOI sample is amorphized resulting in the amorphous signal. However, the

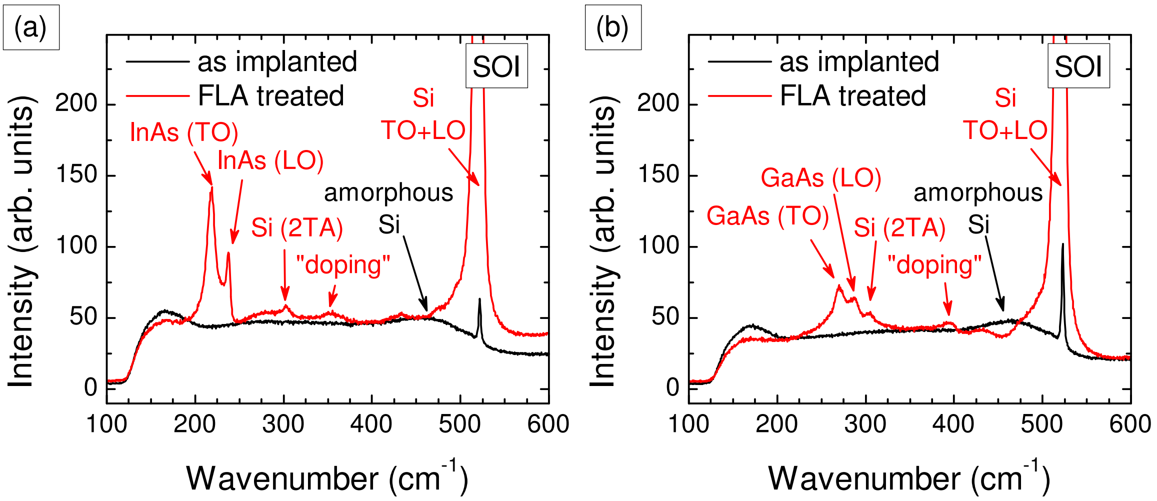

Figure 5.2.1: Raman spectra of SOI samples implanted with As^+ and In^+ (a) or As^+ and Ga^+ (b) ions and treated with FLA at 97.2 J/cm^2 in comparison with *as implanted* samples (black).

Si substrate is not affected by the implantation and remains single-crystalline. Since the excitation depth of the Raman laser is larger than the thickness of the layer stack, the crystalline Si substrate is also probed and gives a small contribution to the spectrum. The Raman spectrum of the As^+/In^+ implanted and FLA treated sample (a, red) features the two typical peaks of crystalline Si at 520 cm^{-1} (Si TO+LO) and 300 cm^{-1} (Si 2TA). Since their intensities are much higher than in the *as implanted* case, their appearance proves the recrystallization of the implanted, thin Si layer by FLA. Additionally, the characteristic TO and LO phonon modes of InAs are observed at 219 cm^{-1} and 237 cm^{-1}, respectively, giving proof of the formation of crystalline InAs in the thin Si layer. Furthermore, there is another Raman peak around 360 cm^{-1}. This peak can be accounted to Si doping of InAs NCs, since the Si on a In lattice anti-site defect (Si_{In}) has its local vibrational mode (LVM) at 359 cm^{-1} [419–421]. For the As^+/Ga^+ implanted and FLA treated sample (b, red), the typical Si phonon modes at 520 cm^{-1} (Si TO+LO) and 300 cm^{-1} (Si 2TA) are also present. The characteristic phonon signals for crystalline GaAs are visible at 269 cm^{-1} (TO) and 286 cm^{-1} (LO) indicating GaAs NC formation in thin Si layers [414, 415]. For the GaAs sample, an additional peak around 390 cm^{-1} can be seen similar to the InAs sample, which is again attributed to Si doping. The LVMs of Si anti-site defects in GaAs are located at 383 cm^{-1} (Si_{Ga}) and 398 cm^{-1} (Si_{As}), and also a LVM of the Si_{Ga}-Si_{As} donor-acceptor pair at 393 cm^{-1} is possible [422–424]. The appearance of these defect-related Raman peaks indicates heavily Si-doped III-V NCs.

In comparison to the Raman spectra of III-V NCs in bulk substrates, the characteristic phonon modes of InAs and GaAs are more prominent in the thin Si layer samples. This is due to their higher ratio of the probed volume, since the SiO_2 layer underneath the thin Si layer does not give any Raman signal in the observed range. Furthermore, the Raman signal regarded to Si doping only appears for heavily doped samples, that is why, Si doping of the III-V NCs is also expected for the bulk samples although the Raman peaks are not visible in figure 5.1.1.

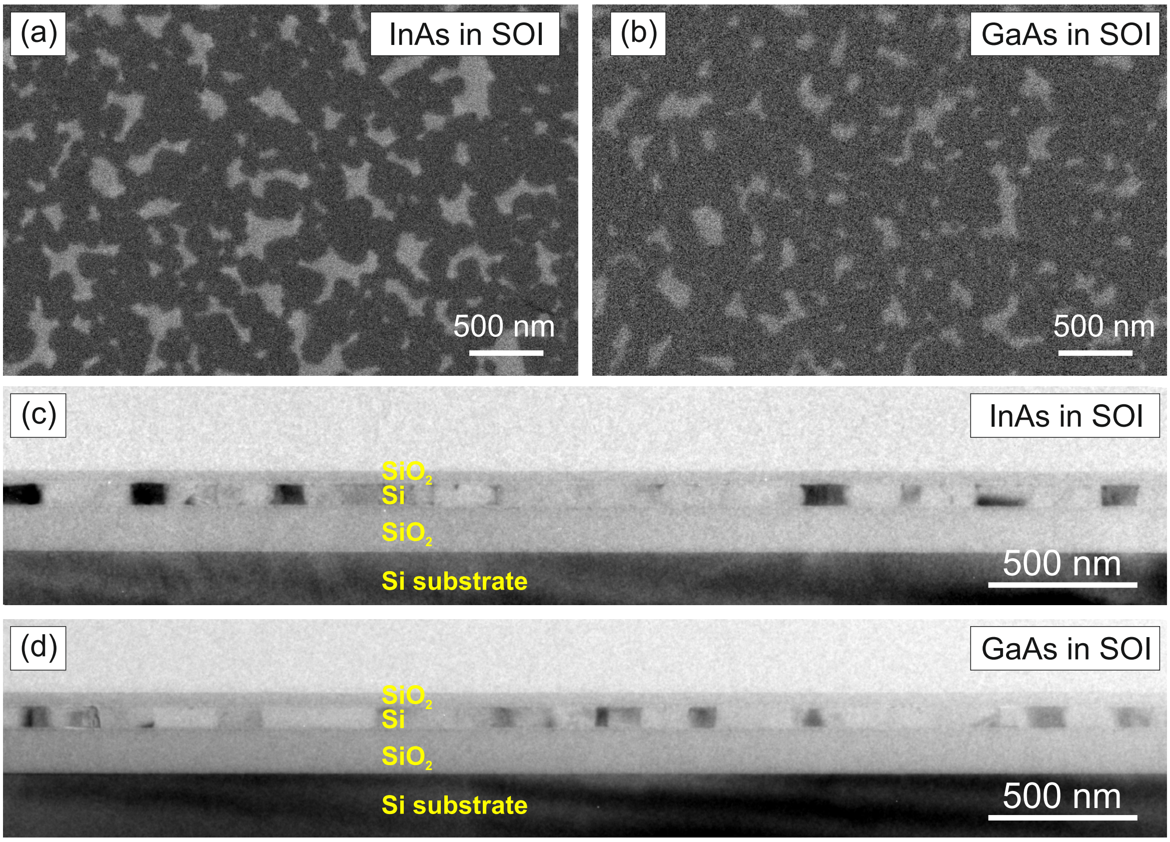

Figure 5.2.2: SEM and cross-sectional TEM images of As^+/In^+ (a, c) and As^+/Ga^+ (b, d) implanted SOI samples treated by FLA with σ_{FLA} of 97.2 J/cm^2.

In figure 5.2.2(a), the SEM image of the As^+/In^+ SOI sample annealed with an σ_{FLA} of 97.2 J/cm^2 shows arbitrarily shaped bright areas representing InAs NCs. They possess a rather large variation in size ranging from a few nm up to about 500 nm. The SEM image of the As^+/Ga^+ implanted sample (b) does not look very different; shape and size variation of the GaAs NCs are similar to the InAs NCs, only the number of NCs is smaller. The corresponding cross-sectional TEM images depicted in figures 5.2.2(c) (InAs) and (d) (GaAs) give an overview of the SOI layer stack. From top to bottom, there are a thin SiO_2 layer, the implanted Si layer, the SiO_2 box layer and the Si substrate. The thin Si layer in both samples shows a number of regions with different contrasts. These various contrasts are caused by differences in the scattering probabilities which are either due to different orientations or higher atomic number. Hereby, the light and medium grey areas are accounted to Si grains with different orientations while the dark grey or black areas are attributed to the III-V NCs. These III-V precipitates possess mainly a rectangular shape and their height is limited by the Si/SiO_2 interfaces. There are also some smaller III-V precipitates which are located directly at the Si/SiO_2 interfaces.

When comparing the SEM pictures of the implanted SOI samples with the images from the bulk Si samples, the quality of the III-V NCs is worse due to their random shape and large range of NC size. However, the TEM images show that the Si/SiO_2 interfaces act as growth barriers resulting in rectangular precipitates which allows a certain level of control over the size and shape of the III-V NCs.

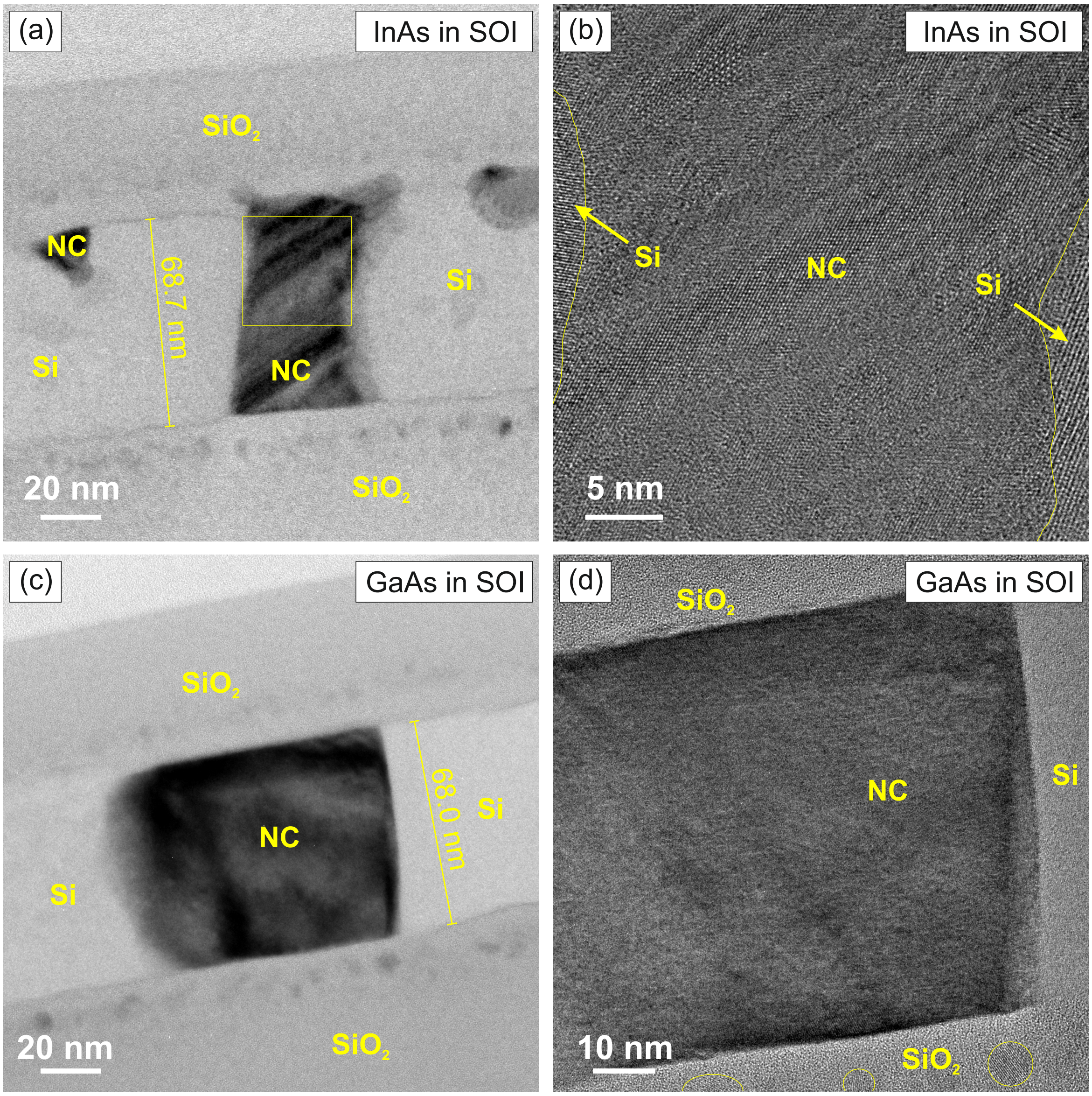

Figure 5.2.3: Enlarged cross-sectional TEM and HRTEM images of As^+/In^+ (a, b) and As^+/Ga^+ (c, d) implanted SOI samples treated by FLA with σ_{FLA} of 97.2 J/cm^2.

The enlarged cross-sectional TEM of the As^+/In^+ implanted SOI layer stack in figure 5.2.3(a) gives a more detailed picture. The bright Si layer surrounded by the two bright SiO_2 layers comprises a darker rectangular precipitate which extends over the full layer thickness and a smaller, darker precipitate which is located on the upper Si/SiO_2 interface. The Si layer has a thickness of about 69 nm, which is about 15 % more than the initial thickness. Several parallel stripes with different contrast can be observed within the big NC. Hereby, the different contrast is attributed to changes in the crystal orientation or quality. Both NCs have sharp interfaces to the surrounding Si and SiO_2. The Si/SiO_2 interfaces, itself, possess thin dark lines. During FLA treatment, the interfaces act as diffusion barriers for the implanted ions. A part of the implanted ions accumulate at the interfaces and appear as dark lines. Furthermore, there are also dark spots in both SiO_2 layers close their respective SiO_2/Si interfaces. To further investigate the big, block-like NC, a HRTEM image has been taken from the area marked by the yellow box and is depicted in figure 5.2.3(b). The HRTEM image shows a crystalline NC with several slightly disordered regions in the centre and single-crystalline Si areas at the sides. A FFT taken from the center of the NC (not shown) reveals a fcc crystal structure oriented in [111] zone axis. The analysis of the reflexes gives lattice plane distances which fit well to those of InAs, however, the InAs NC seems to be tensilely strained in [101] direction since the particular reflexes give higher lattice plane distances.

In figure 5.2.3(c), an enlarged cross-sectional TEM image of the As^+/Ga^+ implanted SOI sample is displayed. The image is very similar to the cross-sectional TEM images of the InAs precipitate and possesses the same features, including the block-like GaAs precipitate with sharp interfaces, the increased Si layer thickness, the decorated Si/SiO_2 interfaces, and the dark spots within the SiO_2 layer close to their particular interfaces. In HRTEM image of the GaAs NC (d) only a badly ordered crystalline structure can be observed. This is similar to the observations done in the bulk samples where the crystalline quality of the GaAs NCs was also not as good as that of the InAs NCs. Furthermore, even the Si area at the right edge of the images seems not to be recrystallized completely. The dark spots located in the SiO_2 box layer are also visible in the HRTEM image and show a crystalline structure. These small circular, crystalline dots are probably GaAs NCs as well. As shown in section 4.1.1, the implantation profiles of the group-III and -V ions extend into the surrounding SiO_2 layers, and the ions can form III-V precipitates during FLA treatment within these layers [375, 425].

The HAADF-STEM images of the As^+/In^+ and As^+/Ga^+ implanted SOI samples are depicted in figure 5.2.4(a) and (b), respectively. In both images, there are several features visible which have already been observed in the cross-sectional TEM images. The thin Si layers in the middle comprise bright, block-like precipitates which extend over the full Si thickness. The InAs sample (a) also shows a smaller triangular shaped precipitate located at the upper Si/SiO_2 interface which is connected by a filament to the lower Si/SiO_2 interface. The block-like precipitate in the GaAs sample (b) is separated into two parts of different contrast, an almost white and a light grey section, however, even the light grey part is still brighter than the surrounding Si or the SiO_2 layers. The differences in the contrast are attributed to different atomic masses of the various areas for both samples. Furthermore, the surrounding SiO_2 layers also contain small stripes of brighter features which correlate to the small, circular, crystalline dots

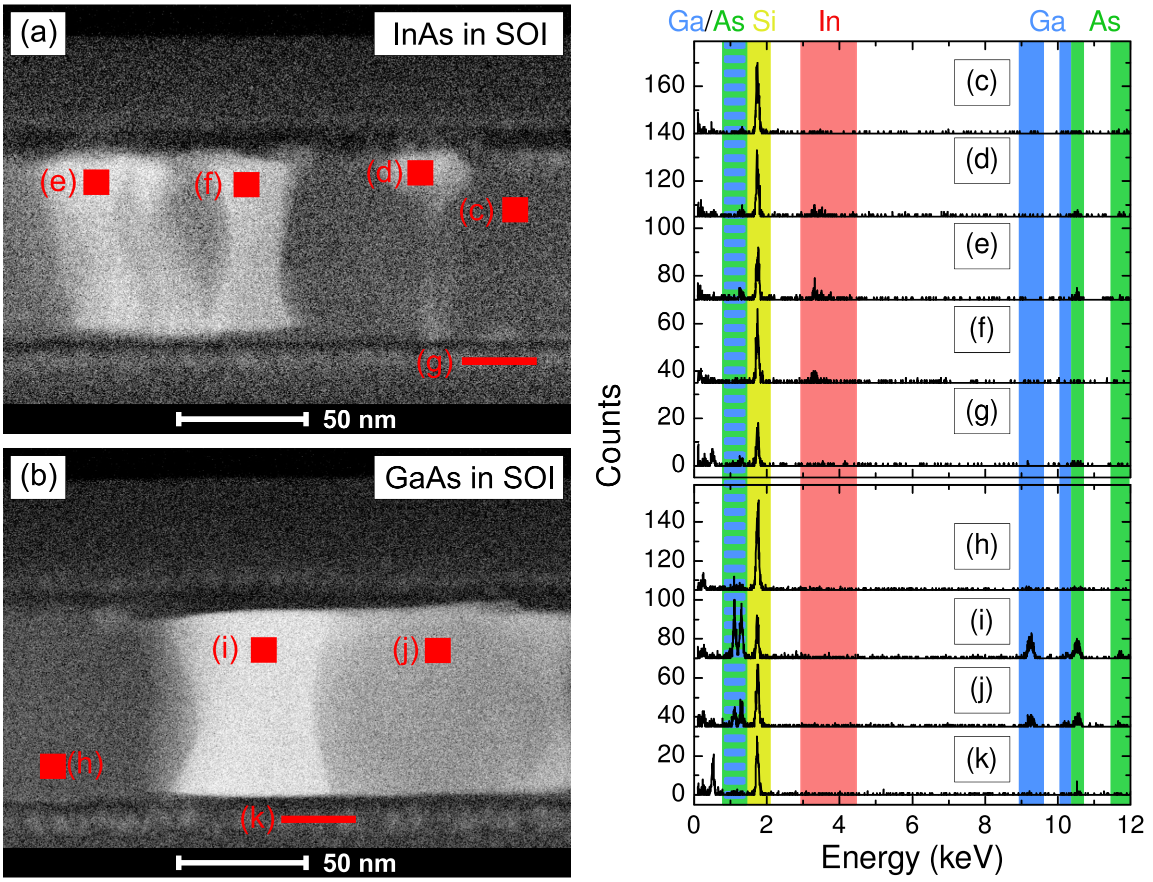

Figure 5.2.4: HAADF-STEM images of As^+/In^+ (a) and As^+/Ga^+ (b) implanted SOI samples treated by FLA with σ_{FLA} of 97.2 J/cm^2 and corresponding EDXS spectra taken from areas marked by the red boxes (c-k).

seen in the cross-sectional TEM images and the HRTEM image of the GaAs sample in figure 5.2.3 indicating that these dots have a higher atomic mass. The EDXS spectra (c-k) give the atomic composition of the areas marked by the red boxes in the InAs (c-g) and GaAs (h-k) samples. All of these EDXS spectra feature weak signals at the left edge of the measurement range which are accounted to either carbon or oxygen.

In the InAs sample, the spectra taken from the host material (c) gives a strong Si signal (yellow bar) and very weak signals for In (red bar) and As (green bars). The In and As peaks are related to doping of the Si layer. The EDXS spectra taken from the small triangular (d) and from the left block-like NC (e) feature a reduced Si signal, stronger In and As signals. The detection of In and As as well as the reduced amount of Si at these specific regions explains the increased brightness in the HAADF-STEM image due to higher atomic mass and is an indication for the InAs NC formation. The EDXS spectrum acquired from the right block-like precipitate (f) shows only the In related peaks but no peaks for As. Therefore, this precipitate is assumed to be a metallic In cluster. The thin bright stripe in the lower SiO_2 layer (g) shows a similar EDXS spectrum as the spectrum taken from the Si layer (c) but with lower intensity of the Si peak. However, the As signals are as weak as in the Si layer, which favours a random distribution of the implanted ions within this region although the HAADF-STEM and HRTEM images show crystalline features of higher atomic mass.

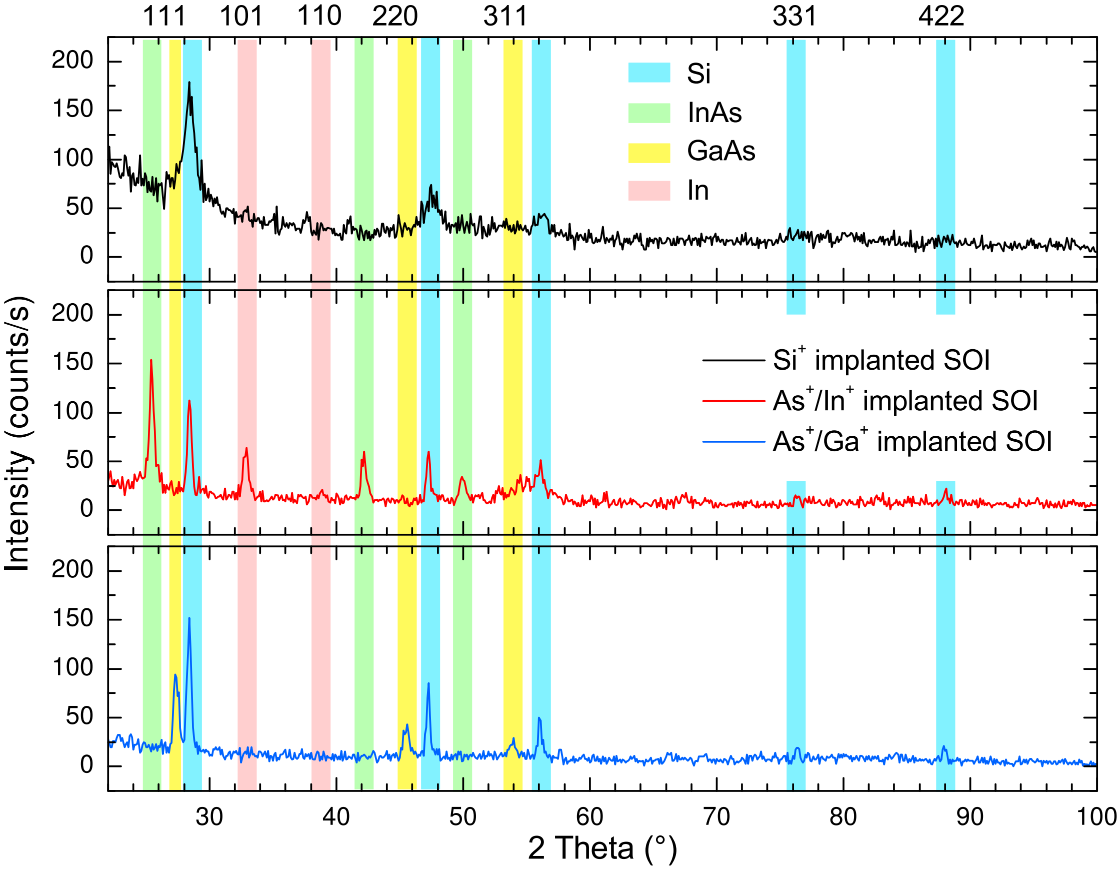

Figure 5.2.5: XRD 2θ scans of an As^+/In^+ (red curve) and As^+/Ga^+ (blue curve) SOI sample are compared with a XRD diffractogram of a Si^+ implanted SOI reference sample (black curve). XRD peaks are marked with coloured bars for Si (blue bar), InAs (green bar), GaAs (yellow bar) and metallic In (red bar) and indicated with their corresponding Miller indices.

In the GaAs sample, the EDXS spectra acquired from the thin Si layer (h) displays a strong Si signal and several weak features for Ga (blue bars) and As (green bars), which again accounts to the doping of the Si layer by the group-III and -V ions. The EDXS spectra taken from the big block-like NC (i and j) show stronger signals for As and Ga while at the same time the Si peak is weaker than in region (h). Therefore, both regions are assumed to belong to a GaAs NC. The separation of this NC into two parts seen in the HAADF-STEM image is also reflected in the EDXS spectra since the As and Ga peaks in region (i) have higher intensity than in region (j) but an equivalent ratio and the Si peak is more intense in region (j). Hence, the light grey part of the big precipitate is suspected to be an overlap of the GaAs NC and Si, where the Si is either behind or in front of the GaAs NC. The EDXS spectrum from region (k) gives similar results as region (g) for the InAs sample showing a decreased Si and increased O peak, and weak signals for As. The investigated area consists of SiO_2 with small amounts of As.

In figure 5.2.5, the XRD patterns of an As^+/In^+ (red curve), As^+/Ga^+ (blue curve) and a Si^+ implanted SOI reference sample (black curve) are compared. The Si^+ reference sample has been implanted with an implantation fluence of 6×10^{16} ions/cm^2 and an implantation energy of 60 keV in order to possess an equivalent projected range and implanted fluence as the III$^+$/V$^+$ implanted samples. The samples have been FLA treated with σ_{FLA} of 97.2 J/cm^2.

All three patterns have in common that they show the Bragg peaks of crystalline Si, which is mainly due the recrystallized thin Si layer. The Si (111) reflection at 28.4° is the strongest Si peak followed by the Si (220) peak at 47.3° and the Si (311) reflection at 56.1°. Additionally, two weak Si reflections are observed in the III$^+$/V$^+$ implanted SOI samples at 76.4° (Si (331)) and 88.0° (Si (422)) which are not present in the Si$^+$ implanted reference sample. The presence of the Si related reflections in these samples verifies the recrystallization of the thin Si layers after FLA treatment. Comparing the Si$^+$ implanted and the III$^+$/V$^+$ implanted samples, it can be observed that the Si reflections are broader in the Si$^+$ sample. This line broadening may have several reasons, e.g. variation in crystallite size or strain. The XRD patterns of the III$^+$/V$^+$ implanted samples show additional Bragg peaks originating from the III-V compounds. In the As$^+$/In$^+$ implanted SOI sample, reflections characteristic for InAs are visible at 25.4° (InAs (111)), 42.2° (InAs (220)) and 49.9° (InAs (311)). Furthermore, there are two Bragg peaks at 32.9° and 38.9° which can be attributed the crystalline (metallic) indium. The existence of these peaks verifies the assumption from the EDXS analysis (figure 5.2.4(f)) that there are also metallic In cluster formed by ion implantation and FLA. In the As$^+$/Ga$^+$ implanted SOI sample, characteristic GaAs reflections are observed at 27.3°, 45.6° and 54.0° representing the GaAs (111), (220) and (311) lattice planes, respectively. No metallic Ga has been detected. The presence of the reflections of both III-V compounds gives a further proof of the NC formation after FLA treatment of the ion implanted samples. A more detailed analysis of the XRD patterns will be given in section 5.2.3.

5.2.3 $\mathrm{In_xGa_{1\text{-}x}As}$ NC formation in SOI samples

As binary III-V compounds have been successfully fabricated by the combination of ion implantation and FLA in SOI samples, an experiment to form ternary III-V compounds has been initiated by adding a third ion implantation step. Various fluence ratios of As$^+$/Ga$^+$/In$^+$ ions, given in table 5.2.1, have been utilised in order to form $\mathrm{In_xGa_{1\text{-}x}As}$ with different compositions. The column named "$\mathrm{In_xGa_{1\text{-}x}As}$ composition - nominal (x_{nom})" denotes the composition of the ternary III-V NCs regarding to the fluence ratio of the implanted ions. For example, when the fluence ratio for the sequential As$^+$/Ga$^+$/In$^+$ implantation is 3/1.5/1.5 (10^{16} ions/cm^2), then x_{nom} is 0.5 and it is expected that $\mathrm{In_{0.5}Ga_{0.5}As}$ NCs form after FLA treatment.

Figure 5.2.6(a) displays the Raman spectra of the As$^+$/Ga$^+$/In$^+$ implanted samples (coloured) treated with σ_{FLA} of 97.2 J/cm^2 in comparison with the Si$^+$ implanted reference sample (black). In the spectrum of the reference sample, the characteristic phonon modes of crystalline Si are observed at 520 cm^{-1} (Si TO+LO) and 300 cm^{-1} (Si 2TA). The Si TO+LO phonon mode has a tail at the low wavenumber side which is due to small Si crystallites evolving during recrystallization of the amorphized thin Si$^+$ implanted Si layer after FLA. The Raman spectra of the binary compounds, InAs (red) and GaAs (pink), are identical to those presented in figure 5.2.1. They show the typical phonon modes of the respective III-V compound and those of the recrystallized Si. The Raman spectra of the samples implanted with all three ion species show a slightly

Table 5.2.1: Implantation fluences of Si^+ and group-III and -V ions in SOI samples. Nominal (x_{nom}) and calculated $In_xGa_{1-x}As$ compositions from Raman spectroscopy (x_{Raman}) and XRD measurement (x_{XRD}). For samples, where two ternary phases have been observed during XRD, both compositions are given and the major contribution is marked by an asterisk (*).

sample	ion fluence (10^{16} ions/cm^2)				$In_xGa_{1-x}As$ composition		
	Si	As	Ga	In	nominal (x_{nom})	Raman (x_{Raman})	XRD (x_{XRD})
Si reference	6	–	–	–	–	–	–
InAs	–	3	–	3	1	1	1
$In_xGa_{1-x}As$	–	3	0.75	2.25	0.75	0.6(1)	0.53(4)* 0.79(5)
$In_xGa_{1-x}As$	–	3	1.5	1.5	0.5	0.3(1)	0.17(3)* 0.75(3)
$In_xGa_{1-x}As$	–	3	2.25	0.75	0.25	0.1(1)	0.04(1)* 0.79(17)
GaAs	–	3	3	–	0	0	0

different picture. The phonon modes related to the III-V NCs are at different positions and their intensities also change with varying composition. The shift of the peak positions is displayed in figure 5.2.6(b). The filled symbols depict the experimental values deduced by fitting the particular Raman spectra. In comparison, the lines represent theoretical curves of phonon mode positions (ω) depending on the In content (x_{nom}) in $In_xGa_{1-x}As$, which are calculated by [426]:

$$\omega_{\mathrm{LO,\ GaAs\text{-}like}} = 290.98 - 19.00x - 31.05x^2\ (\mathrm{cm}^{-1}), \tag{5.1}$$

$$\omega_{\mathrm{TO,\ GaAs\text{-}like}} = 268.75 - 20.125x - 8.74x^2\ (\mathrm{cm}^{-1}), \tag{5.2}$$

$$\omega_{\mathrm{LO,\ InAs\text{-}like}} = 230.29 + 5.11x + 2.15x^2\ (\mathrm{cm}^{-1}), \tag{5.3}$$

and

$$\omega_{\mathrm{TO,\ InAs\text{-}like}} = 230.19 + 2.32x - 17.73x^2\ (\mathrm{cm}^{-1}). \tag{5.4}$$

When decreasing the In content, the InAs-like phonon modes lose intensity and converge until they vanish completely for $x \leq 0.2$ [426]. The GaAs-like phonon modes separate with decreasing In content and gain intensity. However, they do not vanish for $x \to 1$ but converge with the InAs-like LO phonon mode. This kind of phonon mode behaviour depending on the composition of a mixed crystal is called partly two-mode phonon behaviour [131, 426, 427]. The experimentally determined phonon mode positions follow the trend of the theoretical curves but a slight deviation from the theoretical values can be observed indicating different compositions. Therefore, equations (5.1)-(5.4) are utilized to calculate the composition of the III-V NCs fabricated by ion implantation and FLA. The calculated compositions from the Raman spectra (x_{Raman}) are given in table 5.2.1 and imply that the $In_xGa_{1-x}As$ NCs are Ga-rich compared to the nominal composition ($x_{\mathrm{Raman}} < x_{\mathrm{nom}}$).

Figure 5.2.7 displays the XRD 2θ scans taken from the SOI samples implanted with As^+, Ga^+ and In^+ ions at different fluence ratios. Again, the Si^+ implanted reference

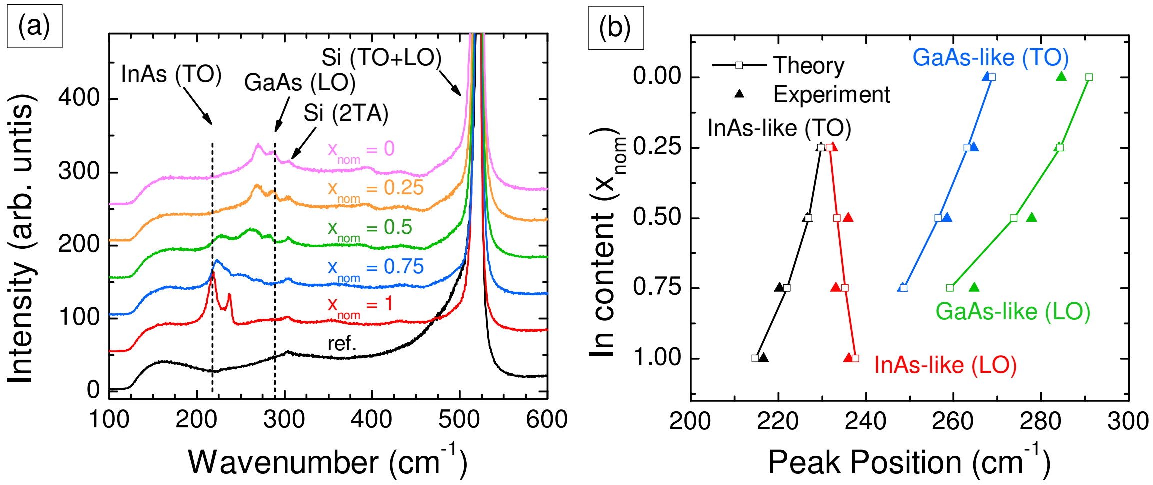

Figure 5.2.6: (a) Raman spectra of SOI samples implanted with different fluence ratios of As^+, Ga^+ and In^+ ions and treated with FLA at 97.2 J/cm^2 in comparison with a Si^+ implanted reference sample (black). (b) Measured phonon mode positions in comparison with theoretical peak positions of $In_xGa_{1-x}As$ [426].

sample is included. All six samples have been annealed with a σ_{FLA} of 97.2 J/cm^2. Both XRD patterns of the binary III-V compounds, InAs (red, $x_{\mathrm{nom}} = 1$) and GaAs (pink, $x_{\mathrm{nom}} = 0$), are identical to those patterns presented in figure 5.2.5. All curves share the Bragg peaks of crystalline Si (blue bars) at 28.4°, 47.3° and 56.1° for the Si (111), Si (220) and Si (311) reflections, respectively. The (111) Bragg peak of the III-V compounds (yellow bar) shifts with decreasing In content (x_{nom}) from the InAs position at 25.4° towards the GaAs position at 27.3°. This XRD peak shift is also observed for the (220) and (311) reflections of the III-V compounds which implies a change in the composition of the fabricated ternary $In_xGa_{1-x}As$ NCs with the implantation fluence variation. However, the peak shift does not behave linearly with the decrease of the In content (x_{nom}). The XRD peak position of the ternary phases tend to be located more towards the GaAs positions for the particular implantation fluence ratio, indicating Ga-rich $In_xGa_{1-x}As$ NCs. Furthermore, a splitting of the reflections of the ternary phases can be observed, especially for the sample implanted with equal fluence of Ga^+ and In^+ ions (green, $x_{\mathrm{nom}} = 0.5$). Due to the peak splitting it is suspected that at least two ternary $In_xGa_{1-x}As$ phases with different composition form. Two additional Bragg peaks can be detected at 32.9° and 39.1° in samples implanted with In^+ ($x_{\mathrm{nom}} \geq 0.25$) that can be accounted to metallic In precipitates (In (101) and (110) reflections). The existence of these precipitates supports the appearance of Ga-rich $In_xGa_{1-x}As$ NCs since In which is incorporated in metallic precipitates cannot be consumed for the formation of III-V compounds NCs.

In order to get detailed information about the ternary phases within the thin Si layer, a Williamson-Hall analysis [428] of the XRD 2θ scans has been performed. Therefore, the XRD peak positions in 2θ and the full-width at half maximum (FWHM) in 2θ have been accessed by fitting the particular pattern for each nominal composition. These two values have then been used to plot Δq against q to form a Williamson-Hall plot, as exemplarily depicted in figure 5.2.8 for the sample with $x_{\mathrm{nom}} = 0.5$. The parameters

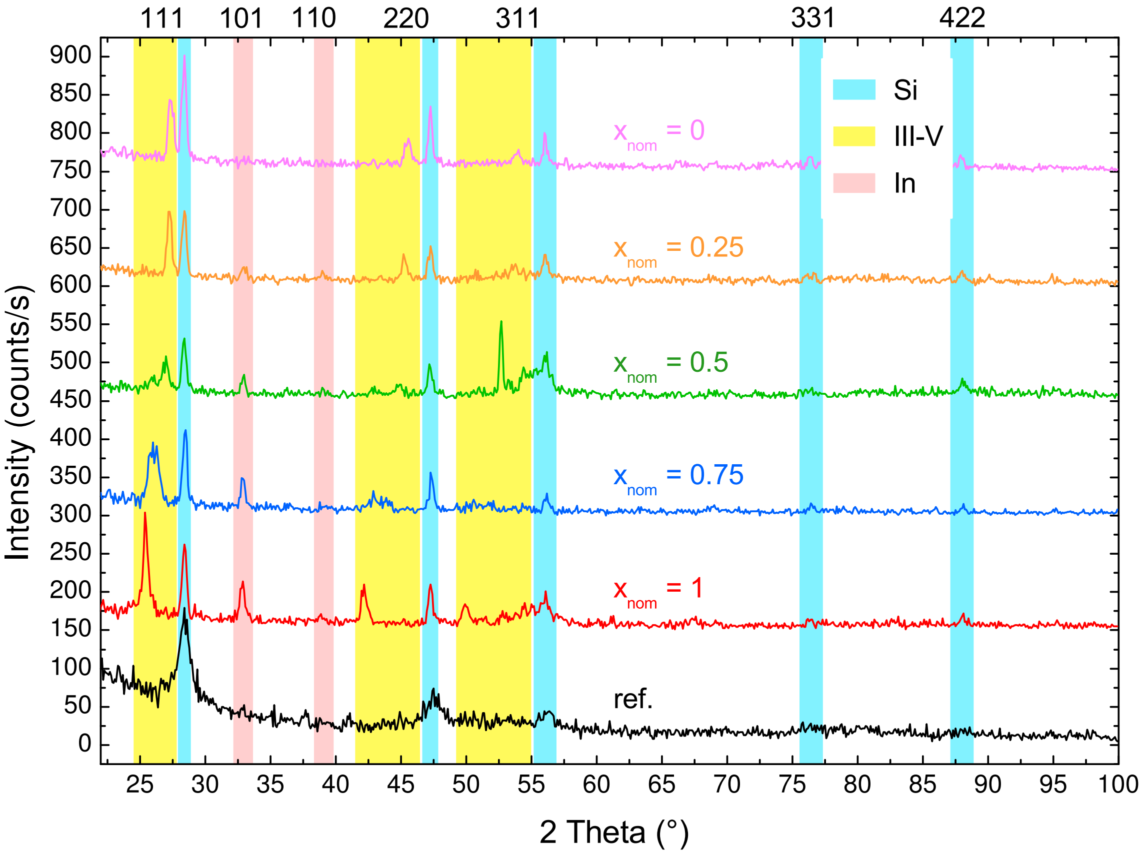

Figure 5.2.7: XRD 2θ scans of SOI samples implanted with different fluence ratios of As^+, Ga^+ and In^+ and annealed with FLA at 97.2 J/cm^2 in comparison with the Si^+ implanted reference.

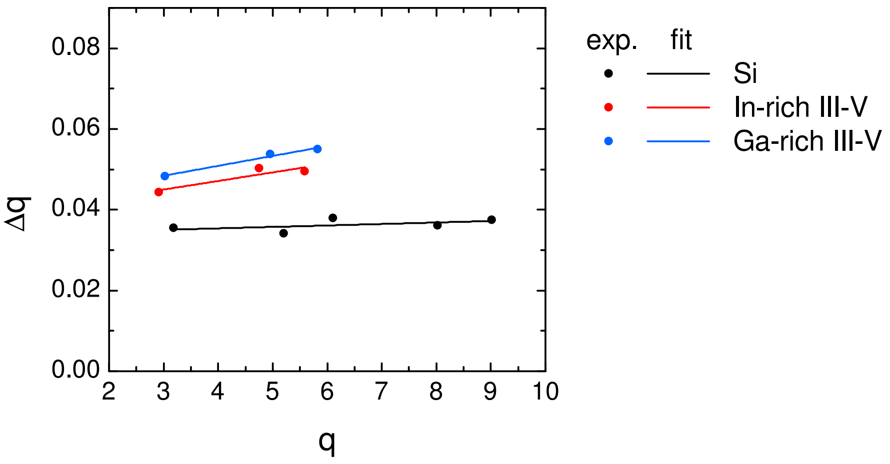

Figure 5.2.8: Williamson-Hall plot of the SOI sample implanted with $x_{\mathrm{nom}} = 0.5$ annealed with a σ_{FLA} of 97.2 J/cm^2).

q and Δq are defined by

$$q = \frac{2}{\lambda} \cdot \sin\theta \tag{5.5}$$

and

$$\Delta q = \frac{2}{\lambda} \cdot \Delta\theta \cdot \cos\theta, \tag{5.6}$$

where $\Delta\theta = \mathrm{FWHM}/2$ (in rad) and λ is the wavelength of the incident X-ray beam, namely Cu-Kα with $\lambda = 0.154\,\mathrm{nm}$. The pairs of variates of each particular group of reflections, e.g. III-V reflections, are then modelled by a linear fit $\Delta q = Aq + B$. The fitting parameters, the slope A and the intersection with the y-axis B, for the fits in figure 5.2.8 are given in table 5.2.2. Data for the Bragg peaks caused by the In precipitates is not shown since there are only one or two peaks in each XRD 2θ scan.

Both deduced fitting parameters can be converted into properties of the particular crystallites of each species. The intersection with the y-axis B displays the reciprocal value of the mean crystallite size and the slope A gives the μ-strain of the crystallite when divided by a factor of two. The Williamson-Hall analysis of the SOI sample with $x_{\mathrm{nom}} = 0.5$ yields a mean Si crystallite size of 30(2) nm and mean sizes of 26(3) nm and 24(1) nm for the In-rich and Ga-rich III-V NCs, respectively. The mean μ-strain, which describes the non-uniform disorder of atoms in the lattice caused by dislocations, for example, has values of $1.1(5) \times 10^{-3}$ for the In-rich and $1.2(2) \times 10^{-3}$ for the Ga-rich III-V NCs. The mean μ-strain of the Si crystallites is $0.2(2) \times 10^{-3}$.

A Williamson-Hall analysis has been performed for all SOI sample implanted with As$^+$, Ga$^+$ and In$^+$ ions at different fluence ratios and for the Si$^+$ implanted reference sample. Figures 5.2.9(a) and (b) display the results for the crystallite size and the μ-strain depending on the In content (x_{nom}), respectively. The III$^+$/V$^+$ implanted samples show similar crystallite sizes for Si crystallites as well as for the In$_{\mathrm{x}}$Ga$_{1\text{-}\mathrm{x}}$As NCs independent of the In content (x_{nom}) nominally used. Their mean crystallite size

Table 5.2.2: Fitting parameters for linear fits of the Williamson-Hall plot of the SOI sample implanted with $x_{\mathrm{nom}} = 0.5$.

	slope A	mean crystallite size (nm)	intersection with y-axis B (1/nm)	mean μ-strain (10^{-3})
Si	0.0004(3)	30(2)	0.034(2)	0.2(2)
In-rich	0.0021(9)	26(3)	0.039(4)	1.1(5)
Ga-rich	0.0025(4)	24(1)	0.041(2)	1.2(2)

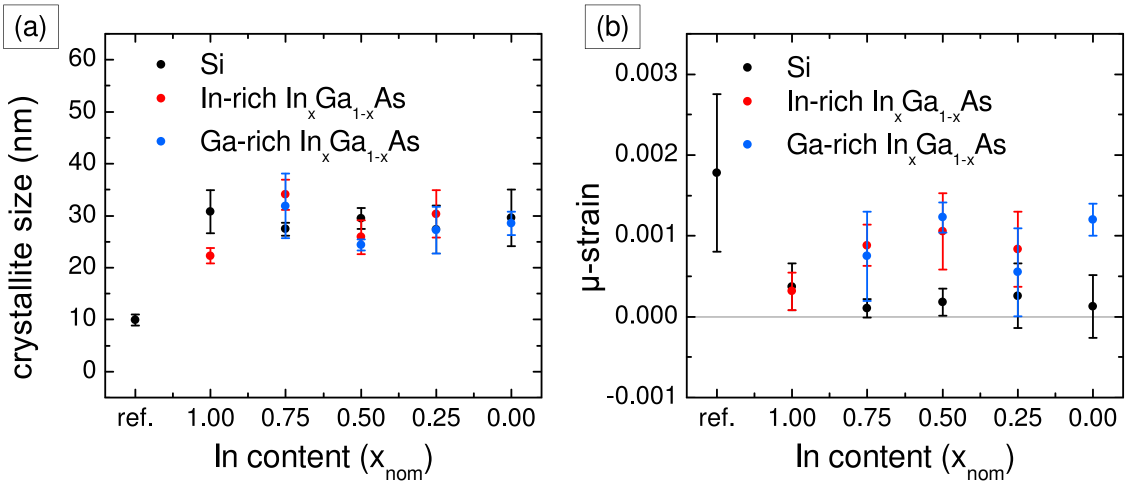

Figure 5.2.9: Results deduced from Williamson-Hall plot analysis of SOI samples implanted with $\mathrm{As}^+/\mathrm{Ga}^+/\mathrm{In}^+$ at various fluence ratios, including crystallite size (a) and μ-strain (b).

is 28(3) nm while the Si^+ implanted reference sample shows only a crystallite size of 10(1) nm, in contrast. The μ-strain draws an inverse picture, the crystallites in the Si^+ sample ($2(1) \times 10^{-3}$) are more strained than the Si and $\mathrm{In_xGa_{1\text{-}x}As}$ crystallites in the $\mathrm{III}^+/\mathrm{V}^+$ implanted samples. Within the $\mathrm{III}^+/\mathrm{V}^+$ implanted samples, the Si crystallites are less strained ($0.2(2) \times 10^{-3}$) than the $\mathrm{In_xGa_{1\text{-}x}As}$ NCs (mean: $0.9(3) \times 10^{-3}$). Furthermore, a slight trend of increasing μ-strain with decreasing In content (x_{nom}) can be observed for the $\mathrm{In_xGa_{1\text{-}x}As}$ NCs.

Since the Williamson-Hall analysis reveals that crystallites have only a small strain, a shift of the XRD peak due to strain is neglected. Therefore, the measured XRD peak positions can be used to determine the lattice parameter of the particular species. For a cubic crystal structure, e.g. for InAs, the lattice spacing d can determined by

$$\frac{1}{d^2} = \frac{h^2 + k^2 + l^2}{a^2}, \tag{5.7}$$

where h, k and l are the Miller indices, and a is the lattice parameter of the particular material. Combining equation (5.7) with the Bragg equation (4.1) (assuming $n = 1$) and rearranging it to

$$a = \frac{\lambda \cdot \sqrt{h^2 + k^2 + l^2}}{2 \sin\theta}, \tag{5.8}$$

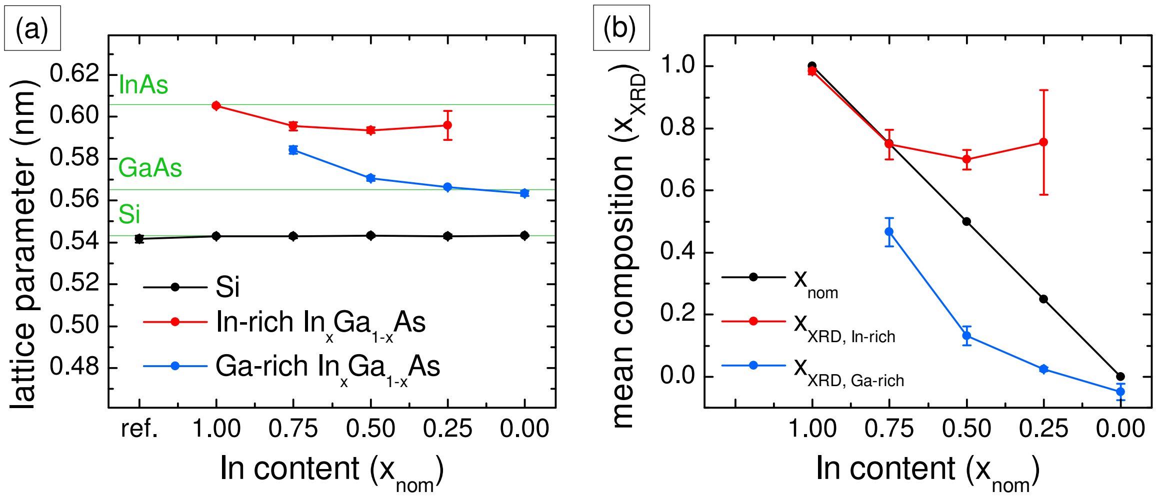

Figure 5.2.10: Mean lattice parameter (a) of the crystallites and mean composition (b) of the ternary phases calculated from XRD peak positions.

the lattice parameter for a specific XRD reflex can be calculated. Figure 5.2.10(a) gives the mean lattice parameter determined by equation (5.8) for the Si crystallites as well as for the different $\mathrm{In_xGa_{1\text{-}x}As}$ phases depending on the In content (x_{nom}). As a guide to the eye, the literature values for the lattice parameter of Si, GaAs and InAs are inserted as green lines. For the reference sample, the Si crystallites (black) possess a lattice parameter which is in good agreement with the literature value. Within the $\mathrm{As^+}$, $\mathrm{Ga^+}$ and $\mathrm{In^+}$ implanted samples, this is true as well. Concerning the III-V related crystallites, the lattice parameters of InAs (red, $x_{\mathrm{nom}} = 1$) and GaAs (blue, $x_{\mathrm{nom}} = 0$) are also in good agreement with literature values. With decreasing In content (x_{nom}), the lattice parameters of both $\mathrm{In_xGa_{1\text{-}x}As}$ phases decrease separately indicating different compositions.

These different compositions deduced from XRD measurement (x_{XRD}) can be determined by taking Vegard's law [429] into account. For mixed crystals of the same crystal structure, the lattice parameter a changes linearly with the change of composition. For the $\mathrm{In_xGa_{1\text{-}x}As}$ mixed crystal, this means

$$a_{\mathrm{In_xGa_{1\text{-}x}As}} = x_{\mathrm{XRD}} \cdot a_{\mathrm{InAs}} + (1 - x_{\mathrm{XRD}}) \cdot a_{\mathrm{GaAs}}, \tag{5.9}$$

where a_{InAs} and a_{GaAs} represent the literature values for the lattice parameters of InAs and GaAs, respectively. In the case of compound semiconductors, a deviation from the linear change predicted by Vegard's law occurs [430, 431]. Using the model proposed by Fournet [432], the deviation ξ from Vegard's law for $\mathrm{In_xGa_{1\text{-}x}As}$ is expressed by

$$\xi = x \cdot (1 - x) \cdot (a_{\mathrm{GaAs}} - a_{\mathrm{InAs}}) \cdot \left[\frac{\dfrac{\kappa_{\mathrm{InAs}}}{\kappa_{\mathrm{GaAs}}} - 1}{x + (1 - x) \cdot \dfrac{\kappa_{\mathrm{InAs}}}{\kappa_{\mathrm{GaAs}}}} \right], \tag{5.10}$$

where $\kappa_{\mathrm{InAs}} = 1.72\,\mathrm{GPa^{-1}}$ and $\kappa_{\mathrm{GaAs}} = 1.34\,\mathrm{GPa^{-1}}$ represent the room temperature volume compressibility of InAs and GaAs, respectively [433].

Since the lattice parameters of the crystallites formed in the SOI samples are known from figure 5.2.10(a), equations (5.9) and (5.10) can be utilized to calculate the com-

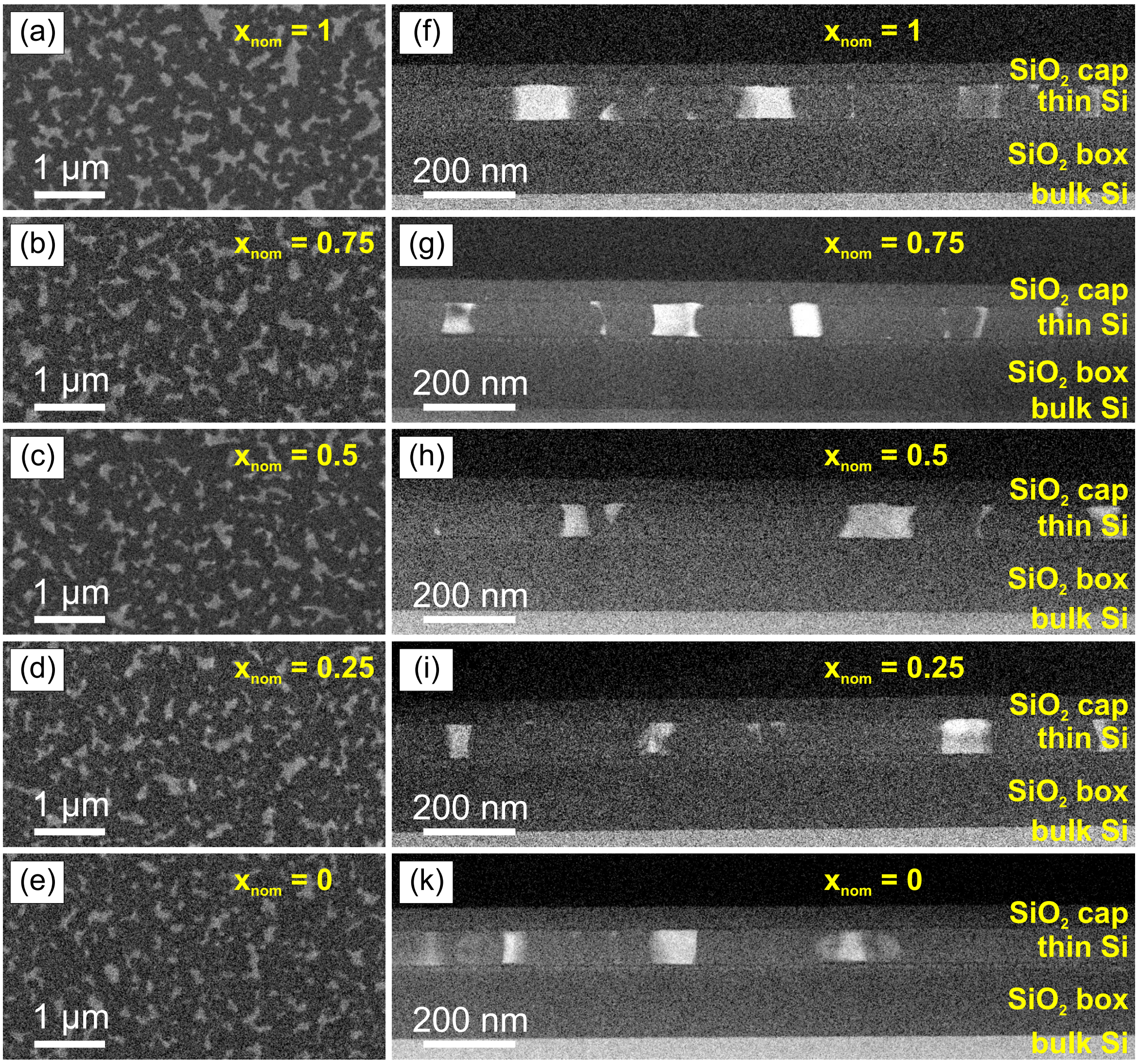

Figure 5.2.11: Top-view SEM (a-e) and corresponding cross-sectional HAADF-STEM (f-k) micrographs of SOI samples implanted with different x_{nom} and annealed with FLA at 97.2 J/cm^2.

position (x_{XRD}) of the particular $\mathrm{In_xGa_{1\text{-}x}As}$ phases. The resulting x_{XRD} values are displayed in figure 5.2.10(b) and are also given in table 5.2.1 in comparison with the nominal compositions (x_{nom}) and the composition values determined by using Raman spectroscopy (x_{Raman}). It can be observed that the two different $\mathrm{In_xGa_{1\text{-}x}As}$ phases split up into an In-rich and a Ga-rich phase with respect to the nominal composition (x_{nom}). By considering the ratio of the peak intensities defined by the area under the XRD reflections, it becomes clear that the Ga-rich $\mathrm{In_xGa_{1\text{-}x}As}$ NCs represent the dominating ternary III-V phase, which is also supported by the appearance of the metallic In Bragg peaks.

A comparison of SEM and corresponding HAADF-STEM images recorded from the SOI samples implanted with different fluence ratios of $\mathrm{As^+}$, $\mathrm{Ga^+}$ and $\mathrm{In^+}$ ions are displayed in figure 5.2.11. The NC shape depicted in the top-view SEM images (a-e) is arbitrary as already observed for the binary III-V compounds in figures 5.2.2 and 5.2.3. The size distribution of the III-V particles is rather broad, ranging from

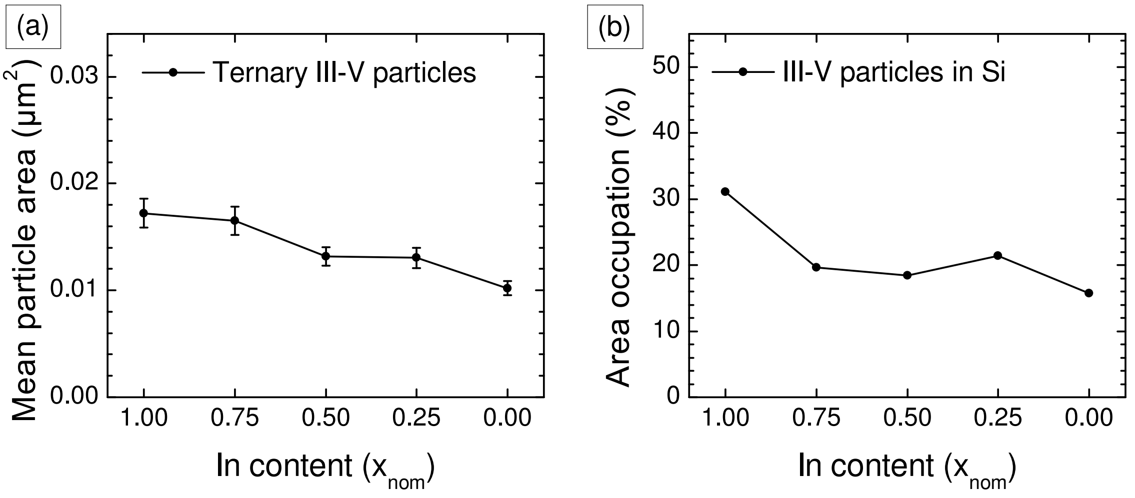

Figure 5.2.12: In content dependencies of the mean particle size (a) and area occupation (b) of the ternary III-V NCs.

a few to several hundreds of nanometres. Comparing the samples implanted with different fluence ratios, a decrease of the mean particle size with decreasing In content ($x_{\mathrm{nom}} \rightarrow 0$) is visible. In contrast, the particle number does not change significantly resulting in a decrease of the relative volume fraction of the III-V NCs in Si. In the corresponding HAADF-STEM micrographs (f-k), the cross-sections present the expected layer stack of the SiO_2 capping layer, the thin Si device layer, the SiO_2 buried oxide layer on top of the bulk Si for each sample. The Si device layer of each sample comprises several bright areas representing the III-V precipitates. These particles obtain mainly a block-like cross-section and their height is limited by the surrounding SiO_2 layers. At the Si/SiO_2 interfaces, smaller NCs are located which are eventually connected by thin filaments. The reduction of particle size with decreasing In content, as observed in the SEM images, is not observed in the HAADF-STEM micrographs as the number of precipitates is not high enough for a proper statistical analysis. Similar to the sample containing binary III-V NCs, dotted lines of bright spots are detected in the surrounding SiO_2 layers adjacent to the Si/SiO_2 interfaces in addition to the III-V precipitates present within the Si device layer.

In order to investigate the particle size dependence on the implantation fluence ratio, a statistical evaluation of the SEM micrographs compared in figures 5.2.11(a-e) is performed using the open source software ImageJ [418], as it has already been done for the bulk samples in figure 5.1.4. In figure 5.2.12, the results of this particle size analysis are depicted including the mean particle area (a) and the relative area occupation (b) of the III-V NCs. The mean particle area of the III-V precipitates decreases with decreasing In content (x_{nom}) from 0.0172(14) μm^2 for the InAs sample to 0.0102(7) μm^2 for the GaAs sample. This verifies the trend seen in the SEM images and proves the size reduction of the III-V NCs with lowering the In amount within the III-V precipitates. Furthermore, the variation of the mean particle area (error bars) decreases with decreasing In content as well, which shows that the size distribution gets narrower. The overall area occupation of the III-V NCs shows a similar trend. For the InAs sample, approximately 31 % of the surface area can be accounted to the III-V particles while only about 16 % are related to the III-V precipitates in the GaAs sample.

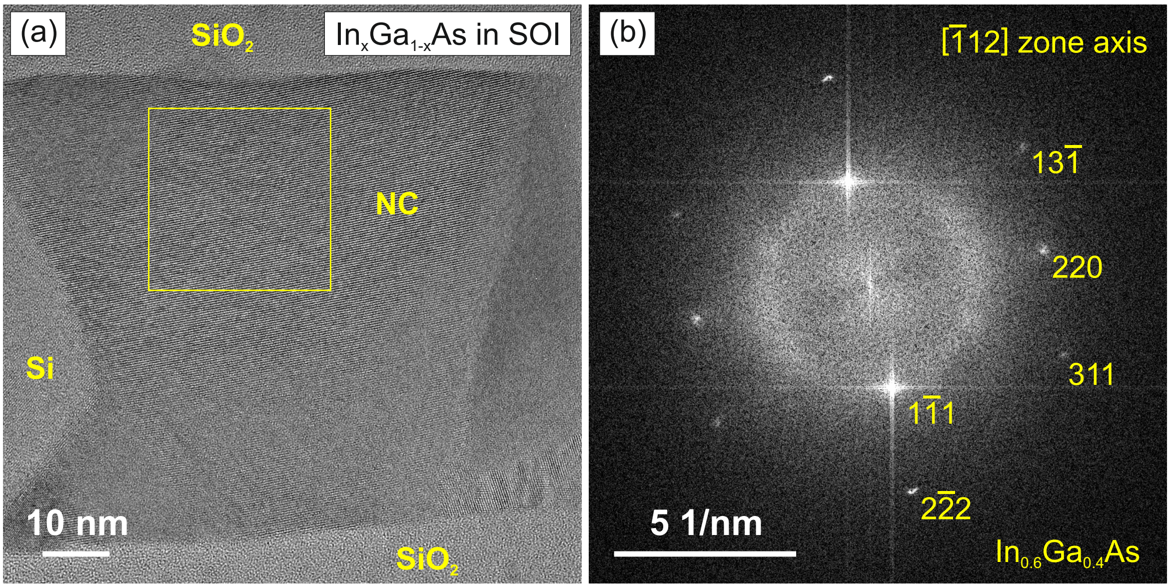

Figure 5.2.13: HRTEM images of a ternary $In_xGa_{1-x}As$ NC (a) and its corresponding FFT (b) taken from the area marked by the yellow box.

Figure 5.2.13(a) shows the HRTEM image of an $In_xGa_{1-x}As$ NC in the SOI sample implanted with $x_{\mathrm{nom}} = 0.5$. The NC extends through the full thickness of the Si layer and its lateral size is even bigger. The NC has a good crystalline order although there are several defects, e.g. stacking faults, and small disordered regions within the crystallite. Despite these defects, the NC appears to be single-crystalline. The corresponding FFT, taken from the region marked by the yellow box, is depicted in figure 5.2.13(b) and shows strong reflexes in a hexagonal arrangement. Additionally, a ring is visible around the central spot which originates from disorder within the NC. The analysis of the FFT yields a fcc crystal oriented in $[\bar{1}12]$ zone axis. By determining the distances between particular spots and the central spot, the NC could be identified as an $In_xGa_{1-x}As$ mixed crystal with a lattice parameter of 0.588(7) nm giving a composition of $x = 0.6(2)$. The $In_xGa_{1-x}As$ NC is In-rich with respect to x_{nom}, but fits to the composition of the minor contribution deduced from XRD results. However, since this is only a specific NC, it is hard to draw a conclusion about the composition of the $In_xGa_{1-x}As$ crystallites in general and as the Raman and XRD techniques are integrating over a larger area, these measurements are more appropriate to draw generalized conclusions.

5.2.4 Binary III-Vs in thin Si layers grown by PECVD

In figure 5.2.14, the RBS depth profiles of PECVD samples implanted with P^+ and Ga^+ ions are shown and the *as implanted* sample (a, b) is compared with a *FLA treated* (c, d) one, which has been exposed to a pre-heating of 600 °C and a σ_{FLA} of 63.3 J/cm^2. For all spectra, the abscissae can be converted into a nm-scale dividing the given depth in 10^{15} at/cm^2 by the atomic density of the matrix material. The overview profiles (a, c) display the distributions of Si, O, P and Ga and the extensions of the PECVD-grown layer stack can be determined. The top SiO_2 layer has been partly sputtered away by the ion implantation step leading to a decrease in thickness from

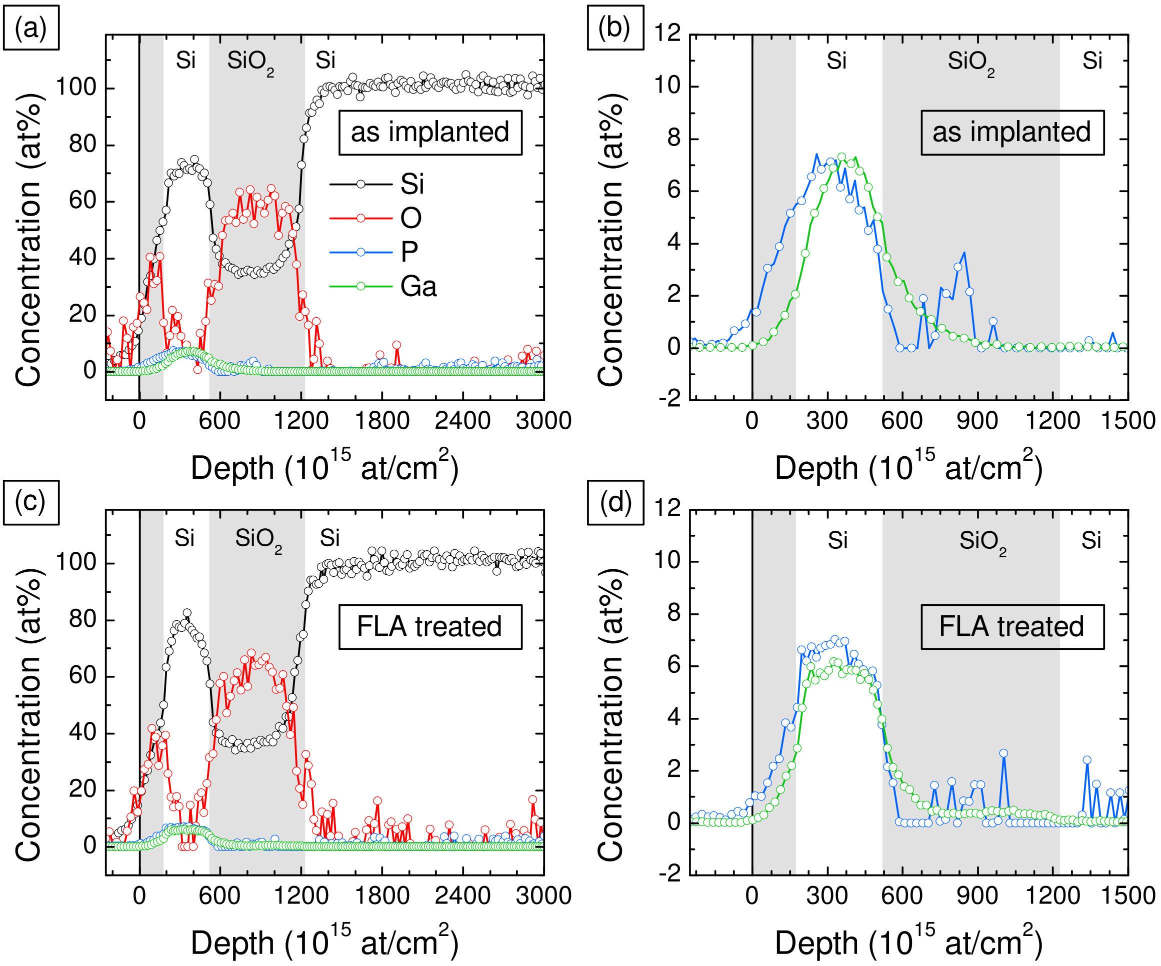

Figure 5.2.14: RBS depth profiles of PECVD samples implanted with P^+ and Ga^+. The *as implanted* case (a, b) is compared with a *FLA treated* sample (c, d) treated with a σ_{FLA} of 63.3 J/cm^2 after a preheating to 600 °C.

35 nm to 25 nm. For the thin Si layer, a thickness of about 68 nm can be extracted which equals a swelling of about 13 % by the introduction of the III^+/V^+ ions by ion implantation. The thickness of SiO_2 box layer extracted from the RBS measurement matches the deposited value of 100 nm and the atomic concentrations of Si (36 at%) and O (61 at%) are close to a stoichiometric SiO_2.

In the *as implanted* sample, the depth profiles of P and Ga show a Gaussian-like distribution (figure 5.2.14(b)) which is centred within the thin Si layer but the tails extend into the surrounding SiO_2 layers. The P profile has a slightly lower depth than the Ga profile. Both elements show a maximum atomic concentration of about 7 at%. The depth profiles of the *as implanted* samples measured by RBS are in good agreement with the simulated profiles using SRIM. By applying FLA treatment, the shape of the profiles changes from a Gaussian-like distribution to a box-like distribution (figure 5.2.14(d)). The box-like profiles indicate a homogeneous distribution of the implanted ions in the thin Si layer after FLA. In the top SiO_2 layer, the P concentration is reduced while it is redistributed in the thin Si layer. Nevertheless, both atom species have approximately the same atomic concentration of about 6 %, which is constant over the complete Si layer.

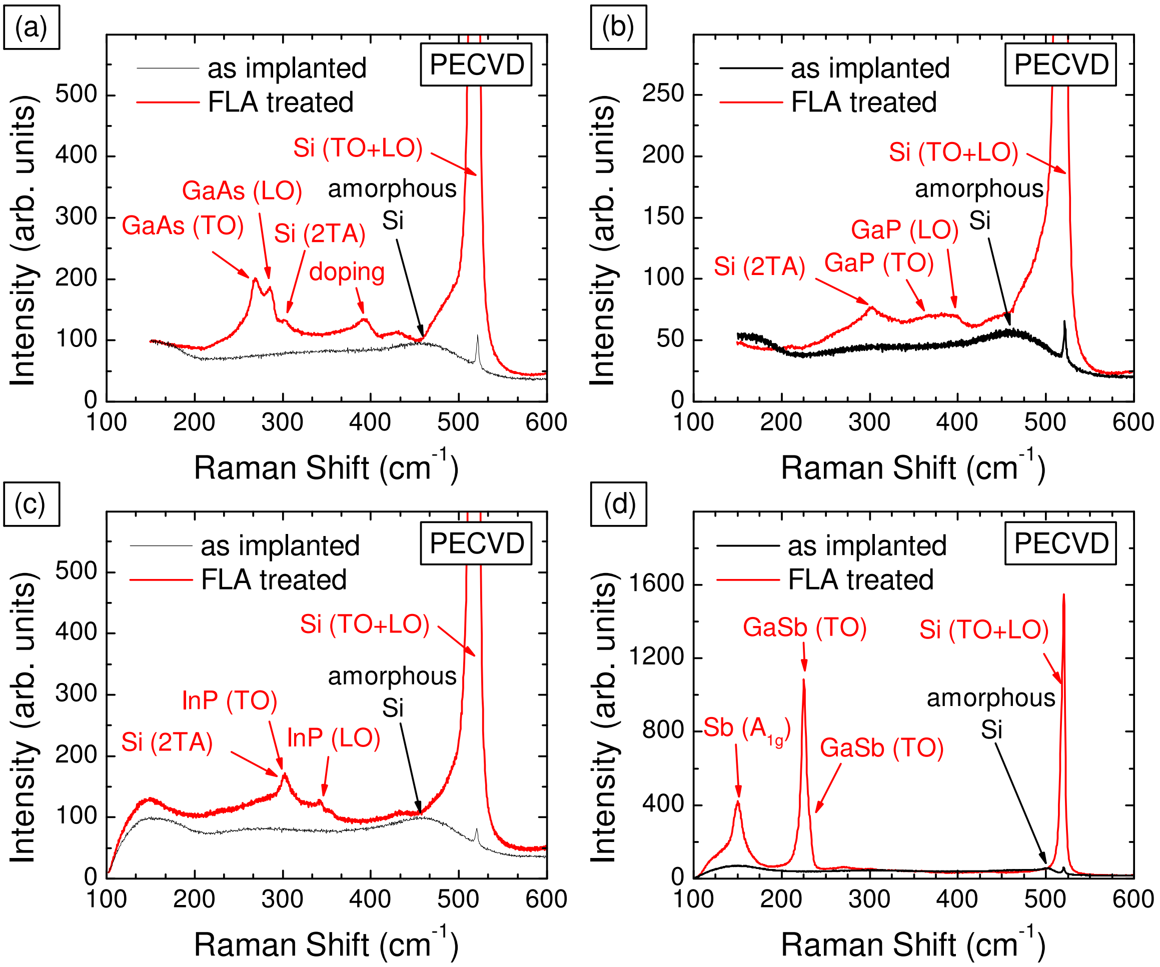

Figure 5.2.15: Raman spectra of PECVD samples implanted with (a) As^+/Ga^+, (b) P^+/Ga^+, (c) P^+/In^+, and (d) Sb^+/Ga^+ and *FLA treated* (red) with σ_{FLA} of 92.6 J/cm^2 in comparison with the *as implanted* spectra (black).

Figure 5.2.15 shows the Raman spectra of the PECVD samples implanted with As^+/Ga^+ (a), P^+/Ga^+ (b), P^+/In^+ (c), and Sb^+/Ga^+ (d) comparing the *as implanted* (black) with the *FLA treated* case (red) of samples annealed with σ_{FLA} of 92.6 J/cm^2. In the *as implanted* spectra only the broad peaks of a-Si and a weak Si TO+LO phonon mode contribution from the crystalline Si substrate can be observed. Considering the *FLA treated* samples, all four Raman spectra show the typical crystalline Si related phonon modes. The Raman spectrum of the GaAs PECVD sample (a) looks similar to the spectra taken from the SOI and bulk samples showing the characteristic phonon modes of GaAs as well as the peak related to Si doping in the GaAs NCs. For the P^+/Ga^+ implanted sample, only a very broad signal is detected besides the c-Si peaks. However, the characteristic phonon modes of crystalline GaP at 367 cm^{-1} (TO) and 403 cm^{-1} (LO) [434] are located under this broad peak which confirms the formation of GaP NCs. The broadening of the peaks can be attributed to a small size of the crystallites. In the Raman spectrum taken from the P^+/In^+ implanted PECVD sample (c), a small peak at 345 cm^{-1} is observed, which originates from the InP LO phonon mode [434], and proves InP NC formation. The InP TO phonon mode is located at 304 cm^{-1} but coincides with the Si 2TA phonon mode and cannot be distinguished clearly. Figure 5.2.15(d) displays a very intense Raman peak for the GaSb TO and

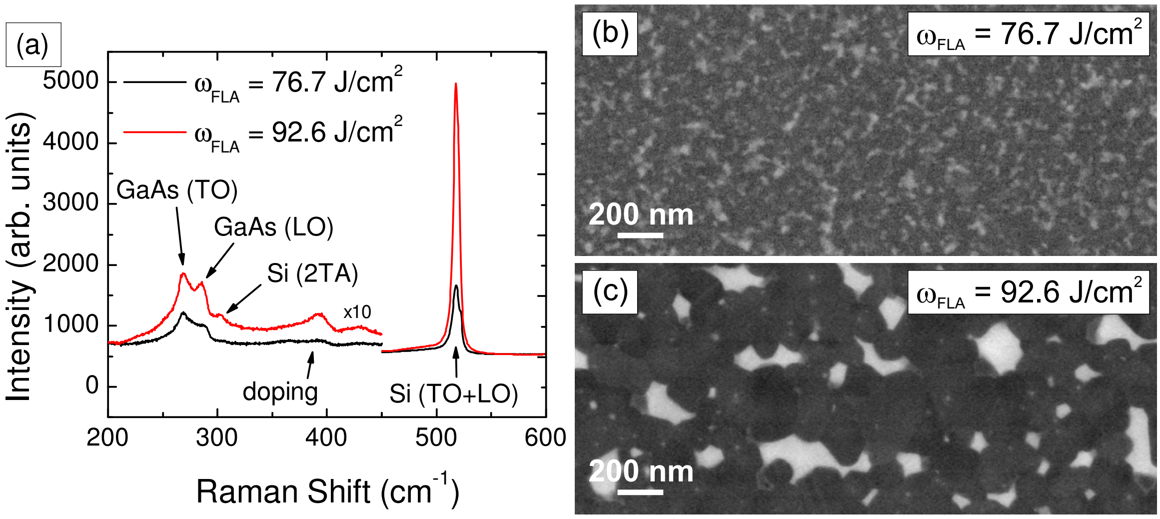

Figure 5.2.16: Raman spectra (a) and corresponding SEM images (b, c) of two PECVD samples implanted with As^+/Ga^+ treated with σ_{FLA} of 76.7 J/cm^2 (black, b) and 92.6 J/cm^2 (red, c).

LO phonon modes at 223 cm^{-1} and 232 cm^{-1}, respectively, verifying GaSb NC formation. In contrast to the other III-V compounds, the GaSb peak is almost as intense as the Si TO+LO phonon mode. The high intensity can probably be attributed to the high atomic mass of Sb. Additionally, there is a signal at 150 cm^{-1} originating from the Sb A_{1g} phonon mode, which indicates the presence of elemental Sb within this particular sample. For the sample implanted with N^+/Ga^+, no GaN related peak could be observed (not shown). Therefore, it is suspected that in the case of GaN no NC formation took place.

In figure 5.2.16, two As^+/Ga^+ implanted PECVD samples annealed with different σ_{FLA} are compared. The characteristic phonon modes of GaAs are more intense and sharper in the spectrum taken from the sample annealed with higher σ_{FLA} (red). This observation indicates that a better crystallization of GaAs NCs is achieved with higher σ_{FLA}. The corresponding SEM images (b, c) support this fact by showing a strong difference in GaAs NC number and size. In the sample annealed with the lower σ_{FLA} (b) a lot of small crystallites are present while large GaAs precipitates are observed with a higher σ_{FLA}. The Si TO+LO phonon mode is also more intense in the Raman spectrum with higher σ_{FLA} which leads to the assumption that the lower σ_{FLA} is not sufficient to fully recrystallize the amorphous Si layer.

Figure 5.2.17 displays the TEM analysis of the As^+/Ga^+ implanted PECVD sample annealed with a σ_{FLA} of 76.7 J/cm^2. The bright-field cross-sectional TEM image (a) shows the layer stack grown by PECVD including the thin Si layer with several dark features. In the corresponding dark-field STEM image (b) some of these features can be identified as GaAs NCs according to their higher brightness. Additionally, small bright spots can be observed in both SiO_2 layers close to the interface. These small features are suspected to be GaAs NCs as well which are caused by the implantation profiles extending into the surrounding SiO_2 layers. The HRTEM image of the trapezoidal NC (c) reveals a single-crystalline precipitate on top of a larger crystallite with different crystalline order. However, there are also disordered regions in the Si layer which

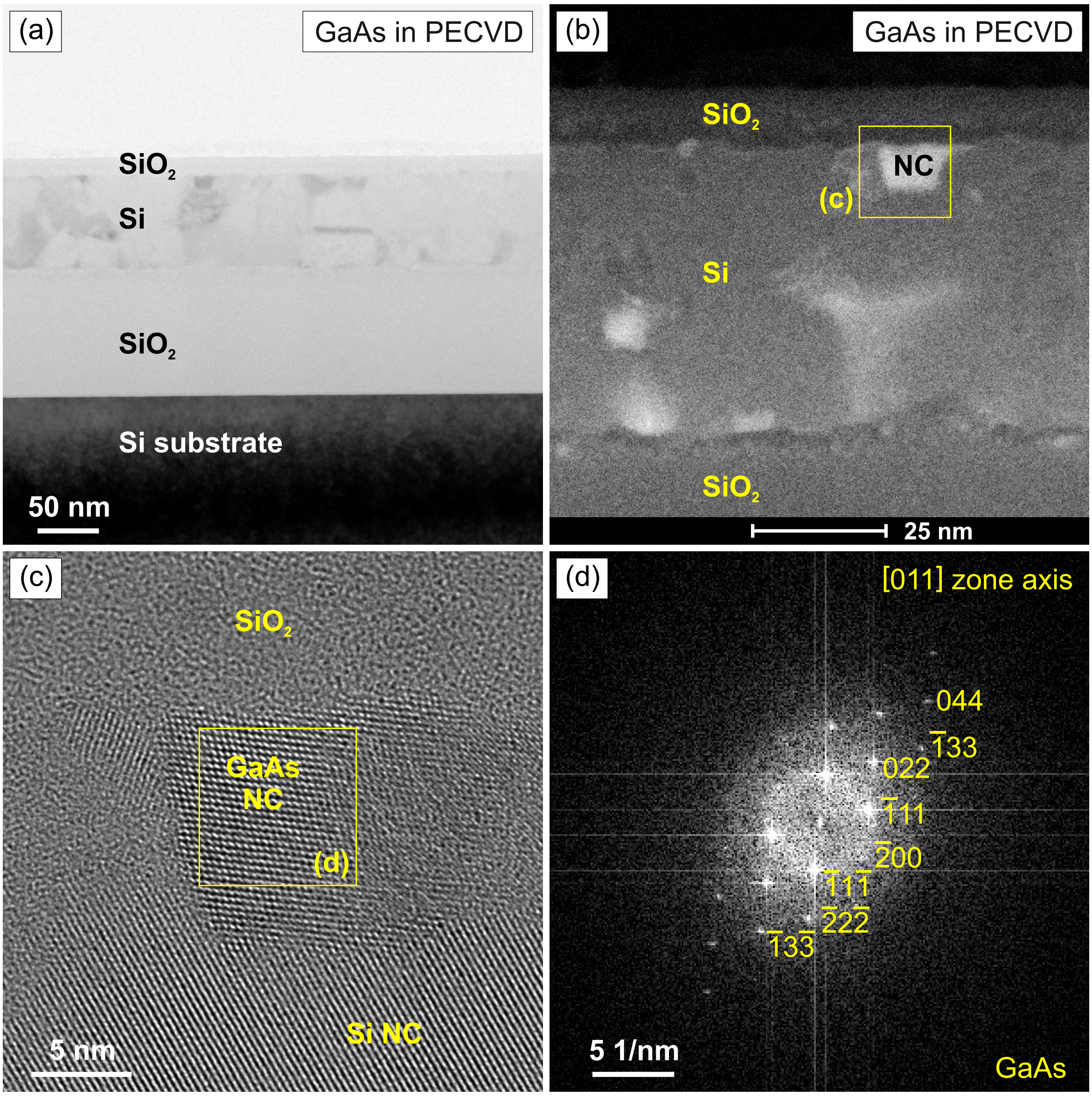

Figure 5.2.17: TEM investigation of the PECVD sample implanted with As$^+$/Ga$^+$ and FLA treated with σ_{FLA} of 76.7 J/cm^2 including (a) cross-sectional TEM, (b) dark-field STEM, (c) HRTEM images, and (d) corresponding FFT.

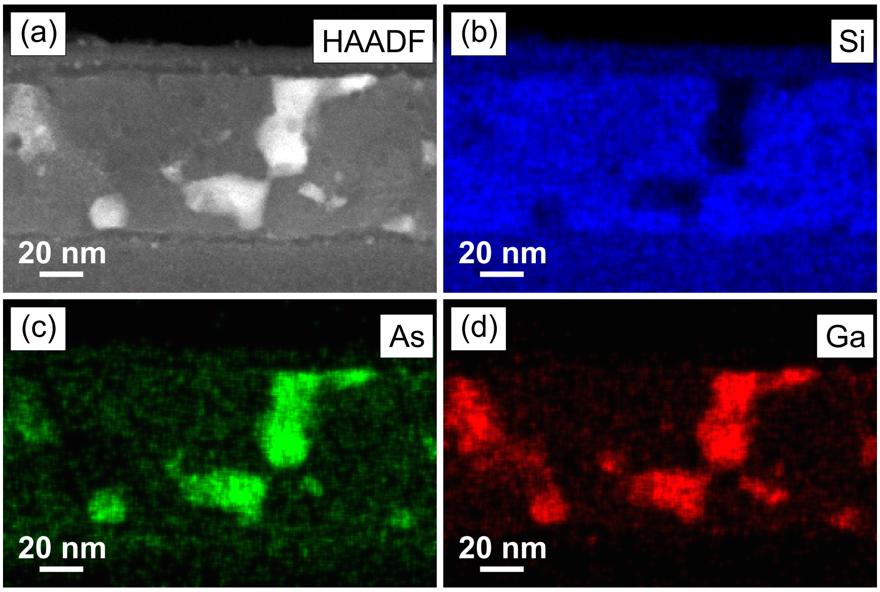

Figure 5.2.18: Cross-sectional HAADF-STEM image (a) of the PECVD sample implanted with As^+/Ga^+ and FLA treated with σ_{FLA} of 76.7 J/cm^2 with corresponding Si (b), As (c), and Ga (d) EDXS element maps.

are accounted to an incomplete recrystallization after FLA treatment proving the previous statement of an insufficient σ_{FLA}. Nevertheless, the trapezoidal NC shows a good crystalline quality and the analysis of the FFT (d) reveals a fcc lattice in [011] zone axis with lattice plane distances of GaAs. The crystallite below is identified as Si NC. The interface between these two NCs is sharp and without defects supporting an epitaxial growth of the GaAs NC on this particular Si NC.

Another region of this particular sample has been investigated by HAADF-STEM and EDXS to perform element mapping, which is shown in figure 5.2.18. The HAADF-STEM image (a) displays the Si layer surrounded by the SiO_2 layers and including precipitates which are depicted by the bright areas. The arbitrarily shaped precipitates are also visible in the EXDS element maps by either reduced intensity for Si (b) or higher intensity for As (c) and Ga (d). The absence of Si and the coincident accumulation of As and Ga within the same areas support GaAs NC formation. However, As and Ga are also detected with lower intensity independently of the precipitates in the whole Si layer as well as in the surrounding SiO_2 layers. The distribution of the implanted ions within the Si layer is accounted to doping by As and Ga since these two elements are known dopants in Si. The presence of As and Ga in the SiO_2 layers is due to the initial implantation profiles which have tails leaking into the surrounding layers. For the InP, GaP and GaSb samples, dark-field STEM images are given in figure A.2.2 in Appendix A.2.

The transfer of this III-V integration method using ion implantation and FLA to PECVD grown thin Si layers has successfully been shown for several III-V compound semiconductors including GaP, GaAs, GaSb and InP. For the combined implantation of N^+ and Ga^+ ions, no GaN NC formation has been observed. This is accounted to the high diffusivity of N in Si in comparison with the other group-III and -V ions. The N diffuses within the Si layer, through the SiO_2 layers and into the bulk Si which decreases the amount of N available for GaN formation. Furthermore, the melting point of GaN is much higher than the melting points of the other III-V compounds and Si. When the results of the implanted PECVD samples are compared with the SOI samples, the SOI substrates are advantageous regarding NC size and shape as well as crystalline quality after ion implantation and FLA treatment. Furthermore, the interfaces to the surrounding SiO_2 layers are smoother in the SOI substrates than in the PECVD samples. Therefore, only SOI substrates have been used in further investigations.

5.3 Mask-assisted implantation

5.3.1 Mask preparation

In order to get control over the lateral distribution of the III-V compound semiconductor NCs, the initial preparation procedure, including only ion beam implantation and FLA, has been modified. Prior to ion implantation, the sample surface has been covered with an implantation mask. This mask has been designed to prevent the major part of the sample from implantation and to possess only small windows where the ions get through.

Conventional p-type Si (100) wafers as well as SOI (SIMOX) substrates have been used as starting material. On top of the substrates, a SiO_2 capping layer has been either deposited by PECVD or grown by thermal oxidation in order to protect the surface from sputtering during ion implantation. Afterwards, the samples have been transferred to an electron beam evaporator for the deposition of the mask material which was either aluminium or nickel. Then, the samples have been spin-coated with PMMA or ZEP electron beam resist which has afterwards been structured by EBL, including electron beam exposure and removal of the developed resist. The masks contain squares with edge lengths between 100 and 500 nm and circles with equivalent diameters. After removal of the developed resist, the mask structure has been transferred to the underlying Al or Ni layer by a RIBE process step. The samples with processed implantation masks have then been implanted with different III/V ion combinations, including P^+/In^+, As^+/In^+, Sb^+/In^+ and As^+/Ga^+. The implantation fluences have been set at 2×10^{16} or 3×10^{16} ions/cm^2 and the implantation energies have been chosen to result in a projected range 30 nm below the SiO_2/Si interface or centred in the Si device layer for the Si and the SOI substrates, respectively (see tables A.3.1 and A.3.2). After the implantation, the implantation mask has been removed by wet chemistry. Finally, the samples have been thermally annealed with FLA at various energy densities.

5.3.2 Locally implanted samples

Figure 5.3.1 displays the Raman spectra of the Si (a) and SOI (b) samples implanted through an Al implantation mask. In the spectra of the unimplanted areas (black), only phonon modes of crystalline Si are observed which are accounted to the undamaged substrate materials. These typical c-Si phonon modes are also present in the implanted samples but the characteristic phonon modes of the III-V compounds can

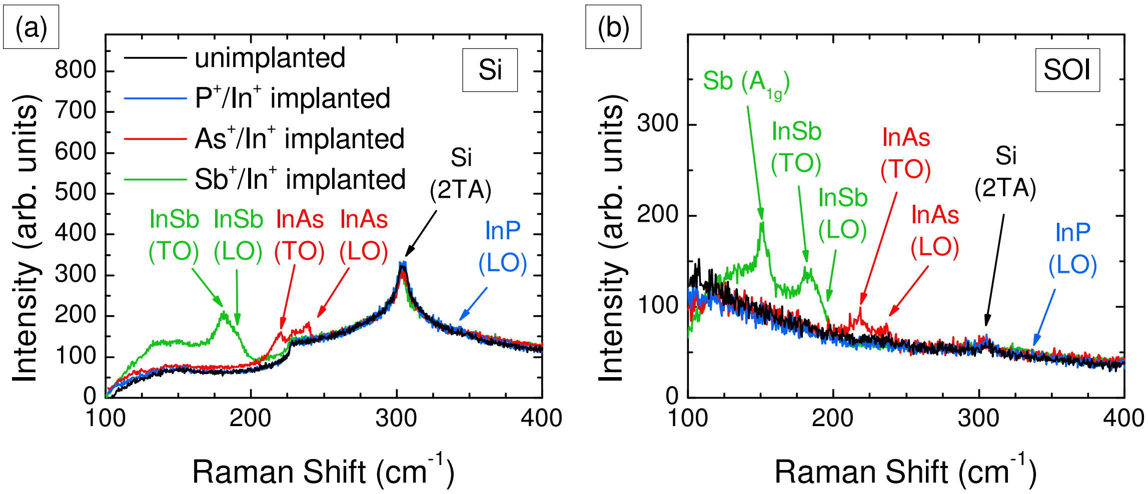

Figure 5.3.1: Raman spectra of Si (a) and SOI samples (b) implanted with As$^+$/In$^+$ (red), P$^+$/In$^+$ (blue) and Sb$^+$/In$^+$ (green) through an Al mask. The samples have been FLA treated at a σ_{FLA} of 63.3 J/cm^2 and 97.2 J/cm^2 for Si and SOI samples, respectively. The black curves show the Raman spectra taken from an unimplanted area on the same samples.

be observed, too. For both matrices, the Raman peaks of crystalline InAs (red) and InSb (green) are detected at 219 cm^{-1} (TO) and 237 cm^{-1} (LO), and at 179 cm^{-1} (TO) and 190 cm^{-1} (LO) [435], respectively. However, the InP phonon modes are barely visible. In contrast to previous measurements of planarly implanted sample, the intensity of the III-V phonon signals compared to the Si phonon modes is reduced which is due to the smaller volume fraction of the III-V NCs. Nevertheless, the observation of the characteristic III-V phonon proves the formation of III-V NCs in spatially confined areas and, therefore, a successful implementation of the implantation mask.

The top-view SEM image in figure 5.3.2(a) shows several implantation windows of a SOI sample locally implanted with As$^+$ and In$^+$ ions. The implanted squares (red box) had an edge length of 500 nm and a spacing of 500 nm between each window. In every square, a few bright spots reside after FLA treatment representing the InAs NCs. Outside of the implantation windows, no InAs NCs have been observed, proving the possibility to control NC position by masked implantation. However, within the implantation windows, the NCs have no fixed position. In the dark-field STEM image (b), the cross-section of a single window is depicted. The implanted part of the Si device layer has an increased height due to swelling caused by the implanted ions. At the edge of the window, a big high-contrast feature is located. The HRTEM image (c) of the interface region of the big precipitate and the unimplanted Si shows crystalline lattices of high order. However, the NC contains a high number of stacking faults while the Si part is less distorted. By analysing the FFTs of the NC (d) and Si (e), both regions show a fcc lattice structure in the [011] zone axis and the NC can be identified as InAs by determining the lattice plane distances. The InAs FFT is tilted by an angle of 72.5° towards the Si spot pattern. Since the Si initially has [100] orientation towards the surface, the InAs NC appears to be in [113] orientation towards the surface. The extension of the InAs NC over the edges of the implanted area is accounted to the straggling of the ion beam inside the Si layer during implantation.

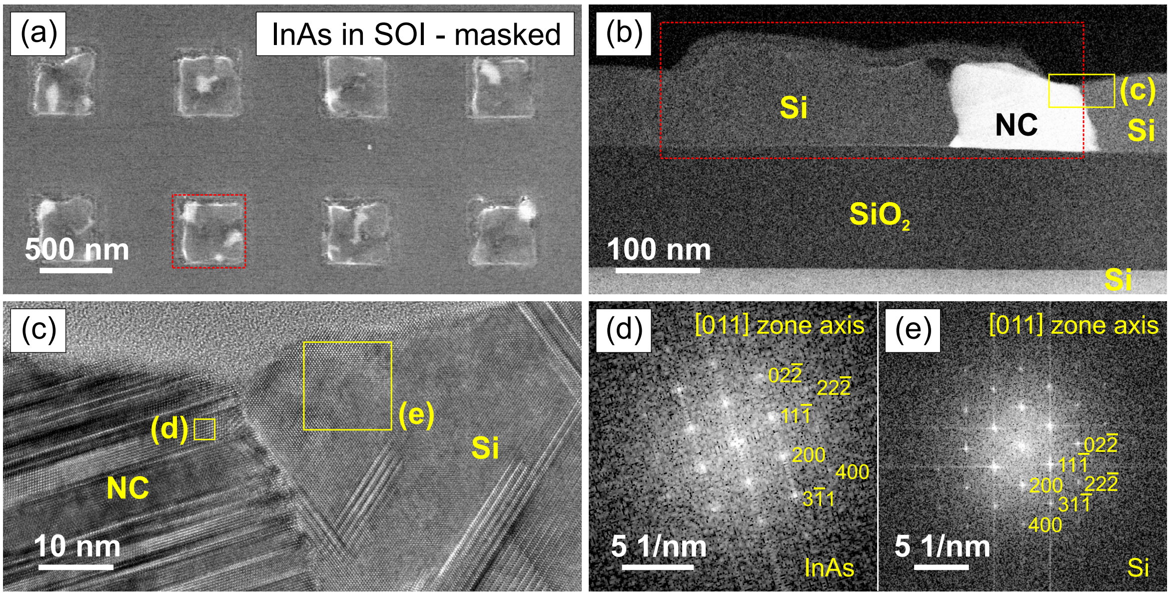

Figure 5.3.2: Top-view SEM (a), dark-field STEM (b) as well as HRTEM image (c) and corresponding FFTs (d, e) from a SOI sample implanted with As$^+$/In$^+$ through a Al mask and treated with FLA at a σ_{FLA} of 97.2 J/cm^2. The red boxes mark the size of the implanted area.

As there are several NCs per implantation window with a window size of 500 nm, another experiment has been conducted to find a correlation between window size and the number of NCs per window. Figure 5.3.3(a) displays the top-view SEM micrograph of a SOI sample implanted through a Ni mask with six different window sizes (red boxes). Similar to the 500 nm windows of the previous samples, the 460 nm windows contain several precipitates. For the smaller ones, the number of NCs is either one or two. In the smallest implantation windows with a edge length of 190 nm, no NCs are observed. In figure 5.3.3(b), the cross-section through such a set of window sizes is depicted by a dark-field STEM image. Besides the characteristic layer structure of the SOI substrate, the InAs NCs are seen within the thin Si device layer for the larger window sizes. For the smaller ones, InAs precipitates are not seen, which is either due to their absence or that during TEM lamella preparation the cut did not go through a NC. Another feature seen in the STEM image is the large sputtering crater for the larger window size which is almost not present for the smaller ones. For a statistical analysis of the NC number per implantation window in dependence on the window size, the SEM images have been used to count the number of NCs in several hundreds of implantation windows of different size. The results are displayed in figure 5.3.3(c) and show a steady increase of the number of NCs per window with increasing size. Below 200 nm window edge length, in less than 20 % of the implantation windows there are precipitates at all. Between 285 and 385 nm window size, there is about one NC per implantation window which is the optimal result. In windows larger than that, generally more than on NC is present in a single implantation window which is not suitable for further processing.

In figure 5.3.4(a), an enlarged dark-field STEM micrograph of the implanted 460 nm window is depicted. In the thin Si device layer, a relatively large precipitate is visible due to the high mass contrast. The precipitate is located in the centre of the implan-

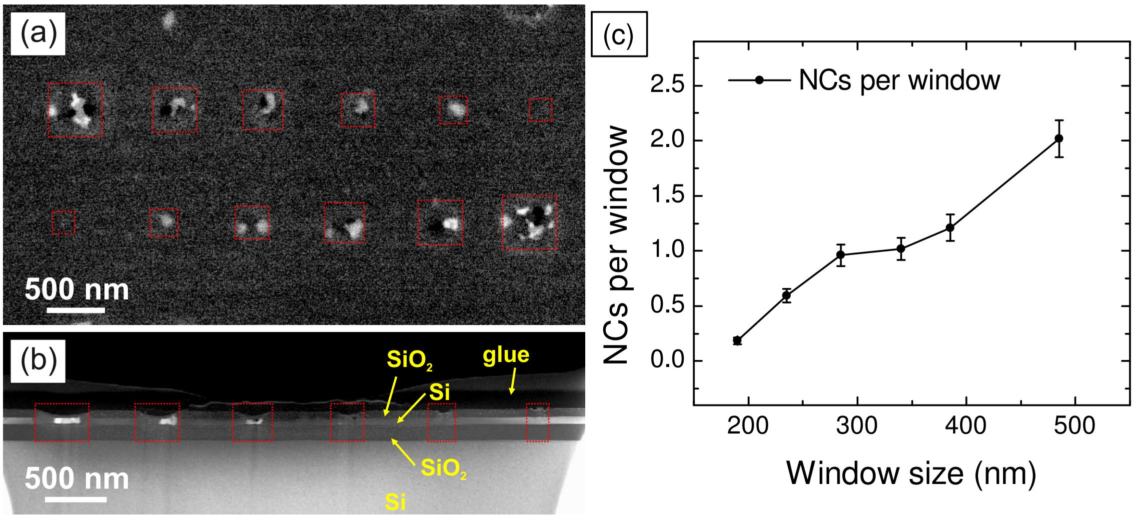

Figure 5.3.3: Top-view SEM (a) and dark-field STEM (b) micrographs from a SOI sample implanted with As^+/In^+ through a Ni mask with different window edge lengths. The red boxes mark the size of the implantation windows, from the left to the right: 460 nm, 385 nm, 340 nm, 285 nm, 235 nm and 190 nm. (c) Evaluation of number of NCs per implantation window for the particular window size.

tation window which is marked by the red box and has a height of about 52 nm limited by the adjacent Si/SiO_2 interfaces. Besides the big precipitate, there are also small precipitates with circular shape in the surrounding SiO_2 layers. Additionally, there is a strong swelling effect of the thin Si device layer at the edge of the implantation window resulting in a maximum extension of 87 nm which is an increase of about 46 % regarding the initial layer thickness of 60 nm. Furthermore, there is a strong sputtering effect reducing the thickness of the SiO_2 capping layer within the implantation window from 65 nm to about 22 nm. Both effects are characteristic for a high fluence ion implantation. In order to get information about the elemental composition of the implanted region, an EDXS element mapping has been performed in the area marked by the yellow box. Figure 5.3.4(b) depicts the combined EDXS element map including the investigated elements Si, O, In, As and Ni which are individually shown in figures 5.3.4(c-g), respectively. The combined element map reflects the SOI layer structure nicely by the green (Si) and orange (SiO_2) regions. The big precipitate in the Si device layer is well separated from the surrounding Si but shows three distinct segments, two blue and one pink. Looking at the individual element maps, the two blue segments can be attributed to a high concentration of In (e) and As (f) in combination with the absence of Si (c) whereas the pink segment is due to high concentrations of Si (c) and Ni (g). Therefore, the blue segments represent InAs NCs while the pink segment is a nickel silicide precipitate. In the other implantation windows, the formation of such precipitates have been observed as well (not shown). The nickel silicide phase forms since there is Ni available in the Si layer after ion implantation. The Ni is probably introduced by sputtering and redeposition from the masking layer during the implantation step causing an intermixing of Ni and the thin Si layer. This effect has not been observed for the samples masked by an aluminium layer although it might be probable as well. Therefore, implantation masks made of metals have to be evaluated

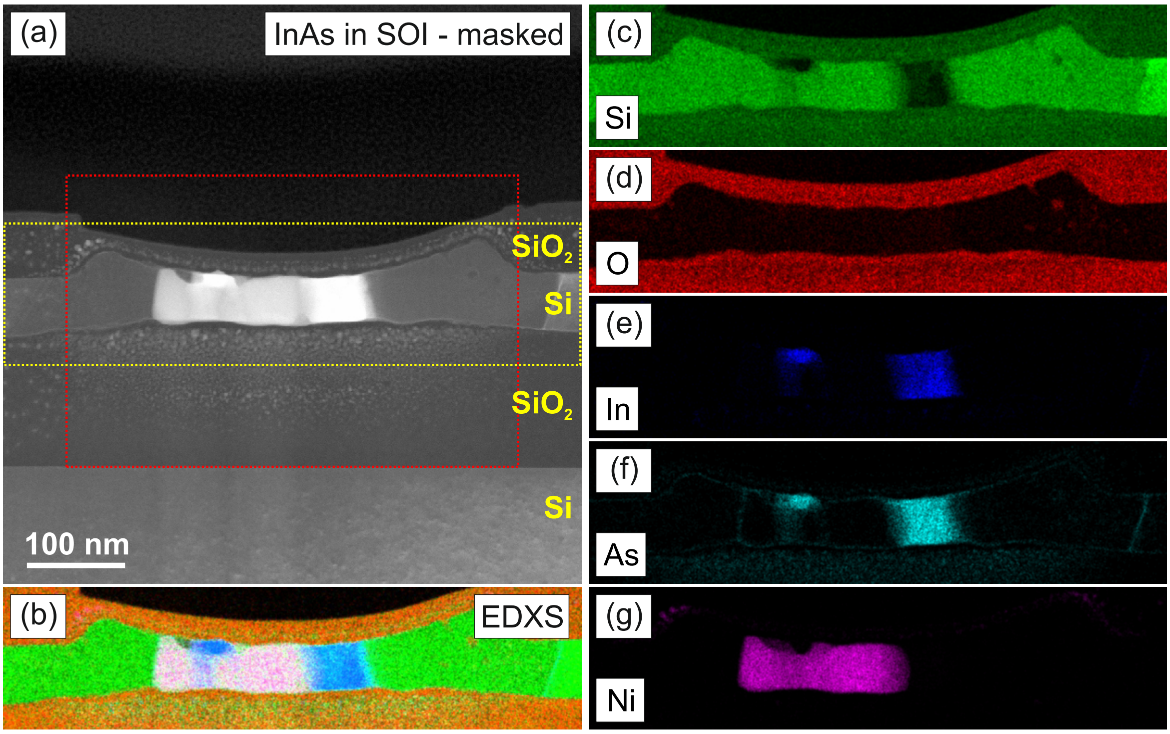

Figure 5.3.4: Dark-field STEM image (a) and corresponding EDXS (b-g) element maps taken from the area marked by the yellow box from a SOI sample implanted with As^+/In^+ through a Ni mask. Implantation window edge length is 460 nm. (b) Combined EDXS element map and single EDXS element maps of (c) Si, (d) O, (e) In, (f) As and (g) Ni.

critically. Finally, the EDXS element maps show that the small circular precipitates in both SiO_2 layer are also composed of In and As indicating InAs NC formation as already observed in the planarly implanted thin layer samples (see section 5.2).

6 Qualitative model for III-V nanocrystal formation in silicon

6.1 General mechanism in bulk materials

Figure 6.1.1 schematically depicts the general formation mechanism of III-V NCs in bulk substrates by liquid phase epitaxy (LPE) and will be described in the following for Si bulk material. After ion implantation, the group-III and -V ions show a Gaussian-like depth profile (a) close to the interface between the SiO_2 capping layer and the Si substrate, as it has been simulated by SRIM (see figure 4.1.2(a)) and measured by RBS (see figure 5.2.14(b)). Due to the high implantation fluence, the upper part of the Si substrate gets amorphized up to a depth of about 150 nm but the deeper regions remain crystalline resulting in a SiO_2/a-Si/c-Si layer stack. The subsequent FLA treatment at high energy densities heats up the surface of the sample and is sufficient to melt the amorphous Si. The underlying crystalline Si bulk material is unaffected and remains in the solid state, as its melting point is about 200 K higher than that for a-Si [130, 143]. This melting point difference is even larger due to the melting point depression by the implanted impurity atoms. In the liquid Si phase, the diffusivity of group-III and -V atoms is increased by several orders of magnitude, e.g. eight orders of magnitude for As (see table 2.2.1), compared to the diffusion in solid Si close to the melting point (1400 °C). Therefore, the mean diffusion length of the implanted ions is much larger than the vertical dimension of the liquid region even for the small time-scale of the FLA pulse. This leads to a homogeneous distribution of the implanted species over the whole molten region within the period of the FLA pulse (b). Immediately after the FLA pulse, the sample starts to cool down. The liquid Si phase recrystallizes because its temperature is lower than the melting point of c-Si and an under-cooled melt is present (c). Herevy, the crystalline Si substrate is acting as a seed layer for epitaxial regrowth. At the liquid/solid interface, an enrichment of group-III and -V atoms in the melt takes place due to segregation since the segregation coefficients of the group-III and -V elements are generally below one. With progress of the crystallization front, a high concentration region of III/V material is pushed ahead and due to their high diffusivity, the concentration of III/V atoms in the whole liquid phase increases constantly with time.

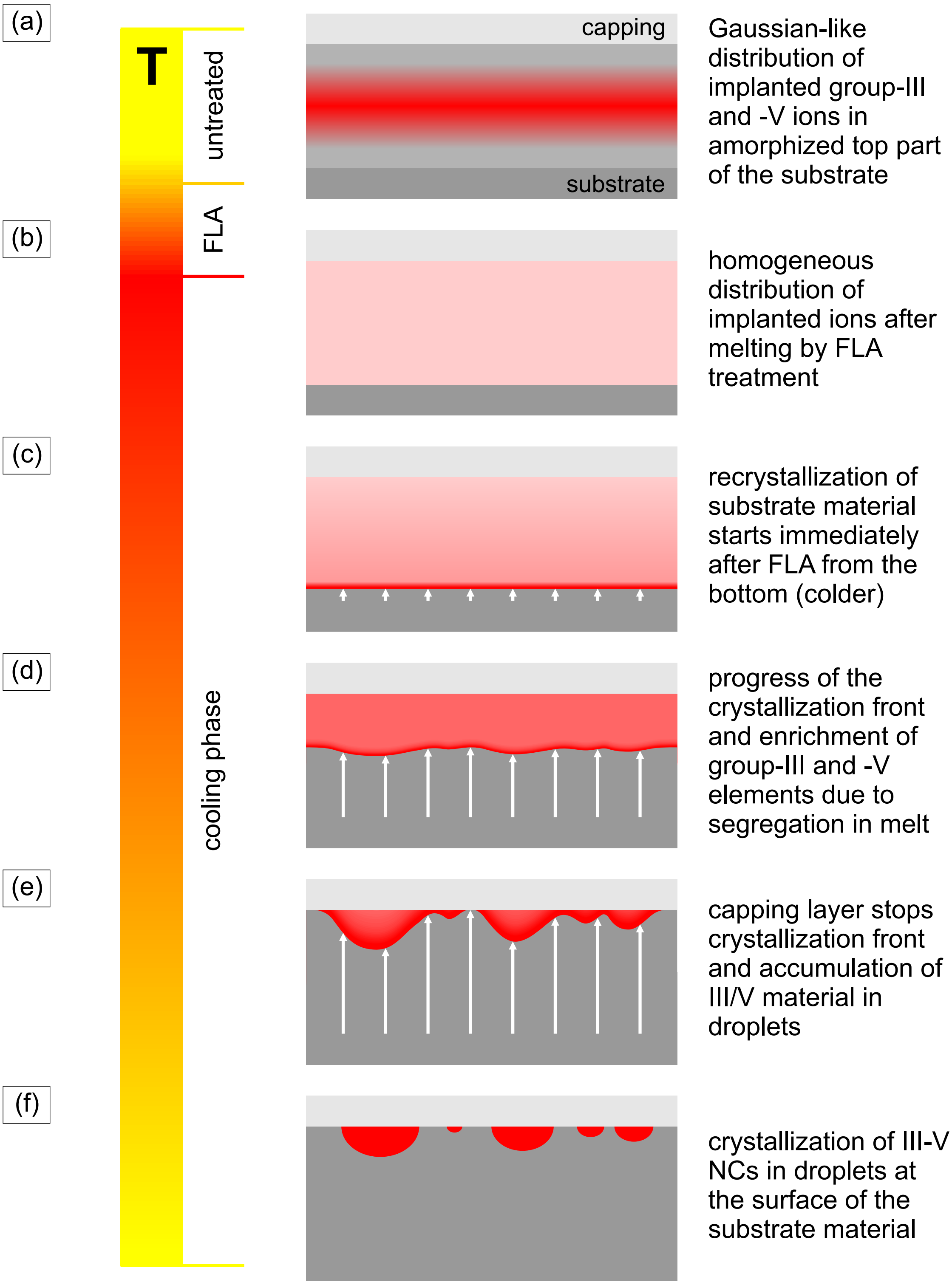

Gaussian-like distribution of implanted group-III and -V ions in amorphized top part of the substrate

homogeneous distribution of implanted ions after melting by FLA treatment

recrystallization of substrate material starts immediately after FLA from the bottom (colder)

progress of the crystallization front and enrichment of group-III and -V elements due to segregation in melt

capping layer stops crystallization front and accumulation of III/V material in droplets

crystallization of III-V NCs in droplets at the surface of the substrate material

Figure 6.1.1: LPE formation mechanism of III-V NCs in bulk substrates.

During further cooling, the crystallization front moves towards the surface and the III/V concentration in the melt rises steadily (d). There will be regions where the crystallization is faster than in other regions which leads to an uneven crystallization front with wells. This can be caused by defects, local temperature fluctuations or local differences in the crystallization temperature of the melt due to III/V concentration fluctuations. When the crystallization front reaches the interface to the capping layer, the vertical crystallization is stopped and the phase transformation continues laterally (e). Hereby, the melt gets separated into droplets of different sizes where the III/V material is accumulated. Finally, the liquid phase mainly consists of III/V material and when the temperature decreases below the melting point of the particular III-V compound semiconductor, the III/V melt starts to recrystallize as well (f). During this III-V recrystallization, the recrystallized Si substrate acts as a template for the epitaxial formation of III-V NCs. Their shape and size is governed by the droplets resulting in mainly hemispherical precipitates of various sizes which are located directly at the interface to the capping layer, as it can be seen in figures 5.1.5 and 5.1.7. Furthermore, the size of the final NCs, or more precisely, the mean value of the size distribution is also strongly dependent on the implantation fluence of the particular ions. A higher implantation fluence leads to a larger amount of the consumable III/V material which, in turn, results in larger III-V NCs.

6.2 Influence of the substrate type

Thin layer system

For a thin layer system, the LPE mechanism is similar to the formation process in bulk materials except that there is no initial crystalline template for the recrystallization of the thin layer after melting. As depicted in figure 6.2.1(a), the implanted group-III and -V ions have a Gaussian-like depth profile centred in the thin Si layer surrounded by two SiO_2 layers. When the FLA pulse is applied, the implanted thin Si layer melts and the III/V ions get homogeneously distributed due to their high diffusivity (b). Since the whole Si layer is molten, no crystalline Si remains and there is no template for epitaxial regrowth. However, the temperature of the alloyed, liquid Si phase is below the melting point of crystalline Si which leads to the spontaneous formation of Si seeds preferably at the interfaces (c). These Si seeds grow radially with further cooling and form larger grains. Considering the segregation of the III/V ions, the Si grains push a III/V enriched region ahead, leading to an increase of the overall concentration of the implanted species in the melt (d).

With time, the Si grains expand until they come into contact with other Si grains or the surrounding SiO_2 layers. When this happens, the crystallization is stopped in this particular direction but continues along the respective interface region until another barrier appears (e). The SiO_2 layers limit the maximum height of the Si grains to the layer thickness of the Si layer but their lateral size varies over a wide range. In between the Si grains, the III/V material is accumulated and when the temperature is low enough, III-V NCs start to crystallize (f). In contrast to bulk material systems, the crystalline Si grains acts as epitaxial template for the III-V NC growth. However, due to the spontaneous formation of the Si seeds after the FLA pulse, the Si grains have different orientations. Obviously, a III-V NCs starts to crystallize epitaxially on

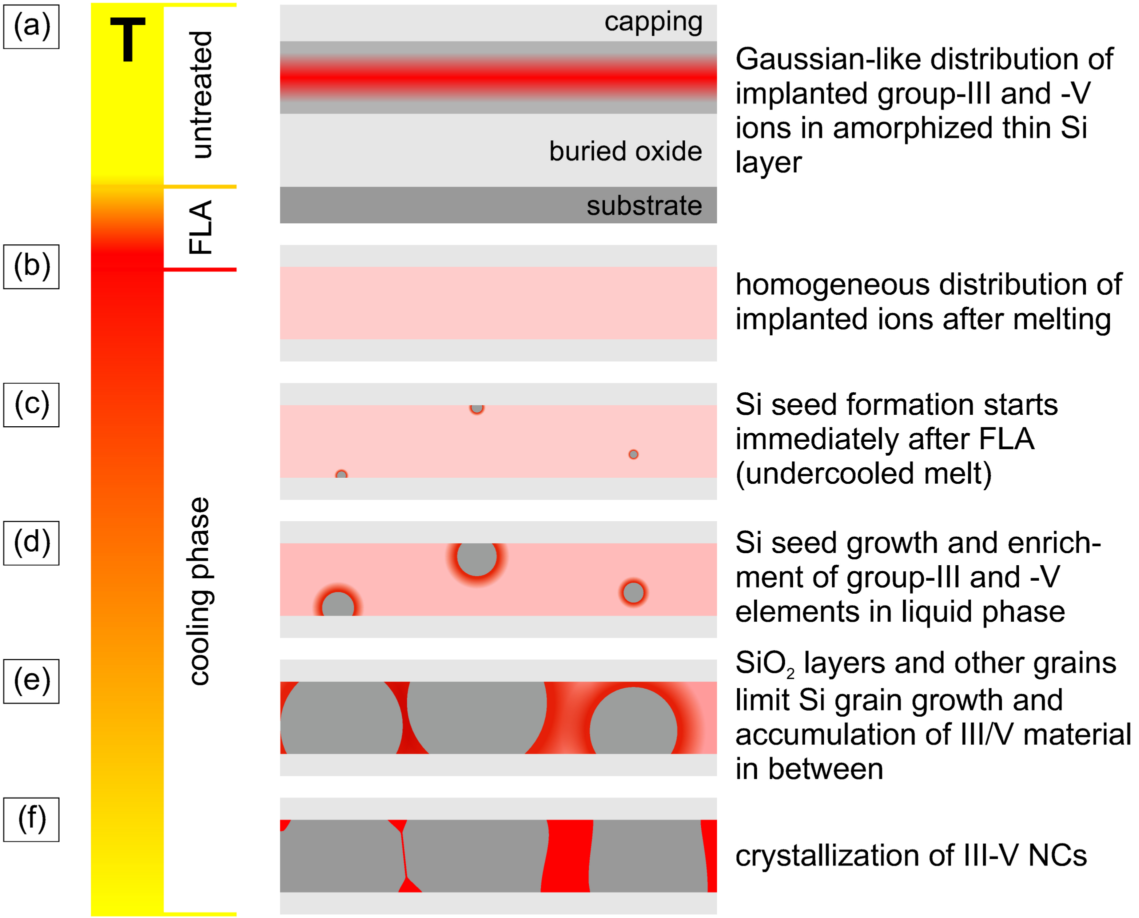

Figure 6.2.1: LPE formation mechanism of III-V NCs in thin film substrates.

only one particular Si grain and, therefore, gets a specific orientation. When this III-V NC reaches the next Si grain, there probably is a difference in the crystal orientation and the interface region is disordered.

The size and shape of the III-V NCs can be manifold and strongly depends on the space between the Si grains. If the Si grains are in direct contact to each other, the III-V precipitates are located at the Si/SiO_2 interfaces and feature triangular shapes, e.g. in figure 5.2.3(a). Eventually, the interface region of the Si grains gets decorated by the III/V material and a filament forms connecting two of these triangular shaped NCs, as it can be observed in figure 5.2.4(a). When the space between two Si grains is larger, block-like III-V NCs form, e.g. depicted in 5.2.2(c) and (d). These block-like III-V precipitates are limited in height by the surrounding SiO_2 layers. Therefore, the NC height is controllable by choosing the proper Si layer thickness and by considering the swelling due to ion implantation. However, the lateral dimension of the NCs varies over a wide range but depends on the available III/V material which is connected to the implantation fluence, as already mentioned for bulk systems. Using a higher implantation fluence leads to a larger mean lateral size of the NCs, see also [392]. Comparing the two different starting materials, SOI wafers and the PECVD-grown layer system, the difference in the crystalline quality of the NCs might be accounted to quality of initial thin Si layer, although this is unlikely as the implantation fluence in both cases is sufficient to amorphise the thin Si layer. However, the H-content in the PECVD-grown Si layer negatively affects the recrystallization process after FLA.

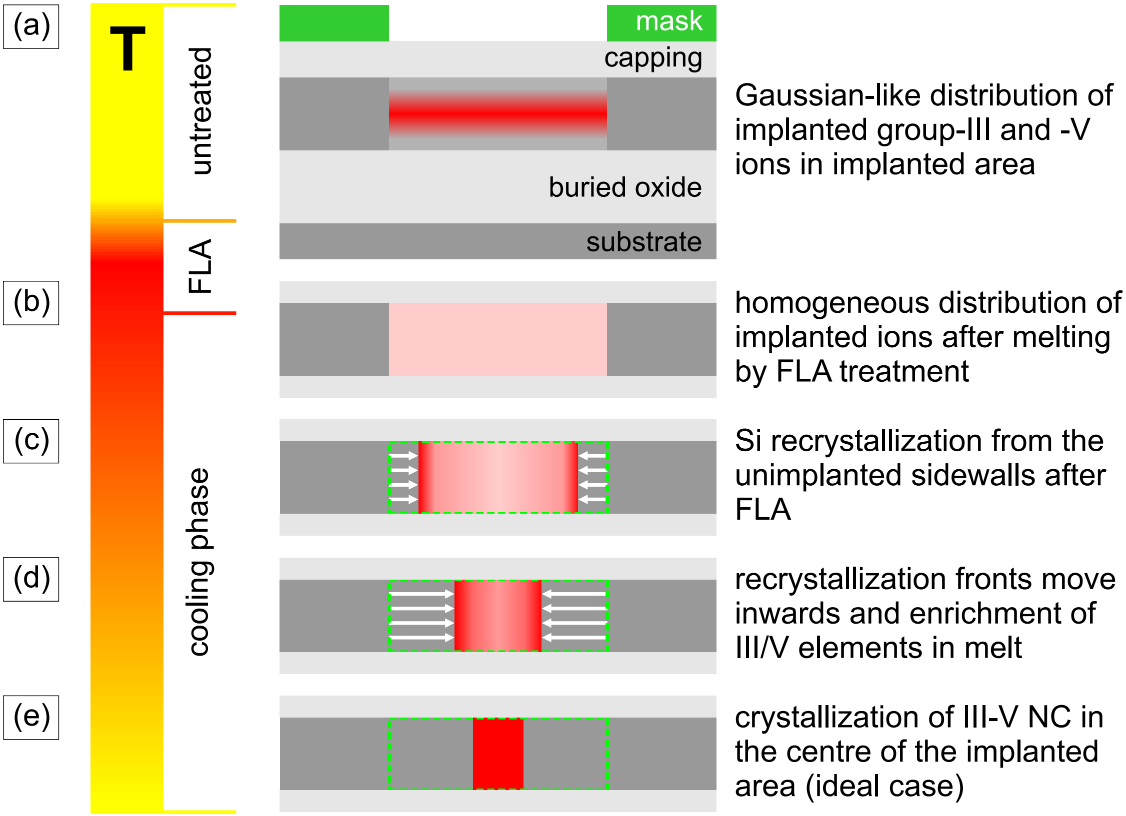

Figure 6.2.2: LPE formation mechanism of III-V NCs in thin film substrates implanted through a mask.

Local implantation into thin layers

When the thin SOI layer system is implanted through a mask, only the implanted areas are amorphised while the unimplanted regions remain crystalline. The LPE formation mechanism is similiar to the mechanisms in bulk material and planarly implanted thin layers. After masked implantation, the III/V ions obtain the typical Gaussian-like depth profile, but only in the uncovered areas, as depicted in figure 6.2.2(a). The FLA treatment, which is applied after mask removal, leads to the melting of the implanted regions but does not affect the crystalline part of the thin Si layer as $T_{\mathrm{melt}}^{\mathrm{a\text{-}Si}} < T_{\mathrm{FLA}} < T_{\mathrm{melt}}^{\mathrm{c\text{-}Si}}$. Due to their high diffusivities, the group-III and -V specimen are homogeneously distributed in the locally confined volume of the implantation window (b). In contrast to the planarly implanted thin layer system, the unaffected crystalline Si regions act as template for the epitaxial Si recrystallization of the alloyed Si melt. Therefore, the recrystallization starts at liquid/solid interface at the sidewalls of the implanted areas immediately after the FLA pulse (c). During cooling, the crystallization fronts move towards the centre of the implanted area and similar to the other systems, the concentration of the III/V elements within the liquid phase increases due to segregation (d). Finally, the III-V material crystallizes epitaxially on the recrystallized Si and a III-V NC is formed within the implantation window (e).

Considering the ideal case, a single III-V NC should form per implantation window, located directly in the centre of this window and with a height determined by the layer thickness of the Si device layer. In general, the ideal case is not met and there are more than one NC and they have a random position within the implantation windows, see figure 5.3.3(a). The positioning of the III-V NCs depends mainly on the progress of the Si crystallization fronts during cooling. If these fronts would move smoothly from the edges towards the middle, all the III/V material would be accumulated in the centre of the implantation window. However, the movement of the crystallization fronts can be distorted by various factors. For example, a minimal time delay of the beginning of recrystallization at the different edges would lead to a shift of the NC towards one edge. Additionally, the progress of the recrystallization fronts can be affected by defects, local fluctuations in temperature or III/V concentration, similar to bulk materials. Furthermore, the spontaneous formation of Si seeds in the molten phase and their growth during cooling, as described for the thin layer systems, influences the final position of the III-V NCs as well. The number of III-V precipitates depends strongly on the amount of available group-III and -V material for NC formation which is defined by the size of the implantation windows. If the implantation window is too small, there is not enough III/V material to form a NC extending over the whole layer thickness. On the opposite side, if the windows are too large, the effects influencing the crystallization front progress have a larger impact, especially the Si seed formation. The Si seed formation and the grain growth leads to the formation of separated regions of III/V enriched Si melt, which finally results in the crystallization of multiple III-V NCs within one implantation window.

6.3 Influence of the diffusivity

Diffusion plays a crucial role in the presented LPE formation mechanism. It is the main physical process responsible for the homogeneous distribution of the implanted ions in the molten phase after FLA treatment. Due to the high diffusivities of the group-III and -V elements in liquid Si, their diffusion length L_D, defined by equation (2.7), is much larger than the extension of the molten region. These large diffusion lengths, i.e. L_D of As in liquid Si for the 20 ms period of the FLA treatment is 25.7 µm, ensure a homogeneous distribution of the implanted ions.

Moreover, the size of the III-V NCs fabricated during this work demands large diffusion lengths, since the number of atoms necessary to form these large NCs cannot be accumulated by diffusion in the solid phase on the time-scale of the FLA treatment. Assuming a NC with hemispherical shape, as observed in bulk materials, the volume V of this NC can be calculated by

$$V = \frac{\pi \cdot s}{6} \cdot (3 \cdot R_\mathrm{cap}^2 + s^2) \text{ (spherical cap)}, \tag{6.1}$$

where s is the NC height and R_cap is the radius of the base of the NC approximated by a spherical cap. When the volume is known, the number of atoms within the NC can be determined by considering the atomic density of the particular III-V compound. By comparing the number of atoms within the NC with the III/V concentration in the alloyed Si solution, the volume of the virtual region, where the III/V atoms have to be consumed from for the formation of the NC, can be estimated. The extension of this accumulation region is a measure for the maximum distance the respective III/V atoms have to diffuse in order to form the NC. By comparing this distance with the diffusion lengths in solid and liquid Si, a solid phase formation process can be excluded.

For an exemplary calculation, see Appendix A.1. Furthermore, the diffusion lengths of the implanted group-III and -V ions in the solid phase are smaller than the dimensions of the formed NCs, which supports the liquid phase process even more. The difference in the diffusivities of the particular group-III and -V elements in liquid Si is relatively small and, therefore, does not play a major role since the diffusion lengths are much larger than the extension of the accumulation volume.

Additionally, the diffusion in the solid phase prior to FLA does also influence the formation process. Directly after ion implantation, the implanted ions diffuse within the bulk material. However, this diffusion is generally very slow as the temperature is low and the diffusion coefficients are also small. Nevertheless, there are two exceptions, namely N and P, which feature relatively high diffusion coefficient in solid Si. Therefore, a considerable diffusion is expected already before the samples are exposed to the FLA treatment and for N an additional strong outgassing is expected. This effect influences the amount of these two species consumable for III-V NC formation in the end which leads to small NCs for P-implanted samples while for N-implanted samples NC formation has not been observed.

6.4 Influence of the segregation coefficients

Another factor influencing the III-V NC formation mechanism is segregation since it is responsible for the accumulation of the III/V elements in the liquid phase. This accumulation is due to the segregation coefficients of the group-III and -V elements being below one, see table 3.1.1. For example, k_{As} is 0.35, which means that most of the As impurities will remain in the liquid phase when the Si recrystallizes. The concentration of the III/V material in the Si melt will steadily increase. In the end, the liquid phase actually becomes a III-V melt containing Si impurities which will then form a III-V NC doped with Si. The amount of group-III and -V elements accumulated in the liquid phase defines the amount of III/V material that can be consumed for III-V NC formation. A segregation coefficient which is closer to zero leads to a stronger accumulation of the particular group-III or -V element in the liquid phase, which in turn results in a higher number and/or a larger average size of the final NCs.

Comparing the segregation coefficients of elements of group III and V, the group-III elements feature segregation coefficient which are closer to zero. This leads to an imbalance in the III/V concentration in the liquid phase which is strongly on the side of the group-III elements. As a consequence, the Si melt comprises an excess of group-III material. However, since the binary III-V compounds have a 1:1 III/V ratio, the excess will not be consumed in the NC formation process. In the case of In-containing samples, like InAs, the excess In forms metallic In clusters, as proven by the appearance of the In (101) and (110) Bragg peaks in XRD measurements of figure 5.2.5. For Ga-containing samples, Ga precipitates have not been detected, although its segregation coefficient is also smaller than that for the respective group-V elements.

For the ternary III-V compounds, the difference in the segregation coefficients of the two group-III components may affect the final constitution of III-V NC as well. However, the concentration of the group-V element is the limiting factor, since it will always be smaller than the concentration of the group-III elements. In the case of

$In_xGa_{1-x}As$, the ratio of the segregation coefficients would favour an In-rich nature of the NCs, theoretically, as the segregation coefficient of In is about 20 times smaller than that of Ga but the experiments show Ga-rich $In_xGa_{1-x}As$ precipitates. Therefore, another physical effect must be responsible for the final constitution.

6.5 Influence of the III-V melting point

The melting point of the III-V compound semiconductor mainly determines the point in time when the III-V NCs start to recrystallize during cooling after FLA. As the melting points of the III-V compounds are in general at lower temperatures than that of Si, see table 3.1.1, the recrystallization of Si starts earlier. There are two exceptions, the first is GaN which has a melting point which is much higher than that of Si and the second is GaP whose melting point is higher but close to that of Si. For GaN, no NCs have been observed which is mainly accounted to the diffusion of N in the solid phase after ion implantation that there is not enough N present to be consumed for NC formation. However, the high melting point makes it also improbable that NCs would form even when there would be enough N. For GaP, the difference between the melting points of GaP and Si is small and both substances are in an undercooled melt, which probably leads to a simultaneous seed formation of Si and GaP. Therefore, the GaP NCs have only small sizes as the melt is not enriched as much as for the III-V compounds with lower melting points.

For the other materials, the difference between the melting points of the III-V compound and Si is determining the delay between the start of the Si recrystallization and the formation of the III-V NCs. When this difference is larger, the III/V material will stay longer in the liquid phase and the recrystallized Si areas grow larger. This leads to the formation of a low number of bigger III-V precipitates for high melting point differences, while for low melting point differences, a high number of smaller precipitates is formed. When comparing InAs and GaAs, the melting points are 948 °C and 1241 °C, respectively. Therefore, the GaAs NCs start to crystallize earlier than the InAs NCs, which leads to a smaller mean size of the NCs but a higher number of these precipitates, as it is depicted in the SEM micrographs of figure 5.1.4 as well as in the particular particle size distributions of these two samples. The discrepancy between the melting points of these two III-V compounds is also the reason for the formation of mainly Ga-rich $In_xGa_{1-x}As$ NCs for the ternary case. As a Ga-rich $In_xGa_{1-x}As$ phase has a slightly higher melting point than an In-rich phase, it starts to form earlier and then grows by incorporating surrounding III/V material by retaining its chemical composition. Therefore, more Ga is present within the $In_xGa_{1-x}As$ NCs and the excess In forms metallic precipitates.

6.6 Influence of the substrate material

For different substrate materials, the previously mentioned parameters are also affecting the NC formation process in a similar way. However, the properties of the substrate material can also have another impact on the III-V NCs. By comparing Si and Ge, two important properties are the different melting points and lattice parameters. The first has a similar influence than the melting point of the particular III-V compound. As the melting point of Ge is lower than that of Si, lower energy densities are necessary and the temperature of the liquid phase is lower. Therefore, the melting point of the GaAs is not surpassed and no GaAs NC formation could be observed. Additionally, the observation of two kinds of InAs precipitates in Ge leads to the assumption that the InAs crystallization starts already before the Ge recrystallization is completed which is due to the low melting point difference.

The lattice parameter of the substrate material and the consequential lattice mismatch with the III-V compounds mainly influences the epitaxial growth of the III-V NC, its crystalline orientation and the interface quality. For example, the lattice mismatch of InAs to Si and Ge is 11.6 % and 7.1 %, respectively. In the case of Ge, this lattice mismatch is below the limit of pseudomorphic growth [261, 262], which means that the InAs NC epitaxially grows with the same crystalline orientation as the Ge substrate material. In Si, this limit is exceeded and the InAs NC epitaxially grows with a different crystalline orientation than the Si substrate in order to reduce strain.

7 A future perspective - A III-V nanocluster within a Si nanowire

7.1 Preliminary results - Nanowire fabrication

7.1.1 ZEP-based process

In order to integrate III-V NCs into Si NWs, a top-down NW preparation process has been developed and is schematically depicted in figure 7.1.1. Initially, a SOI substrate is spin-coated with a negative resist (ZEP-520) and exposed to EBL. After development of the exposed resist, a Ni layer is deposited by electron beam evaporation. In the following lift-off step, the Ni NW hard mask is prepared which is then used for the RIE of the Si device layer. Finally, the Ni hard mask is chemically removed to uncover the Si NWs.

Figure 7.1.2 shows the Ni hard mask for Si NW preparation after lift-off of the deposited Ni layer with low (a, 307x), medium (b, 13640x) and high magnification (c, 115760x). For the two lower magnifications, the Ni NWs appear as sharp and straight lines, however, for the highest magnification, the grain structure of Ni is visible and the NWs show a certain edge roughness. The Ni NWs have a width between 55 and 60 nm which is in good agreement with the intended width of 60 nm.

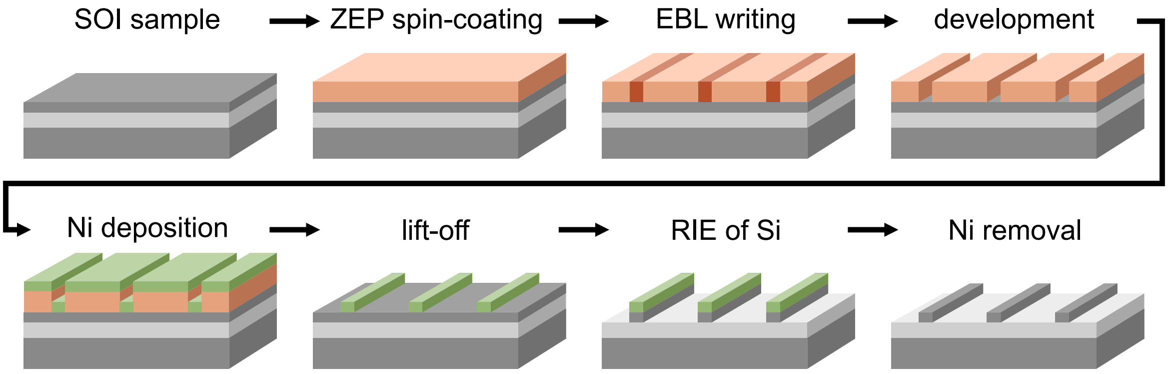

Figure 7.1.1: Preparation process flow schematic for Si NWs by using a Ni hard mask.

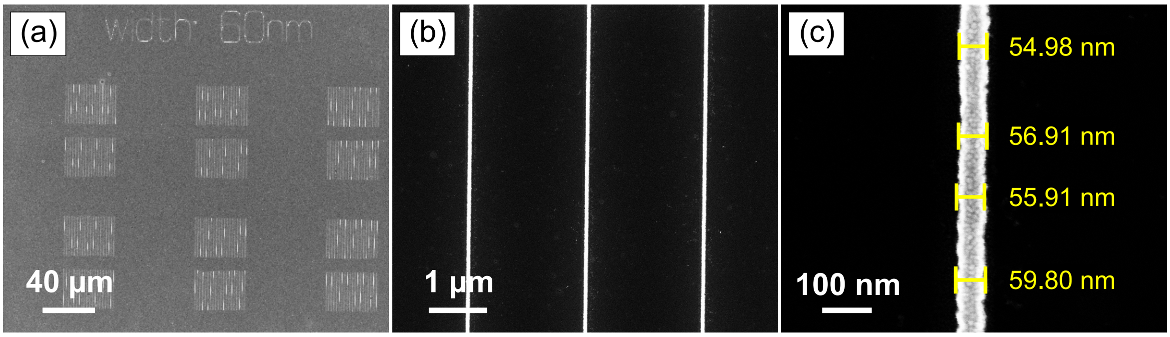

Figure 7.1.2: Top-view SEM micrographs of the Ni mask for Si NW preparation with different magnifications.

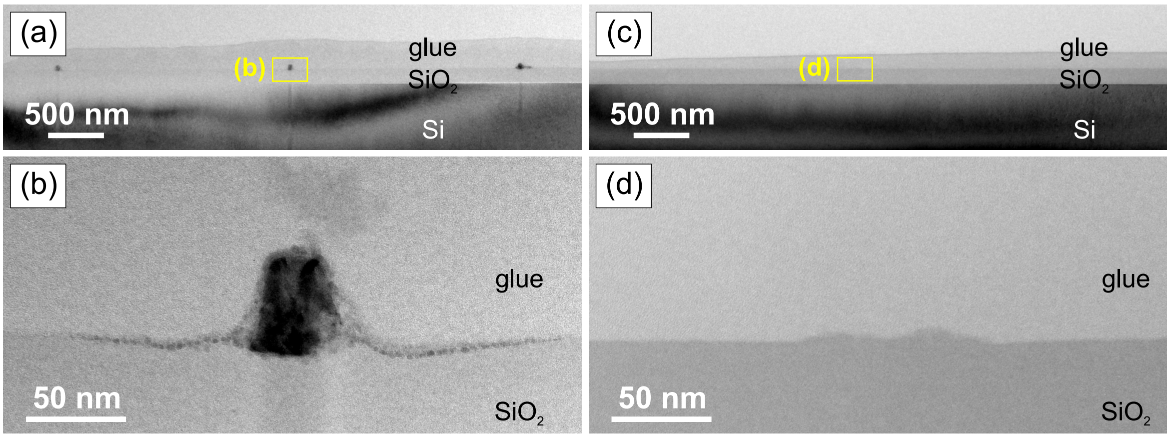

Figure 7.1.3: Cross-sectional TEM micrographs of Si NW samples prepared by using a Ni hard mask after first RIE test. (a, b) Before Ni removal. (c, d) After Ni removal.

This Ni hard mask has been used for a RIE recipe test cycle. During the first RIE recipe test, the samples has been etched for 30 s with a RF power of 50 W and an ICP power of 150 W. In the cross-sectional TEM micrographs of figure 7.1.3, the NW samples after the first RIE recipe test before (a, b) and after Ni removal (c, d) are depicted. Before Ni removal (a), three NWs can be seen on top of the SiO$_2$ layer and the magnification of the central NW (b) shows a trapezoidal NW cross-section and some small decorations of the SiO$_2$ surface close to the NW. After Ni removal, only the SiO$_2$ layer on top of the bulk Si substrate are observed. In the magnified cross-sectional TEM micrograph (d), the SiO$_2$ surface has only small imprints where the Si NW should have been. Obviously, there are no Si NWs after Ni removal. To identify the process step where the Si NWs are removed, an EDXS analysis of a NW structure before Ni removal has been conducted.

The results of this analysis are given in figure 7.1.4 showing the HAADF-STEM (a) micrograph and the corresponding EDXS element maps for Si (b), Ni (c) and Ag (d) of one of the NW structures which can be seen in figure 7.1.3(a). According to the HAADF-STEM micrograph, the NW cross-section gives a higher mass contrast than the underlying SiO$_2$ and the Si substrate. Besides the NW, there are also contaminations on both sides. The EDXS element maps identify the NW to be mainly made of Ni (b) whereas the spherical contaminations contain mainly Ag (d). These results

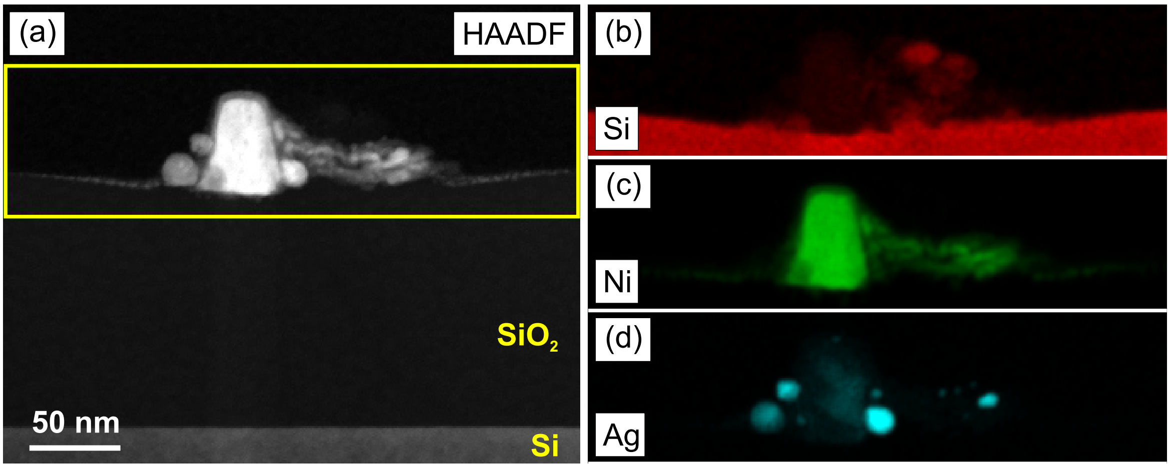

Figure 7.1.4: Cross-sectional HAADF-STEM image (a) and EDXS element maps (b-e) of a Si NW sample after first RIE test and before Ni removal.

show that the etch rate during RIE was too high and the Ni hard mask must have been under-etched.

With a RIE recipe optimization series, the etch rate has been decreased from about 35 nm/s achieved with the parameters from the first RIE test to about 3 nm/s by reducing the ICP power to 0 W. Figure 7.1.5 displays the SEM micrograph of the Si NW samples RIE etched with the optimized etch recipe before (a, b) and after Ni removal (c, d). The top-view SEM micrographs display straight NWs with a lot of contaminations on both sides before (a) and after Ni removal (c). Nevertheless, there are NWs after Ni removal. The tilted SEM micrographs (b, d) show steep

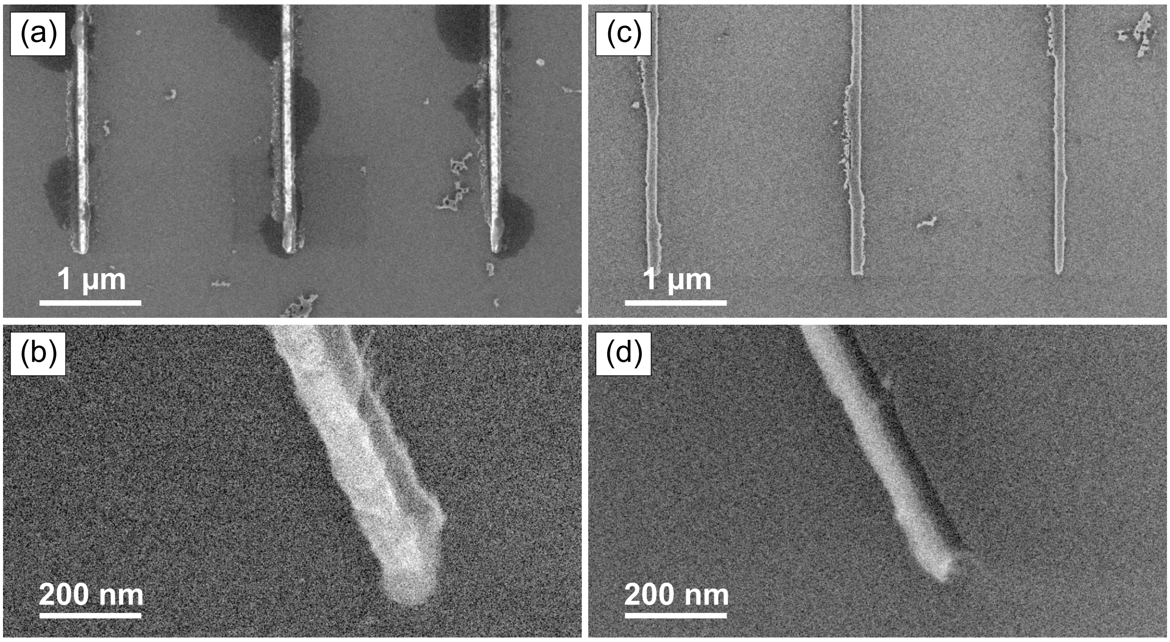

Figure 7.1.5: SEM micrographs of Si NWs, etched with optimised RIE recipe, before (a, b) and after (c, d) removal of Ni hard mask. (a, c) Top-view SEM micrographs with low magnification. (b, d) 30° tilted SEM micrographs with high magnification.

sidewalls which is accounted to a good anisotropy of the etching. With the optimized RIE etching recipe it is possible to fabricate Si NWs by transferring the EBL written structure of the Ni hard mask into a Si layer. However, the bad shape of the Ni hard mask resulting from the lift-off process is also transferred into the Si NWs which makes them unsuitable for further processing.

7.1.2 HSQ-based process

To avoid the lift-off process, a different Si NW preparation process has been introduced. By using a positive EBL resist (HSQ), as depicted schematically in figure 7.1.6, the additional Ni deposition as well as the lift-off step can be excluded. The HSQ resist is deposited on top of the clean SOI substrate by spin-coating. Afterwards the NW structures are directly written into the HSQ layer, transforming the HSQ into SiO_2. In the following step, the resist is developed by a NaOH/NaCl solution and only the EBL written NWs remain. In the subsequent RIE of Si, the NW pattern is transferred into the underlying Si layer. Finally, the residual SiO_2 (HSQ) can be removed by wet chemistry, which has to be done carefully in order to avoid the etching of the buried SiO_2 layer and accidentally remove the Si NWs.

Figure 7.1.7 displays the first results obtained with the HSQ-based Si NW preparation process after RIE. The top-view SEM image in figure 7.1.7(a) shows four bright lines with a length of 20 µm and a spacing of 10 µm in between representing the fabricated NWs. The magnification of one of these NWs is given in (b). The sidewalls of the NW are rough but look better than for the ZEP-based process. The width of the NW is around 84 nm which is considerably thicker than the intended width of 60 nm. Additionally, there are small bright spots around the NW which can be accounted to residuals from the etching procedure. In the cross-section SEM micrograph in figure 7.1.7(c), accessed by a focussed ion beam cut, the Si NW can be clearly distinguished from its SiO_2 (HSQ) mask, lying on top of the buried oxide layer from the original SOI substrate. The NW has a trapezoidal shape. The baseline width is around 130 nm which more the double the intended width. The baseline angle of the trapezoidal cross-section is 75°. In order to improve the sidewall steepness aiming a baseline angle 90°, the RIE recipe has to be adjusted. Comparing both NW fabrication processes, the Si NWs produced with the HSQ-based recipe yield better results.

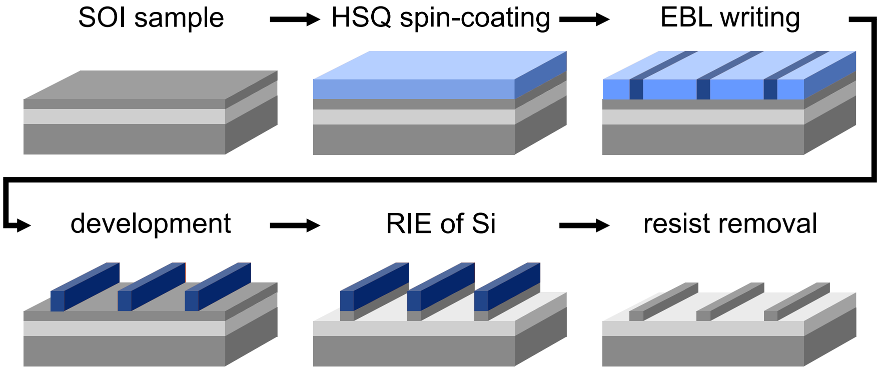

Figure 7.1.6: Preparation process flow schematic for Si NWs by using a HSQ resist.

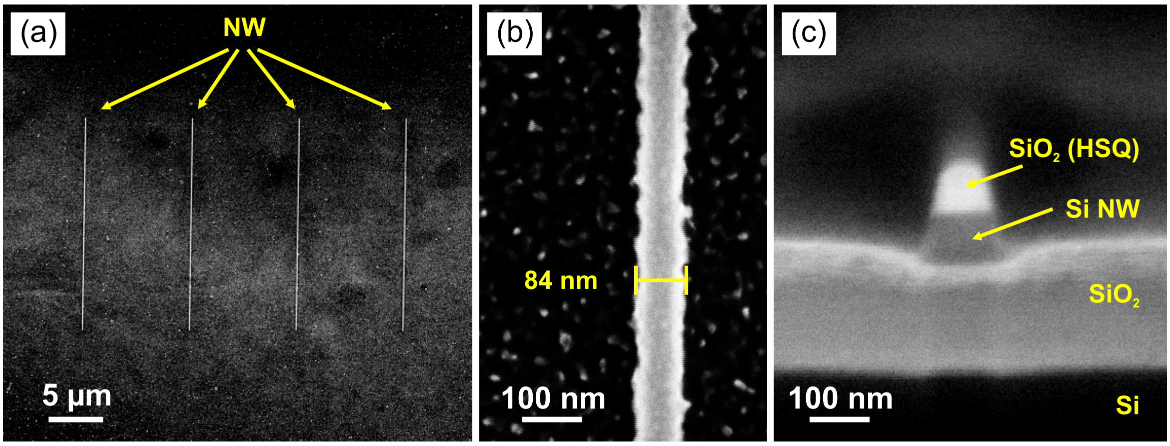

Figure 7.1.7: Top-view SEM images of Si NWs processed with the HSQ resist with (a) low and (b) high magnification and (c) a cross-section SEM image of a single NW.

7.2 Outlook - III-V integration into Si nanowires

For the integration of III-V NCs into Si NWs, the NW fabrication process using the HSQ resist has to be combined with the mask-assisted, sequential implantation of group-III and -V ions, presented in section 5.3. With the aim to produce a working device, additional contact deposition at the ends of the NW as well as the deposition of a gate dielectric have to be performed. In figure 7.2.1, the full preparation process for a III-V-in-Si-NW transistor is depicted schematically.

As starting point, again a SOI substrate is used (a). An EBL step is performed to prepare alignment markers for the subsequent processing steps in order to ensure proper positioning of the NWs, implantation windows and contacts. After that, the HSQ resist based EBL process is employed to fabricate a etching mask for the Si NWs (b). Larger pads are attached at both ends of the NW structure with the purpose to get better contact formation and to achieve higher mechanical stability of the NWs. In a RIE process, the HSQ mask is transferred to the underlying thin Si layer and the Si NW is fabricated (c). Afterwards, the implantation mask is prepared similar to the process described in section 5.3 using the optimal window size deduced from the statistical analysis of the experiments (d). Hereby, an implantation window is placed over the centre of a Si NW to get a III-V NC in the middle of this particular NW. The next step is the sequential ion implantation of the group-III and -V ions. The removal of the implantation mask reveals then a Si NW with a Gaussian-like depth distribution of the III/V ions within the implanted area (e). Subsequent FLA treatment induces the LPE formation process, discussed in chapter 6, leading to the formation of a III-V NC located in the centre of the Si NW (f). Around the III-V NC, the gate dielectric is deposited (g). The last step is the deposition of the metal contacts to form the source (S), drain (D) and gate (G) contacts (h).

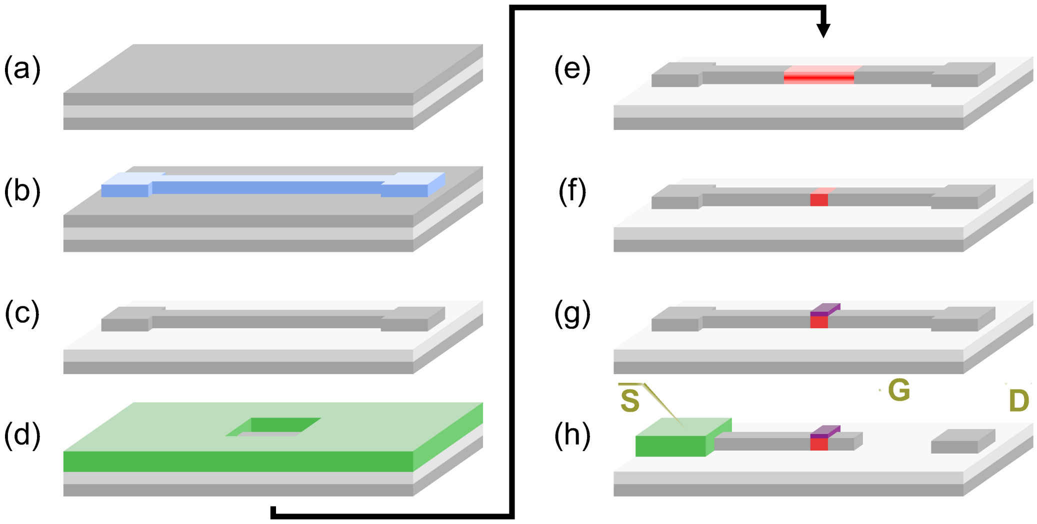

Figure 7.2.1: Process schematic for the fabrication of a gated III-V-NC-in-Si-NW structure. (a) SOI substrate. (b) NW mask using the HSQ resist. (c) RIE of masked Si layer to fabricate a Si NW on SiO_2. (d) Implantation mask preparation. (e) III-V implanted Si NW. (f) III-V NC formation in Si NW by FLA. (g) Deposition of the gate dielectric. (h) Ni deposition for source (S), drain (D) and gate (G) contacts.

8 Summary and conclusions

Within the scope of this work, the integration of III-V compound semiconductors into Si and Ge substrates by the combination of ion implantation and FLA has been studied. Therefore, different substrate material systems including bulk Si, thin a-Si layers grown by PECVD on a SiO_2/Si system, SOI wafers and bulk Ge substrates have been sequentially implanted with different combinations of group-III and -V elements. The subsequent thermal treatment with FLA in the millisecond-range has led to the formation of NCs of several III-V compounds, namely GaP, GaAs, GaSb, InP, InAs and InSb. The fabricated III-V NCs have been experimentally investigated to characterise their structural quality and optical properties. The obtained results have been employed to derive a detailed qualitative model of the formation mechanism.

During the preparation of the implantation procedure, the depth profiles of the various group-III and -V ions have been simulated with the SRIM code in order to achieve matching profiles for the particular III/V combination. Furthermore, the implantation energies have been chosen to ensure a suitable projected range of implanted ions located 30 nm below the surface for bulk materials or centred within the thin Si layer for the PECVD and SOI substrates. The optimal implantation energies are given in tables A.3.1 and A.3.2 in Appendix A.3. The ion fluences, namely 2×10^{16} and 3×10^{16} ions/cm^2 per ion species, induce a lot of damage to the crystalline lattice of the substrate material and lead to an amorphisation of the implanted region and a swelling of the thin Si layers.

Additionally, the temperature profile within a bulk Si wafer during 20 ms FLA treatment has been simulated using the wave transfer method in combination with solving the one-dimensional heat equation with FlexPDE. The simulation reveals a steep temperature increase of the wafer surface during exposure to the Xe flash lamps and a fast cooling after 25 ms. The backside of the wafer is also heated very fast but the heating is delayed with respect to the front side and the temperature during heating is not as high. After approximately 40 ms, the temperatures of the front and backside have equalized and the whole wafer cools down at a slow rate. At FLA energy densities above 72.2 J/cm^2, the wafer surface temperature will be higher than the melting point of a-Si but still lower than that of c-Si. Therefore, FLA at such energy densities is sufficient to melt the amorphized part but does not affect the crystalline substrate beneath.

The first substrate material investigated during this work has been bulk Si capped by a thin SiO_2 layer in order to prevent sputtering effects during ion implantation. With sequential ion implantation and FLA, InAs and GaAs NCs have been formed successfully. After implantation, the Raman spectra only display a broad peak accounted to amorphous Si. After FLA, however, the characteristic phonon mode peaks of InAs and GaAs are visible in Raman spectroscopy which verifies that there is a crystalline order within the NCs. The strong Raman signal originating from crystalline Si (TO+LO phonon mode) proves recrystallization of the amorphized top Si region by FLA. Structural investigations by SEM and TEM reveal regularly shaped circles or rectangles in top-view SEM, with hemispherical cross-sections located at SiO_2/Si interface. The NCs obtain a rather broad size distribution ranging from specimen with few tens of nm to a maximum diameter of about 400 nm whereas the InAs NCs have a larger mean size than the GaAs ones for the same annealing conditions. HRTEM micrographs of specific NCs show highly ordered crystals with a few number of defects, e.g. stacking faults, and with atomically sharp interfaces to the surrounding Si substrate material. The HRTEM images indicate epitaxial growth of the III-V compounds on the recrystallized Si substrate.

The underlying formation mechanism has been identified as LPE and is described in detail in chapter 6. After ion implantation, the top region of the Si substrate material is amorphous and it has a lowered melting point with respect to the crystalline Si material below. The subsequent FLA at an appropriate energy density melts the amorphous part but does not affect the crystalline bulk. Within the liquid phase, the implanted ions are distributed homogeneously due to their high diffusivities. A liquid solution of III/V atoms in the molten Si is formed. As the temperature during FLA stays below the melting point of c-Si, the liquid phase is in an under-cooled state which leads to a non-equilibrium crystallization process. After the FLA pulse, the liquid phase starts to recrystallize epitaxially on the underlying crystalline Si bulk material. The crystallization front moves from the bottom towards the Si/SiO_2 interface and pushes a region with increased III/V concentration ahead since there is segregation of these elements in Si. The crystallization front is stopped at the interface to the capping layer and the heavily enriched III/V melt accumulates in droplets. Finally, when the temperature drops below the melting point of the III-V compound, the NCs crystallize using the surrounding c-Si as epitaxial template. One important factor influencing this formation process is the melting point of the involved substances. Comparing InAs and GaAs with respect to Si, the melting point difference for the InAs/Si case is larger than in the GaAs/Si case leading to a different mean size of the NCs, for example. The GaAs starts to crystallize at a higher temperature and, hence, earlier than the InAs. This results in more seeds nucleating from the liquid, which, however, grow not as big as the InAs NCs as there is less III/V material available to be consumed for NC growth for each particular seed.

In bulk Ge, the fabrication of InAs NC has also been successfully accomplished using ion implantation and FLA. Similar to the Si substrate, Raman measurements show the characteristic phonon modes of InAs as well as a strong signal due to the Ge substrate proving InAs NC formation and recrystallization of the amorphous Ge after FLA. Unfortunately, the phonon modes of GaAs have not been detected and the formation of GaAs NCs in Ge could not be confirmed undoubtedly. The melting point of GaAs is higher than that of Ge, therefore, there is no GaAs NC formation. In contrast to the Si substrate, the InAs NCs display an arbitrary shape in the top-view SEM micrographs. In the TEM analysis, two kinds of precipitates are discovered: (1) elongated precipitates attached to the SiO_2/Ge interface and (2) circular dots located at a depth of about 100 nm. The precipitates of group (1) have a maximum height of about 50 nm but extend several hundreds of nm laterally. The HRTEM images of these NCs show crystalline order but a lot of defects and a rough interface with the Ge substrate. The circular NCs of group (2), however, are smaller with a maximum extension of about 50 nm and show almost perfect crystalline quality. The InAs/Ge interface of these circular dots shows Moiré fringes in the HRTEM image indicating epitaxial growth of the InAs NC. The integration of III-V compound semiconductor NCs in Ge by ion implantation and FLA has been achieved for the first time and the results have been published in Ref. [396].

Comparing the bulk Si and Ge substrates, the fabricated InAs NCs appear slightly different in both materials. While in Si, there is only one species of InAs NCs at the Si/SiO_2 interface, there are two in the Ge substrate. The buried InAs NCs in Ge are similar to the precipitates in Si regarding their structural properties and quality, however, the InAs NCs at the Ge/SiO_2 interface possess a different shape and the quality is worse. The different NC depths in Si and Ge are accounted to the melting point difference between InAs and the particular substrate material. This difference is smaller in the InAs/Ge system than in the InAs/Si system which leads to an earlier starting point of NC formation in Ge with respect to the recrystallization of the substrate material. In Ge, the recrystallization of the substrate material is not as advanced as in Si when the InAs NCs start to evolve. Therefore, InAs NCs are incorporated into the bulk and reside not only at the surface.

After the investigation of bulk substrates, thin Si layer systems have been studied. Hereby, two systems with similar structure have been evaluated, namely SOI and PECVD-grown substrates. The main differences between both systems are the initial state of the intermediate Si layer which is single-crystalline for SOI and amorphous in the PECVD samples as well as the high H-content of the PECVD-grown system. In SOI, the formation of InAs and GaAs NCs was successfully achieved using the presented integration method. Again, Raman spectroscopy has displayed the characteristic phonon modes of the particular III-V compounds proving NC formation as well as the typical Si phonon modes confirming recrystallization of the thin Si device layer. Top-view SEM images have revealed arbitrarily shaped precipitates. However, the cross-section TEM micrographs show mainly block-like NCs limited in height by the surrounding SiO_2 layers. In the HRTEM analysis, the NCs appear single-crystalline and have sharp interfaces to Si for both III-V compounds but feature a moderate amount of stacking faults. Additional small, circular and crystalline III-V precipitates have been observed in both adjacent SiO_2 layers. The XRD analysis of these samples shows the Bragg peaks of the (111), (220) and (311) lattice planes of the particular III-V compound and Si verifying the presence of III-V NCs in recrystallized Si. Besides the reflexes from InAs and Si, additional features appear in the XRD 2θ scans of the In^+ implanted samples which are attributed to metallic indium. The presence of these In clusters can be accounted to the large difference in the segregation coefficients of In and As in Si. During solidification of Si, more In remains in the liquid phase than As leading to different concentrations of both elements in the melt. During III-V formation the excess of In is not consumed and forms In precipitates in the end.

For the PECVD-grown layer system, GaP, GaAs, GaSb and InP NCs have been successfully integrated into the thin Si layer. Unfortunately, the formation of GaN NCs has not been achieved. For the other III-V compounds, the Raman spectra of the *FLA treated* samples display the characteristic phonon modes proving NC formation. The RBS analysis of these samples reveals a change from a Gaussian-like depth profile for the *as implanted* state to a box-like depth profile for *FLA treated* state indicating a strong diffusion of the implanted ions due to melting by FLA. SEM and TEM images show arbitrarily shaped precipitates with different size and crystalline quality. For both thin film systems, the formation mechanism is similar to the mechanism in bulk substrate, except that there is no template for epitaxial growth. However, as the melting point of c-Si is higher than for the most of the III-V compounds, nucleation of Si starts at first. These Si seeds grow into larger grains which finally act as templates for epitaxial growth of the III-V compounds. Comparing the SOI and the PECVD system, the III-V NCs in the SOI sample have better structural properties. The results of III-V integration in thin PECVD-grown layers including a detailed description of the NC formation via LPE has been published in Ref. [395].

Additionally to binary III-V compounds, the integration of ternary $In_xGa_{1-x}As$ NCs into SOI substrates has been performed successfully. For this experiment, the three ion species have been implanted sequentially and with varying fluence ratio between In and Ga to achieve different $In_xGa_{1-x}As$ compositions. The Raman spectra display a shift of the characteristic phonon modes from the InAs positions to the GaAs position with decreasing In implantation fluence and a partly two-mode phonon behaviour is observed for the mixed crystals. The XRD 2θ scans show a shift of the III-V related Bragg peaks from the InAs position towards the GaAs positions with decreasing In content. Both methods prove the formation of $In_xGa_{1-x}As$ with varying composition. Using the respective peak positions from both measurements, the average composition of the III-V NCs is deduced and a deviation from the nominal composition (implanted In/Ga ratio) is observed. The fabricated $In_xGa_{1-x}As$ NCs are mainly Ga-rich. Furthermore, a splitting of the Bragg peaks has been detected during XRD analysis, resulting in two different compositions of $In_xGa_{1-x}As$ for these samples. The Williamson-Hall analysis of the XRD scans shows that the III-V NCs are almost unstrained and have a mean crystallite size of around 30 nm. Similar to the binary III-V compounds, SEM micrographs display arbitrarily shaped precipitates and TEM micrographs show NCs with block-like cross-sections limited in height by the Si layer thickness. A particle size analysis of the SEM images reveals a slight trend to smaller NC size with decreasing In content. The investigation of the crystalline quality by HRTEM obtains mainly single-crystalline $In_xGa_{1-x}As$ precipitates growing epitaxially on the surrounding Si grains. The Ga-rich nature of the $In_xGa_{1-x}As$ NCs is accounted to the difference in the melting points of GaAs and InAs, leading to an earlier nucleation of crystals with higher Ga content.

For all substrate types, a correlation between NC size and annealing temperature (FLA energy density) can be drawn. Below a certain threshold, there is only Si recrystallization and no III-V NC formation. Above this threshold, NCs start to evolve and they become bigger for higher FLA energy densities until the temperature gets too high during FLA and the system decomposes. The threshold energy density for the bulk Si samples lies between 46.4 and 54.5 J/cm^2 and marks the transition from a solid phase to a liquid phase crystallization mechanism. In the solid phase, the diffusion coefficients of the implanted elements are too low to achieve a III/V concentration sufficient for crystal growth and, therefore, III-V NCs are not formed below the threshold energy density.

As the III-V NCs have random lateral distributions, an additional experiment using an implantation mask has been conducted in order to control the position of the NCs. Therefore, bulk Si and SOI substrates have been covered by either Al or Ni masks structured via an EBL process. The Raman spectra of the implanted samples display the characteristic signals for InAs, InP and InSb proving successful NC formation. The microstructural investigation by SEM and TEM reveals that the III-V NCs have formed within the implantation windows exclusively while the surrounding Si remains unaffected. This proves the possibility to control NC by the introduction of an additional implantation mask. The evaluation of different window sizes gives a minimum window size of 200 nm side length to achieve NC formation at all and an optimal window size of approximately 300 nm side length for the formation of one NC per implantation window. Looking at the masking materials, an incorporation of Ni into the thin Si layer is detected resulting in the formation of nickel silicide precipitates. This is due to the sputtering and redeposition of the mask material during ion implantation, and is probably also present for the Al mask, although it was not observed.

The final experiments have been dedicated to the integration of a III-V NC into a Si NW. For VLS-grown Si NWs randomly distributed over a Si wafer, this integration approach has already been achieved by *S Prucnal* using a masked implantation [393]. Such III-V-in-Si-nanowires have recently been utilized as avalanche LEDs [394]. A top-down approach, however, is more suitable for device fabrication as it gives more control over the positioning of the Si NW. Therefore, experiments regarding the top-down processing of Si NWs have been conducted. Two different EBL preparation processes have been used including (1) a negative ZEP-520 resist in combination with a lift-off to fabricate a Ni hard mask which can then be utilized for the transfer of NWs into Si by RIE and (2) a positive HSQ resist which directly acts as a mask for the pattern transfer via RIE. Both processes have been successfully applied for the Si NW fabrication, however, the HSQ-based process is more suitable since the NWs have better sidewall roughness, there is less contamination and the number of process steps is smaller than using process (1). As a perspective, the Si NWs prepared with this approach can be implanted using an implantation mask to integrate a single III-V NC in the centre of the NW. A further high-k gate dielectric preparation and a dedicated contact formation would allow the fabrication of transistor-like Si NW device.

Conclusively, with a successful fabrication of Si NWs, the integration of III-V NCs in the middle of such NWs via ion beam synthesis in combination with a masking procedure is a promising approach for the realisation of a III-V in Si avalanche diode like it has been already presented in [394]. Due to the versatility of the ion beam synthesis, different III-V compounds can be prepared and, therefore, a relatively broad wavelength range can be accessed. In contrast to the VLS-grown NWs, top-down fabrication gives better control over the position of the NWs, which leads to a better control of the further processing steps towards the avalanche diode structure. On the side of microelectronics, III-V compounds offer higher charge carrier mobilities than Si which makes them applicable in fast switching devices. Integrated into Si NWs, they present promising candidates for upcoming technology nodes when certain challenges like III-V/Si interface quality and the III-V NC size distribution are optimized.

A Appendix

A.1 Calculations

Virtual volume of the alloyed liquid Si region necessary for III-V NC size

To determine the volume of the virtual regions, where III/V material is drawn from, several assumptions have to be made:

1. The III-V NC has a hemispherical shape and can therefore be modelled by a spherical cap.
2. The binary III-V compound has a III/V ratio of 1:1.
3. The whole amount of the implanted III/V ions is located within the amorphized top region of the substrate material.
4. The implanted III/V ions are homogeneously distributed.
5. The shape of the virtual volume is a cylinder with the height of the amorphous top region of the substrate.
6. There is no volume change due to temperature change or phase transitions neither in the III-V compound nor in the substrate material.

The exemplary calculation is performed for the InAs NC depicted in figure 5.1.7(a) which has a lateral size of 346 nm and a height of 118 nm. The volume of this particular NC is given by

$$\begin{aligned} V_{\mathrm{NC}} &= \frac{\pi \cdot s_{\mathrm{NC}}}{6} \cdot (3 \cdot R^2_{\text{cap, NC}} + s^2_{\mathrm{NC}}) = \frac{\pi \cdot 118\,\mathrm{nm}}{6} \cdot (3 \cdot (173\,\mathrm{nm})^2 + (118\,\mathrm{nm})^2) \\ &= 6.41 \times 10^6\,\mathrm{nm}^3 = 6.41 \times 10^{-15}\,\mathrm{cm}^3. \end{aligned} \tag{A.1}$$

InAs has an atomic density ρ_{InAs} of 3.59×10^{22} atoms/cm^3. Therefore, the number of atoms $N_{\mathrm{InAs\ NC}}$ within the InAs NC is determined by

$$\begin{aligned} N_{\mathrm{InAs\ NC}} &= \rho_{\mathrm{InAs}} \cdot V_{\mathrm{NC}} = 3.59 \times 10^{22}\,\mathrm{atoms/cm}^3 \cdot 6.41 \times 10^{-15}\,\mathrm{cm}^3 \\ &= 2.30 \times 10^8\,\mathrm{atoms}. \end{aligned} \tag{A.2}$$

Considering assumption (2), the number of As atoms in the InAs NC is $N_{\text{InAs NC}}/2 = 1.15 \times 10^{8}$ atoms. It is now known, how much As atoms have to be present after implantation. The next step is to calculate the volume of implanted Si material which comprises this number of As atoms. Therefore, the concentration of As atoms in Si ($c_{\text{As in Si}}$) after the implantation with a fluence of 3×10^{16} atoms/cm^2 has to be determined. It is assumed that the implantation amorphizes the upper 200 nm of the Si substrate material. Respecting assumption (3), $c_{\text{As in Si}}$ is given by

$$c_{\text{As in Si}} = \frac{3 \times 10^{16}\,\text{atoms/cm}^2}{200\,\text{nm}} = 1.5 \times 10^{21}\,\text{atoms/cm}^3. \tag{A.3}$$

The necessary volume of the virtual region V_{virtual} is then determined by

$$V_{\text{virtual}} = \frac{N_{\text{InAs NC}}}{2 \cdot c_{\text{As in Si}}} = \frac{2.66 \times 10^{8}\,\text{atoms}}{2 \cdot 1.5 \times 10^{21}\,\text{atoms/cm}^3} = 7.67 \times 10^{-14}\,\text{cm}^3. \tag{A.4}$$

With assumption (5), the maximum distance the atoms need to travel to form the InAs NC can be determined by calculating the radius of the virtual cylinder (R_{virtual}) using

$$R_{\text{virtual}} = \sqrt{\frac{V_{\text{virtual}}}{\pi \cdot 200\,\text{nm}}} = \sqrt{\frac{8.87 \times 10^{-14}\,\text{cm}^3}{\pi \cdot 200\,\text{nm}}} = 349\,\text{nm}. \tag{A.5}$$

For the evaluation of R_{virtual}, the diffusion lengths of As in liquid and solid Si have to be determined using

$$L_{\text{D}}\,\textit{(liquid, As)} = \sqrt{D_{\text{L}} \cdot t} = \sqrt{3.3 \times 10^{-4}\,\text{cm}^2/\text{s} \cdot 0.02\,\text{s}} = 25.7\,\mu\text{m}, \tag{A.6}$$

and

$$L_{\text{D}}\,\textit{(solid, As)} = \sqrt{D_{\text{S}} \cdot t} = \sqrt{3.5 \times 10^{-12}\,\text{cm}^2/\text{s} \cdot 0.02\,\text{s}} = 2.6\,\text{nm}. \tag{A.7}$$

Comparing the diffusion lengths with R_{virtual}, the diffusion length of As in solid Si is much smaller than R_{virtual}. Therefore, it is evident that the formation mechanism of the III-V NCs takes place via the liquid phase.

A.2 Figures

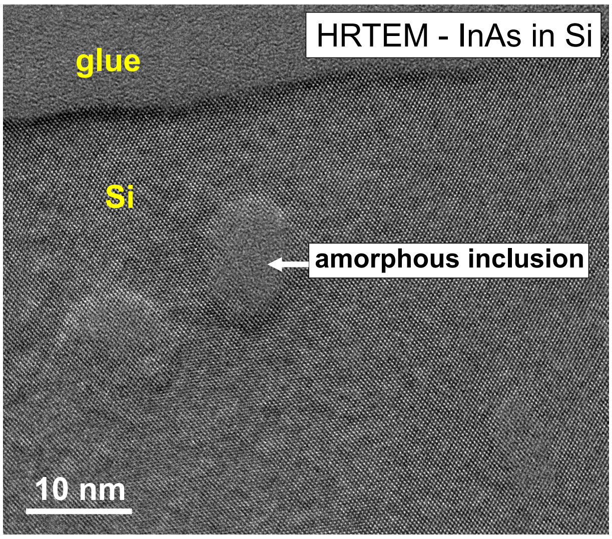

Figure A.2.1: HRTEM of InAs bulk Si sample displaying an amorphous inclusion after FLA treatment.

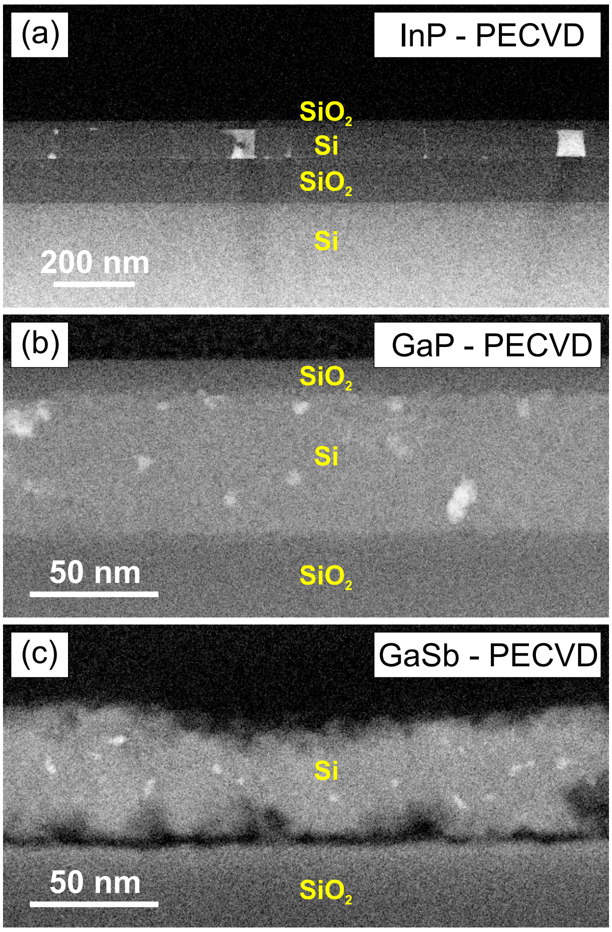

Figure A.2.2: Dark-field STEM images of the InP (a), GaP (b) and GaSb (c) PECVD samples. For the GaSb sample, the SiO_2 capping has been etched before TEM analysis.

A.3 Tables

Table A.3.1: Implantation energies for different group-III and -V ions calculated by SRIM simulations for the two-layer systems with different layer thicknesses.

Layer system	Layer thickness (nm)	Implanted ion species	Implantation energy (keV)
SiO_2/Si	35/bulk	N	22
		P	45
		As	90
		Sb	125
		Ga	90
		In	125/130
	50/bulk	P	60
		As	130
		Sb	190
		In	190
	65/bulk	As	140/150
		Ga	140/150
		In	190/200
SiO_2/Ge	35/bulk	As	130
		Ga	130
		In	180

Table A.3.2: Implantation energies for different group-III and -V ions calculated by SRIM simulations for the multilayer system with different layer thicknesses.

Layer system	Layer thickness (nm)	Implanted ion species	Implantation energy (keV)
SiO_2/Si/SiO_2/Si	35/60/100/bulk	N	22
		P	45
		As	90
		Sb	125
		Ga	90
		In	125
	65/60/150/bulk	As	140/150
		Ga	140/150
		In	190/200
	50/90/150/bulk	P	60
		As	130
		Sb	190
		In	190

References

1. Faraday, M. Experimental Researches in Electricity. Fourth Series. *Philosophical Transactions of the Royal Society* **123,** 507–522 (Jan. 1833).
2. Smith, W. Effect of Light on Selenium during the Passage of an Electric Current. *Nature* **7,** 303–303 (Feb. 1873).
3. Adams, W. G. & Day, R. E. The Action of Light on Selenium. *Proceedings of the Royal Society of London* **25,** 113–117 (Jan. 1876).
4. Fritts, C. On a new form of selenium cell, and some electrical discoveries made by its use. *American Journal of Science* **26,** 465–472 (Dec. 1883).
5. Braun, F. Ueber die Stromleitung durch Schwefelmetalle. *Annalen der Physik* **229,** 556–563 (1875).
6. Bose, J. C. US patent 755840 A (1904).
7. Pickard, G. W. US patent 836531 A (1906).
8. Wilson, A. H. The Theory of Electronic Semi-Conductors. *Proceedings of the Royal Society A* **133,** 458–491 (1931).
9. Wilson, A. H. The Theory of Electronic Semi-Conductors II. *Proceedings of the Royal Society A* **134,** 277–287 (1931).
10. Lilienfeld, J. E. US patent 1745175 A (1930).
11. Lilienfeld, J. E. CA patent 272437 A (1927).
12. Lilienfeld, J. E. US patent 1900018 A (1933).
13. Heil, O. GB patent 439457 A (1935).
14. Ohl, R. S. US patent 2402662 A (1946).
15. Bardeen, J. & Brattain, W. H. The Transistor, A Semi-Conductor Triode. *Physical Review* **74,** 230–231 (July 1948).
16. Brattain, W. H. & Bardeen, J. US patent 2524035 A (1950).
17. Shockley, W. The Theory of p-n Junctions in Semiconductors and p-n Junction Transistors. *Bell System Technical Journal* **28,** 435–489 (July 1949).
18. *The Nobel Prize in Physics 1956* Nobel Media AB 2014. <`http://www.nobelprize.org/nobel_prizes/physics/laureates/1956/`>.
19. Koch, R. C. US patent 2892931 (1959).
20. Riordan, M. The lost history of the transistor. *IEEE Spectrum* **41,** 44–49 (May 2004).
21. Teal, G. K. Some recent developments in silicon and germanium materials and devices. *Institute of Radio Engineers (IRE) National Conference on Airborne Electronics,* Dayton, Ohio (1954).
22. Tanenbaum, M., Valdes, L. B., Buehler, E. & Hannay, N. B. Silicon n-p-n Grown Junction Transistors. *Journal of Applied Physics* **26,** 686 (1955).

23. Chapin, D. M., Fuller, C. S. & Pearson, G. L. A New Silicon p-n Junction Photocell for Converting Solar Radiation into Electrical Power. *Journal of Applied Physics* **25,** 676 (1954).
24. Frosch, C. J. & Derick, L. Surface Protection and Selective Masking during Diffusion in Silicon. *Journal of the Electrochemical Society* **104,** 547–552 (Sept. 1957).
25. Kilby, J. S. US 3138743 A (1964).
26. Noyce, R. N. US patent 2981877 A (1961).
27. *The Nobel Prize in Physics 2000* Nobel Media AB 2014. <`http://www.nobelprize.org/nobel_prizes/physics/laureates/2000/`>.
28. Kahng, D. US patent 3102230 A (1963).
29. Wanlass, F. & Sah, C. *Nanowatt logic using field-effect metal-oxide semiconductor triodes* in *Solid-State Circuits Conference. Digest of Technical Papers. 1963 IEEE International* **VI** (Feb. 1963), 32–33.
30. Wanlass, F. M. US patent 3356858 A (1967).
31. Moore, G. E. Cramming more components onto integrated circuits. *Electronics* **38** (Apr. 1965).
32. Kerwin, R. E., Klein, D. L. & Sarace, J. C. US patent 3475234 A (1969).
33. Faggin, F. & Klein, T. Silicon gate technology. *Solid-State Electronics* **13,** 1125–1144 (Aug. 1970).
34. Biard, J. R. US patent 3463975 A (1969).
35. Tarui, Y., Hayashi, Y., Teshima, H. & Sekigawa, T. *Transistor Schottky-Barrier diode integrated-logic circuit* in *Solid-State Circuits Conference. Digest of Technical Papers. 1968 IEEE International* **XI** (Feb. 1968), 164–165.
36. Dennard, R. H., Gaensslen, F. H., Rideout, V. L., Bassous, E. & LeBlanc, A. R. Design of ion-implanted MOSFET's with very small physical dimensions. *IEEE Journal of Solid-State Circuits* **9,** 256–268 (Oct. 1974).
37. Hoeneisen, B. & Mead, C. A. Fundamental Limitations in Microelectronics - I. MOS Technology. *Solid-State Electronics* **15,** 819–829 (July 1972).
38. Moore, G. E. *Progress in digital integrated electronics* in *Electron Devices Meeting, 1975 International* **21** (1975), 11–13.
39. Jenkins, T. A brief history of ... semiconductors. *Physics Education* **40,** 430–439 (Sept. 2005).
40. Łukasiak, L. & Jakubowski, A. History of Semiconductors. *Journal of Telecommunications and Information Technology* **1,** 3–9 (2010).
41. *The Silicon Engine - A Timeline of Semiconductors in Computers* Computer History Museum. <`http://www.computerhistory.org/siliconengine/`>.
42. Bohr, M. *The new era of scaling in an SoC world* in *2009 IEEE International Solid-State Circuits Conference - Digest of Technical Papers* (Feb. 2009), 23–28.
43. Chau, R. *et al.* Application of high-κ gate dielectrics and metal gate electrodes to enable silicon and non-silicon logic nanotechnology. *Microelectronic Engineering* **80,** 1–6 (June 2005).
44. Chen, T.-C. *Where CMOS is going: trendy hype vs. real technology* in *2006 IEEE International Solid State Circuits Conference - Digest of Technical Papers* (Feb. 2006), 1–18.
45. Mizuno, T. *et al.* Electron and hole mobility enhancement in strained-Si MOSFET's on SiGe-on-insulator substrates fabricated by SIMOX technology. *IEEE Electron Device Letters* **21,** 230–232 (May 2000).
46. Singh, N. *et al. Ultra-Narrow Silicon Nanowire Gate-All-Around CMOS Devices: Impact of Diameter, Channel-Orientation and Low Temperature on Device Performance* in *2006 International Electron Devices Meeting* (Dec. 2006), 1–4.

47. Liu, Y. *et al. Advanced FinFET CMOS Technology: TiN-Gate, Fin-Height Control and Asymmetric Gate Insulator Thickness 4T-FinFETs* in *2006 International Electron Devices Meeting* (Dec. 2006), 1–4.
48. Colinge, J. Multi-gate SOI MOSFETs. *Microelectronic Engineering* **84,** 2071–2076 (Sept. 2007).
49. Shang, H. *et al. High mobility p-channel germanium MOSFETs with a thin Ge oxynitride gate dielectric* in *Electron Devices Meeting, 2002. IEDM '02. International* (Dec. 2002), 441–444.
50. Chau, R. *et al.* Benchmarking nanotechnology for high-performance and low-power logic transistor applications. *IEEE Transactions on Nanotechnology* **4,** 153–158 (Mar. 2005).
51. Kim, D. H. & del Alamo, J. A. *Logic Performance of 40 nm InAs HEMTs* in *2007 IEEE International Electron Devices Meeting* (Dec. 2007), 629–632.
52. Passlack, M., Doornbos, G., Wann, C. & Sun, Y. C. *Classification and benchmarking of III-V MOSFETs for CMOS* in *2010 Symposium on VLSI Technology* (June 2010), 155–156.
53. Chau, R., Doyle, B., Datta, S., Kavalieros, J. & Zhang, K. Integrated nanoelectronics for the future. *Nature Materials* **6,** 810–812 (Nov. 2007).
54. Del Alamo, J. A. Nanometre-scale electronics with III-V compound semiconductors. *Nature* **479,** 317–323 (Nov. 2011).
55. Tomioka, K., Yoshimura, M. & Fukui, T. A III-V nanowire channel on silicon for high-performance vertical transistors. *Nature* **488,** 189–192 (Aug. 2012).
56. Tang, M. *et al.* 1.3 µm InAs/GaAs quantum-dot lasers monolithically grown on Si substrates using InAlAs/GaAs dislocation filter layers. *Optics Express* **22,** 11528–11535 (May 2014).
57. Yu, P. Y. & Cardona, M. *Fundamentals of Semiconductors* 4th ed. (eds Stanley, H. E. & Rhodes, W. T.) (Springer-Verlag Berlin Heidelberg, 2010).
58. Goldstein, A. N., Echer, C. M. & Alivisatos, A. P. Melting in Semiconductor Nanocrystals. *Science* **256,** 1425–1427 (1992).
59. Vossmeyer, T. *et al.* CdS Nanoclusters: Synthesis and Characterization and Size Dependent Oscillator Strength and Temperature and Shift of the Excitonic Transition Energy and Reversible Absorbance Shift. *Journal of Physical Chemistry* **98,** 7665–7673 (1994).
60. Norris, D. J. & Bawendi, M. G. Measurement and assignment of the size-dependent optical spectrum in CdSe and quantum dots. *Physical Review B* **53,** 16338–16346 (1996).
61. Nordell, K. J., Boatman, E. M. & Lisensky, G. C. A Safer, Easier, Faster Synthesis for CdSe Quantum Dot Nanocrystals. *Journal of Chemical Education* **82,** 1697–1699 (2005).
62. Efros, A. L. & Rosen, M. The electronic structure of semiconductor nanocrystals. *Annual Review of Materials Science* **30,** 475–521 (Aug. 2000).
63. Ekimov, A. I., Efros, A. L. & Onushchenko, A. A. Quantum Size Effect in Semiconductor Microcrystals. *Solid State Communications* **56,** 921–924 (1985).
64. Yoffe, A. Low-dimensional systems: quantum size effects and electronic properties of semiconductor microcrystallites (zero-dimensional systems) and some quasi-two-dimen-sional systems. *Advances in Physics* **42,** 173–262 (Apr. 1993).
65. Efros, A. L. & Efros, A. L. Interband absorption of light in a semiconductor sphere. *Soviet Physics Semiconductors – USSR* **16,** 772–775 (1982).
66. Brus, L. Electron-electron and electron-hole interactions in small semiconductor crystallites: The size dependence of the lowest excited electronic state. *The Journal of Chemical Physics* **80,** 4403–4409 (1984).

67. Brus, L. Electronic wave functions in semiconductor clusters: experiment and theory. *Journal of Physical Chemistry* **90,** 2555–2560 (June 1986).
68. Miller, D. A. B. *et al.* Band-Edge Electroabsorption in Quantum Well Structures: The Quantum-Confined Stark Effect. *Physical Review Letters* **53,** 2173–2176 (Nov. 1984).
69. Brus, L. Quantum crystallites and nonlinear optics. *Applied Physics A-Materials Science & Processing* **53,** 465–474 (Dec. 1991).
70. Dingle, R., Wiegmann, W. & Henry, C. H. Quantum States of Confined Carriers in Very Thin $Al_xGa_{1-x}As$-GaAs-$Al_xGa_{1-x}As$ Heterostructures. *Physical Review Letters* **33,** 827–830 (Sept. 1974).
71. Waldrop, J. R., Kraut, E. A., Farley, C. W. & Grant, R. W. Measurement of AlAs/InP and InP/$In_{0.52}Al_{0.48}As$ heterojunction band offsets by x-ray photoemission spectroscopy. *Journal of Vacuum Science & Technology B* **8,** 768 (July 1990).
72. Nakagawa, A., Kroemer, H. & English, J. H. Electrical properties and band offsets of InAs/AlSb n-N isotype heterojunctions grown on GaAs. *Applied Physics Letters* **54,** 1893 (1989).
73. Sakaki, H., Chang, L. L., Sai-Halasz, G. A., Chang, C. A. & Esaki, L. Two-dimensional electronic structure in InAs-GaSb superlattices. *Solid State Communications* **26,** 589–592 (1978).
74. Esaki, L. & Tsu, R. Superlattice and Negative Differential Conductivity in Semiconductors. *IBM Journal of Research and Development* **14,** 61–65 (Jan. 1970).
75. Chang, Y.-C. & Schulman, J. N. Interband optical transitions in GaAs-$Ga_{1-x}Al_xAs$ and InAs-GaSb and superlattices. *Physical Review B* **31,** 2069–2079 (Feb. 1985).
76. Patanè, A. & Fromhold, M. Novel regimes of electron dynamics in superlattices. *Philosophical Transactions of the Royal Society A: Mathematical, Physical and Engineering Sciences* **364,** 3477–3492 (Dec. 2006).
77. Tsu, R. & Döhler, G. Hopping conduction in a “superlattice”. *Physical Review B* **12,** 680–686 (July 1974).
78. Alivisatos, A. P. Semiconductor clusters, nanocrystals, and quantum dots. *Science* **271,** 933–937 (Feb. 1996).
79. Beenakker, C. W. J. Theory of Coulomb-blockade oscillations in the conductance of a quantum dot. *Physical Review B* **44,** 1646–1656 (July 1991).
80. Kastner, M. A. The single-electron transistor. *Reviews of Modern Physics* **64,** 849–859 (July 1992).
81. Likharev, K. K. Single-Electron Devices and Their Applications. *Proceedings of the IEEE* **87,** 602–632 (Apr. 1999).
82. Mehrer, H. *Diffusion in Solids* 1st ed. (Springer-Verlag Berlin Heidelberg, 2007).
83. Einstein, A. Über die von der molekularkinetischen Theorie der Wärme geforderte Bewegung von in ruhenden Flüssigkeiten suspendierten Teilchen. *Annalen der Physik* **17,** 549–560 (1905).
84. Smoluchowski, M. Zur kinetischen Theorie der Brownschen Molekularbewegung und der Suspensionen. *Annalen der Physik* **21,** 756–780 (1906).
85. Kodera, H. Diffusion coefficients of impurities in silicon melt. *Japanese Journal of Applied Physics* **2,** 212 (1963).
86. Bracht, H. & Stolwijk, N. A. in *Diffusion in Semiconductors* (ed Beke, D. L.) 2-1–2-257 (Springer-Verlag Berlin Heidelberg, 1998).
87. Burton, J. A. Impurity centers in Ge and Si. *Physica* **20,** 845–854 (1954).
88. Hall, R. N. in *Fortschritte der Hochfrequenztechnik* (Akademische Verlagsgesellschaft mbH, Frankfurt a. M., 1959).
89. Hall, R. N. Segregation of impurities during the growth of germanium and silicon crystals. *Journal of Physical Chemistry* **57,** 836–839 (Aug. 1953).

90. Tang, K., Øvrelid, E. J., Tranell, G. & Tangstad, M. in *Crystal Growth of Si for Solar Cells* (eds Nakajima, K. & Usami, N.) 219–251 (Springer-Verlag, Berlin Heidelberg, Jan. 2009).
91. Yatsurugi, Y., Akiyama, N., Endo, Y. & Nozaki, T. Concentration, Solubility, and Equilibrium Distribution Coefficient of Nitrogen and Oxygen in Semiconductor Silicon. *Journal of the Electrochemical Society* **120,** 975–979 (1973).
92. Hänggi, P., Talkner, P. & Borkovec, M. Reaction-rate theory: fifty years after Kramers. *Reviews of Modern Physics* **62,** 251–341 (Apr. 1990).
93. Frenkel, J. Über die Wärmebewegung in festen und flüssigen Körpern. *Zeitschrift für Physik* **35,** 652–669 (1926).
94. Fukai, Y. & Sugimoto, H. Diffusion of hydrogen in metals. *Advances in Physics* **34,** 263–326 (Jan. 1985).
95. Fahey, P. M., Griffin, P. B. & Plummer, J. D. Point defects and dopant diffusion in silicon. *Reviews of Modern Physics* **61,** 289–384 (Apr. 1989).
96. King, J. R., Sharp, T. E., Tuck, B. & Rogers, T. G. Mathematical Modelling of the Interstitialcy Diffusion Mechanism. *Proceedings: Mathematical and Physical Sciences* **450,** 623–649 (Sept. 1995).
97. Car, R., Kelly, P. J., Oshiyama, A. & Pantelides, S. T. Microscopic Theory of Atomic Diffusion Mechanisms in Silicon. *Physical Review Letters* **52,** 1814–1817 (May 1984).
98. Huntington, H. B. & Seitz, F. Mechanism for Self-Diffusion in Metallic Copper. *Physical Review* **61,** 315–325 (Mar. 1942).
99. Zener, C. Ring diffusion in metals. *Acta Crystallographica* **3,** 346–354 (1950).
100. Frank, F. C. & Turnbull, D. Mechanism of Diffusion of Copper in Germanium. *Physical Review* **104,** 617–618 (Nov. 1956).
101. Gösele, U., Frank, W. & Seeger, A. Mechanism and Kinetics of the Diffusion of Gold in Silicon. *Applied Physics* **23,** 361–368 (1980).
102. Mehrer, H. The Effect of Pressure on Diffusion. *Defect and Diffusion Forum* **129–130,** 57–76 (1996).
103. Toor, H. L. Diffusion in three-component gas mixtures. *AIChE Journal* **3,** 198–207 (1957).
104. Taylor, R. & Krishna, R. *Multicomponent Mass Transfer* (John Wiley & Sons, Inc., 1993).
105. Maginn, E. J., Bell, T. & Theodorou, D. N. Transport Diffusivity of Methane in Silicalite from Equilibrium and Nonequilibrium Simulations. *Journal of Physical Chemistry* **97,** 4173–4181 (1993).
106. Wheeler, D. R. & Newman, J. Molecular Dynamics Simulations of Multicomponent Diffusion. 2. Nonequilibrium Method. *The Journal of Physical Chemistry B* **108,** 18362–18367 (Nov. 2004).
107. Enderby, J. E. & Barnes, A. C. Liquid semiconductors. *Reports on Progress in Physics* **53,** 85–179 (1990).
108. Salmon, P. S. A neutron diffraction study on the structure of liquid germanium. *Journal of Physics F: Metal Physics* **18,** 2345–2352 (1988).
109. Johnson, S. L. *et al.* Properties of Liquid Silicon Observed by Time-Resolved X-Ray Absorption Spectroscopy. *Physical Review Letters* **91,** 157403 (Oct. 2003).
110. Iida, T., Guthrie, R. & Tripathi, N. A Model for Accurate Predictions of Self-Diffusivities in Liquid Metals, Semimetals, and Semiconductors. *Metallurgical and Materials Transactions B* **37B,** 559–564 (Aug. 2006).
111. Tang, K., Øvrelid, E. J., Tranell, G. & Tangstad, M. Critical assessment of the impurity diffusivities in solid and liquid silicon. *Journal of the Minerals, Metals and Materials Society* **61,** 49–55 (2009).

112. Gupta, Y. P. Solute diffusion in liquid metals. *Advances in Physics* **16,** 333–350 (Apr. 1967).
113. Cahoon, J. R. A Modified "Hole" Theory for Solute Impurity Diffusion in Liquid Metals. *Metallurgical and Materials Transactions A* **28A,** 583–593 (Mar. 1997).
114. Alder, B. J. Studies in Molecular Dynamics. VIII. The Transport Coefficients for a Hard-Sphere Fluid. *The Journal of Chemical Physics* **53,** 3813 (1970).
115. Bruson, A. & Gerl, M. Diffusion coefficient of ^{113}Sn and ^{124}Sb and ^{110m}Ag and ^{195}Au in liquid Sn. *Physical Review B* **21,** 5447–5454 (June 1980).
116. Liu, Y., Long, Z., Wang, H., Du, Y. & Huang, B. A predictive equation for solute diffusivity in liquid metals. *Scripta Materialia* **55,** 367–370 (Aug. 2006).
117. Markov, I. V. *Crystal Growth for Beginners* 2nd ed. (World Scientific Publishing Co. Pte. Ltd., 2004).
118. Becker, R. & Döring, W. Kinetische Behandlung der Keimbildung in übersättigten Dämpfen. *Annalen der Physik* **24,** 719–752 (1935).
119. Lothe, J. & Pound, G. M. Reconsiderations of Nucleation Theory. *The Journal of Chemical Physics* **36,** 2080 (1962).
120. Volmer, M. & Weber, A. Keimbildung in übersättigten Gebilden. *Zeitschrift für physikalische Chemie* **119,** 277 (1926).
121. Farkas, L. Keimbildungsgeschwindigkeit in übersättigten Dämpfen. *Zeitschrift für physi-kalische Chemie* **125,** 236–242 (1927).
122. Oxtoby, D. W. Homogeneous nucleation: theory and experiment. *Journal of Physics: Condensed Matter* **4,** 7627–7650 (1992).
123. Sear, R. P. Nucleation: theory and applications to protein solutions and colloidal suspensions. *Journal of Physics: Condensed Matter* **19,** 033101 (Jan. 2007).
124. Turnbull, D. Kinetics of Heterogeneous Nucleation. *The Journal of Chemical Physics* **18,** 198 (1950).
125. Chernov, A. A. Formation of crystals in solutions. *Contemporary Physics* **30,** 251–276 (July 1989).
126. Burton, W. K., Cabrera, N. & Frank, F. C. The Growth of Crystals and the Equilibrium Structure of their Surfaces. *Philosophical Transactions of the Royal Society A: Mathematical, Physical and Engineering Sciences* **243,** 299–358 (June 1951).
127. Williams, E. D. & Bartelt, N. C. Thermodynamic of Surface Morphology. *Science* **251,** 393–400 (Jan. 1991).
128. De Yoreo, J. J. & Vekilov, P. G. Principles of Crystal Nucleation and Growth. *Reviews in Mineralogy and Geochemistry* **54,** 57–93 (Jan. 2003).
129. Teichert, C. Self-organization of nanostructures in semiconductor heteroepitaxy. *Physics Reports* **365,** 335–432 (2002).
130. Donovan, E. P. Heat of crystallization and melting point of amorphous silicon. *Applied Physics Letters* **42,** 698 (1983).
131. Brodsky, M. H. & Lucovsky, G. Infrared Reflection Spectra of $\mathrm{Ga_{1\text{-}x}In_xAs}$: A New Type of Mixed-Crystal Behavior. *Physical Review Letters* **21,** 990–993 (1968).
132. Zellama, K. Crystallization in amorphous silicon. *Journal of Applied Physics* **50,** 6995 (1979).
133. Thomas, P. A., Brodsky, M. H., Kaplan, D. & Lepine, D. Electron spin resonance of ultrahigh vacuum evaporated amorphous silicon: In situ and ex situ studies. *Physical Review B* **18,** 3059–3073 (Oct. 1978).
134. Olson, G. L. & Roth, J. A. Kinetics of Solid Phase Crystallization in Amorphous Silicon. *Materials Science Reports* **3,** 1–78 (1988).
135. Spinella, C., Lombardo, S. & Priolo, F. Crystal grain nucleation in amorphous silicon. *Journal of Applied Physics* **84,** 5383 (1998).

136. Iverson, R. B. & Reif, R. Recrystallization of amorphized polycrystalline silicon films on SiO_2: Temperature dependence of the crystallization parameters. *Journal of Applied Physics* **62,** 1675 (1987).
137. Heinig, K. H. & Geiler, H.-D. Phenomenological theory of explosive solid phase crystallization of amorphous silicon I: Stationary Solutions. *Physica Status Solidi A* **92,** 421–430 (1985).
138. Heinig, K. H. & Geiler, H.-D. Phenomenological theory of explosive solid phase crystallization of amorphous silicon II: Dynamic Processes. *Physica Status Solidi A* **93,** 99–104 (1986).
139. Götz, G. Explosive Crystallization Processes in Silicon. *Applied Physics A* **40,** 29–36 (1986).
140. Geiler, H.-D., Glaser, E., Götz, G. & Wagner, M. Explosive crystallization in silicon. *Journal of Applied Physics* **59,** 3091–3098 (1986).
141. Geiler, H.-D. *et al.* Explosive crystallization phenomena in SOI structures. *Journal of Materials Research* **4,** 1473–1479 (Nov. 1989).
142. Ohdaira, K., Tomura, N., Ishii, S. & Matsumura, H. Lateral Crystallization Velocity in Explosive Crystallization of Amorphous Silicon Films Induced by Flash Lamp Annealing. *Electrochemical and Solid-State Letters* **14,** H372 (2011).
143. Thompson, M. *et al.* Melting Temperature and Explosive Crystallization of Amorphous Silicon during Pulsed Laser Irradiation. *Physical Review Letters* **52,** 2360–2363 (1984).
144. Auvert, G., Bensahel, D., Perio, A., Nguyen, V. T. & Rozgonyi, G. A. Explosive crystallization of a-Si films in both the solid and liquid phases. *Applied Physics Letters* **39,** 724–726 (Nov. 1981).
145. Leamy, H. J. Explosive crystallization of amorphous germanium. *Applied Physics Letters* **38,** 137 (1981).
146. Geiler, H.-D., Glaser, E. R., Götz, G. & Wagner, M. Explosive Liquid-Phase Crystallization of Ion-Implanted Silicon. *Physica Status Solidi A* **73,** K161–K163 (1982).
147. Andrä, G., Geiler, H.-D., Götz, G., Heinig, K. H. & Woittennek, H. Explosive Liquid-Phase Crystallization of Thin Si Films during Pulse Heating. *Physica Status Solidi A* **74,** 511–515 (1982).
148. Ohdaira, K., Fujiwara, T., Endo, Y., Nishizaki, S. & Matsumura, H. Explosive crystallization of amorphous silicon films by flash lamp annealing. *Journal of Applied Physics* **106,** 044907 (2009).
149. Ohdaira, K., Ishii, S., Tomura, N. & Matsumura, H. Microstructure of Polycrystalline Silicon Films Formed through Explosive Crystallization Induced by Flash Lamp Annealing. *Japanese Journal of Applied Physics* (2011).
150. Ohdaira, K., Sawada, K., Usami, N., Varlamov, S. & Matsumura, H. Large-Grain Polycrystalline Silicon Films Formed through Flash-Lamp-Induced Explosive Crystallization. *Japanese Journal of Applied Physics* **51,** 10NB15 (2012).
151. Loisel, B., Guenais, B., A, P. & Henoc, P. Flash Lamp Crystallization of Amorphous Silicon Films on Glass Substrates. *Thin Solid Films* **117,** 117–123 (1984).
152. Smith, M., McMahon, R., Voelskow, M., Panknin, D. & Skorupa, W. Modelling of flash-lamp-induced crystallization of amorphous silicon thin films on glass. *Journal of Crystal Growth* **285,** 249–260 (Nov. 2005).
153. Pécz, B. *et al.* Crystallization of amorphous-Si films by flash lamp annealing. *Applied Surface Science* **242,** 185–191 (Mar. 2005).
154. Trumbore, F. A. Solid Solubilities of Impurity Elements in Germanium and Silicon. *Bell System Technical Journal* **39,** 205–233 (1960).
155. Schnohr, C. S. Compound semiconductor alloys: From atomic-scale structure to bandgap bowing. *Applied Physics Reviews* **2,** 031304 (Sept. 2015).

156. Yin, Z. & Tang, X. A review of energy bandgap engineering in III-V semiconductor alloys for mid-infrared laser applications. *Solid-State Electronics* **51,** 6–15 (2007).
157. Heyns, M. & Tsai, W. Ultimate Scaling of CMOS Logic Devices with Ge and III-V Materials. *MRS Bulletin* **34,** 485–492 (July 2009).
158. Kim, D.-H. & del Alamo, J. A. 30-nm InAs PHEMTs With $f_T = 644\,\mathrm{GHz}$ and $f_{\mathrm{max}} = 681\,\mathrm{GHz}$. *IEEE Electron Device Letters* **31,** 806–808 (Aug. 2010).
159. Egard, M. *et al.* Vertical InAs Nanowire Wrap Gate Transistors with $f_t > 7\,\mathrm{GHz}$ and $f_{max} > 20\,\mathrm{GHz}$. *Nano Letters* **10,** 809–812 (Mar. 2010).
160. Gunapala, S. D., Levine, B. F., Ritter, D., Hamm, R. & Panish, M. B. InGaAs/InP long wavelength quantum well infrared photodetectors. *Applied Physics Letters* **58,** 2024–2026 (May 1991).
161. Phillips, J., Kamath, K. & Bhattacharya, P. Far-infrared photoconductivity in self-organized InAs quantum dots. *Applied Physics Letters* **72,** 2020 (1998).
162. Kim, E.-T., Madhukar, A., Ye, Z. & Campbell, J. C. High detectivity InAs quantum dot infrared photodetectors. *Applied Physics Letters* **84,** 3277 (2004).
163. Rogalski, A. Quantum well photoconductors in infrared detector technology. *Journal of Applied Physics* **93,** 4355 (2003).
164. Ting, D. Z. Y. *et al.* A high-performance long wavelength superlattice complementary barrier infrared detector. *Applied Physics Letters* **95,** 023508 (July 2009).
165. Campbell, J. C. & Madhukar, A. Quantum-dot infrared photodetectors. *Proceedings of the IEEE* **95,** 1815–1827 (Sept. 2007).
166. Xu, S. J. *et al.* Characteristics of InGaAs quantum dot infrared photodetectors. *Applied Physics Letters* **73,** 3153 (1998).
167. Chakrabarti, S. *et al.* High-performance mid-infrared quantum dot infrared photodetectors. *Journal of Physics D: Applied Physics* **38,** 2135–2141 (June 2005).
168. Liu, H. C., Gao, M., McCaffrey, J., Wasilewski, Z. R. & Fafard, S. Quantum dot infrared photodetectors. *Applied Physics Letters* **78,** 79–81 (Jan. 2001).
169. Liu, H. C. Quantum dot infrared photodetector. *Opto-Electronics Review* **11,** 1–5 (Mar. 2003).
170. Liu, H. C., Buchanan, M. & Wasilewski, Z. R. How good is the polarization selection rule for intersubband transitions? *Applied Physics Letters* **72,** 1682 (1998).
171. Krishna, S. Quantum dots-in-a-well infrared photodetectors. *Journal of Physics D: Applied Physics* **38,** 2142–2150 (2005).
172. Ariyawansa, G. *et al.* Effect of well width on three-color quantum dots-in-a-well infrared detectors. *IEEE Photonics Technology Letters* **17,** 1064–1066 (May 2005).
173. Ling, H. S., Wang, S. Y., Lee, C. P. & Lo, M. C. High quantum efficiency dots-in-a-well quantum dot infrared photodetectors with AlGaAs confinement enhancing layer. *Applied Physics Letters* **92,** 193506 (2008).
174. Raghavan, S. *et al.* Normal-incidence InAs/$\mathrm{In}_{0.15}\mathrm{Ga}_{0.85}\mathrm{As}$ quantum dots-in-a-well detector operating in the long-wave infrared atmospheric window (8-12 µm). *Journal of Applied Physics* **96,** 1036 (2004).
175. Gunapala, S. D. *et al.* 640 x 512 Pixels Long-Wavelength Infrared (LWIR) Quantum-Dot Infrared Photodetector (QDIP) Imaging Focal Plane Array. *IEEE Journal of Quantum Electronics* **43,** 230–237 (Mar. 2007).
176. Gaponenko. *Optical Properties of Semiconductor Nanocrystals* (Cambridge University Press, Cambridge, UK, 1998).
177. Parrish, W. Results of the IUCr precision lattice-parameter project. *Acta Crystallographica* **13,** 838–850 (Oct. 1960).
178. Welber, B., Kim, C., Cardona, M. & Rodriguez, S. Dependence of the indirect energy gap of silicon on hydrostatic pressure. *Solid State Communications* **17,** 1021–1024 (1975).

179. Desai, P. D. Thermodynamic Properties of Iron and Silicon. *Journal of Physical and Chemical Reference Data* **15,** 967–983 (1986).
180. Morin, F. J. & Maita, J. P. Electrical Properties of Silicon Containing Arsenic and Boron. *Physical Review* **96,** 28–35 (1 Oct. 1954).
181. Baker, J. F. C. & Hart, M. An absolute measurement of the lattice parameter of germanium using multiple-beam X-ray diffractometry. *Acta Crystallographica Section A* **31,** 364–367 (May 1975).
182. Macfarlane, G. G., McLean, T. P., Quarrington, J. E. & Roberts, V. Fine Structure in the Absorption-Edge Spectrum of Ge. *Physical Review* **108,** 1377–1383 (6 Dec. 1957).
183. Hall, H. T. The Melting Point of Germanium as a Function of Pressure to 180,000 Atmospheres. *The Journal of Physical Chemistry* **59,** 1144–1146 (1955).
184. Prince, M. B. Drift Mobilities in Semiconductors. I. Germanium. *Physical Review* **92,** 681–687 (3 Nov. 1953).
185. Mizuta, M., Fujieda, S., Matsumoto, Y. & Kawamura, T. Low Temperature Growth of GaN and AlN on GaAs Utilizing Metalorganics and Hydrazine. *Japanese Journal of Applied Physics* **25,** L945 (1986).
186. Powell, R. C., Lee, N.-E., Kim, Y.-W. & Greene, J. E. Heteroepitaxial wurtzite and zinc-blende structure GaN grown by reactive-ion molecular-beam epitaxy: Growth kinetics, microstructure, and properties. *Journal of Applied Physics* **73,** 189 (1993).
187. Ambacher, O. Thermal stability and desorption of Group III nitrides prepared by metal organic chemical vapor deposition. *Journal of Vacuum Science & Technology B* **14,** 3532–3542 (Nov. 1996).
188. Kim, J. G., Frenkel, A. C., Liu, H. & Park, R. M. Growth by molecular beam epitaxy and electrical characterization of Si-doped zinc blende GaN films deposited on β-SiC coated (001) Si substrates. *Applied Physics Letters* **65,** 91 (1994).
189. As, D. J. *et al.* p- and n-type cubic GaN and epilayers on GaAs. *Physical Review B* **54,** R11118–R11121 (Oct. 1996).
190. Osamura, K. & Murakami, Y. Relative Integrated Intensity of the X-Ray Diffraction and Effective Charge in $\mathrm{GaAs_{1\text{-}x}P_x}$ Compounds. *Japanese Journal of Applied Physics* **10,** 835 (1971).
191. Auvergne, D., Merle, P. & Mathieu, H. Phonon-assisted transitions in gallium-phosphide modulation spectra. *Physical Review B* **12,** 1371–1376 (4 Aug. 1975).
192. Tmar, M., Gabriel, A., Chatillon, C. & Ansara, I. Critical analysis and optimization of the thermodynamic properties and phase diagrams in the III-V compounds: The In-P and Ga-P systems. *Journal of Crystal Growth* **68,** 557–580 (1984).
193. Kao, Y. C. & Eknoyan, O. Electron and hole carrier mobilities for liquid phase epitaxially grown GaP in the temperature range 200-550 K. *Journal of Applied Physics* **54,** 2468 (1983).
194. Pond, S. F. & Handler, P. Flatband Electroreflectance of Gallium Arsenide. II. Comparison of Theory and Experiment. *Physical Review B* **8,** 2869–2879 (6 Sept. 1973).
195. Itagaki, K. & Yamaguchi, K. High temperature heat contents of III-V semiconductor systems. *Thermochimica Acta* **163,** 1–12 (1990).
196. Miki, H. & Otsubo, M. High Purity GaAs Crystals Grown by Liquid Phase Epitaxy. *Japanese Journal of Applied Physics* **10,** 509 (1971).
197. Mears, A. L. & Stradling, R. A. Cyclotron resonance and Hall measurements on the hole carriers in GaAs. *Journal of Physics C: Solid State Physics* **4,** L22 (1971).
198. Straumanis, M. E. & Kim, C. D. Lattice Parameters, Thermal Expansion Coefficients, Phase Width, and Perfection of the Structure of GaSb and InSb. *Journal of Applied Physics* **36,** 3822–3825 (1965).
199. Joullié, A., Eddin, A. Z. & Girault, B. Temperature dependence of the $L_6^c - \Gamma_6^c$ energy gap in gallium antimonide. *Physical Review B* **23,** 928–930 (2 Jan. 1981).

200. Yamaguchi, K., Itagaki, K. & Yazawa, A. High Temperature Heat Content Measurements of III-V (III: Al, Ga, In V: N, P, As, Sb) Compounds. *Journal of the Japan Institute of Metals and Materials* **53,** 764–770 (1989).
201. Turner, G. W. Molecular-beam epitaxial growth of high-mobility n-GaSb. *Journal of Vacuum Science & Technology B* **11,** 864 (May 1993).
202. Heller, M. W. & Hamerly, R. G. Hole transport in gallium antimonide. *Journal of Applied Physics* **57,** 4626–4632 (May 1985).
203. Giesecke, G. & Pfister, H. Präzisionsbestimmung der Gitterkonstanten von A^{III}-B^{V}-Verbindungen. *Acta Crystallographica* **11,** 369–371 (May 1958).
204. Bugajski, M. & Lewandowski, W. Concentration-dependent absorption and photoluminescence of n-type InP. *Journal of Applied Physics* **57,** 521–530 (1985).
205. Zhu, L. D., Chan, K. T. & Ballantyne, J. M. Very high mobility InP grown by low pressure metalorganic vapor phase epitaxy using solid trimethylindium source. *Applied Physics Letters* **47,** 47 (1985).
206. Benzaquen, M., Belache, B., Blaauw, C. & Bruce, R. A. Electrical characteristics of zinc-doped indium phosphide. *Journal of Applied Physics* **68,** 1694–1701 (Aug. 1990).
207. Lukeš, F. Electroreflectance spectrum of InAs in the range of E_0 and $E_0 + \Delta_0$ transitions. *Physica Status Solidi B* **84,** K113–K117 (1977).
208. Folberth, O. G., Madelung, O. & Weiss, H. Die elektrischen Eigenschaften von Indiumarsenid II. *Zeitschrift für Naturforschung A* **9,** 954–958 (Nov. 1953).
209. Fang, Z. M., Ma, K. Y., Jaw, D. H., Cohen, R. M. & Stringfellow, G. B. Photoluminescence of InSb, InAs, and InAsSb grown by organometallic vapor phase epitaxy. *Journal of Applied Physics* **67,** 7034–7039 (1990).
210. Tsukamoto, S., Bhattacharya, P., Chen, Y. C. & Kim, J. H. Transport properties of $InAs_xSb_{1-x}$ ($0 \leq x \leq 0.55$) on InP grown by molecular-beam epitaxy. *Journal of Applied Physics* **67,** 6819 (1990).
211. Schönwald, H. Die Beweglichkeit der langsamen und schnellen Löcher in Indiumantimonid. *Zeitschrift für Naturforschung A* **19,** 1276–1296 (Nov. 1964).
212. Hall, R. N., Fenner, G. E., Kingsley, J. D., Soltys, T. J. & Carlson, R. O. Coherent light emission from GaAs junctions. *Physical Review Letters* **9,** 366–369 (Nov. 1962).
213. Nathan, M. I., Dumke, W. P., Burns, G., Dill, F. H. & Lasher, G. Stimulated emission of radiation from GaAs p-n junctions. *Applied Physics Letters* **1,** 62 (1962).
214. Sarace, J. C., Kaiser, R. H., Whelan, J. M. & Leite, R. C. C. Injection Luminescence in GaAs by Direct Hole-Electron Recombination. *Physical Review* **137,** 623–626 (1965).
215. Grimmeiss, H. G. & Scholz, H. Efficiency of Recombination Radiation in GaP. *Physics Letters* **8,** 233–235 (1964).
216. Logan, R. A. Efficient green electroluminescence in nitrogen-doped GaP p-n junctions. *Applied Physics Letters* **13,** 139 (1968).
217. Pankove, J. I., Miller, E. A., Richman, D. & Berkeyheiser, J. E. Electroluminescence in GaN. *Journal of Luminescence* **4,** 63–66 (1971).
218. Pankove, J. I., Miller, E. A. & Berkeyheiser, J. E. GaN blue Light-emitting diodes. *Journal of Luminescence* **5,** 84–86 (1972).
219. Pankove, J. I., Miller, E. A. & Berkeyheiser, J. E. GaN yellow-light emitting diodes. *Journal of Luminescence* **6,** 54–60 (1973).
220. Maruska, H. P., Stevenson, D. A. & Pankove, J. I. Violet luminescence of Mg-doped GaN. *Applied Physics Letters* **22,** 303 (1973).
221. Kawabata, T., Matsuda, T. & Koike, S. GaN blue light emitting diodes prepared by metalorganic chemical vapor deposition. *Journal of Applied Physics* **56,** 2367 (1984).
222. Amano, H. *et al.* Electron beam effects on blue Luminescence of zinc-doped GaN. *Journal of Luminescence* **40&41,** 121–122 (1988).

223. Amano, H., Kito, M., Hiramatsu, K. & Akasaki, I. P-Type Conduction and in Mg-Doped and GaN Treated and with Low-Energy and Electron Beam and Irradiation. *Japanese Journal of Applied Physics* **28,** L2112–L2114 (1989).
224. Yoshimoto, N., Matsuoka, T., Sasaki, T. & Katsui, A. Photoluminescence of InGaN films grown at high temperature by metalorganic vapor phase epitaxy. *Applied Physics Letters* **59,** 2251 (1991).
225. Amano, H., Sawaki, N., Akasaki, I. & Toyoda, Y. Metalorganic vapor phase epitaxial growth of a high quality GaN film using an AlN buffer layer. *Applied Physics Letters* **48,** 353–355 (1986).
226. Nakamura, S. & Mukai, T. High-Quality InGaN Films Grown on GaN films. *Japanese Journal of Applied Physics* **31,** L1457–L1459 (1992).
227. Nakamura, S., Senoh, M. & Mukai, T. P-GaN/N-InGaN/N-GaN Double-Heterostructure and Blue-Light-Emitting Diodes. *Japanese Journal of Applied Physics* **32,** L8–L11 (1993).
228. Akasaki, I. & Amano, H. Crystal growth of column III nitrides and their applications to short wavelength light emitters. *Journal of Crystal Growth* **146,** 455–461 (1995).
229. Akasaki, I. *et al.* Stimulated Emission by Current Injection from an AlGaN/GaN/GaInN Quantum Well Device. *Japanese Journal of Applied Physics* **34,** L1517–L1519 (1995).
230. Nakamura, S. *et al.* InGaN-Based Multi-Quantum-Well-Structure Laser Diodes. *Japanese Journal of Applied Physics* **35,** L74–L76 (1996).
231. Nakamura, S. III-V Nitride Based Light-emitting Devices. *Solid State Communications* **102,** 237–248 (1997).
232. Nakamura, S. InGaN quantum-well structure blue LEDs and LDs. *Journal of Luminescence* **72–74,** 55–58 (1997).
233. Nakamura, S. Blue light emitting laser diodes. *Thin Solid Films* **343–344,** 345–349 (1999).
234. *The Nobel Prize in Physics 2014* Nobel Media AB 2014. <`http://www.nobelprize.org/nobel_prizes/physics/laureates/2014/`>.
235. Maruska, H. P. & Rhines, W. C. A modern perspective on the history of semiconductor nitride blue light sources. *Solid-State Electronics* **111,** 32–41 (Sept. 2015).
236. Hocevar, M. *et al.* InAs nanocrystals on SiO_2/Si by molecular beam epitaxy for memory applications. *Applied Physics Letters* **91,** 133114–133116 (Sept. 2007).
237. Hocevar, M., Regreny, P., Poncet, A., Gendry, M. & Souifi, A. Electron retention in InAs-nanocrystals embedded in SiO_2/Si for non-volatile memories. *Physica Status Solidi C* **5,** 3601–3604 (2008).
238. Marent, A., Nowozin, T., Geller, M. & Bimberg, D. The QD-Flash: a quantum dot-based memory device. *Semiconductor Science and Technology* **26,** 014026 (Dec. 2011).
239. Hocevar, M., Baboux, N., Poncet, A., Gendry, M. & Souifi, A. Large improvement of data retention in nanocrystal-Based memories on silicon using InAs quantum dots embedded in SiO_2. *IEEE Transactions on Electron Devices* **56,** 2657–2663 (Nov. 2009).
240. Marent, A. *et al.* 10^6 years extrapolated hole storage time in GaSb/AlAs quantum dots. *Applied Physics Letters* **91,** 242109 (2007).
241. Olson, J. US patent 4667059 A. US Patent 4,667,059 (1987).
242. Bailey, S. G., Raffaelle, R. & Emery, K. Space and terrestrial photovoltaics: synergy and diversity. *Progress in Photovoltaics: Research and Applications* **10,** 399–406 (2002).
243. Dimroth, F. High-efficiency solar cells from III-V compound semiconductors. *Physica Status Solidi C* **3,** 373–379 (Mar. 2006).

244. Dahal, R., Pantha, B., Li, J., Lin, J. Y. & Jiang, H. X. InGaN/GaN multiple quantum well solar cells with long operating wavelengths. *Applied Physics Letters* **94,** 063505 (Feb. 2009).
245. Bosi, M. & Pelosi, C. The potential of III-V semiconductors as terrestrial photovoltaic devices. *Progress in Photovoltaics: Research and Applications* **15,** 51–68 (2006).
246. Neufeld, C. J. *et al.* High quantum efficiency InGaN/GaN solar cells with 2.95 eV band gap. *Applied Physics Letters* **93,** 143502 (2008).
247. Jani, O., Ferguson, I., Honsberg, C. & Kurtz, S. Design and characterization of GaN/InGaN solar cells. *Applied Physics Letters* **91,** 132117 (2007).
248. Essig, S. *et al.* Realization of GaInP/Si Dual-Junction Solar Cells With 29.8 % 1-Sun Efficiency. *IEEE Journal of Photovoltaics,* 1–8 (2016).
249. Dimroth, F. *et al.* Four-Junction Wafer-Bonded Concentrator Solar Cells. *IEEE Journal of Photovoltaics* **6,** 343–349 (Jan. 2016).
250. Yamaguchi, M. Dislocation density reduction in heteroepitaxial III-V compound films on Si substrates for optical devices. *Journal of Materials Research* **6,** 376–384 (1991).
251. Lester, S. D., Ponce, F. A., Craford, M. G. & Steigerwald, D. A. High dislocation densities in high efficiency GaN-based light-emitting diodes. *Applied Physics Letters* **66,** 1249 (1995).
252. Yonezu, H. Control of structural defects in group III-V-N and alloys grown on Si. *Semiconductor Science and Technology* **17,** 762–768 (2002).
253. Mi, Z. III-V compound semiconductor nanostructures on silicon: epitaxial growth, properties, and applications in light emitting diodes and lasers. *Journal of Nanophotonics* **3,** 031602 (Jan. 2009).
254. Glaser, E. R., Bennett, B. R., Shanabrook, B. V. & Magno, R. Photoluminescence studies of self-assembled InSb, GaSb, and AlSb quantum dot heterostructures. *Applied Physics Letters* **68,** 3614–3616 (1996).
255. Tasco, V. *et al.* Structural and optical properties of InSb quantum dots for mid-IR applications. *Physica Status Solidi B-Basic Solid State Physics* **243,** 3959–3962 (Dec. 2006).
256. Moison, J. M. *et al.* Self-organized growth of regular nanometer-scale InAs dots on GaAs. *Applied Physics Letters* **64,** 196 (1994).
257. Ledentsov, N. N. *et al.* Quantum dot heterostructures: fabrication, properties, lasers (Review). *Semiconductors* **32,** 343–365 (Apr. 1998).
258. Marzin, J.-Y., Gérard, J.-M., Izraël, A. & Barrier, D. Photoluminescence of Single and InAs Quantum and Dots Obtained and by Self-Organized and Growth on GaAs. *Physical Review Letters* **73,** 716–719 (Aug. 1994).
259. Tersoff, J. Self-Organization in Growth of Quantum Dot Superlattices. *Physical Review Letters* **76,** 1675–1678 (1996).
260. Yoffe, A. Semiconductor quantum dots and related systems: electronic and optical, luminescence and related properties of low dimensional systems. *Advances in Physics* **50** (2001).
261. Frank, F. C. & van der Merve, J. H. One-Dimensional Dislocations. I. Static Theory. *Proceedings of the Royal Society of London. Series A, Mathematical and Physical Sciences* **198,** 205–216 (1949).
262. Frank, F. C. & Van der Merve, J. H. One-Dimensional Dislocations. II. Misfitting Monolayers and Oriented Overgrowth. *Proceedings of the Royal Society of London. Series A, Mathematical and Physical Sciences* **198,** 246–225 (1949).
263. Andersson, T. G., Chen, Z. G., Kulakovskii, V. D., Uddin, A. & Vallin, J. T. Variation of the critical layer thickness with In content in strained $\mathrm{In_xGa_{1\text{-}x}As}$-GaAs quantum wells grown by molecular beam epitaxy. *Applied Physics Letters* **51,** 752–754 (1987).

264. Fritz, I. J. *et al.* Dependence of critical layer thickness on strain for $In_xGa_{1\text{-}x}As$/GaAs strained-layer superlattices. *Applied Physics Letters* **46,** 967–969 (1985).
265. Roedel, R. J., Neida, A. . R. V., Caruso, R. & Dawson, L. R. The Effect of Dislocations in $Ga_{1\text{-}x}AI_1As$:Si Light-Emitting Diodes. *Journal of the Electrochemical Society* **126,** 637–641 (1979).
266. Dai, Q. *et al.* Internal quantum efficiency and nonradiative recombination coefficient of GaInN/GaN multiple quantum wells with different dislocation densities. *Applied Physics Letters* **94,** 111109 (2009).
267. Hur, J.-H. & Jeon, S. III-V compound semiconductors for mass-produced nano-electronics: theoretical studies on mobility degradation by dislocation. *Scientific Reports* **6,** 22001 (Feb. 2016).
268. Usui, A., Sunakawa, H., Sakai, H. & Yamaguchi, A. A. Thick GaN and Epitaxial Growth and with Low and Dislocation Density and by Hydride and Vapor Phase and Epitaxy. *Japanese Journal of Applied Physics* **36,** L899 (1997).
269. Nam, O.-H., Bremser, M. D., Zheleva, T. S. & Davis, R. F. Lateral epitaxy of low defect density GaN layers via organometallic vapor phase epitaxy. *Applied Physics Letters* **71,** 2638 (1997).
270. Vennéguès, P., Beaumont, B., Bousquet, V., Vaille, M. & Gibart, P. Reduction mechanisms for defect densities in GaN using one- or two-step epitaxial lateral overgrowth methods. *Journal of Applied Physics* **87,** 4175 (2000).
271. Fitzgerald, E. A. & Chand, N. Epitaxial Necking and in GaAs and Grown on and Pre-patterned Si and Substrates. *Journal of Electronic Materials* **20,** 839–853 (1991).
272. Langdo, T. A. *et al.* High quality Ge on Si by epitaxial necking. *Applied Physics Letters* **76,** 3700–3702 (June 2000).
273. Park, J.-S. *et al.* Defect reduction of selective Ge epitaxy in trenches on Si(001) substrates using aspect ratio trapping. *Applied Physics Letters* **90,** 052113 (2007).
274. Fiorenza, J. G. *et al.* Aspect Ratio Trapping: A Unique Technology for Integrating Ge and III-Vs with Silicon CMOS. *ECS Transactions* **33,** 963–976 (2010).
275. Xia, Y. *et al.* One-Dimensional Nanostructures: Synthesis. Characterisation, and Applications. *Advanced Materials* **15,** 353–389 (2003).
276. Wagner, R. S. & Ellis, W. C. Vapor-Liquid-Solid Mechanism of Single Crystal Growth. *Applied Physics Letters* **4,** 89 (1964).
277. Givargizov, E. Fundamental aspects of VLS growth. *Journal of Crystal Growth* **31,** 20–30 (1975).
278. Nguyen, P., Ng, H. T. & Meyyappan, M. Catalyst Metal Selection for Synthesis of Inorganic Nanowires. *Advanced Materials* **17,** 1773–1777 (2005).
279. Dubrovskii, V. G., Sibirev, N. V., Cirlin, G. E., Harmand, J. C. & Ustinov, V. M. Theoretical analysis of the vapor-liquid-solid mechanism of nanowire growth during molecular beam epitaxy. *Physical Review E* **73,** 021603 (Feb. 2006).
280. Ihn, S.-G., Song, J.-I., Kim, Y.-H. & Lee, J. Y. GaAs nanowires on Si substrates grown by a solid source molecular beam epitaxy. *Applied Physics Letters* **89,** 053106 (2006).
281. Ihn, S.-G. & Song, J.-I. InAs nanowires on Si and substrates grown by solid source molecular beam epitaxy. *Nanotechnology* **18,** 355603–355606 (2007).
282. Chuang, L. C. *et al.* Critical diameter for III-V nanowires grown on lattice-mismatched substrates. *Applied Physics Letters* **90,** 043115 (2007).
283. Tateno, K., Hibino, H., Gotoh, H. & Nakano, H. Vertical GaP nanowires arranged at atomic steps on Si(111) substrates. *Applied Physics Letters* **89,** 033114 (2006).
284. Mårtensson, T. *et al.* Epitaxial III-V Nanowires on Silicon. *Nano Letters* **4,** 1987–1990 (Oct. 2004).
285. Caroff, P. *et al.* Controlled polytypic and twin-plane superlattices in III-V nanowires. *Nature Nanotechnology* **4,** 50–55 (Nov. 2008).

286. Bao, J. *et al.* Optical Properties of Rotationally Twinned InP Nanowire Heterostructures. *Nano Letters* **8,** 836–841 (Mar. 2008).
287. Stiles, M. D. & Hamann, D. R. Electron transmission through silicon stacking faults. *Physical Review B* **41,** 5280–5282 (Mar. 1990).
288. Joyce, H. J. *et al.* Twin-Free Uniform Epitaxial GaAs Nanowires Grown by a Two-Temperature Process. *Nano Letters* **7,** 921–926 (Apr. 2007).
289. Tchernycheva, M. *et al.* Growth of GaN free-standing nanowires by plasma-assisted molecular beam epitaxy: Structural and optical characterization. *Nanotechnology* **18,** 385306 (2007).
290. Bar-Sadan, M., Barthel, J., Shtrikman, H. & Houben, L. Direct Imaging of Single Au Atoms Within GaAs Nanowires. *Nano Letters* **12,** 2352–2356 (May 2012).
291. Allen, J. E. *et al.* High-resolution detection of Au catalyst atoms in Si nanowires. *Nature Nanotechnology* **3,** 168–173 (Feb. 2008).
292. Gu, G. *et al.* Growth and electrical transport of germanium nanowires. *Journal of Applied Physics* **90,** 5747–5751 (Dec. 2001).
293. Colombo, C., Spirkoska, D., Frimmer, M., Abstreiter, G. & i Morral, A. F. Ga-assisted catalyst-free growth mechanism of GaAs nanowires by molecular beam epitaxy. *Physical Review B* **77,** 155326 (Apr. 2008).
294. Jabeen, F., Grillo, V., Rubini, S. & Martelli, F. Self-catalyzed growth of GaAs and nanowires on cleaved Si and by molecular beam epitaxy. *Nanotechnology* **19,** 275711 (2008).
295. Plissard, S. *et al.* Gold-free growth of GaAs nanowires on silicon: arrays and polytypism. *Nanotechnology* **21,** 385602 (Sept. 2010).
296. Dimakis, E. *et al.* In situ doping of catalyst-free InAs nanowires with Si: Growth, polytypism, and local vibrational modes of Si. *Applied Physics Letters* **103,** 143121 (Sept. 2013).
297. Noborisaka, J., Motohisa, J. & Fukui, T. Catalyst-free growth of GaAs nanowires by selective-area metalorganic vapor-phase epitaxy. *Applied Physics Letters* **86,** 213102 (2005).
298. Mohan, P., Motohisa, J. & Fukui, T. Controlled growth of highly uniform, axial/radial direction-defined, individually addressable InP nanowire arrays. *Nanotechnology* **16,** 2903–2907 (2005).
299. Tomioka, K., Motohisa, J., Hara, S. & Fukui, T. Control of InAs Nanowire Growth Directions on Si. *Nano Letters* **8,** 3475–3480 (Oct. 2008).
300. Tomioka, K., Tanaka, T., Hara, S., Hiruma, K. & Fukui, T. III-V nanowires on Si substrate: selective-area growth and device applications. *IEEE Journal of Selected Topics in Quantum Electronics* **17,** 1112–1129 (July 2011).
301. Borg, M. *et al.* Vertical III-V nanowire device integration on Si(100). *Nano Letters* **14,** 1914–1920 (Apr. 2014).
302. Björk, M. T. *et al.* One-dimensional Steeplechase for Electrons Realized. *Nano Letters* **2,** 87–89 (Feb. 2002).
303. Hocevar, M. *et al.* Growth and optical properties of axial hybrid III-V/silicon nanowires. *Nature Communications* **3,** 1266 (Dec. 2012).
304. Tomioka, K., Motohisa, J., Hara, S., Hiruma, K. & Fukui, T. GaAs/AlGaAs core multishell nanowire-based light-emitting diodes on Si. *Nano Letters* **10,** 1639–1644 (May 2010).
305. Dimakis, E. *et al.* Coaxial multishell (In,Ga)As/GaAs nanowires for near-infrared emission on Si substrates. *Nano Letters* **14,** 2604–2609 (May 2014).
306. Tomioka, K. & Fukui, T. Vertical III-V nanowire-channel on Si. *Semiconductors, Dielectrics, and Metals for Nanoelectronics 11* **58,** 99–114 (Aug. 2013).

307. Tomioka, K. & Fukui, T. Recent progress in integration of III-V nanowire transistors on Si substrate by selective-area growth. *Journal of Physics D: Applied Physics* **47,** 394001 (2014).
308. Thelander, C. *et al.* Single-electron transistors in heterostructure nanowires. *Applied Physics Letters* **83,** 2052 (2003).
309. Moselund, K. E. *et al.* InAs-Si nanowire heterojunction tunnel FETs. *IEEE Electron Device Letters* **33,** 1453–1455 (2012).
310. Yang, T., Hertenberger, S., Morkötter, S., Abstreiter, G. & Koblmüller, G. Size, composition, and doping effects on In(Ga)As nanowire/Si tunnel diodes probed by conductive atomic force microscopy. *Applied Physics Letters* **101** (Dec. 2012).
311. Qian, F., Gradecăk, S., Li, Y., Wen, C.-Y. & Lieber, C. M. Core/Multishell Nanowire Heterostructures as Multicolor, High-Efficiency Light-Emitting Diodes. *Nano Letters* **5,** 2287–2291 (Nov. 2005).
312. Chuang, L. C. *et al.* GaAs-based nanoneedle light emitting diode and avalanche photodiode monolithically integrated on a silicon substrate. *Nano Letters* **11,** 385–390 (Feb. 2011).
313. Chen, R. *et al.* Nanolasers grown on silicon. *Nature Photonics* **5,** 170–175 (Mar. 2011).
314. Lee, A., Liu, H. & Seeds, A. Semiconductor III-V lasers monolithically grown on Si substrates. *Semiconductor Science and Technology* **28,** 015027 (2013).
315. Moutanabbir, O. & Gösele, U. Heterogeneous integration of compound semiconductors. *Annual Review of Materials Research* **40,** 469–500 (2010).
316. Gösele, U. & Tong, Q.-Y. Semiconductor Wafer Bonding. *Annual Review of Materials Research* **28,** 215–241 (1998).
317. Lehmann, V., Mitani, K., Stengl, R., Mii, T. & Gösele, U. Bubble-Free Wafer and Bonding of GaAs and InP on Silicon and in a Microcleanroom. *Japanese Journal of Applied Physics* **28,** L2141–L2143 (Dec. 1989).
318. Pasquariello, D., Camacho, M., Ericsson, F. & Hjort, K. Crystalline Defects and in InP-to-Silicon and Direct Wafer and Bonding. *Japanese Journal of Applied Physics* **40,** 4837–4844 (Aug. 2001).
319. Yu, L. S. *et al.* Photocurrent method for characterizing the interface of hydrophobically bonded Si wafers. *Applied Physics Letters* **82,** 916–918 (Feb. 2003).
320. Akatsu, T., Plössl, A., Scholz, R., Stenzel, H. & Gösele, U. Wafer bonding of different III-V compound semiconductors by atomic hydrogen surface cleaning. *Journal of Applied Physics* **90,** 3856–3862 (Oct. 2001).
321. Tong, Q.-Y., Gan, Q., Hudson, G., Fountain, G. & Enquist, P. Low temperature InP/Si wafer bonding. *Applied Physics Letters* **84,** 732–734 (Feb. 2004).
322. Chiao, M. & Lin, L. Hermetic wafer bonding based on rapid thermal processing. *Sensors and Actuators A: Physical* **91,** 398–402 (2001).
323. Esashi, M. Wafer level packaging of MEMS. *Journal of Micromechanics and Microengineering* **18,** 073001 (May 2008).
324. Kwon, Y., Seok, J., Lu, J.-Q., Cale, T. S. & Gutmann, R. J. Thermal Cycling Effects on Critical Adhesion Energy and Residual Stress in Benzocyclobutene-Bonded Wafers. *Journal of the Electrochemical Society* **152,** G286–G294 (2005).
325. Lu, J.-Q. 3-D Hyperintegration and Packaging Technologies for Micro-Nano Systems. *Proceedings of the IEEE* **97,** 18–30 (Jan. 2009).
326. Lee, S. H., Chen, K.-N. & Lu, J. J.-Q. Wafer-to-Wafer Alignment for Three-Dimensional Integration: A Review. *Journal of Microelectromechanical Systems* **20,** 885–898 (Aug. 2011).
327. Roelkens, G. *et al.* III-V/Si photonics by die to wafer bonding. *Materials Today* **10,** 36–43 (July 2007).

328. Ghosh, S. *et al.* Optical Isolator for TE Polarized Light Realized by Adhesive Bonding of Ce:YIG on Silicon-on-Insulator Waveguide Circuits. *IEEE Photonics Journal* **5,** 6601108–6601108 (June 2013).
329. Khan, S., Chiles, J., Ma, J. & Fathpour, S. Silicon-on-nitride waveguides for mid- and near-infrared integrated photonics. *Applied Physics Letters* **102,** 121104 (2013).
330. Niklaus, F., Stemme, G., Lu, J. .-.-Q. & Gutmann, R. J. Adhesive wafer bonding. *Journal of Applied Physics* **99,** 031101 (2006).
331. Yacobi, B. G., Martin, S., Davis, K., Hudson, A. & Hubert, M. Adhesive bonding in microelectronics and photonics. *Journal of Applied Physics* **91,** 6227–6262 (May 2002).
332. Gui, C., Elwenspoek, M., Gardeniers, J. G. E. & Lambeck, P. V. Present and Future Role of Chemical Mechanical Polishing in Wafer Bonding. *Journal of the Electrochemical Society* **145,** 2198–2204 (June 1998).
333. Liang, D. *et al.* High-Quality 150 mm InP-to-Silicon Epitaxial Transfer for Silicon Photonic Integrated Circuits. *Electrochemical and Solid-State Letters* **12,** H101–H104 (2009).
334. McClelland, R. W., Bozler, C. O. & Fan, J. C. C. A technique for producing epitaxial films on reuseable substrates. *Applied Physics Letters* **37,** 560–562 (Sept. 1980).
335. Yonehara, T., Sakaguchi, K. & Sato, N. Epitaxial layer transfer by bond and etch back of porous Si. *Applied Physics Letters* **64,** 2108–2110 (Apr. 1994).
336. Yablonovitch, E., Gmitter, T., Harbison, J. P. & Bhat, R. Extreme selectivity in the lift-off of epitaxial GaAs films. *Applied Physics Letters* **51,** 2222–2224 (Dec. 1987).
337. Bruel, M. *et al.* *"Smart": a promising new SOI material technology* in *SOI Conference, 1995. Proceedings., 1995 IEEE International* (Oct. 1995), 178–179.
338. Chao, Y.-L., Scholz, R., Reiche, M., Gösele, U. & Woo, J. S. C. Characteristics of Germanium-on-Insulators and Fabricated by Wafer and Bonding and Hydrogen. *Japan-ese Journal of Applied Physics* **45,** 8565–8570 (2006).
339. Jalaguier, E. *et al.* Transfer of 3in GaAs film on silicon substrate by proton implantation process. *Electronics Letters* **34,** 408–409 (Feb. 1998).
340. Tong, Q.-Y., Chao, Y.-L., Huang, L.-J. & Gösele, U. Low temperature InP layer transfer. *Electronics Letters* **35,** 341–342 (Feb. 1999).
341. Hobart, K. D. & Kub, F. J. Transfer of GaSb thin film to insulating substrate via separation by hydrogen implantation. *Electronics Letters* **35,** 675–676 (Apr. 1999).
342. Moutanabbir, O. *et al.* Stress Adjustment and Bonding of H-Implanted 2 in. Freestanding GaN Wafer: The Concept of Double-Sided Splitting. *Electrochemical and Solid-State Letters* **12,** H105–H108 (2009).
343. Cioccio, L. D., Jalaguier, E. & Letertre, F. III-V layer transfer onto silicon and applications. *Physica Status Solidi A* **202,** 509–515 (Mar. 2005).
344. Kim, S. *et al.* Direct wafer bonding technology for large-scale InGaAs-on-insulator transistors. *Applied Physics Letters* **105,** 043504 (July 2014).
345. Yokoyama, M. *et al.* Thin Body III-V-Semiconductor-on-Insulator Metal-Oxide-Semiconductor Field-Effect Transistors on Si Fabricated Using Direct Wafer Bonding. *Applied Physics Express* **2,** 124501 (2009).
346. Yokoyama, M. *et al.* Formation of III-V-on-insulator and structures on Si and by direct wafer bonding. *Semiconductor Science and Technology* **28,** 094009–094018 (2013).
347. Geum, D.-M. *et al.* Ultra-high-throughput Production of III-V/Si Wafer for Electronic and Photonic Applications. *Scientific Reports* **6,** 20610 (Feb. 2016).
348. Dai, X., Nguyen, B. M., Hwang, Y., Soci, C. & Dayeh, S. A. Novel Heterogeneous Integration Technology of III-V Layers and InGaAs FinFETs to Silicon. *Advanced Functional Materials* **24,** 4420–4426 (July 2014).

349. Ko, H. *et al.* Ultrathin compound semiconductor on insulator layers for high-performance nanoscale transistors. *Nature* **468,** 286–289 (Nov. 2010).
350. Wang, C. *et al.* Self-aligned, extremely high frequency III-V metal-oxide-semiconductor field-effect transistors on rigid and flexible substrates. *Nano Letters* **12,** 4140–4145 (Aug. 2012).
351. Nah, J. *et al.* III-V complementary metal-oxide-semiconductor electronics on silicon substrates. *Nano Letters* **12,** 3592–3595 (July 2012).
352. Takagi, S. *et al.* III-V/Ge CMOS Device Technologies for High Performance Logic Applications. *ECS Transactions* **53,** 85–96 (2013).
353. Takagi, S. *et al.* III-V/Ge channel MOS and device technologies in nano CMOS and era. *Japanese Journal of Applied Physics* **54,** 06FA01 (2015).
354. Chen, S. *et al.* Electrically pumped continuous-wave III-V quantum dot lasers on silicon. *Nature Photonics* **10,** 307–311 (Mar. 2016).
355. Cao, Y. C. Impurities Enhance Semiconductor Nanocrystal Performance. *Science* **332,** 48–49 (Apr. 2011).
356. Bondarenko, O., Fang, C.-Y., Vallini, F., Smalley, J. S. T. & Fainman, Y. Extremely compact hybrid III-V/SOI lasers: design and fabrication approaches. *Optics Express* **23,** 2696–2712 (Jan. 2015).
357. Keyvaninia, S. *et al.* III-V-on-silicon multi-frequency lasers. *Optics Express* **21,** 13675 (May 2013).
358. Justice, J. *et al.* Wafer-scale integration of group III-V lasers on silicon using transfer printing of epitaxial layers. *Nature Photonics* **6,** 610–614 (Sept. 2012).
359. Roelkens, G. *et al.* III-V/silicon photonics for on-chip and intra-chip optical interconnects. *Laser & Photonics Reviews* **4,** 751–779 (2010).
360. Tanabe, K., i Morral, A. F., Atwater, H. A., Aiken, D. J. & Wanlass, M. W. Direct-bonded GaAs/InGaAs tandem solar cell. *Applied Physics Letters* **89,** 102106 (2006).
361. Tanabe, K., Watanabe, K. & Arakawa, Y. III-V/Si hybrid photonic devices by direct fusion bonding. *Scientific Reports* **2,** 349–354 (Apr. 2012).
362. Dimroth, F. *et al.* Wafer bonded four-junction GaInP/GaAs//GaInAsP/GaInAs concentrator solar cells with 44.7 % efficiency. *Progress in Photovoltaics: Research and Applications* **22,** 277–282 (Jan. 2014).
363. Shimizu-Iwayama, T. *et al.* Visible photoluminescence related to Si precipitates in Si^+-implanted SiO_2. *Journal of Physics: Condensed Matter* **5,** L375 (1993).
364. Mutti, P. *et al.* Room-temperature visible luminescence from silicon nanocrystals in silicon implanted SiO_2 layers. *Applied Physics Letters* **66,** 851–853 (Feb. 1995).
365. Mestanza, S. N. M., Doi, I., Swart, J. W. & Frateschi, N. C. Fabrication and characterization of Ge nanocrystalline growth by ion implantation in SiO_2 matrix. *Journal of Materials Science* **42,** 7757–7761 (June 2007).
366. Yu, C., Chao, D., Chen, Y.-F. & Liang, J. Photoluminescent characteristics of ion beam synthesized Ge nanoparticles in thermally grown SiO_2 films. *Nuclear Instruments and Methods in Physics Research Section B-Beam Interactions with Materials and Atoms* **307,** 171–176 (July 2013).
367. Lifshitz, I. M. & Slyozov, V. V. The kinetics of precipitation from supersaturated solid solutions. *Journal of Physics and Chemistry of Solids* **19,** 35–50 (1961).
368. Voorhees, P. W. Ostwald ripening of two-phase mixtures. *Annual Review of Materials Research* **22,** 197–215 (1992).
369. Li, K.-D. Modeling of nanocluster formation by ion beam implantation. *Journal of Applied Physics* **110,** 044318 (2011).
370. White, C. W. *et al.* GaAs nanocrystals formed by sequential ion implantation. *Journal of Applied Physics* **79,** 1876–1880 (Feb. 1996).

371. Kanemitsu, Y., Tanaka, H., Kushida, T., Min, K. S. & Atwater, H. A. GaAs nanocrystals fabricated by sequential ion implantation: structural and luminescence properties. *Physica E: Low-dimensional Systems and Nanostructures* **7,** 322–325 (May 2000).
372. Kanemitsu, Y. *et al.* Visible light emission from GaAs nanocrystals in SiO_2 films fabricated by sequential ion implantation. *Physical Review B* **62,** 5100–5108 (Aug. 2000).
373. White, C. W., Budai, J. D., Zhu, J. G., Withrow, S. P. & Aziz, M. J. Ion-beam synthesis and stability of GaAs nanocrystals in silicon. *Applied Physics Letters* **68,** 2389 (1996).
374. Budai, J. D., White, C. W., Withrow, S. P., Zuhr, R. A. & Zhu, J. G. *Synthesis, Optical Properties, and Microstructure of Semiconductor Nanocrystals Formed by Ion Implantation* in *Symposium Q – Advances in Microcrystalline and Nanocrystalline* **452** (1996), 89–98.
375. White, C. W. *et al.* Encapsulated semiconductor nanocrystals formed in insulators by ion beam synthesis. *Nuclear Instruments & Methods in Physics Research Section B-Beam Interactions with Materials and Atoms* **141,** 228–240 (May 1998).
376. White, C. W. *et al.* Formation of CdS and CdSe nanocrystals by sequential implantation. *Nuclear Instruments & Methods in Physics Research Section B-Beam Interactions with Materials and Atoms* **148,** 991–996 (Jan. 1999).
377. Tchebotareva, A. L., Brebner, J. L., Roorda, S. & White, C. W. Properties of InAs nanocrystals in silicon formed by sequential ion implantation. *Nuclear Instruments & Methods in Physics Research Section B-Beam Interactions with Materials and Atoms* **175,** 187–192 (Apr. 2001).
378. Tchebotareva, A., Brebner, J. L., Roorda, S., Desjardins, P. & White, C. W. Structural properties of InAs nanocrystals formed by sequential implantation of In and As ions in the Si (100) matrix. *Journal of Applied Physics* **92,** 4664–4671 (Oct. 2002).
379. Meldrum, A., Boatner, L. A., White, C. W. & Ewing, R. C. Ion irradiation effects in nonmetals: formation of nanocrystals and novel microstructures. *Materials Research Innovations* **3,** 190–204 (Mar. 2000).
380. Meldrum, A., Boatner, L. A. & White, C. W. Nanocomposites formed by ion implantation: Recent developments and future opportunities. *Nuclear Instruments & Methods in Physics Research Section B-Beam Interactions with Materials and Atoms* **178,** 7–16 (May 2001).
381. Meldrum, A., Haglund, R. F., Boatner, L. A. & White, C. W. Nanocomposite materials formed by ion implantation. *Advanced Materials* **13,** 1431–1444 (Oct. 2001).
382. Budai, J. D. *et al.* Controlling the size, structure and orientation of semiconductor nanocrystals using metastable phase recrystallization. *Nature* **390,** 384–386 (Nov. 1997).
383. Komarov, F. *et al.* Formation of InAs nanocrystals in Si by high-fluence ion implantation. *Nuclear Instruments & Methods in Physics Research Section B-Beam Interactions with Materials and Atoms* **266,** 3557–3564 (Aug. 2008).
384. Komarov, F. *et al.* Nanocrystal- and Dislocation-Related Luminescence in Si Matrix with InAs Nanocrystals. *Acta Physica Polonica A* **120,** 204–207 (July 2011).
385. Komarov, F. *et al.* Structure and optical properties of silicon layers with GaSb nanocrystals created by ion-beam synthesis. *Physica Status Solidi A* **209,** 148–152 (Jan. 2012).
386. Khelifi, R. *et al.* Ion beam synthesis of embedded III-As nanocrystals in silicon substrate. *Physica Status Solidi C* **12,** 55–59 (Oct. 2015).
387. Prucnal, S. *et al.* Formation of InAs quantum dots in silicon by sequential ion implantation and flash lamp annealing. *Applied Physics B-Lasers and Optics* **101,** 315–319 (Oct. 2010).

388. Prucnal, S. *et al.* Optical and microstructural properties of self-assembled InAs quantum structures in silicon. *Central European Journal of Physics* **9,** 338–343 (Apr. 2011).
389. Prucnal, S. *et al.* InP nanocrystals on silicon for optoelectronic applications. *Nanotechnology* **23,** 485204–485211 (Dec. 2012).
390. Prucnal, S. *et al.* Conductivity type and crystal orientation of GaAs nanocrystals fabricated in silicon by ion implantation and flash lamp annealing. *Nuclear Instruments & Methods in Physics Research Section B-Beam Interactions with Materials and Atoms* **312,** 104–109 (Oct. 2013).
391. Prucnal, S. *et al.* n-InAs nanopyramids fully integrated into Silicon. *Nano Letters* **11,** 2814–2818 (July 2011).
392. Prucnal, S. *et al.* III-V/Si on silicon-on-insulator platform for hybrid nanoelectronics. *Journal of Applied Physics* **115,** 074306–074313 (Feb. 2014).
393. Prucnal, S. *et al.* III-V semiconductor nanocrystal formation in silicon nanowires via liquid-phase epitaxy. *Nano Research* **7,** 1769–1776 (Sept. 2014).
394. Glaser, M. *et al.* Synthesis, Morphological, and Electro-optical Characterizations of Metal/Semiconductor Nanowire Heterostructures. *Nano Letters* **16,** 3507–3513 (June 2016).
395. Wutzler, R. *et al.* Liquid phase epitaxy of binary III-V nanocrystals in thin Si layers triggered by ion implantation and flash lamp annealing. *Journal of Applied Physics* **117,** 175307 (2015).
396. Wutzler, R. *et al.* III-V nanocrystal formation in ion-implanted Ge and Si via liquid phase epitaxy during short-time flash lamp annealing. *Materials Science in Semiconductor Processing* **42,** 166–169 (Feb. 2016).
397. Ziegler, J. F. Srim-2003. *Nuclear Instruments & Methods in Physics Research Section B-Beam Interactions with Materials and Atoms* **219,** 1027–1036 (June 2004).
398. Saleh, B. E. A. & Teich, M. C. *Fundamentals of Photonics* 2nd ed. (ed Goodman, J. W.) (John Wiley & Sons, Inc., New York, NY, 2007).
399. *FlexPDE 6, www.pdesolutions.com, 2014* 6th ed. PDE Solutions Inc. (Spokane Valley, WA, USA). <`www.pdesolutions.com`>.
400. Du, W., Yang, X., Povolny, H., Liao, X. & Deng, X. Impact of hydrogen dilution on microstructure and optoelectronic properties of silicon films deposited using trisilane. *Journal of Physics D: Applied Physics* **38,** 838–842 (Mar. 2005).
401. Kim, H. Y., Lee, K. Y. & Lee, J. Y. The influence of hydrogen dilution ratio on the crystallization of hydrogenated amorphous silicon films prepared by plasma-enhanced chemical vapor deposition. *Thin Solid Films* **302,** 17–24 (June 1997).
402. Zhu, F. R., Kohara, H., Fuyuki, T. & Matsunami, H. Structural and optical properties of polycrystalline silicon thin films deposited by the plasma enhanced chemical vapour deposition method. *Japanese Journal of Applied Physics Part 1 - Regular Papers, Short Notes & review Papers* **35,** 3321–3326 (June 1996).
403. Vetterl, O. *et al.* Intrinsic microcrystalline silicon: A new material for photovoltaics. *Solar Energy Materials and Solar Cells* **62,** 97–108 (2000).
404. Watanabe, M. & Tooi, A. Formation of SiO_2 Films by Oxygen-Ion Bombardment. *Japanese Journal of Applied Physics* **5,** 737–738 (1966).
405. Izumi, K., Ōmura, Y. & Sakai, T. Simox technology and its application to CMOS LSIS. *Journal of Electronic Materials* **12,** 845–861 (1983).
406. Sharkeev, Y. P., Gritsenko, B. P., Fortuna, S. V. & Perry, A. J. Modification of metallic materials and hard coatings using metal ion implantation. *Vacuum* **52,** 247–254 (1999).
407. Renk, T. J. *et al.* Materials modification using intense ion beams. *Proceedings of the IEEE* **92,** 1057–1081 (2004).
408. Keller, A. & Facsko, S. Ion-Induced Nanoscale Ripple Patterns on Si Surfaces: Theory and Experiment. *Materials* **3,** 4811–4841 (Oct. 2010).

409. Jeynes, C. *et al.* Elemental thin film depth profiles by ion beam analysis using simulated annealing - a new tool. *Journal of Physics D: Applied Physics* **36,** R97–R126 (Apr. 2003).
410. Smith, J. E., Brodsky, M. H., Crowder, B. L. & Nathan, M. I. Raman Spectra of Amorphous Si and Related Tetrahedrally Bonded Semiconductors. *Physical Review Letters* **26,** 642–646 (Mar. 1971).
411. Winer, K. Structural and vibrational properties of a realistic model of amorphous silicon. *Physical Review B* **35,** 2366–2374 (1987).
412. Temple, P. A. & Hathaway, C. E. Multiphonon Raman Spectrum of Silicon. *Physical Review B* **7,** 3685–3697 (Apr. 1973).
413. Aoki, K., Anastassakis, E. & Cardona, M. Dependence of raman frequencies and scattering intensities on pressure in GaSb, InAs, and InSb semiconductors. *Physical Review B* **30,** 681–687 (July 1984).
414. Holtz, M., Zallen, R., Geissberger, A. E. & Sadler, R. A. Raman-scattering studies of silicon-implanted gallium arsenide: The role of amorphicity. *Journal of Applied Physics* **59,** 1946–1951 (Mar. 1986).
415. Giannozzi, P., de Gironcoli, S., Pavone, P. & Baroni, S. Ab initio calculation of phonon dispersions in semiconductors. *Physical Review B Condensed Matter* **43,** 7231–7242 (Mar. 1991).
416. Bermejo, D. & Cardona, M. Raman scattering in pure and hydrogenated amorphous Germanium and Silicon. *Journal of Non-Crystalline Solids* **32,** 405–419 (1979).
417. Weinstein, B. A. & Cardona, M. Second-Order Raman Spectrum of Germanium. *Physical Review B* **7,** 2545–2551 (Mar. 1973).
418. Rasband, W. S. *ImageJ* U. S. National Institutes of Health (Bethesda, Maryland, USA, 1997-2015). <`http://imagej.nih.gov/ij/`>.
419. Wagner, J., Koidl, P. & Newman, R. C. Resonance effects in Raman scattering by dopant-induced local vibrational modes in III-V semiconductors. *Applied Physics Letters* **59,** 1729 (1991).
420. Addinall, R. *et al.* Local vibrational mode spectroscopy of Si donors and Be acceptors in MBE InAs and InSb studied by infrared absorption and Raman scattering. *Semiconductor Science and Technology* **6,** 147–154 (1991).
421. Uematsu, M. Raman scattering of Si localized vibrational modes in InAs. *Journal of Applied Physics* **69,** 1781 (1991).
422. Theis, W. M. & Spitzer, W. G. High-resolution measurements of localized vibrational mode infrared absorption of Si-doped GaAs. *Journal of Applied Physics* **56,** 890 (1984).
423. Wagner, J., Ramsteiner, M., Stolz, W., Hauser, M. & Ploog, K. Incorporation of Si in δ-doped GaAs studied by local vibrational mode spectroscopy. *Applied Physics Letters* **55,** 978 (1989).
424. Murray, R. *et al.* The calibration of the strength of the localized vibrational modes of silicon impurities in epitaxial GaAs revealed by infrared absorption and Raman scattering. *Journal of Applied Physics* **66,** 2589–2596 (Sept. 1989).
425. Prucnal, S. *et al.* III-V quantum dots in dielectrics made by ion implantation and flash lamp annealing. *Acta Physica Polonica A* **123,** 935–938 (May 2013).
426. Yamazaki, S., Ushirokawa, A. & Katoda, T. Effect of clusters on long-wavelength optical phonons in $\mathrm{Ga_{1-x}In_xAs}$. *Journal of Applied Physics* **51,** 3722 (1980).
427. Pearsall, T. P. Single longitudinal-mode optical phonon scattering in $\mathrm{Ga_{0.47}In_{0.53}As}$. *Applied Physics Letters* **42,** 436 (1983).
428. Williamson, G. K. & Hall, W. H. X-ray line broadening from filed aluminium and wolfram. *Acta Metallurgica* **1,** 22–31 (Jan. 1953).
429. Vegard, L. Die Konstitution der Mischkristalle und die Raumfüllung der Atome. *Zeitschrift für Physik* **5,** 17–26 (1921).

430. Villaggi, E. *et al.* Deviation from Vegard and Law in Lattice-Matched and InGaAs/InP Epitaxial and Structures. *Japanese Journal of Applied Physics* **41,** 1000–1003 (2002).
431. Bocchi, C. *et al.* Measurement of aluminum concentration in the $Ga_{1-x}Al_xSb/GaSb$ epitaxial system. *Journal of Applied Physics* **86,** 1298–1305 (Aug. 1999).
432. Fournet, G. Étude de la loi de Vegard. *Journal de Physique et le Radium* **14,** 374–380 (1953).
433. Camphausen, D. L., Connell, G. A. N. & Paul, W. Calculation of Energy-Band Pressure Coefficients from the Dielectric Theory of the Chemical Bond. *Physical Review Letters* **26,** 184–188 (4 Jan. 1971).
434. Mooradian, A. & Wright, G. B. First order and Raman effect in III-V compounds. *Solid State Communications* **4,** 431–434 (1966).
435. Kiefer, W., Richter, W. & Cardona, M. Second-order Raman and scattering in InSb. *Physical Review B* **12,** 2346–2354 (1975).

Selbstständigkeitserklärung

Hiermit versichere ich, dass ich die vorliegende Arbeit mit dem Titel *Integration of III-V compound nanocrystals in silicon via ion beam implantation and flash lamp annealing* selbstständig und ohne unzulässige Hilfe Dritter verfasst habe. Es wurden keine anderen als die in der Arbeit angegebenen Hilfsmittel und Quellen benutzt. Die wörtlichen und sinngemäß übernommenen Zitate habe ich als solche kenntlich gemacht. Es waren keine weiteren Personen an der geistigen Herstellung der vorliegenden Arbeit beteiligt. Mir ist bekannt, dass die Nichteinhaltung dieser Erklärung zum nachträglichen Entzug des Hochschulabschlusses führen kann.

Dresden, 21. März 2017

Rene Wutzler